

**DAMPING HIGHER ORDER MODES IN THE  
PEP-II B-FACTORY STORAGE RING COLLIDER**

By

Stephen Weathersby

A DISSERTATION

Submitted to  
Michigan State University  
in partial fulfillment of the requirements  
for the degree of

DOCTOR OF PHILOSOPHY

Department of Physics and Astronomy

2007

# Abstract

## DAMPING HIGHER ORDER MODES IN THE PEP-II B-FACTORY STORAGE RING COLLIDER

By

Stephen Weathersby

The PEP-II B-Factory storage ring collider at SLAC provides crucial experimental evidence for the physics of CP violation. To investigate rare B-meson decays requires high luminosity which comes mainly from increasing bunch currents and reducing bunch sizes. Electromagnetic effects of intense bunch fields in the form of wake fields couple into accelerator components, inducing Joule heating at levels detrimental to vacuum chamber components. Additionally, wake fields contribute to beam instability, decreasing luminosity. These effects are limiting B-factory performance.

Computer simulations and experimental evidence indicate that beam collimators produce wake fields in the form of dipole and quadrupole waveguide modes which can propagate tens of meters from their source before depositing energy at remote locations. Simulations confirm that coupling through narrow slots into bellows cavities occurs for beam pipe modes.

Two proposals are set forth to mitigate wake field effects. The first proposal is to reduce the quality factor of resonant structures with a water cooled dielectric lossy material. Electromagnetic energy coupling into resonant structures can be isolated and safely dissipated. Prototype devices have been built and have been shown to reduce resistive heating in large pumping chambers coupled to the beam chamber. Designs and simulations which incorporate such techniques into bellows devices are presented.

The second proposal incorporates novel devices introduced in the accelerator vac-

uum chamber which selectively traps dipole and quadrupole propagating wake fields before they can couple into sensitive beam line components without introducing impedance to the beam. Scattering parameter analysis is used to tailor device response to specific modes. Dangerous modes are extracted from the beam chamber, trapped and dissipated in a water cooled lossy material. Modes which represent an impedance to the beam are not affected. After design optimization, production and installation, beam line devices registered a factor of two decrease in electromagnetic heating in the vicinity of the installed device.

Methods for reducing harmful wake field effects resulting from intense charge densities have been demonstrated. This enables the higher bunch currents and shorter bunch lengths required to achieve productive B-factory operations at the highest possible luminosity.

To Thomas and Chiyoko Weathersby

# ACKNOWLEDGMENTS

First and foremost I am grateful and honored to have as my SLAC advisor and VUBeam mentor Alexander (Sasha) Novokhatski, who has showed me how to look through difficult problems to the underlying simple physical processes and whose ideas form the basis for this work. His guidance and friendship has been influential in my accomplishments and has shaped and matured my perspectives and appreciation of the subject matter.

I am much indebted to Michigan State University, in particular to MSU major professors Martin Berz and Kyoko Makino whose gracious encouragements have propelled me to complete the VU Beam program. I wish to thank the staff and graduate students of the MSU Physics and Astronomy Department for their assistance, advice and hospitality.

I would like to thank John Seeman, Nadine Kurita, Jay Langton, Ho Dong, and Nick Reek for sponsoring this work and ultimately making our collective ideas a reality.

I would like to thank Michael Stanek, Roger Erickson and the Accelerator Operations Department staff at Stanford Linear Accelerator Center for the invaluable experience I have gained working those many years in the control room, along with their encouragement and at times, sacrifices made for my benefit during these educational pursuits.

Many thanks to John Seeman, Michael Zisman, and Patrick Krejcik, who first launched me on this journey.

A very special thanks to Victoria Schwerin, my partner in life, who shares my trials and tribulations with patience, understanding and steadfast optimism.

# Contents

<b>List of Tables</b>	<b>viii</b>
<b>List of Figures</b>	<b>ix</b>
<b>1 Introduction</b>	<b>1</b>
1.1 Electromagnetic Effects of Intense Charged Particle Beams . . . . .	1
1.2 The PEP II Asymmetric B-Factory . . . . .	4
1.3 The SLAC Injector . . . . .	7
1.4 Charge-Parity (CP) Violation . . . . .	7
1.5 Luminosity . . . . .	9
1.6 Collision Cross Section and Bunch Length Effects on Luminosity . . .	10
1.7 Scope of Work . . . . .	11
<b>2 Wake Fields and Higher Order Modes</b>	<b>14</b>
2.1 Relativistic Beam Fields . . . . .	14
2.2 Wake Fields and HOMs . . . . .	20
2.3 Surface Currents . . . . .	29
2.4 Wake Field Sources . . . . .	30
2.5 Coupled Bunch Instability . . . . .	33
2.6 Bunch Length and Bunch Spacing . . . . .	34
2.7 Machine Performance Limitations . . . . .	35
2.8 Bellows . . . . .	36
2.9 IP Vertex Bellows . . . . .	39
2.10 NEG Pumps . . . . .	39
2.11 BPMs . . . . .	41
2.12 HOM Measurements . . . . .	42
<b>3 Method of Calculation</b>	<b>45</b>
3.1 Numerical Tools . . . . .	45
3.1.1 The Finite Integration Technique . . . . .	46
3.1.2 NOVO[14] Wake Field Calculations . . . . .	57
3.2 Mode Analysis . . . . .	61
3.2.1 Pillbox Cavity Analysis . . . . .	62
3.2.2 $Q$ factor . . . . .	67
3.2.3 Bellows Modes . . . . .	74
3.2.3.1 A Simple Coax Model . . . . .	75
3.2.3.2 Coupling Studies . . . . .	76
3.2.3.3 Slot Width and Coupling . . . . .	79

3.3	Scattering Parameter . . . . .	82
3.3.1	Method . . . . .	83
3.4	Wake Field Computations . . . . .	89
3.4.1	Vertex Chamber Wake Fields . . . . .	92
3.4.2	Power in the Bellows . . . . .	94
3.4.3	Collimator Wake Fields . . . . .	97
3.4.3.1	Collimator Loss Factor . . . . .	101
3.4.4	Dual Collimator Wake Field Analysis . . . . .	103
3.4.4.1	Dual Collimator Loss Factor . . . . .	103
<b>4</b>	<b>Results and Analysis</b>	<b>105</b>
4.1	LER Region 4 HOMs . . . . .	105
4.1.1	LER Arc Ante-Chamber Absorber . . . . .	113
4.1.2	Collimator HOM Experiment . . . . .	116
4.1.3	Straight Bellows Absorber Device . . . . .	117
4.1.3.1	Operational Results with the Straight Absorber Device	122
4.2	Interaction region HOMs . . . . .	130
4.2.1	Q2 Bellows Absorber Device . . . . .	132
4.2.2	High Efficiency Absorber for the Interaction Region . . . . .	142
4.2.3	LER Q4 Bellows Absorber . . . . .	147
4.2.4	Vertex Bellows Absorber . . . . .	150
4.2.5	Vertex Bellows 2-Dimensional Calculations . . . . .	151
4.2.6	IP Vertex Bellows Q Factors . . . . .	157
4.2.7	Introduction of Absorbing Media in the Existing Vertex Bellows	157
4.2.8	New Vertex Bellows Proposals . . . . .	162
<b>5</b>	<b>Conclusion</b>	<b>164</b>
5.1	Plans and Future Work . . . . .	166
	<b>APPENDICES</b>	<b>169</b>
<b>A</b>	<b>Properties of Some Lossy Dielectrics</b>	<b>169</b>
<b>B</b>	<b>BPM Scattering Parameters</b>	<b>172</b>
	<b>Bibliography</b>	<b>173</b>

# List of Tables

3.1	MAFIA and analytic evaluation of frequency for several modes of a copper pillbox cavity of radius 0.06858 m and length 0.0889 m. Mesh size .001 m with 6 iterations and 15 modes. Third column contains the fractional difference. . . . .	70
3.2	MAFIA and analytic $Q$ factor evaluation for several modes of a copper pillbox cavity of radius 0.06858 m and length 0.0889 m. Mesh size .001 m with 6 iterations and 15 modes. Third column contains the fractional difference. . . . .	70
4.1	Mode frequencies for the vertex bellows cavity. The second and third column frequencies correspond to additional nodes in the longitudinal dimension. The calculation assumes cylindrical symmetry. . . . .	152

# List of Figures

1.1	Beam lines of the Stanford Linear Accelerator Center. The PEP-II injection lines are extracted from the main linac at the 4 GeV and 9 GeV points respectively for the low energy positron ring (LER) and the high energy electron ring (HER). . . . .	6
1.2	Luminosity enhancement from shortening bunch lengths. Transverse cross section $A$ is reduced by increasing angular divergence with magnetic focusing (left picture). Shorter bunch lengths increase the fractional longitudinal overlap in the region of the common volume where the transverse size is small. (right picture). . . . .	10
2.1	Coordinates of a moving charge $Q$ in the lab frame $K$ and in the charge rest frame $K'$ moving along the $z$ axis at velocity $v$ . Observer is at point $P (b, 0, 0)$ in the lab frame. . . . .	17
2.2	Electric field $\vec{E}$ for a relativistic particle of charge $Q$ and velocity $v$ in a beam pipe has an opening angle of about $1/\gamma$ and surface charges (-) at the beam pipe surface where the electric field lines terminate. . . .	19
2.3	Electric field lines of wake fields produced by a 1.8 mm bunch traversing a PEP RF cavity from a NOVO[14] simulation. Courtesy A. Novokhatski[17]. The bunch is travelling to the right in this picture. .	21
2.4	Illustration of relativistic beam wake field interaction. Wake fields excited by a relativistic point charge $Q$ catch up with the charge after a time $t$ . $b$ : the distance from the beam axis to the wake field source. $c$ : speed of light. $v$ : velocity of the bunch. . . . .	23
2.5	Depiction of wake fields excited by the bunch head catching up with bunch particles at a distance $s$ following the bunch head. $b$ : the distance from the beam axis to the wake field source. $c$ : speed of light. $v$ : velocity of the bunch. $t$ : time at which wake fields catch up to trailing particles at a distance $s$ behind the bunch head. . . . .	24

2.6	Frames in a simulation of relativistic bunch fields approaching and interacting with an iris. At time $T_2$ , part of the bunch fields are severed by the iris, becoming independent wake fields. Bunch fields are distorted at the iris. . . . .	27
2.7	Bunch field distortion begins to propagate along bunch force lines. Tail bunch particles are first to be affected where a longitudinal field is developing. A significant fraction of the wake fields are propagating in the opposite direction. . . . .	27
2.8	Wake fields are produced at the corner where the beam pipe and iris intersect. Some of these will propagate in the beam direction. Bunch particles begin to interact with the bunch field distortions as the distortions arrive at the bunch particle positions. At this time bunch particles are losing energy to the longitudinal forces. . . . .	28
2.9	Bunch fields are starting to recover their radial orientation as wakes fields chase the bunch. . . . .	28
2.10	Decomposing the total field (left) into wake fields and bunch field distortion (center) and the initial bunch field. The field energy which goes to wake fields is opposite to the energy of the bunch field distortion. Courtesy A. Novokhatski . . . . .	29
2.11	Charge $Q$ moving at speed $v_z c$ in a cylindrical vacuum chamber of radius $a$ surrounded by a dielectric cylinder of radius $b > a$ . Electric field lines are bent at the dielectric/vacuum interface. . . . .	32
2.12	Electric force lines from a relativistic Gaussian beam in a dielectric canal computed with a modified NOVO[14] program for two different canal dielectric constants. From [39]. . . . .	33
2.13	Spectrum of a beam position monitoring electrode signal for a bunch spacing of 4.2 ns and bunch length of 1.2 cm. Spectrum is dominated by spikes at the bunch spacing harmonics extending up to 13 GHz. Courtesy A. Novokhatski. . . . .	35
2.14	Simplified illustration of a generic bellows. Gaps between the fingers are exaggerated for this illustration. The inboard fingers are springs which maintain electrical contact to the outboard fingers. Typically the springs will press the outer fingers against an outer sleeve (not shown). . . . .	37

2.15	HER bellows temperature in Fahrenheit as a function of HER current in mA. The bellows exhibits a HOM driven resonance above 1.0 A of HER current. . . . .	38
2.16	Detailed cut-away of a NEG pump in the interaction region. The NEG material is in the form of stacked wafers. The NEG chamber is separated from the beam chamber by a shielding perforated screen through which HOMs enter the NEG chamber. Courtesy L. Bertolini et al[41]. . . . .	40
2.17	1/4 symmetry beam position monitoring (BPM) structures with and without button. Loss of the button reveals a cavity and protruding stem on which the button was mounted. . . . .	41
2.18	Interaction HOM spectra from a gated BPM signal. Circled peaks show amplitude correlation with detector bellows thermocouple readings. Courtesy A. Novokhatski. . . . .	43
2.19	HOM $I^2$ dependence of extracted HOM power from a LER NEG pumping chamber. Courtesy A. Novokhatski. . . . .	44
3.1	Representation of a cylindrical cavity for numerical electromagnetic calculations using the finite integration theory. The left picture depicts a 3D representation of the metal (dark material) and cavity volume. The right picture is a 2D projection indicating the ideal curved inner surface and the cellular approximation. The empty cavity is also composed of cells given characteristics of vacuum. . . . .	47
3.2	One cell of a grid used in the Finite Integration Technique. The sides and faces are assigned with electric and magnetic field components. . . . .	48
3.3	Interlaced electric and magnetic grid construction for the Finite Integration Technique showing the assignment of quantities associated with Maxwell's equations 3.1 and 3.3. . . . .	53
3.4	Interlaced electric and magnetic grid construction for the Finite Integration Technique showing the assignment of quantities associated with Maxwell's equations 3.2 and 3.4. . . . .	54
3.5	Coupling primary and dual grid quantities through the constitutive relations. . . . .	55

3.6	Cylindrical pillbox cavity geometry. Cavity length is $g$ , radius $R$ in cylindrical coordinates $(r, \phi, z)$ . . . . .	63
3.7	MAFIA fractional frequency error $ f_M - f_A /f_A$ relative to analytic results versus mesh cell size for several modes where $f_M$ is the frequency determined from MAFIA and $f_A$ is the analytical value. Six iterations searching for 15 modes with a uniform cubic mesh. Pillbox example of radius $r = 0.06858$ m and length $g = 0.0889$ m . . . . .	65
3.8	Log-log plot of MAFIA CPU time in seconds for pillbox modes computation versus mesh cell size in meters. Six iterations searching for 15 modes. Pillbox example of radius $r = 0.06858$ m and length $g = 0.0889$ m. . . . .	66
3.9	Current $I$ flowing in a small pillbox cavity conductive wall element of area $dx \cdot dl$ with a skin depth $\delta$ as a result of tangential magnetic field $\vec{H}$ . 69	
3.10	Stair case approximation for pillbox cavity geometry generated by MAFIA[13]. . . . .	71
3.11	Two views of the TM010 mode magnetic fields in a pillbox cavity calculated with MAFIA[13]. Left $y$ - $z$ plane. Right $x$ - $y$ plane. The field is constant on the cylindrical conductor surface $r = R$ , and has a Bessel function $J_1$ radial dependence. . . . .	72
3.12	$Q$ factor vs mesh cell size for the TM010 mode. Six iterations searching for 15 modes. . . . .	73
3.13	$Q$ factor vs number of iterations for the TM010 mode. Mesh cell size .0025 m searching for 15 modes. . . . .	73
3.14	Dipole mode in a 3D coax model of a bellows cavity. . . . .	75
3.15	Dipole electric field modes in a simulated beam chamber and bellows chamber. Dimensions in meters. . . . .	77
3.16	Geometry for the dipole coupling studies showing the beam cavity, bellows cavity and slots. Only half of this geometry is used in the quadrupole studies. . . . .	78
3.17	Variation of beam and bellows cavity dipole mode frequencies and their differences as a function of beam cavity chamber length. Strength of the coupling is related to the minimum separation of .075 GHz. . . .	79

3.18	Variation of beam and bellows cavity quadrupole mode frequencies and their differences as a function of beam cavity chamber length. Strength of the coupling is related to the minimum separation of 0.23 GHz. . .	80
3.19	Minimum mode separation vs fractional slot width for constant slot length. The data is fit to a analytic expression derived from the polarizability of small apertures. . . . .	81
3.20	Device under test placed in a uniform circular waveguide between two ports. The ports are simulated as infinitely long waveguides. The device consists of a cavity filled with a high permittivity lossy dielectric absorbing media coupled to the beam pipe waveguide by slots. . . . .	86
3.21	Waveguide electric field eigenmodes for scattering parameter port excitation . . . . .	86
3.22	Port signal amplitudes vs time in seconds. p1_in is the input or excitation signal into port 1. p1_out is the signal reflected back from the device out of port 1. p2_out is the signal transmitted from port 1 which comes out of port 2. . . . .	87
3.23	FFT of port signals for the dipole mode excitation. 2out=port 2 output spectrum, 1out=port 1 out spectrum, 1in=port 1 input excitation spectrum. . . . .	88
3.24	Scattering parameters $s_{11}$ , $s_{21}$ and absorption $1 - s_{11}^2 - s_{21}^2$ for a dipole mode excitation as a function of frequency. . . . .	88
3.25	Illustration of point charge $Q_1$ fields scattering from a vacuum chamber irregularity generating wake fields $\vec{E}$ , $\vec{B}$ which interact with a witness charge $Q_2$ following at a distance $s$ . . . . .	90
3.26	Layout of the IP vertex chamber showing beam trajectories and synchrotron radiation masks in upstream LER. Dimensions are in mm. .	93
3.27	Upstream LER model for IP wake computation with simulated bellows and coupling slots. . . . .	94
3.28	Straight pipe model for IP wake field comparison with the same simulated bellows and coupling slots as in the model of figure 3.27. . . . .	95

3.29	IP vertex chamber (top) and comparable straight pipe model (bottom) and the electric field pattern snap shots after passage of 1.3 cm Gaussian 14 nC line charge. Snap shots are from the same time frame of the simulation. No coupling was evident at any time for the straight pipe model . . . . .	96
3.30	Axially symmetric profiles for NOVO 2d wake potential computation. Dimensions are in mm. . . . .	97
3.31	Longitudinal wake potentials calculations using 3d MAFIA for the vertex chamber model of figure 3.27 (circles) and 2d NOVA with the top axial symmetric profile in figure 3.30 (solid line) along with the 1.3 cm Gaussian bunch charge distribution (dashed line) as a function of distance in the bunch frame. . . . .	98
3.32	Cross section views of a tapered collimator model for wake field analysis with dimensions in meters. Computational length is 1.4 m. Collimator height is 0.033 m. Beam pipe diameter is 0.088 m. . . . .	99
3.33	Collimator mesh with dipole and quadrupole fields after the passage of a 1.4 cm long Gaussian bunch past the single tapered collimator structure at the downstream end. These are two snapshots at the same location separated in time. The quadrupole component dominates at shorter time scales. The dipole mode persists at longer times. Collimator length and height: 0.6 m $\times$ .033 m. . . . .	99
3.34	Poynting vector flux $\frac{1}{\mu_0} \int (\vec{E} \times \vec{B})_z da$ through upstream (solid) and downstream (dashed) locations from a single collimator as a function of time in seconds. First large pulse indicate the passage of the beam. Negative values correspond to propagation in the upstream direction. The upstream and downstream monitoring planes are 1.3 m apart. . .	100
3.35	Collimator loss factor as a function of bunch length. . . . .	101
3.36	Loss factor as a function of vertical and horizontal beam position at the vertical collimator. . . . .	102
3.37	Dual collimator configuration. . . . .	103
3.38	Poynting flux $\frac{1}{\mu_0} \int (\vec{E} \times \vec{B})_z da$ upstream and downstream of dual collimator structure during and after passage of 14 nC Gaussian bunch of 1.3 cm sigma vs time in seconds. . . . .	104

3.39	Snap shot of electric field pattern at a downstream end of the dual collimator structure 7 nS after passage of 14 nC 1.3 cm long Gaussian bunch show a predominantly quadrupole component persisting at long time scales. . . . .	104
4.1	PEP ring region 4 straight to arc transition layout. Circled area indicates location of HOM heating, 15 meters downstream of the straight collimator section. The LER beam moves counter clockwise in the diagram. . . . .	106
4.2	Photo of the region 4 straight to arc transition, where excessive HOM heating is observed. Vacuum chamber changes from circular to elliptical cross section at the bellows, shown surrounded with cooling fans. . . . .	107
4.3	Hot bellows located at PR04:2012, 15 meters downstream of a collimator in a straight section of the low energy ring. Substantial air cooling installed in the form of fans which blow air into the bellows convolutions. . . . .	108
4.4	LER arc ante-chamber cross section diagram. As the beam is bent synchrotron radiation follows a path from the beam chamber through the x-ray slot into the pump out chamber where it is intercepted by a water cooled photon stop. The x-ray slot couples HOMs into the pump chamber. . . . .	109
4.5	Photograph showing LER ante-chamber in an arc section of the PEP-II beam lines with attached cylindrical Titanium sublimation pump (TSP). . . . .	110
4.6	Location of damaged TSP feed through in LER region 4. Escaping HOMs can be detected with small lossy dielectric and antenna. . . . .	111
4.7	Spectrum from the antenna placed in the PEP-II tunnel near the Ti sublimation pump feed through at PR04:1163 with 1.6 A of LER beam. Marked modes correlate with the temperature of the small lossy ceramic detector. Courtesy A. Novokhatski. . . . .	112

4.8	Picture of prototype LER ante-chamber absorber and measured power extracted at two locations. At nominal currents over 1 kW of power is extracted with the arc ante-chamber absorber device at PR04:2010. Top right picture shows the installation in the ante-chamber pump port. The small squares are absorber material brazed to copper support columns flanked by a stainless steel water cooling pipe (right bottom). The device is angled at the pump port to extend toward the center of the ante-chamber. . . . .	114
4.9	Pump temperature reduction attributable to LER antechamber water cooled absorber of figure 4.8. Reduction of a factor of two in temperature rise for the same current. . . . .	115
4.10	Power extracted from the ante-chamber absorber and vertical beam position at two vertical collimators located 15 and 65 meters upstream of the absorber as a function of time. In both cases moving the beam away from the collimator reduces extracted power at the ante-chamber absorber. . . . .	117
4.11	Absorption $1 - s_{11}^2 - s_{21}^2$ of the optimized straight bellows absorber and a section of the computational model. Slot length: 70 mm. Slot width: 6 mm. Absorber thickness: 16.7 mm. . . . .	120
4.12	Straight bellows absorber mechanical design showing absorber material behind coupling slots. Absorber is brazed to a water cooled copper jacket. Adjacent bellows cavity is exposed to the absorber to also damp bellows modes. . . . .	121
4.13	Assembled straight absorber device ready for installation. Here ceramic absorber tiles can be seen under copper coupling slots next to an array of bellows fingers. . . . .	122
4.14	Straight absorber device as installed in the low energy ring beam line showing copper cooling lines for removing absorber HOM power. Small wires are thermocouples attached to the water supply and return lines. Note that the adjacent bellows no longer needs air cooling. Immediately to the right of the bellows is vacuum valve 2015. . . . .	123
4.15	Straight bellows absorber device location with respect to upstream vertical collimator at the end of the straight section of the LER. The straight bellows absorber device is 15 meters downstream of the collimator. . . . .	124

4.16	Section of straight to arc transition in LER immediately downstream of the straight bellows absorber device. Vacuum valve 2015 is immediately to the left in the photo. . . . .	125
4.17	Top plot: Thermocouple reading ( $^{\circ}\text{F}$ ) at the overheating bellows 2012 before and after straight absorber device installation shows a factor of two decrease in temperature rise after installation of the straight bellows absorber on May 1, 2006. . . . .	126
4.18	HOM power extracted from an arc ante-chamber absorbing device as a function of LER current before and after installation of the straight absorber system. Data is quadratic with current with coefficients of 145 and 82 W/ $\text{mA}^2$ for data before and after installation of the straight bellows absorber device. This represents a reduction of 42% in HOM power infiltrating the ante-chamber. . . . .	127
4.19	HOM power extracted from the straight bellows absorbing device as a function of LER current for two values of LER gap voltage. The upper trace was taken at a gap voltage of 4.5 MV, the lower trace at gap voltage of 4.05 MV. . . . .	128
4.20	Additional straight absorber devices deployed in region 4 straight section of LER. Left photo show an installation at PR04:2032 to take power from upstream horizontal collimator at PR04:2041 which is 4.5 meters away. Right photo shows a straight absorber device installation at PR04:2072 which takes power from upstream horizontal collimator PR04:2081 which is 5 meters away. . . . .	128
4.21	Photo of the region 10 straight bellows absorber device located at PR10:2145 between two horizontal momentum collimators 5 meters away on either side of the device. . . . .	129
4.22	A 3D cut-away of the interaction region and the BaBar detector showing detector systems and combined magnet and vacuum chamber assemblies Q2, Q4, Q5 which are interconnected by bellows modules. The vertex bellows are situated well within the detector. . . . .	131
4.23	Mechanical drawing of Q2 bellows area. Q2 bellows is immediately adjacent to the crotch where the two beam lines merge. Dimensions are in mm. . . . .	132

4.24	Existing Q2 bellows chamber with ceramic absorbing tiles braised to copper support columns. The bellows is located between the two sets of ceramic absorbing tiles. The tiles are fully exposed to the beam fields.	133
4.25	Existing Q2 bellows module computational scattering parameter model and the waveguide mode electric field patterns. There are two dipole mode polarizations designated <i>dipole</i> and <i>dipole-</i> . The bellows are not included.	135
4.27	Computational model of existing Q2 bellows module with the addition of coupling slots above the absorbing tiles on both sides of the bellows (not shown).	136
4.26	Absorption spectra for the existing Q2 chamber model (middle) of figure 4.25 for the monopole, dipole, dipole second polarization ( <i>dipole-</i> ) and quadrupole excitation. The absorption (abs=) is quantified as the mean of the absorption over the range contained within the vertical lines spanning the cutoff frequency and the highest excitation frequency. The high value for the monopole absorption indicates a potential for beam impedance.	136
4.28	S-parameter absorption for the configuration of coupling slots added to the Q2 existing bellows model of figure 4.27. This configuration successfully reduces monopole mode absorption, but also reduces dipole and quadrupole mode absorption.	137
4.29	Computation model for incorporating coupling slot length into the bellows finger geometry with a center ring for structural support. Dimensions shown are in inches.	138
4.30	Absorption for the model of figure 4.29. The bellows shielding fingers are adapted to provide additional slot length to increase the effective dipole and quadrupole coupling.	139
4.31	Summary of absorption vs slot length for both dipole modes and the quadrupole mode. The two dipole modes are designated <i>dipole1</i> and <i>dipole2</i> . Horizontal dashed lines are existing exposed tile configuration absorption (/open). The open circles indicate slot length required to achieve existing absorption for each mode (break even). Small solid circles are the absorption values for the full slot length with the structural support ring configuration of figure 4.29.	140

4.32	New Q2 bellows HOM absorbing device. Bellows is moved to one side to consolidate slot and absorber length. Ceramic absorbing material is depicted in blue. Coupling slots are 3.4 inches long. . . . .	141
4.33	High efficiency absorber device model (top) and absorption spectra (bottom). Slot length 8.3 inches, slot width 0.09-0.13 inches. Absorber thickness is 0.23 inches. Dimensions are in inches. The short axis dipole mode is not well absorbed at only 25% compared to the long axis absorption of 63%. . . . .	143
4.34	Optimized high efficiency absorbing device (top). Modified slot length, and absorber geometry to enhance short axis dipole absorption. Slot length is 9.3 inches. Slot width 0.09 to 0.13 inches. Absorber thickness 0.5 inches at the short axis, 0.23 inches at the long axis. Absorber volume is removed at the corner to simplify fabrication. This device features 54% short axis dipole mode absorption (bottom). . . . .	145
4.35	Mechanical drawing of high efficiency absorbing device based on optimized model of figure 4.34 Absorbing tiles are brazed to copper support columns embedded in a copper block with water cooling channels. . . . .	146
4.36	Photograph of installed high efficiency absorbing device in the upstream LER interaction region. The device is flanked by two bellows modules which are cooled by external fans. The high efficiency absorber is expected to reduce heating of a nearby NEG pumping chamber. . . . .	146
4.37	Q4 bellows model version 3 and quality factors with and without absorber. . . . .	147
4.38	Electric field plot of 2.14 GHz high $Q$ mode in the Q4 bellows model version 3. High field strength is far from absorbing tiles. . . . .	148
4.39	Q4 bellows model version 5 and quality factors with and without absorber. . . . .	149
4.40	Mechanical design for the Q4 bellows absorbing device. Photo of installed Q4 bellows absorbing device at the downstream LER side of the IP. . . . .	149
4.41	Vertex bellows picture and schematic. Collisions occur 20 cm to the right of the bellows. Beam pipe diameter is about 5 cm. . . . .	150

4.42	FFT of a gated oscilloscope BPM button signal in the gap between bunch trains. The circled peaks at 4.6 and 5.4 GHz show amplitude correlation with the vertex bellows thermocouple temperature. Courtesy A. Novokhatski. . . . .	152
4.43	Monopole mode magnetic field energy density integrated over $2\pi$ radians of azimuth calculated with the NOVO[14] program. Lighter shades are higher density. . . . .	153
4.44	Dipole mode magnetic field energy density integrated over $2\pi$ radians of azimuth calculated with MAFIA[13]. The highest intensity is at bellows convolutions. . . . .	154
4.45	Quadrupole magnetic field energy density integrated over $2\pi$ radians of azimuth calculated with MAFIA[13]. The highest intensity is at the bellows convolutions. . . . .	155
4.46	Magnetic field patterns at two azimuthal planes $\phi = 0$ and $\phi = \pi/2$ , illustrating high intensity at regions of longitudinal variation for the dipole mode. . . . .	156
4.47	Existing vertex bellows model (Control) eigenmode and $Q$ factors assuming stainless steel material. . . . .	158
4.48	Modes calculated for absorber placed near bellows convolutions. The absorber material is shown as a cross section of an annular ring or washer of ceramic absorbing material placed on a flange near the bellows convolutions. Left picture shows a mode which the absorber does not touch and consequently is not damped. Right picture shows a low frequency mode trapped in the absorber. Bellows walls assumed to have the conductivity of copper. $Q$ values for this configuration are given in figure 4.53. . . . .	159
4.49	$Q$ factors for absorber placed near bellows convolution flange and the existing control configuration with no absorber. Existing vertex bellows modes are not appreciably damped. Lower frequency low $Q$ modes are new modes trapped in the absorber. Bellows walls assumed to have the conductivity of copper. . . . .	160

4.51	Absorber above fingers (inset) and comparison of $Q$ factors. This configuration works best to damp existing bellows modes. $Q$ factors with absorbers of various radial thickness are presented, indicating better damping is achieved with progressively thicker absorbers. Bellows walls assumed to have the conductivity of copper. . . . .	160
4.50	Absorber on flange near fingers (inset) and effect on Cu bellows $Q$ factors. Data shown with absorber thickness of one and two millimeters. Most of the existing $Q$ factors are not appreciably damped in this configuration. Bellows walls assumed to have the conductivity of copper.	161
4.52	Large (left) and small (right) aspect ratio absorber configuration models for the vertex bellows. The absorbing ceramic is shown supported by copper columns which aid in thermal stress relief and thermal conductivity. . . . .	163
4.53	$Q$ factors vs frequency for the stainless steel vertex bellows absorber configurations large (*) and small (x) aspect along with existing bellows $Q$ factors (Control +). . . . .	163
A.1	Properties of lossy dielectric ceramic microwave absorbers from Cera-dyne, Inc. . . . .	170
A.2	Properties of lossy dielectric ceramic microwave absorbers from Cera-dyne, Inc. . . . .	171
B.1	1/4 symmetry BPM structures with and without button. Loss of the button reveals a cavity and protruding stem on which the button was mounted. . . . .	172
B.2	Scattering parameters $s_{11}$ , $s_{21}$ and absorption $1 - s_{11}^2 - s_{21}^2$ for BPM with intact button for the monopole waveguide mode. Signals at less than 5 GHz and greater than 8 GHz are outside the excitation range. No absorption is seen for the missing button case. . . . .	174

# Chapter 1

## Introduction

### 1.1 Electromagnetic Effects of Intense Charged Particle Beams

Concentrated bunched relativistic charged particle beams generate intense electromagnetic fields which interact with their surroundings. These interactions can be utilized to manipulate the beam energy as in an RF cavity. Often, interactions of this type can dissipate destructive amounts of energy into accelerator structures. These interactions have become evident as charged particle intensities are increased to meet current storage ring physics demands. Such effects are limiting performance of the current generation of B-factory storage ring colliders and will be a concern for future generations of high current charged particle storage ring light sources.

Beam generated electromagnetic fields will couple to parasitic resonances in beam line structures where resistive heating can cause damage, often resulting in a catastrophic vacuum breach. Additionally such fields will interact back on the beam, inducing instability. Current generation storage rings are designed and upgraded to mitigate these effects to some degree, but at currents of several amperes, destructive levels of electromagnetic energy persist.

This dissertation seeks a deeper understanding of beam induced electromagnetic

energy in storage ring accelerators with the aim of developing new mitigating measures to control and eliminate its destructive tendencies. This is in hopes of enabling storage ring physics programs to progress at higher levels of efficiency and productivity. The PEP-II B-factory at the Stanford Linear Accelerator Center provides an ideal case study for this work.

Beam induced electromagnetic effects are documented in the accelerator literature [32, 33, 42, 22]. Some simple idealized problems have closed solutions, and the computational problem for all but the most simple geometries is numerically complex. One of the most important means to quantify the beam-accelerator interaction is the *loss factor* or *loss parameter*  $k$  which relates the amount of electromagnetic energy dissipated in a structure by a charged particle bunch to the bunch charge. It depends on the structure geometry, materials and the bunch charge distribution and trajectory. For a given accelerator structure the loss factor is defined as the amount of energy lost by the beam per unit of beam charge squared and is quoted in volt per pico-Coulomb [ V/pC]. For simple beam pipe geometries analytical formulas and approximations exist. Typical values for PEP-II RF cavities are 0.5 V/pC. For practical accelerator structures computational techniques are employed. Intense beam current accelerators should incorporate loss factor minimization in the design process wherever possible to prevent beam instability and RF heating.

Beams lose energy to accelerator structures through *wake fields*. As surface charges on the walls of the beam pipe follow the beam, disruptions in the pipe geometry give rise to surface charge radiation. This radiation reacts back on the beam. These wake fields are also known as *higher order modes* or (*HOMs*). Some basic approaches of evaluating wake field effects are outlined:

- Evaluation of energy loss from cavity modes: This is applicable to cavity-like structures for which the cavity resonant modes are known. Wake fields are expressed in terms of a superposition of normal modes. Each mode has a specific

loss factor which is evaluated from the electric field along the bunch path. The total energy loss/gain a bunch sees from a structure can be given in terms of a summation over mode loss factors. The effects of the beam pipe apertures are not taken into account. Resonant mode frequencies and fields must be known to high frequencies for accurate loss factor calculation[33].

- Wake field calculations: This requires a time domain solution of Maxwell's equations for the problem of a bunch traversing an accelerator structure. Each particle sees the scattered fields caused by the geometry of the structure (wake fields) from previous beam charges and gets a resultant potential change (wake potential) after passage through the structure. The loss factor for the structure can be evaluated given the bunch charge distribution and the wake potential. This is a more general approach which is applicable to arbitrary geometries but is computationally intensive and susceptible to numerical error[37]. Consideration must be given to the effect of the boundary of the computational domain through which a relativistic charge must pass [43].
- Scattering parameter approach: This approach considers wake fields as a sum of orthogonalized beam pipe propagating waveguide modes. The loss factor can then be evaluated in terms of the effect of the individual waveguide modes. In analogy to electrical network analysis the waveguide boundaries are matched to the particular mode to eliminate reflection errors that occur with the previous two methods. This method is computationally simpler than the wake field calculation and well suited to evaluating propagating wake field effects in arbitrary geometries.

The above analysis methods and experimental observations reveal certain aspects of electromagnetic effects of intense beams in accelerator structures which are important in considering mitigating measures. In particular, it is determined that wake field

sources such as collimators generate power which can propagate large distances away and affect remote components, a fact that is verified experimentally[9]. Additionally, a coupling mechanism exists for these propagating wake fields[7]. Based on these results, research progressed along two paths:

- Remove power from affected components: When wake fields couple into resonant structures dangerous resistive heating occurs. Introduction of a high permittivity absorbing medium can reduce the quality factor of the resonant modes and contain the electromagnetic energy. The analysis methods above are utilized in the design of devices to isolate and extract this power from affected components.
- Remove wake fields from the beam pipe: A superior solution involves the extraction of propagating modes from the beam pipe before they reach sensitive components. Introducing a device into the beam pipe has the undesirable potential of presenting added impedance to the beam which can detrimentally affect beam stability. The scattering parameter analysis is instrumental in designing an effective wake field extraction device with minimal beam impedance.

Devices incorporating these features have been designed and tested in the PEP-II B-factory storage ring collider. HOM absorbing devices are shown to be effective in removing HOM energy from affected devices using these two methods. These successes have initiated further efforts at reducing HOM effects in the IP area where HOM producing elements are concentrated and stringent mechanical tolerances constrain the usable volume. New devices have been built and will be installed which feature optimized absorbing capabilities and minimized beam impedance characteristics specifically designed for the IP region.

## **1.2 The PEP II Asymmetric B-Factory**

The PEP-II B-factory is a storage ring collider designed to investigate charge-parity violation in B-meson decays. It consists of two independent storage rings designated

LER (Low Energy Ring) and HER (High Energy Ring). The LER stores up to 2.8 A of 3.1 GeV positrons and is physically mounted above the HER except at the interaction point (IP) where the two beams share a common beam chamber. The BaBar detector surrounds the IP. The HER stores up to 1.8 A of 9 GeV electrons.

The two rings have a circumference of 2.2 km in the configuration shown in figure 1.1. A series of magnetic dipoles in each ring confine the beams to a circulating trajectory. The circulating beams of charged particles will radiate synchrotron radiation. This is the main source of energy loss which amounts to several megawatts at maximum currents. RF Cavities in the straight sections replenish lost energy with 476 MHz CW RF. The stored beams consist of up to 1700 bunches nominally separated by twice the RF frequency, or about 4.2 ns. There is a gap with no bunches in the bunch pattern for the ramp up time of the machine protection abort kicker. Bunch lengths are of the order of 0.8-1.3 cm, depending on the RF configuration.

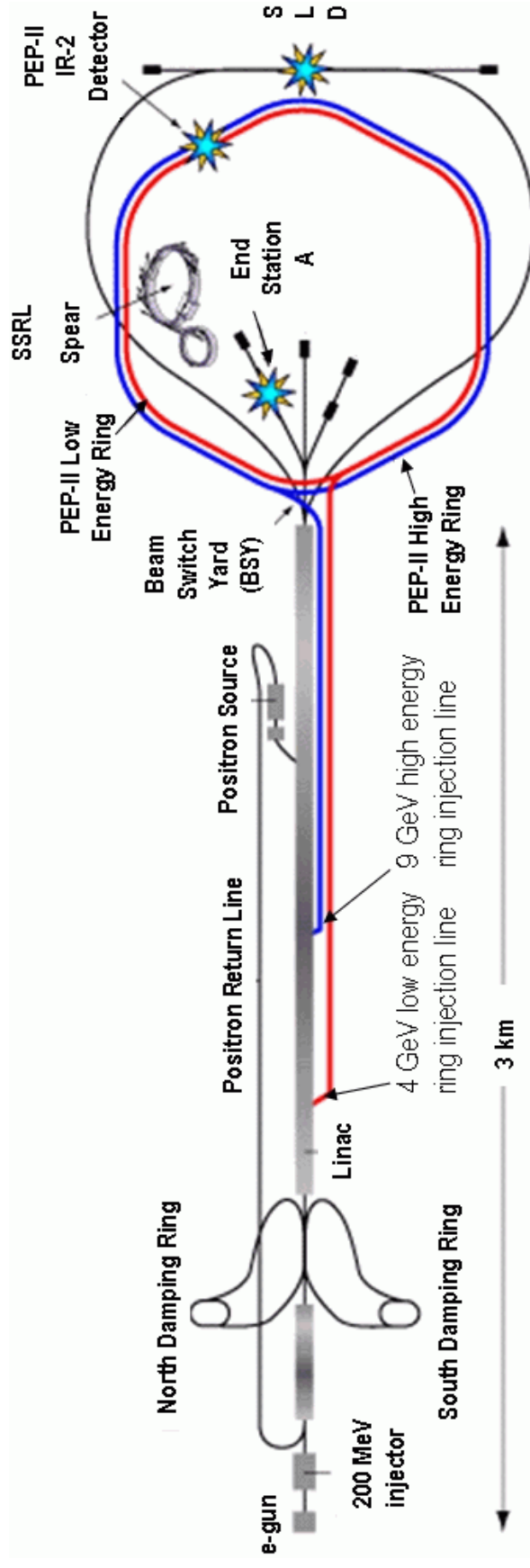


Figure 1.1. Beam lines of the Stanford Linear Accelerator Center. The PEP-II injection lines are extracted from the main linac at the 4 GeV and 9 GeV points respectively for the low energy positron ring (LER) and the high energy electron ring (HER).

Beam stability and colliding beam considerations favour a flat beam transverse profile [54]. On the average, horizontal to vertical size ratios are 10:1, reaching 20:1 at the IP with nominal transverse beam size of  $150 \times 7 \mu\text{m}$ .

### 1.3 The SLAC Injector

The PEP-II rings are fed by the two mile linac facility at Stanford Linear Accelerator Center. Electrons are produced at an electron gun from a thermionic filament or a photo cathode, then bunched and accelerated to 1.2 GeV. They are then extracted into the north damping ring, where they circulate long enough to damp transverse emittance before being injected into the main linac. They are accelerated to the 9 GeV point where they can be extracted for injection into the HER. Selected electron bunches are extracted from the linac for positron production at the 33 GeV point. There they strike a titanium target producing a shower of positrons which are collected, bunched and accelerated. Positron transverse emittances are damped in the south damping ring. Damped positrons are subsequently accelerated in the main linac and extracted at the 4 GeV point for LER injection.

### 1.4 Charge-Parity (CP) Violation

A key to understanding the domination of matter over anti-matter in the observable universe in the context of the Standard Model is charge-parity or CP violation. CP violation is a measure of the difference in outcomes of experiments based on how a coordinate system (P) and charge (C) are assigned. The weak force exhibits differences in outcomes with respect to the CP counterpart experiment (ie coordinate transformation  $x \rightarrow -x$ ,  $y \rightarrow -y$ ,  $z \rightarrow -z$  and particles $\rightarrow$ anti-particles). In particular, parity conservation (P) is violated when experimental outcomes depend on the spin axis direction of a particle, in essence distinguishing between north and south poles. Charge conjugation (C) represents an equivalent system where matter is interchanged with anti-matter counterparts. CP symmetry, which added charge conjugation (C)

to parity conservation, was developed as a fundamental conservation law after parity violation was observed. This law was later found to be violated in certain weak force mediated interactions.

CP violation was postulated by Soviet physicist Andre Sakharov[56] to be an essential process in a matter dominated universe. The Standard Model predicts equal amounts of matter and anti-matter are produced in the early universe. Differences in the decay process between matter and anti-matter particles subsequently could account for the preponderance of matter in the present universe. Thus CP violation represents an important test of cosmological theory and particle physics.

The B-mesons provides an experimentally accessible stage to observe CP violation. B-mesons are a family of particles consisting of one bottom quark and one up or down quark. In BaBar they are made in the decay of the  $\Upsilon(4S)$  particle. Collisions of electrons and positrons at the 10 GeV center of mass of the  $\Upsilon(4S)$  resonance maximizes the yield of B-mesons. B-mesons can decay in various ways via the weak force, a small fraction ( $10^{-5}$ ) of which yield information on the statistics of matter/anti-matter production rates in the early universe. The rate differences can be observed as a tiny difference in decay times between a B-meson and its antiparticle into particular final states. Decay times for B-mesons are on the order  $10^{-12}$  seconds. PEP-II is an *asymmetric* B-factory in the sense that the colliding species are at different energies. B-mesons produced in this fashion have relative momentum with respect to the detector so that decay times can be better resolved.

The degree of CP violation in the B-meson system is important for testing the legitimacy of the Standard Model. The Standard Model predicts CP violation in B meson physics. This was first observed at BaBar in 2001. Given the rarity of events which display CP violation, large statistics are required to extract useful physics parameters. A B-factory therefore requires intense rates of collision to produce these events and a sophisticated data acquisition system to identify them[18].

## 1.5 Luminosity

Obtaining the necessary statistics for CP violation observation requires maximizing the luminosity, which in simple terms means increasing the number of collisions. The simplest ways of achieving this is to increase beam currents and shorten the bunch lengths. Both plans will significantly increase the severity of beam induced electromagnetic effects.

Storage ring luminosity  $L$  can be quantified in the following[51]:

$$L = fn \frac{N_+ N_-}{A} \quad (1.1)$$

where  $N_{\pm}$  is the number of positrons (electrons) in a bunch,  $f$  is the revolution frequency,  $n$  is the number of bunches per revolution and  $A$  is the cross sectional area of collision overlap. It is the number of events per second per unit cross section of a process and has units of  $\text{cm}^{-2}\text{s}^{-1}$ . Nominal luminosity for PEP-II is  $1 \times 10^{34} \text{cm}^{-2}\text{s}^{-1}$ .

The revolution frequency  $f$  is set by the speed of light and the circumference of the ring for the relativistic case. The maximum number of bunches (per revolution)  $n$  is set by the RF frequency and the circumference. Further increase in luminosity can come from maximizing the number of particles per bunch  $N_{\pm}$  or reducing the cross sectional area  $A$ .

Stability issues come with increasing bunch currents  $N_{\pm}$ . Coupled bunch instabilities arise with increased bunch currents in both transverse and longitudinal planes caused by long range wake fields. These instabilities have been effectively damped by fast bunch by bunch feedback systems however, anticipated higher bunch charge electromagnetic effects will diminish control margins[15].

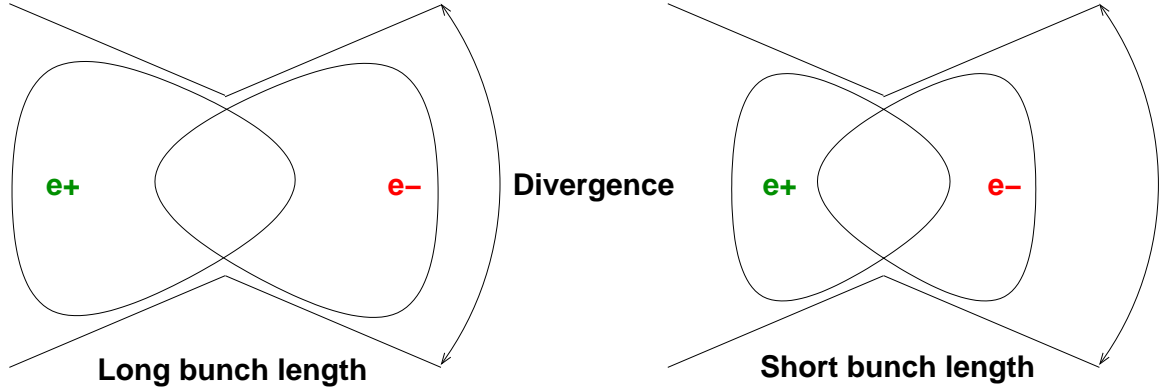


Figure 1.2. Luminosity enhancement from shortening bunch lengths. Transverse cross section  $A$  is reduced by increasing angular divergence with magnetic focusing (left picture). Shorter bunch lengths increase the fractional longitudinal overlap in the region of the common volume where the transverse size is small. (right picture).

## 1.6 Collision Cross Section and Bunch Length Effects on Luminosity

Lowering the cross sectional area  $A$  is achieved through increasing the beam angular divergence at the collision point with stronger magnetic focusing. This realizes smaller transverse size. The true benefit requires shortening the bunch length which additionally decreases the longitudinal extent of the collision volume, thereby increasing the particle density in the longitudinal dimension at the collision point. Figure 1.2 illustrates this geometric effect. Two bunches are shown in collision in a high angular divergence interaction point. The transverse (vertical plane) beam densities are increased at the interaction point (left picture). A further enhancement is obtained by shortening the bunch lengths (right picture). The collision volume encompasses a larger fraction of the bunches in the region where the common transverse size is small, thus increasing the collisional probability for given bunch currents.

Bunch length is manipulated with RF voltage amplitude which changes the gradient of the longitudinal potential well seen by the particles of a bunch in such a way

as to provide longitudinal focusing. Shortening the bunch length also shortens the bunch fields. Electromagnetic effects resulting from shorter bunch fields will span a larger frequency range.

## 1.7 Scope of Work

The mission of the PEP-II B-factory is to investigate the origins of matter in the observable universe through the observation of CP violation in B meson decays. A nominal luminosity of  $L = 1 \times 10^{34} \text{cm}^{-2} \text{s}^{-1}$  requires unprecedented colliding currents of 2.4 Amps positrons and 1.8 Amps electrons at bunch lengths of 1 cm. The cross section for the  $\Upsilon(4S)$  particle is  $\sigma = 1.1 \times 10^{-33} \text{cm}^2$  which yields  $L\sigma \sim 10$   $\Upsilon(4S)$  particles per second, of which almost all decay into  $B\bar{B}$  pairs. The events of interest to CP violation only occur in 1/100,000  $B\bar{B}$  decays. The enormous number of collisions has brought to light CP violation in other more rare B meson decays which will test the limits of the Standard Model.

Obtaining statistically significant data sets in a reasonable time is of prime importance in B-factory performance. Most luminosity gains will come from increasing currents and smaller bunch sizes. Electromagnetic effects of intense short bunches limit the maximum currents and the minimum bunch lengths achievable and therefore limit the maximum luminosity. Significant machine performance enhancements can be achieved if these effects can be addressed.

Through measurement and simulation, models describing the propagation and coupling of beam induced electromagnetic energy are developed. Simulations show that dipole and quadrupole components of wake field beam pipe waves can couple to beam line structures through small apertures. The coupling simulations are based on a model of coupled oscillators where the oscillators are cavity modes of the beam chamber and a bellows chamber coupled by small apertures. Measurements were performed to identify the source of wake fields responsible for heating in a localized

area of the low energy ring. It was found that moving the beam position at collimators strongly modulated the temperatures of beam line structures 10-20 meters downstream of the collimators. Collimators and collimator like structures exhibit long range wake field effects which are verified with wake field simulations. The wake field simulations show that collimators excite propagating waveguide modes which are dominantly dipole and quadrupole. The majority of wake field power is directed in the beam direction where it is coupled into downstream pumping chambers and bellows.

Collimator like protrusions, beam chamber tapers, and crotches are part of the beam line geometry at the interaction point near the BaBar detector. The need for ultra-high vacuum conditions here requires many pumping chambers which are necessarily coupled to the beam chamber. Joule heating from beam induced electromagnetic effects are substantial with kilowatts of power dumped into small volumes. The heating can damage vital accelerator components. Vacuum degradation from heat related out-gassing results in increased detector backgrounds, increased beam sizes and instability, reducing luminosity and data quality. The heating is inversely proportional to the square root of the bunch length and quadratic with currents, limiting the luminosity potential of the PEP-II B-factory.

Based on the simulation results, studies of pump chamber RF coupling, and collimator wake effect measurements, two mitigating approaches are considered to reduce resistive heating. One approach involves modifying affected components, such as bellows and pumping chambers, with a water cooled lossy dielectric material to reduce the quality factors of excited modes. Coupled power can then be safely dissipated. The second approach involves introducing a device to couple out electromagnetic power before it reaches sensitive beam line components. The device is designed to selectively couple to dipole and quadrupole modes. The coupled power is exposed to a water cooled lossy material. The monopole mode, which shares the beam field

geometry, is allowed to pass without attenuation. Attenuation of the monopole mode represents an undesirable impedance to the beam. Designs for both approaches are simulated and optimized with an electromagnetic field solver. Prototypes based on both approaches have been built and installed.

Operational results with a modified pumping chamber show kilowatts of electromagnetic power absorbed in the water cooled dielectric and a 50% reduction in operating temperature for the pump chamber. The selective absorbing device was installed in the low energy ring downstream of the collimator section and proved to reduce the coupled power by 40% and reduce temperatures in a downstream 10 meter vicinity by a factor of two. Specialized selective absorbers suitable for the IP have been designed and produced and are being installed.

## Chapter 2

# Wake Fields and Higher Order Modes

### 2.1 Relativistic Beam Fields

This dissertation concerns the effects of electromagnetic fields of a highly relativistic charge distribution in accelerators. It is useful to first understand electromagnetic fields of a relativistic point charge of fixed velocity. In what follows the electromagnetic field is determined in the accelerator rest frame due to a relativistic point charge  $Q$  of fixed velocity  $\vec{v}$ . In the lab reference frame  $K$  the field at point  $P$  due to a charge  $Q$  moving with velocity  $v$  along the  $z$  axis can be found by first evaluating the electric field in the charge rest frame  $K'$  which is simply given by Coulomb's law for a charge at the origin:

$$\vec{E}' = \frac{Q}{4\pi\epsilon_0 r'^3} \vec{r}' \quad (2.1)$$

and transforming back to the laboratory frame using the Lorentz transformation. Assume at times  $t = 0$  and  $t' = 0$  in inertial reference frames  $K$  and  $K'$ , respectively, the two frames share a common origin  $O$ . After some time  $t > 0$ , the charge will have travelled a distance  $vt = d$  in the lab frame. Let  $P$  be the observation point in the lab frame along the  $x$  axis at  $(b, 0, 0)$  as shown in figure 2.1. The same observation point  $P$  in the charge rest frame  $K'$  has coordinates  $(b, 0, -\gamma d)$ , where the electromagnetic field components can be written as

$$E'_z(b, 0, -\gamma d) = -\frac{Q}{4\pi\epsilon_0} \frac{vt'}{r'^3} = -\frac{Q}{4\pi\epsilon_0} \frac{\gamma d}{(b^2 + \gamma^2 d^2)^{3/2}} \quad (2.2)$$

$$E'_x(b, 0, -\gamma d) = \frac{Q}{4\pi\epsilon_0} \frac{b}{r'^3} = \frac{Q}{4\pi\epsilon_0} \frac{b}{(b^2 + \gamma^2 d^2)^{3/2}} \quad (2.3)$$

$$E'_y(b, 0, -\gamma d) = B'_x(b, 0, -\gamma d) = B'_y(b, 0, -\gamma d) = B'_z(b, 0, -\gamma d) = 0 \quad (2.4)$$

Transforming back to the lab frame  $K$  can be accomplished by the inverse Lorentz transform of the electromagnetic field tensor. The contravariant form of the electromagnetic field tensor is given by[44]

$$F^{\mu\nu} = \begin{bmatrix} 0 & -\frac{1}{c}E_x & -\frac{1}{c}E_y & -\frac{1}{c}E_z \\ \frac{1}{c}E_x & 0 & -B_z & B_y \\ \frac{1}{c}E_y & B_z & 0 & -B_x \\ \frac{1}{c}E_z & -B_y & B_x & 0 \end{bmatrix} \quad (2.5)$$

and the Lorentz transform from the lab frame to a moving frame along the  $z$  axis is[44]:

$$L^\mu_\nu = \begin{bmatrix} \gamma & 0 & 0 & -\beta\gamma \\ 0 & 1 & 0 & 0 \\ 0 & 0 & 1 & 0 \\ -\beta\gamma & 0 & 0 & \gamma \end{bmatrix} \quad (2.6)$$

Here  $\mu$  and  $\nu$  are indicies for the four space time coordinates  $(0, 1, 2, 3)$ ,  $\beta = v/c$  and  $\gamma = [1 - \beta^2]^{-1/2}$ . The time coordinate index is 0, the other indices the three dimensions of space. The transform to the moving frame  $K'$  is performed by evaluating the components of the transformed electromagnetic field tensor  $F'^{\mu\nu}$  through the expression[44]:

$$F'^{\mu\nu} = \sum_{\delta, \lambda=0,1,2,3} L^\mu_\delta L^\nu_\lambda F^{\delta\lambda} \quad (2.7)$$

$$= \begin{bmatrix} 0 & -\frac{\gamma}{c}(E_x - vB_y) & -\frac{\gamma}{c}(E_y - vB_x) & -\frac{1}{c}E_z \\ \frac{\gamma}{c}(E_x - vB_y) & 0 & -B_z & -\gamma\left(\frac{v}{c^2}E_x - B_y\right) \\ \frac{\gamma}{c}(E_y - vB_x) & B_z & 0 & -\gamma\left(\frac{v}{c^2}E_y + B_x\right) \\ \frac{1}{c}E_z & \gamma\left(\frac{v}{c^2}E_x - B_y\right) & \gamma\left(\frac{v}{c^2}E_y + B_x\right) & 0 \end{bmatrix}$$

By comparison with equation 2.5 the Lorentz transformed fields in the moving frame  $K'$  in terms of the lab frame field components can be obtained by inspection:

$$E'_x = \gamma (E_x - vB_y) \quad (2.8)$$

$$E'_y = \gamma (E_y - vB_x) \quad (2.9)$$

$$E'_z = E_z \quad (2.10)$$

$$B'_x = \gamma \left( \frac{v}{c^2} E_y + B_x \right) \quad (2.11)$$

$$B'_y = -\gamma \left( \frac{v}{c^2} E_x - B_y \right) \quad (2.12)$$

$$B'_z = B_z \quad (2.13)$$

Now the fields in the lab frame of a point charge  $Q$  at rest in the moving frame  $K'$  can be found from the inverse transform obtained by setting  $v \rightarrow -v$  and interchanging primed and unprimed components in equations 2.8-2.13. Using the expressions for the point charge fields of equations 2.2-2.4 in the inverse transform, the non-zero field components are :

$$E_z = E'_z = -\frac{Q}{4\pi\epsilon_0} \frac{\gamma d}{(b^2 + \gamma^2 d^2)^{3/2}} \quad (2.14)$$

$$E_x = \gamma E'_x = \frac{\gamma Q}{4\pi\epsilon_0} \frac{b}{(b^2 + \gamma^2 d^2)^{3/2}} \quad (2.15)$$

$$B_y = -\gamma \left( \frac{v}{c^2} E'_x - B'_y \right) = \gamma \frac{v}{c^2} \frac{Q}{4\pi\epsilon_0} \frac{b}{(b^2 + \gamma^2 d^2)^{3/2}} \quad (2.16)$$

The lab frame electric field is directed along the vector  $\vec{r}$  from the charge position to the observation point  $P$ . With reference to figure 2.1, the lab frame electric field can be formulated in terms of the angle  $\psi$  between the  $z$  axis and  $\vec{r}$ [52]:

$$\vec{E} = \frac{Q}{4\pi\epsilon_0} \frac{\vec{r}}{r^3 \gamma^2 (1 - \beta^2 \sin^2 \psi)^{3/2}} \quad (2.17)$$

Along the direction of motion  $\psi \approx 0, \pi$  for fixed radius  $r$  around the charge,  $E \propto \gamma^{-2}$ , a consequence of Lorentz contraction. In the transverse direction,  $\psi \approx \pm\pi/2$ ,

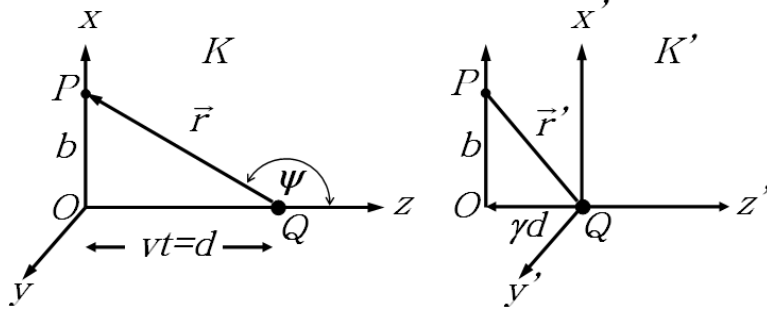


Figure 2.1. Coordinates of a moving charge  $Q$  in the lab frame  $K$  and in the charge rest frame  $K'$  moving along the  $z$  axis at velocity  $v$ . Observer is at point  $P(b, 0, 0)$  in the lab frame.

$E \propto \gamma$ . Longitudinal electric fields are diminished while transverse fields are enhanced as the particle becomes relativistic.

The magnetic field has only an azimuthal  $y$  component which also exhibits relativistic enhancement along planes perpendicular to the velocity near the charge ( $\psi \approx \pm\pi/2$ ).

$$\vec{B} = \frac{v}{c^2} \frac{Q}{4\pi\epsilon_0} \frac{\sin\psi \hat{y}}{r^2 \gamma^2 (1 - \beta^2 \sin^2\psi)^{3/2}} \quad (2.18)$$

For an *ultra*-relativistic particle of charge  $Q$  moving in the  $z$  direction with velocity  $v$  in vacuum the electric field components along the direction of motion are severely Lorentz contracted, leaving only a radial electric field component  $E_r$  and azimuthal magnetic field intensity component  $H_\phi$  perpendicular to the velocity in cylindrical  $(r, \phi, z)$  coordinates. The electric and magnetic fields of a highly relativistic point charge travelling on axis in a cylindrical beam pipe of radius  $b$  with conducting walls can be found from Gauss's law. The electric field has only a radial component  $E_r$ . For a pillbox of small width  $\Delta s$  at the charge location where  $s = z - ct$  and pillbox radius  $r < b$  enclosing a charge  $Q$

$$E_r = \frac{1}{2\pi\epsilon_0 r} \frac{Q}{\Delta s} \quad (2.19)$$

$$= \frac{Q\delta(z - ct)}{2\pi\epsilon_0 r} \quad (2.20)$$

where the term  $Q/\Delta s$  has been replaced with a delta function charge density  $Q\delta(z - ct)$  corresponding to a relativistic point charge.

The magnetic field intensity for an ultra-relativistic point charge is entirely azimuthal and can be found through Ampere's law. A closed path in the form of a circle of radius  $r < b$  around the charge in the azimuthal plane gives

$$\begin{aligned} H_\phi &= \frac{Q\delta(z - ct)c}{2\pi r} \\ &= \frac{E_r}{Z_0} \end{aligned} \quad (2.21)$$

where  $Z_0 = \sqrt{\mu_0/\epsilon_0}$  is the free space impedance.

The deviation from the relativistic limit goes as  $1/\gamma$  which gives the opening angle of the electric field in the direction perpendicular to the velocity. The relativistic limit holds for the case of the PEP-II B-factory with 3 GeV positrons and 9 GeV electrons where  $\gamma$  is 5,870 and 17,600 respectively. Figure 2.2 illustrates the electric field pattern in the lab frame for a relativistic charge in a beam pipe. For a perfectly conducting beam pipe surface charges are induced in the walls which move with the bunch.

For large  $\gamma$  the electric fields are essentially perpendicular to the velocity. Thus, a charged particle in a relativistic bunch will not see fields from adjacent particles ahead or behind it. Furthermore, it can be shown that particles at the same  $z$  position within a relativistic bunch do not experience any force from each other's fields. In cylindrical coordinates with unit direction vectors  $\hat{r}, \hat{\phi}, \hat{z}$ , assume a charge  $q$  in the same transverse plane as another charge  $Q$  separated by  $\vec{r} = r\hat{r}$  both moving with velocity  $\vec{v} = c\hat{z}$ . The electric field at  $q$  due to  $Q$  is radial  $\vec{E} = E_r\hat{r}$  while the magnetic field intensity is azimuthal:  $\vec{H} = H_\phi\hat{\phi} = \frac{E_r}{Z_0}\hat{\phi}$  from equation 2.21. The force on  $q$  from  $Q$  is found from the Lorentz force law:

$$\begin{aligned} \vec{F} &= q(\vec{E} + \vec{v} \times \vec{B}) \\ &= q(E_r - c\mu_0 H_\phi)\hat{r} \\ &= q\left(E_r - c\sqrt{\frac{\mu_0}{\epsilon_0}}\frac{E_r}{Z_0}\right) = 0 \end{aligned}$$

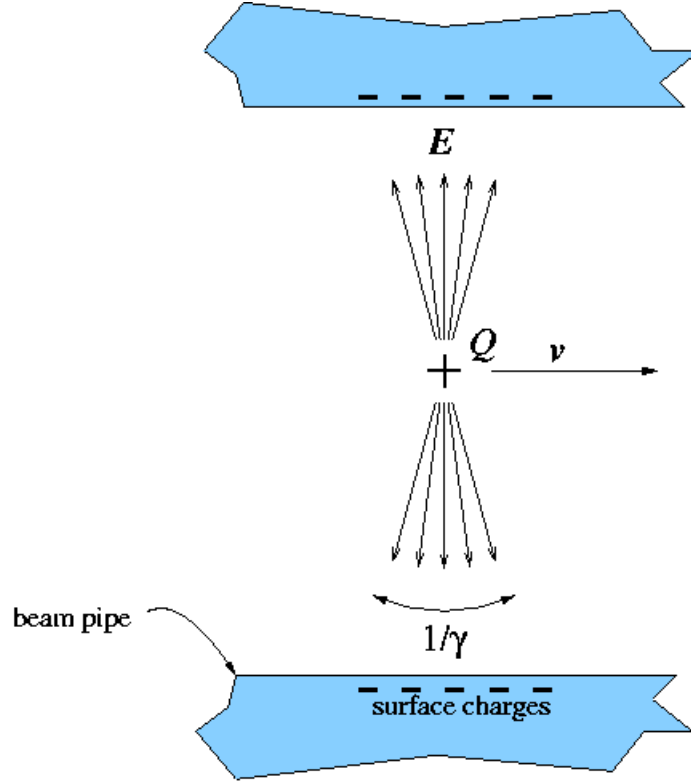


Figure 2.2. Electric field  $\vec{E}$  for a relativistic particle of charge  $Q$  and velocity  $v$  in a beam pipe has an opening angle of about  $1/\gamma$  and surface charges (-) at the beam pipe surface where the electric field lines terminate.

Thus transverse electric and magnetic forces between charged particles in ultra-relativistic beams cancel each other. Accordingly inter-bunch (space charge) effects can be neglected in the relativistic limit[33]. The forces experienced by bunch particles is dominated by external fields from magnets, RF and wake fields.

Another important consequence of the Lorentz force law concerns the means by which a bunch gains or loses energy from electromagnetic fields. The energy change  $\frac{d\epsilon}{dt}$  of a charge  $Q$  moving with velocity  $\vec{v}$  can be written as

$$\frac{d\epsilon}{dt} = \vec{v} \cdot \vec{F} = Q\vec{v} \cdot \vec{E}$$

implying only longitudinal components of an external electric field can contribute to changing the energy of bunch particles.

## 2.2 Wake Fields and HOMs

Wake fields are electromagnetic fields resulting from beam fields scattering from the beam chamber. The beam fields scatter from beam chamber irregularities in much the same way a wave generated by a moving boat in water scatters from solid objects in its path. Wake fields can remain after the passage of a beam and can excite parasitic resonances or propagating waveguide modes depending on the chamber geometry, materials and the beam parameters. A shorter bunch length means the spectrum of wake fields excited by the beam encompass higher frequencies, driving potentially more parasitic resonances.

Wake fields have long and short range effects. They can interact with the tail of the originating bunch, or with subsequent bunches. These effects are both longitudinal and transverse. For a train of bunches, long range wake fields result in coupled bunch instabilities which must be damped by dedicated feedback systems. Short range effects lead to increased energy spread and emittance growth.

Wake fields can be understood in terms of the impedance presented to the beam by the accelerator. Particles within a given bunch will experience the wake fields differently, according to their location within the bunch. Over time the particles will have gained a net potential from the integration of wake field effects. In this way a *wake potential* can be defined as a function of position within the bunch. The impedance of an accelerator vacuum chamber is essentially the Fourier transform of the wake potential of a given charge distribution[32].

Figure 2.3 illustrates wake field generation in a cavity after a 1.8 mm bunch has passed a PEP-II RF cavity. The bunch, shown on the right side of the figure, propagates on the axis of the axis-symmetric structure of the cavity and produces all the field lines shown in and around the cavity. Some energy is left behind in the cavity. Some energy follows the beam and propagates in the beam pipe. This figure is the result of a simulation program NOVO[14].

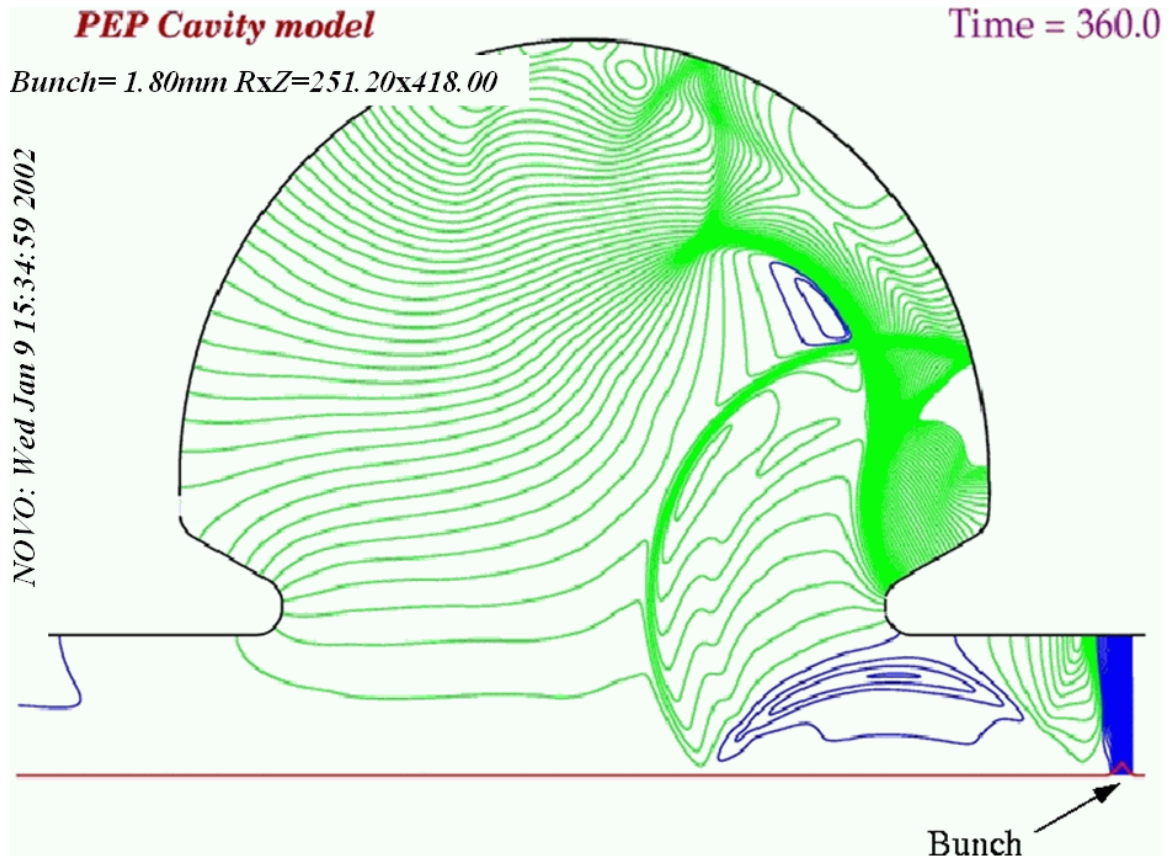


Figure 2.3. Electric field lines of wake fields produced by a 1.8 mm bunch traversing a PEP RF cavity from a NOVO[14] simulation. Courtesy A. Novokhatski[17]. The bunch is travelling to the right in this picture.

Wake fields are often referred to as *higher order mode* or *HOMs* in the literature, particularly when referring to cavities or cavity like structures. HOMs can more precisely be defined as the Fourier transform of the wake fields. For the purposes of this dissertation, HOMs refer to unwanted electromagnetic energy in an accelerator generated by beam fields.

- HOMs can refer to resonant cavity modes which are of higher order than the fundamental. In most cases HOMs are parasitic and produce undesirable effects in an RF cavity. There is considerable design effort toward removing these modes in RF cavities. A compromise is made between accelerating efficiency and beam

impedance in cavity design. At high beam currents, HOM power generated in an accelerator cavity is comparable to the accelerating power produced by the RF system.

- HOMs can refer to excited parasitic resonances in structures with unintended cavities. Propagating wake fields can couple out of the beam chamber through small openings and excite parasitic resonances. This occurs in vacuum pumping chambers, and bellows structures which interconnect lengths of beam line. Propagating waves can reflect from aperture changes and can become trapped in a parasitic cavity between two aperture variations.

The HOM frequency spectrum depends on the bunch length and the bunch pattern. A shorter bunch length excites higher frequency HOMs. If the frequency spectrum (HOMs) includes power at frequencies above the beam chamber cutoff, a certain part of these waves may propagate some distance from its source and deposit energy in another part of the accelerator. This cutoff frequency is a function of the shape and size of the beam chamber cross section. A small cross section has a higher cutoff frequency.

Nominally the PEP-II bunch pattern is a train of 1722 bunches, each bunch separated by 4.2 nanoseconds. The bunch pattern excites frequencies strongly at harmonics of the bunch spacing time. These frequencies couple to bellows cavity resonances. As bellows cavities flex in response to thermal cycles (during injection or coast down), they move in and out of resonance with the bunch spacing frequencies. See figure 2.15 for an example of this phenomenon.

The energy for beam generated HOMs must ultimately come from the beam. The beam can lose energy in two ways:

- Wake fields can catch up with the beam particles and affect their kinetic energies.

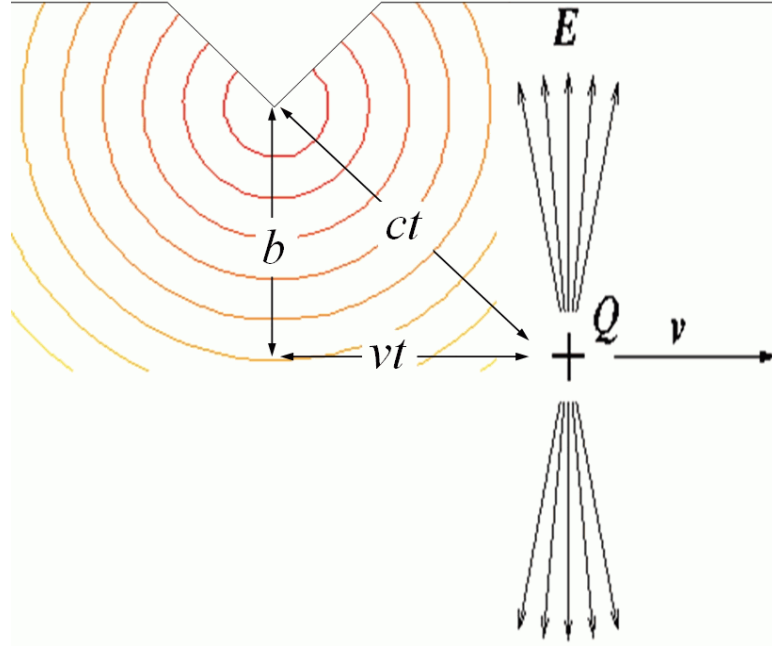


Figure 2.4. Illustration of relativistic beam wake field interaction. Wake fields excited by a relativistic point charge  $Q$  catch up with the charge after a time  $t$ .  $b$ : the distance from the beam axis to the wake field source.  $c$ : speed of light.  $v$ : velocity of the bunch.

- Energy can be taken from the bunch fields. A relativistic bunch traversing a uniform conductive pipe maintains a radial electric field and azimuthal magnetic field, which together form a Poynting vector in the direction parallel to the velocity. When irregularity in the vacuum chamber wall is encountered, the orientation of beam fields at the irregularity will alter the Poynting vector direction, enabling energy to flow from the beam fields to produce the wake fields.

Wake fields take time to travel from the wake field source to the beam position which by this time has traveled a considerable distance. This catchup effect is illustrated in figure 2.4

The Lorentz contracted fields  $E$  of a point charge  $Q$  moving with uniform velocity  $v$  have interacted with an irregularity in the beam chamber. The distance to the

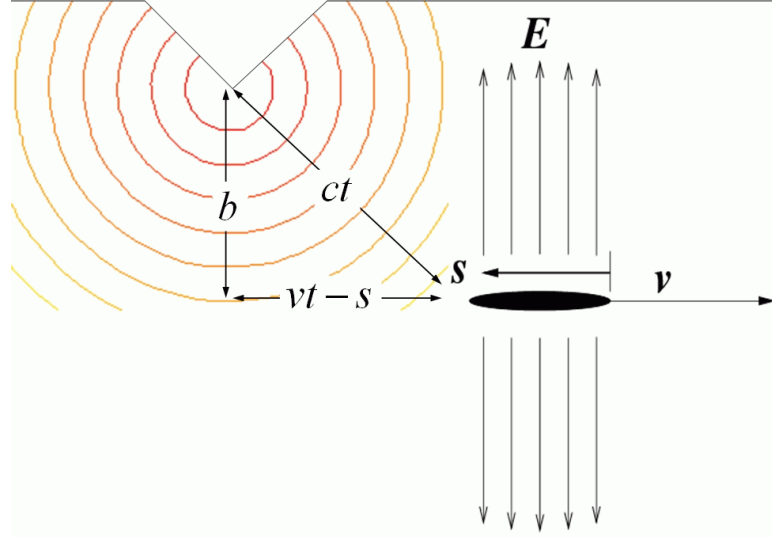


Figure 2.5. Depiction of wake fields excited by the bunch head catching up with bunch particles at a distance  $s$  following the bunch head.  $b$ : the distance from the beam axis to the wake field source.  $c$ : speed of light.  $v$ : velocity of the bunch.  $t$ : time at which wake fields catch up to trailing particles at a distance  $s$  behind the bunch head.

beam chamber irregularity from the beam axis is given as  $b$ . In the time  $t$  it takes wake fields to reach the point charge  $Q$  it will have traveled a distance  $vt$  away from the wake field source. Simple geometric arguments lead to a “catch-up” distance of  $\approx b\gamma$  the point charge travels before interacting with the wake fields and losing energy. For the PEP-II B-factory with average beam chamber radius of several centimeters,  $\gamma = 6,000 - 18,000$  yields a distance of  $\approx 60-180$  meters.

For a realistic longitudinally distributed bunch, particles see wake fields excited by the preceding particles of the same bunch. The bunch - wake field interaction is characterized by a distance  $s$  measured from the first bunch particle to a position along the longitudinal direction opposite to the bunch motion in the bunch frame. This situation is depicted in figure 2.5.

The head of a bunch generates wake fields from a source located a distance  $b$  away at time 0. At a later time  $t$  these wake fields interact with trailing particles in the

same bunch trailing the head by a distance  $s$ . The distance of bunch travel before wake fields catch up to trailing particles at  $s$  is  $vt$ . The catch up distance is  $vt - s$ . Solving for  $t$  in the equation

$$b^2 = (vt - s)^2 + c^2t^2$$

gives a catch up distance

$$vt - s = \frac{-\gamma^2 s}{1 - \frac{1}{\gamma^2}} + \gamma^2 \sqrt{\frac{b^2 + \gamma^2 s^2}{\gamma^2 - 1}} - s. \quad (2.22)$$

For ultra relativistic short bunches  $s \ll b$  and  $\gamma \rightarrow \infty$ , a simpler expression for the catch up distance can be used[32]

$$\frac{b^2 - s^2}{2s}. \quad (2.23)$$

In PEP-II with average beam chamber radius of 2 centimeters and bunch length of 1.0 cm equation 2.22 applies. Wake fields will begin to interact with the tail of a 1.0 cm long bunch just before the tail arrives at the wake field source. The center of the bunch sees wake fields generated by the head about 3 cm after the wake field source.

The bunch's energy is partly kinetic and partly in the bunch electromagnetic field. The energy for wake fields initially comes from the bunch fields at the wake field source. This is manifested in the bunch field distortion from the initial steady state radial configuration. Eventually this bunch field disturbance will propagate toward the bunch particles and affect their energy. Additionally, wake fields which propagate independently of the bunch fields can also catchup with the beam particles and affect bunch particle energy. In this way, a short relativistic bunch passing a cavity leaves energy behind in the cavity before losing kinetic energy. The distortion of the bunch field propagating with the bunch eventually interacts with the bunch particles to produce a force which changes the kinetic energy of the particles. The

bunch fields will evolve back to the normal radial beam field configuration. The bunch particles then experience a net change of kinetic energy which represents energy lost to HOMs.

The nature of wake fields is illustrated in a simulation of a relativistic bunch passing through an iris. In figures 2.6-2.10, snapshots of the electric field lines are shown at different instances as a relativistic bunch in a cylindrical beam pipe passes an iris. The pipe and iris are assumed to have infinite conductivity. This simulation is produced with the NOVO[14] program.

Relativistic bunch fields which are initially purely radial become distorted as they interact with the iris. The bunch fields are represented by the electric force lines which terminate on the bunch particles. At the moment bunch fields interact with the iris in figure 2.6, some field lines no longer terminate on the bunch. This represents wake fields which can propagate independently of the bunch fields. These independently evolving wake fields will have parts which follow the bunch and parts which can be trapped in accelerator structures, leaving energy behind. This energy initially comes from the distortion of the bunch field at the iris.

The field lines which terminate on the bunch become distorted at the iris in order to maintain the boundary condition at the iris surfaces. In figure 2.7, the bunch field distortion starts to disturb more of the bunch electric force lines. The bunch tail particles are first to be affected by the distortion. Wake fields propagating in the opposite direction represent some of the energy lost by the bunch.

In figure 2.8, the bunch field distortions from the iris overtake the bunch, producing forces on the bunch particles. Wake fields generated at the corner of the iris and beam pipe propagate in the beam direction.

In figure 2.9, wake fields generated at the corner of the iris and beam pipe are catching up with the bunch. This part of the wake fields results in a kinetic energy gain for the bunch particles when they catchup to the bunch. This is evident from the

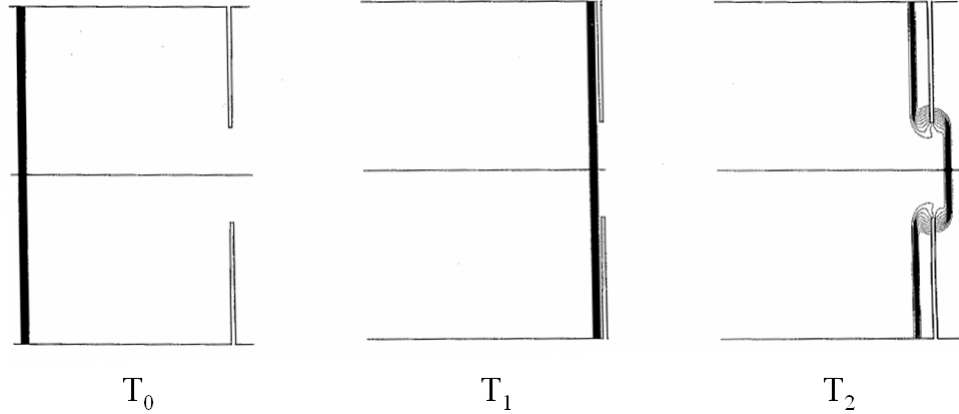


Figure 2.6. Frames in a simulation of relativistic bunch fields approaching and interacting with an iris. At time  $T_2$ , part of the bunch fields are severed by the iris, becoming independent wake fields. Bunch fields are distorted at the iris.

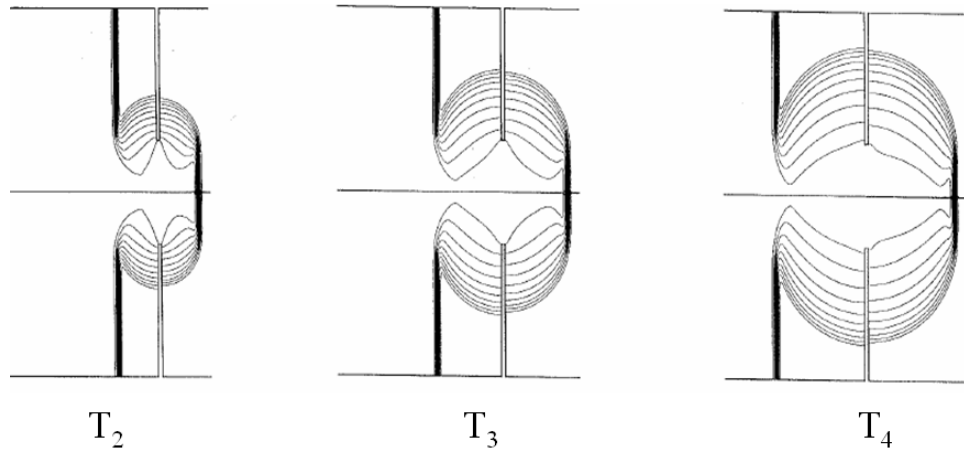


Figure 2.7. Bunch field distortion begins to propagate along bunch force lines. Tail bunch particles are first to be affected where a longitudinal field is developing. A significant fraction of the wake fields are propagating in the opposite direction.

slight longitudinal component in the beam direction. The bunch fields are starting to regain their initial radial distribution.

At any time, the total fields can be considered as a superposition of the steady state initial bunch fields and a pseudo field distribution which represents wake fields and the bunch field distortion. This is illustrated in figure 2.10 for the iris simulation. At

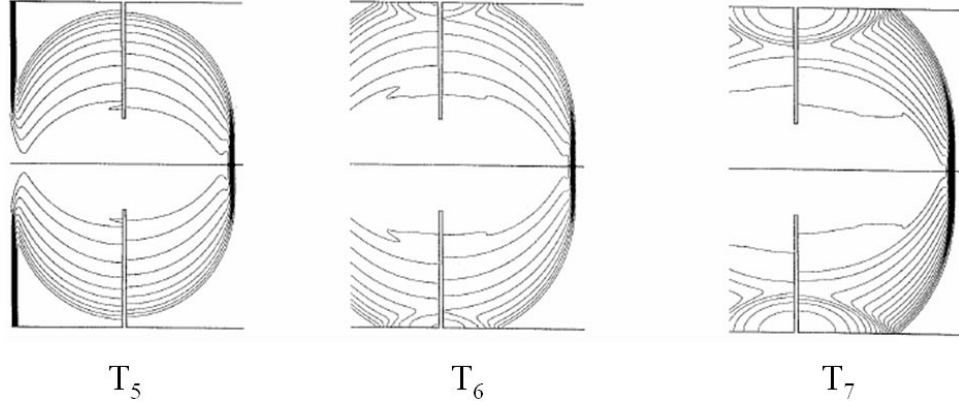


Figure 2.8. Wake fields are produced at the corner where the beam pipe and iris intersect. Some of these will propagate in the beam direction. Bunch particles begin to interact with the bunch field distortions as the distortions arrive at the bunch particle positions. At this time bunch particles are losing energy to the longitudinal forces.

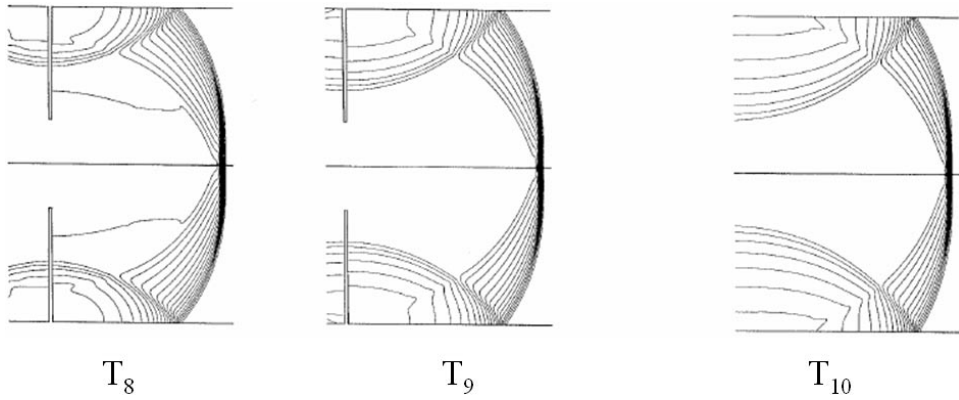


Figure 2.9. Bunch fields are starting to recover their radial orientation as wakes fields chase the bunch.

this time, the wake field has two well-defined parts which are propagating in opposite directions. The wake fields to the right of the iris in figure 2.10 are the bunch field distortion and will interact with the bunch. The part to the left propagates in the opposite direction and represents the energy lost by the bunch to wake fields. The field energy which goes to wake fields is equal but opposite to the bunch field distortion energy, illustrating the conservation of energy.

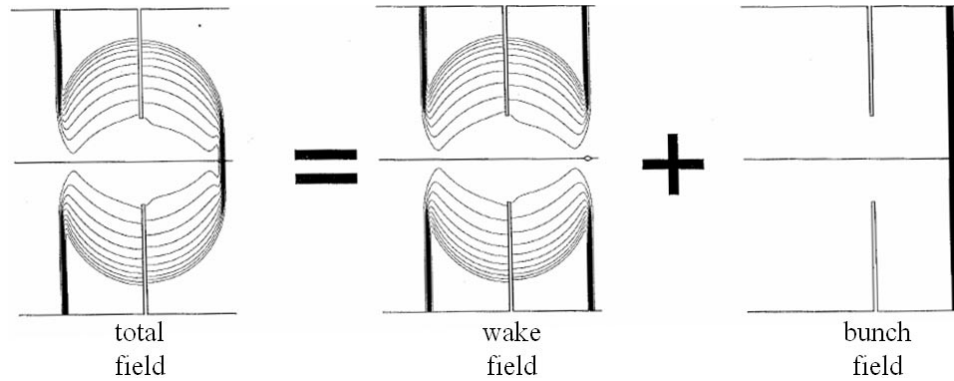


Figure 2.10. Decomposing the total field (left) into wake fields and bunch field distortion (center) and the initial bunch field. The field energy which goes to wake fields is opposite to the energy of the bunch field distortion. Courtesy A. Novokhatski

### 2.3 Surface Currents

A bunch traversing a pipe induces surface currents onto the pipe walls which move with the bunch at the termination of the electric field lines. For a beam pipe of constant cross section and infinite conductivity the surface currents move with the bunch and will not introduce any additional forces on following bunch particles. Wake fields can be understood in terms of the disruption of surface charge motion as it tries to keep up with the beam. Some of the surface charge gets left behind to produce long range wakes or gets trapped in cavities. Sharp irregularities such as an abrupt transition to a different chamber geometry can act as an antenna which radiates when driven by these surface currents. For uniform perfectly conducting beam pipe walls the surface current is formed by distributing the beam current over the circumference of the inner beam wall dimensions. The surface current at any point along the wall is modulated by the proximity of the beam at that point. Beam position monitors use this effect for determining the beam path in the accelerator.

## 2.4 Wake Field Sources

Most modern accelerator structures are designed to have smoothly varying vacuum chamber apertures in order to minimize the impedance to the beam, however, some irregularity is unavoidable. For the finite conductivity case surface charges are not synchronous with the beam but tend to fall behind[33]. This gives rise to resistive wall wake fields affecting following bunch particles. The net effect for PEP-II is beam energy loss and beam pipe heating. For a current of 2.9 A in 1.3 cm long bunches for a circular copper beam pipe of 4.5 cm radius this amounts to 70 kW of power which must be replenished by the RF system[8].

At the IP region, beams must intersect at the interaction point within the detector. Here it is critical to reduce detector backgrounds from synchrotron radiation. This is accomplished by a series of masks which intercept the radiation in the line of sight to the detector. These are water cooled structures capable of intercepting kilowatts of synchrotron radiation. They consist of wedge shaped beam chamber profiles and tapers near the IP and are important sources of HOMs, particularly because both beams traverse a common beam chamber at this area.

When electron and positron beams are brought together at the IP two beam pipes must transition into one common beam pipe. At this transition one inevitably finds a crotch where the walls of the separate beam pipes come together and end. This presents a substantial discontinuity to beam fields traversing the region.

It is necessary to remove transverse beam tails to improve detector backgrounds. These tails can come from off momentum or position injection pulses or stored beam particles populating the outer halo of the central beam core. This is accomplished by means of collimators placed at strategic positions and are meant to scrape off unwanted particles. These structures have sloped wedge shaped profiles and are strong HOM producers due to their proximity to the beam.

Concerns about IP region generated HOM power spurred an initial design in-

volving exposed lossy dielectric material to the beam chamber fields in the Q2 vacuum chamber (see figure 4.24). HOM power is captured, but additional wake fields arise from the direct exposure to beam fields in the dielectric materials[39] through Cerenkov radiation. In classical Cerenkov radiation electromagnetic fields from a moving charged particle polarize molecules of the medium. In the vicinity of a fast charged particle the polarization is seen as a fast transient disruption in the local electromagnetic field. The induced polarization is given up as radiation as the medium depolarizes. If the particle velocity  $v$  exceeds the phase velocity of light in the medium, the radiation interferes constructively along a wavefront emanating at an angle  $\theta$  to the particle velocity given by

$$\cos \theta = \frac{1}{\beta n}$$

where  $n$  is the medium index of refraction and  $\beta = v/c$ . The wavefront takes the form of a cone expanding behind the charge with the vertex at the charge position. Electromagnetic fields for an ultra-relativistic point charge  $Q$  in uniform motion along the  $z$  axis in a dielectric of refractive index  $n$  are given in reference [53] for cylindrical coordinates  $(\rho, \phi, z)$  in cgs units:

$$\begin{aligned} H_\phi &= -\frac{2Q\rho(n^2-1)}{[z^2-\rho^2(n^2-1)]^{3/2}} \\ E_\rho &= -\frac{2Q(n^2-1)}{n^2[z^2-\rho^2(n^2-1)]^{3/2}} \\ E_z &= \frac{2Qz(n^2-1)}{n^2[z^2-\rho^2(n^2-1)]^{3/2}} \end{aligned} \tag{2.24}$$

Here  $z$  measures the distance behind the particle.

In the present case a more realistic treatment concerns a point charge traveling in vacuum on axis through a cylindrical metal beam chamber of radius  $b$  with an inner dielectric layer of radius  $a \ll b$  and permittivity  $\epsilon$  as illustrated in figure 2.11. The charge itself is not propagating in the dielectric, but part of the field of the charge

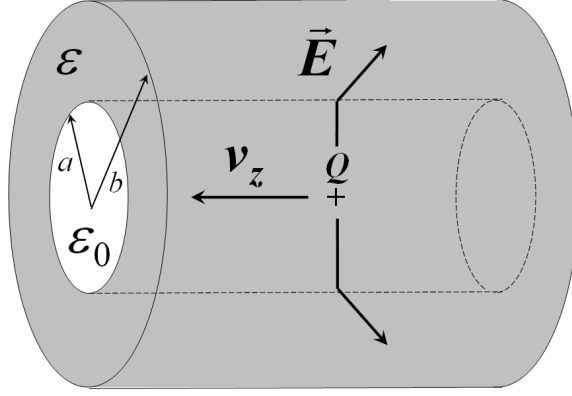


Figure 2.11. Charge  $Q$  moving at speed  $v_z c$  in a cylindrical vacuum chamber of radius  $a$  surrounded by a dielectric cylinder of radius  $b > a$ . Electric field lines are bent at the dielectric/vacuum interface.

at the surface of the dielectric moves with the velocity of the ultra-relativistic charge which is faster than the speed of light in the dielectric. The longitudinal electric field along the particle path is given in cylindrical coordinates for this case as derived by Burov and Novokhatski[39]:

$$E_z(\rho = 0, z) = -\frac{4Q}{a^2} \left\{ \left(1 + \frac{1}{4\epsilon}\right) e^{-z/s_0} - \frac{1}{4\epsilon \left[1 + \frac{z^2}{2a^2(\epsilon-1)}\right]} \right\} \quad (2.25)$$

where

$$s_0 = \frac{a\sqrt{\epsilon-1}}{2\epsilon} \left(1 + \frac{1}{4\epsilon}\right)$$

This allows longitudinal wake potentials and loss factors to be determined. If the dielectric fills the beam chamber completely ie.  $a = 0$ , equation 2.25 reduces to equation 2.24, the classical Cerenkov result for the longitudinal field on the  $z$  axis.

Figure 2.12 shows a NOVO[14] computer simulation of wake fields due to a Gaussian bunch in a dielectric canal for two cases of differing dielectric constants. Electric force lines are plotted for a steady state condition in an infinitely long canal. Electric fields are reflected from the pipe/dielectric boundary and the bunch fields are bent at the characteristic Cherenkov angle at the vacuum dielectric interface.

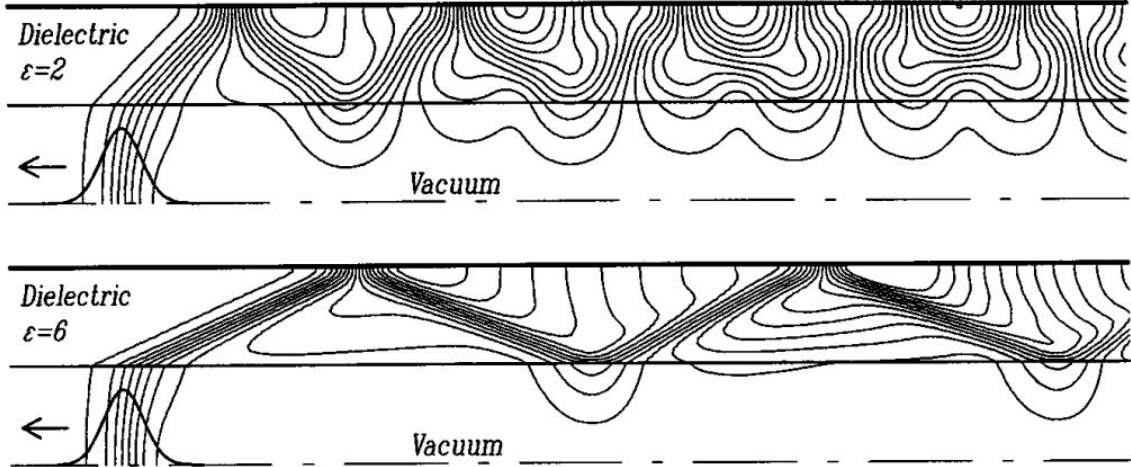


Figure 2.12. Electric force lines from a relativistic Gaussian beam in a dielectric canal computed with a modified NOVO[14] program for two different canal dielectric constants. From [39].

A Gaussian bunch of length  $\sigma$  in a thick canal ( $a \ll b$ ) of length  $L$  satisfying the condition

$$\sigma < \frac{a\sqrt{\epsilon - 1}}{2\epsilon}$$

is found to have a loss factor of[12]

$$k = \frac{cZ_0L}{4\pi a} \frac{1}{\sigma\sqrt{\pi\epsilon}}$$

where  $Z_0$  is the free space impedance. Applied to the Q2 bellows of effective dielectric length of  $L=5$  cm, average radius of  $a=22$  cm, and relative permittivity  $\epsilon = 30$  this predicts a loss factor of 0.069 V/pC for a 13 mm bunch length, and 0.112 V/pC for a 8 mm bunch length. Extrapolating to expected currents of 4.5 Amperes of positrons and 2.2 Amperes of electrons at 8 mm bunch length amounts to about 12 kW of power generated in the ceramic tiles[12].

## 2.5 Coupled Bunch Instability

Long range longitudinal wake fields can change the energy of subsequent bunches. Long range transverse wake fields can impart a transverse kick. The effect on the

whole beam is understood in terms of coupled oscillators where each bunch is treated as an oscillator which can be driven to oscillate longitudinally or transversely. The whole system exhibits motion comprising a superposition of the normal modes which can be damped with bunch-by-bunch RF modulation techniques[15, 25, 54]. These techniques embody fast feedback loops which measure transverse and longitudinal motion of the beam and provide a damping kick on a bunch-by-bunch basis. Growth rates of wake field induced coupled bunch modes increase with increasing currents, while shorter bunch lengths drive higher frequency modes, inevitably reducing feedback stability margins.

The strongest source of coupled bunch longitudinal instability are the RF accelerating cavities. The RF voltage is modulated to damp the lower order longitudinal coupled bunch modes[16]. HOM transverse kicks can be imparted by the RF cavities for bunch trajectories offset from the cavity symmetry axis. Transverse coupled bunch instabilities can come from other wake field sources including collimators, masks, beam chamber tapers and transitions and resistive wake effects. A shorter bunch means more intense wake fields given the higher charge density and shorter excitation time.

## 2.6 Bunch Length and Bunch Spacing

The bunch length plays an important role in the HOM spectrum. A shorter bunch will have a broader excitation spectrum which can couple with higher frequency resonances. By raising the RF amplitude the potential well as seen by the bunch becomes narrower confining the particles to a smaller longitudinal extent. This intensifies the bunch fields. Furthermore the RF potential well is “stiffer” meaning that the longitudinal oscillation frequency increases requiring more bandwidth for effective damping.

The beam spectra is dominated by the bunch spacing of 4.2 ns with bunch spacing harmonics extending to higher frequencies at short bunch lengths. A typical beam

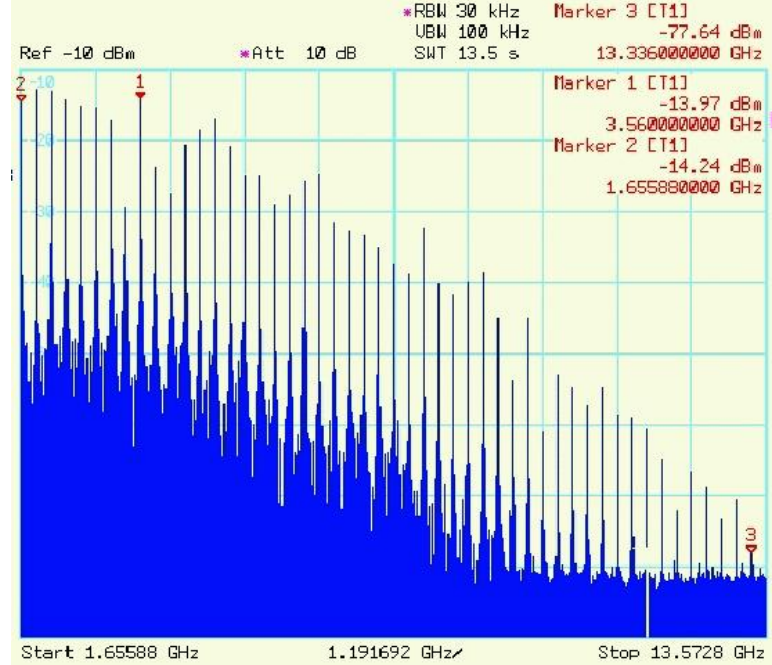


Figure 2.13. Spectrum of a beam position monitoring electrode signal for a bunch spacing of 4.2 ns and bunch length of 1.2 cm. Spectrum is dominated by spikes at the bunch spacing harmonics extending up to 13 GHz. Courtesy A. Novokhatski.

spectrum is shown in figure 2.13 which is a spectrum analyzer signal from a beam position monitoring electrode for 1.2 cm long bunches at a 4.2 ns bunch spacing. The bunch spacing harmonics extend up to 13 GHz.

## 2.7 Machine Performance Limitations

HOM effects scale with the square of current reducing the luminosity potential in a number of ways. Effects of HOMs are undesirable heating of beam line components and beam instability. Excessive HOM heating results in catastrophic vacuum breaches. Temperatures are monitored diligently, and cooling systems employed where feasible. Despite such precautions, HOM thermal stresses are sufficient to cause vacuum breaches. This is of particular concern at the IP region where repair would be difficult.

HOMs infiltrate pump out chambers and liberate absorbed gases from getter materials by heating the getter elements. This causes local pressure bumps resulting in increased detector backgrounds and beam instability as beam particles scatter from gas molecules.

HOM transverse and longitudinal effects increase emittance and energy spread, diluting the density of particles at the collision point, lowering the probability of collisions. Beam particles in a bunch are affected by short range wake fields generated by earlier particles in the same bunch. Beam particles are kicked transversely and longitudinally, increasing the bunch emittance (phase space area). Long range wake fields cause coupled bunch instabilities which must be damped with bunch by bunch feedback systems. In severe cases, this instability results in beam loss or increased detector backgrounds. Additionally, luminosity decreases when transverse or longitudinal beam oscillations take bunches out of collision.

## 2.8 Bellows

Lengths of beam chamber must be mechanically coupled together for structural integrity in the face of thermal expansion from synchrotron radiation and resistive wall heating. This cannot be done completely seamlessly. A bellow structure is employed at the transition of chambers, allowing mechanical movement while preserving vacuum. The bellows itself is a cavity with a resonant structure and must be shielded from fields in the vacuum chamber. This is nominally accomplished by sets of conductive fingers lining the beam pipe in such a way as to preserve the transverse dimension across the transition. Figure 2.14 shows the basic bellows construction. The conductive fingers are meant to slide over each other in response to vacuum chamber expansion. The fingers on one side are springs to ensure finger contact between the springs and an outer sleeve (not shown). There remain some small gaps between the fingers through which wake fields can couple to bellows modes.

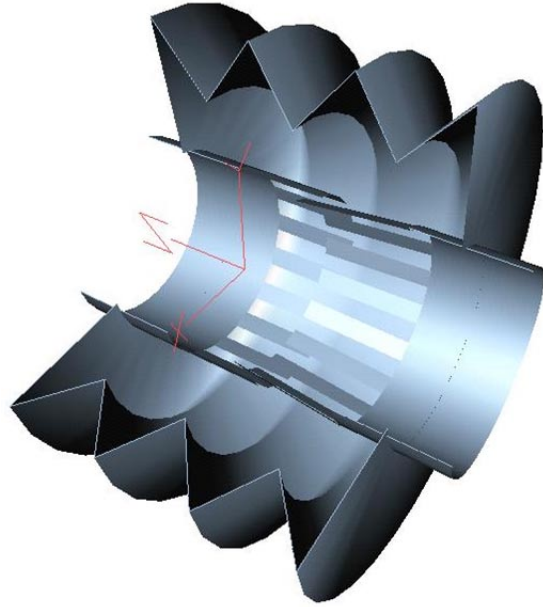


Figure 2.14. Simplified illustration of a generic bellows. Gaps between the fingers are exaggerated for this illustration. The inboard fingers are springs which maintain electrical contact to the outboard fingers. Typically the springs will press the outer fingers against an outer sleeve (not shown).

The bellows length varies with beam pipe thermal expansion which depends on current. As current is increased during injection, the bellows resonance frequency decreases as the bellows are compressed. Beam chamber HOMs near the bellows frequency will then drive the bellows at resonance if a coupling mechanism is present. Numerous arc bellows in PEP-II exhibit behavior which is illustrated in figure 2.15

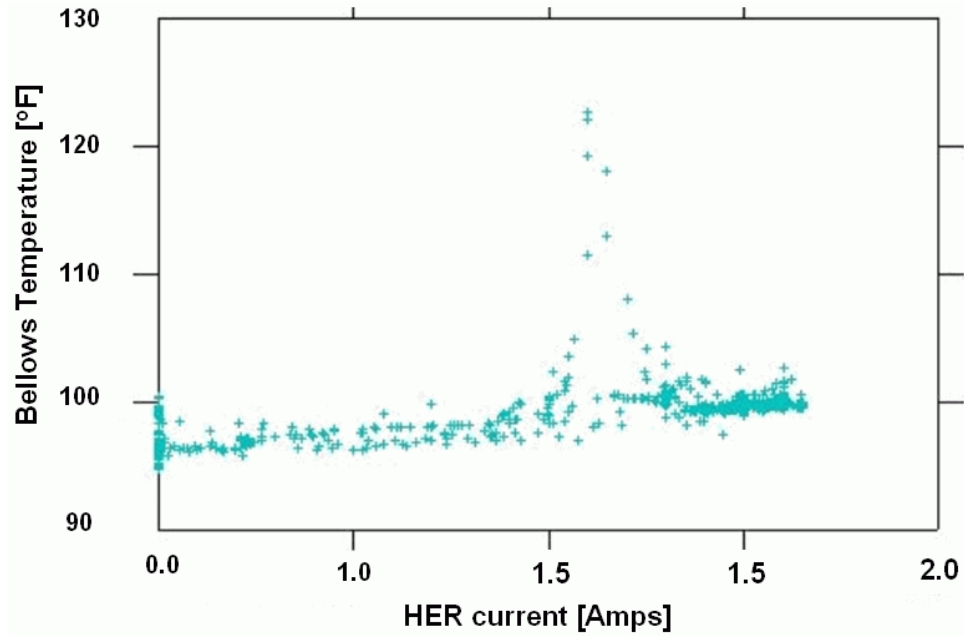


Figure 2.15. HER bellows temperature in Fahrenheit as a function of HER current in mA. The bellows exhibits a HOM driven resonance above 1.0 A of HER current.

for a particular bellows in the HER. A clear resonance above 1.0 A is exhibited. At 1.5 A the contraction of the bellows has shifted the bellows resonance frequency below the driving HOM frequency in the beam chamber, halting the precipitous climb in temperature.

## 2.9 IP Vertex Bellows

As currents were increased to improve luminosity, thermocouples in the IP area registered an alarming rise in temperature localized at a bellows assembly embedded in the detector. Signals from a nearby beam position monitoring button indicated several well defined resonances in the 5 GHz regime which correlated with thermocouple temperature.

The source of the heating is determined to be higher order modes[24]. The bellows had RF shielding fingers which were thought to be impervious to beam induced fields. Evidently some power was coupling in through the slots between the fingers and producing resistive heating within the bellows. It was current dependent and became a limiting performance issue for the PEP-II B-factory. The bellows is embedded within the BaBar detector and would be difficult to repair. During an extended down time while the detector was dismantled additional water and air cooling was added, enabling higher currents to be sustained. The installed cooling capacity will be insufficient for the anticipated high current running and a redesign of the bellows has been done.

## 2.10 NEG Pumps

Vacuum pumps required to maintain high vacuum conditions in the beam chambers necessarily interrupt the beam chamber geometry. Near the interaction region high vacuum is critical to minimize backgrounds and preserve beam lifetime in the presence of high power synchrotron radiation out-gassing of beam line components. Several specialized non-evaporable getter (NEG) pumps are employed in this area. The NEG pump comprises a special material which has high affinity for gas molecules in a high vacuum environment. After some time the material becomes saturated and ceases to be effective as a pump. The material is regenerated during a maintenance period by heating to release the captured gas which must be pumped out by other means.

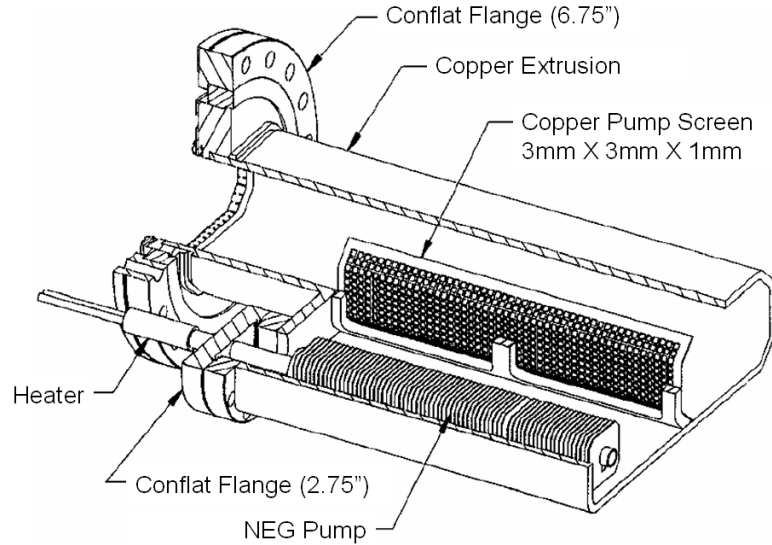


Figure 2.16. Detailed cut-away of a NEG pump in the interaction region. The NEG material is in the form of stacked wafers. The NEG chamber is separated from the beam chamber by a shielding perforated screen through which HOMs enter the NEG chamber. Courtesy L. Bertolini et al[41].

Figure 2.16 details a NEG pump[41]. The NEG chamber is separated from the beam chamber by a thin perforated copper screen.

The NEG's are instrumented with thermocouples. During high current running HOMs were infiltrating the NEG chamber and heating the NEG material. Temperatures approaching the regeneration regime caused the NEG material to give up a small amount of captured gas resulting in increased interaction region vacuum and accompanying detector backgrounds.

Subsequently the NEG screens have been redesigned to reduce coupling with smaller perforations and thicker material. This will reduce pumping efficiency but also reduce HOM heating. A better solution would be to remove HOMs from the beam chamber before they reach the NEG's.

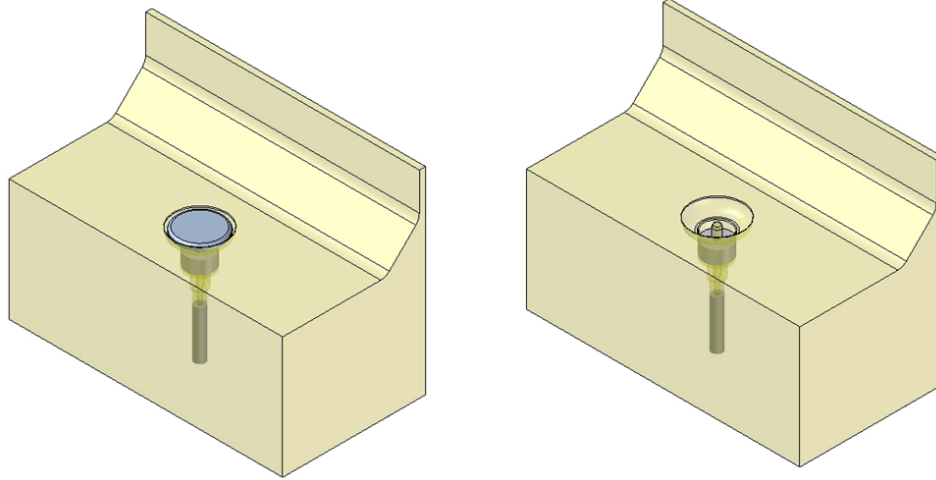


Figure 2.17. 1/4 symmetry beam position monitoring (BPM) structures with and without button. Loss of the button reveals a cavity and protruding stem on which the button was mounted.

## 2.11 BPMs

The beam orbit must be maintained at 100  $\mu\text{m}$  accuracies through the various magnetic elements to ensure low emittance beams. The beam centroid position is determined by a series of small insulated metal buttons which are transversely arrayed along the beam pipe in sets of four. The relative magnitude of the beam signals convey the transverse location of the beam. These signals are electronically processed to yield readback in microns of position relative to the center of the beam pipe. Figure 2.17 shows quarter symmetry BPM structures with and without a button.

At LER currents of 2.4 A and at shortened bunch lengths of 0.8 cm BPM buttons have become hot enough to fall off their mounts near the IP region. HOMs are suspected. On several occasions buttons on the top of the chamber have fallen onto buttons at the bottom of the chamber electrically short circuiting the bottom button to the chamber. With high beam currents traversing the chamber the intense electric fields heat the shorted button and damage the insulating ceramic feed-through. This

has caused several catastrophic vacuum breaches.

Ideally the solution to this problem is to use smaller buttons which are not sensitive to the beam generated field spectrum for the shorter bunch length. Another alternative is to run at longer bunch lengths or lower currents, but this would decrease the luminosity potential.

## 2.12 HOM Measurements

Beam position monitoring electrodes (BPMs) can provide HOM information. They are insulated electrodes embedded in the beam chamber which pick up beam field signals for beam position monitoring. To observe HOMs near the BPM, beam signals must be removed from the BPM signal. In the interaction region this is accomplished by gating out the beam signals and looking during an empty gap in the bunch train. This gap is used for the ramp-up of a machine protection fast abort kicker, which kicks the beam to a dump if imminent damage to the accelerator or detector is detected. The gated signal can then be Fourier transformed to see the HOM spectra. In the case of the detector vertex bellows observations of temperature and beam position (BPM) signal spectra, several modes in the GHz frequency range correlate with heating. Figure 2.18 shows the gated BPM spectra where the two circled peaks at 4.6 and 5.4 GHz were observed to correlate in amplitude with the nearby vertex bellows thermocouple reading. The HOM signal is from both beams: 730 mA HER with 840 mA LER.

HOM power varies as the square of the beam current through Ohm's law. This contrasts to synchrotron heating which goes linearly with current. A relative measure of HOM power comes from cooling water flow and temperatures. Water cooling is used in cooling a ceramic electromagnetic absorber of high loss tangent. Such an absorber is installed in a hot NEG pump chamber for the purpose of removing HOMs from the pump chamber. Given supply and return temperatures and water flow a

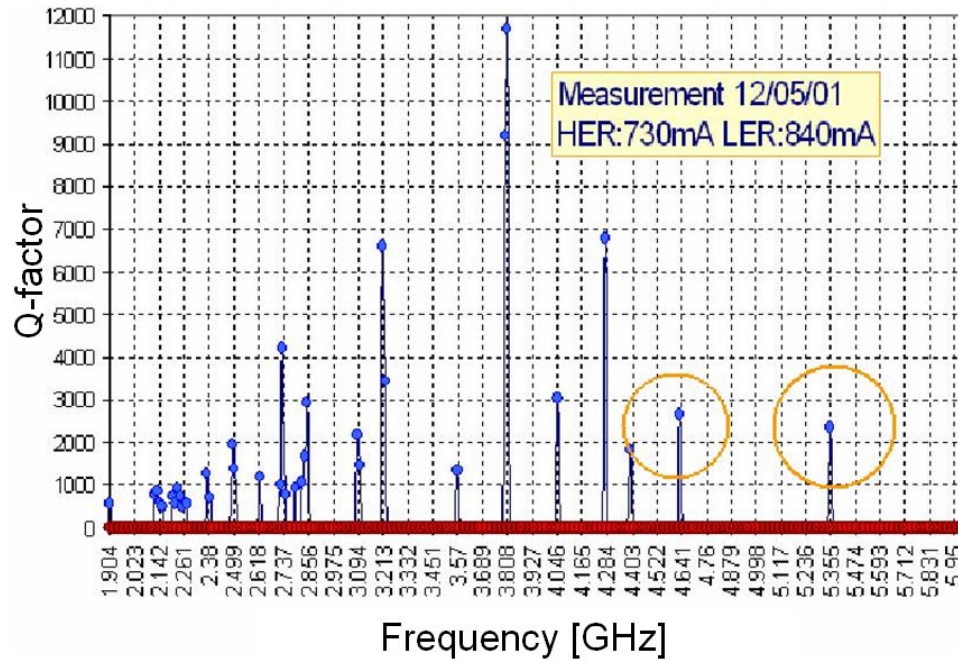


Figure 2.18. Interaction HOM spectra from a gated BPM signal. Circled peaks show amplitude correlation with detector bellows thermocouple readings. Courtesy A. Novokhatski.

measure of extracted power can be determined. This is shown in figure 2.19 as a function of LER current. The quadratic current dependence is an indication of HOM power coupling into the NEG chamber.

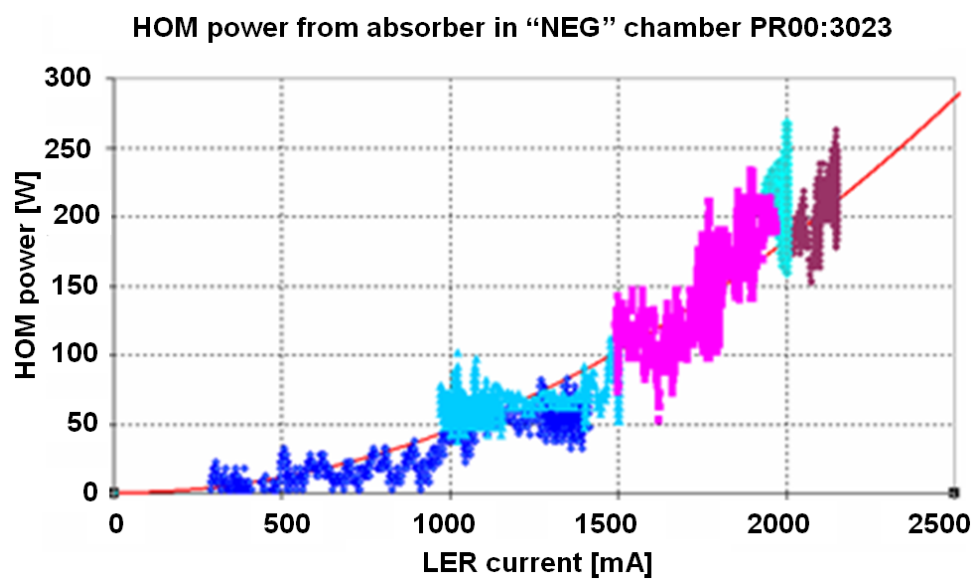


Figure 2.19. HOM  $I^2$  dependence of extracted HOM power from a LER NEG pumping chamber. Courtesy A. Novokhatski.

## Chapter 3

# Method of Calculation

### 3.1 Numerical Tools

To understand the sources and effects of HOMs several computational methods can be employed. Essential calculations involve determination of cavity modes and frequencies, time domain field solutions and scattering parameter analysis. The analysis in this dissertation employs a commercial finite integration technique field solver MAFIA[13] and a proprietary wake field code NOVO[14], using an implicit finite difference time domain scheme, written by A. Novokhatski. Analytic computations are performed for the simple pillbox cavity as a check of the methods.

### 3.1.1 The Finite Integration Technique

Maxwell's equations can be equivalently written in an integral formulation in linearly isotropic polarizable media of permittivity  $\epsilon$ , permeability  $\mu$ :

$$\oint \vec{E} \cdot d\vec{s} = - \int \int_A \frac{\partial \vec{B}}{\partial t} \cdot d\vec{A} \quad (3.1)$$

$$\oint \vec{H} \cdot d\vec{s} = \int \int_A \left( \frac{\partial \vec{D}}{\partial t} + \vec{J} + \rho \vec{v} \right) \cdot d\vec{A} \quad (3.2)$$

$$\int \int_V \vec{B} \cdot d\vec{A} = 0 \quad (3.3)$$

$$\int \int_V \vec{D} \cdot d\vec{A} = \int \int_V \rho d\vec{A} \quad (3.4)$$

$$\int \int_V \left( \frac{\partial \vec{D}}{\partial t} + \vec{J} + \rho \vec{v} \right) \cdot d\vec{A} = 0 \quad (3.5)$$

$$\vec{B} = \mu \vec{H} \quad (3.6)$$

$$\vec{D} = \epsilon \vec{E} \quad (3.7)$$

$$\vec{J} = \sigma \vec{E} \quad (3.8)$$

where  $\vec{E}$  is the electric field,  $\vec{B}$  is the magnetic flux density,  $\vec{s}$  is the boundary of an arbitrary area  $A$  with surface normal  $\vec{A}$ ,  $\vec{H}$  is the magnetic field strength,  $\vec{D}$  is the electric displacement,  $\rho$  is the charge density,  $V$  is an arbitrary closed volume with surface normal  $\vec{A}$ ,  $\vec{J}$  is the current density,  $\mu$  is the permeability,  $\epsilon$  is the permittivity,  $\sigma$  is the conductivity.

In the finite integration technique (FIT)[22, 34], a computational volume is subdivided into elemental volumes or cells, each assigned an appropriate material parameter which best describes the permittivity, permeability, and conductivity characteristics of the problem. The cells are small enough to where the electromagnetic field is assumed to not vary within the cell volume. Maxwell's integral equations are applied to each of these cells. This technique is employed in the field solver MAFIA[13].

For illustrative purposes, cells faces (facets) are orthogonal and a Cartesian grid is assumed, although the FIT method has been extended to other coordinate systems,

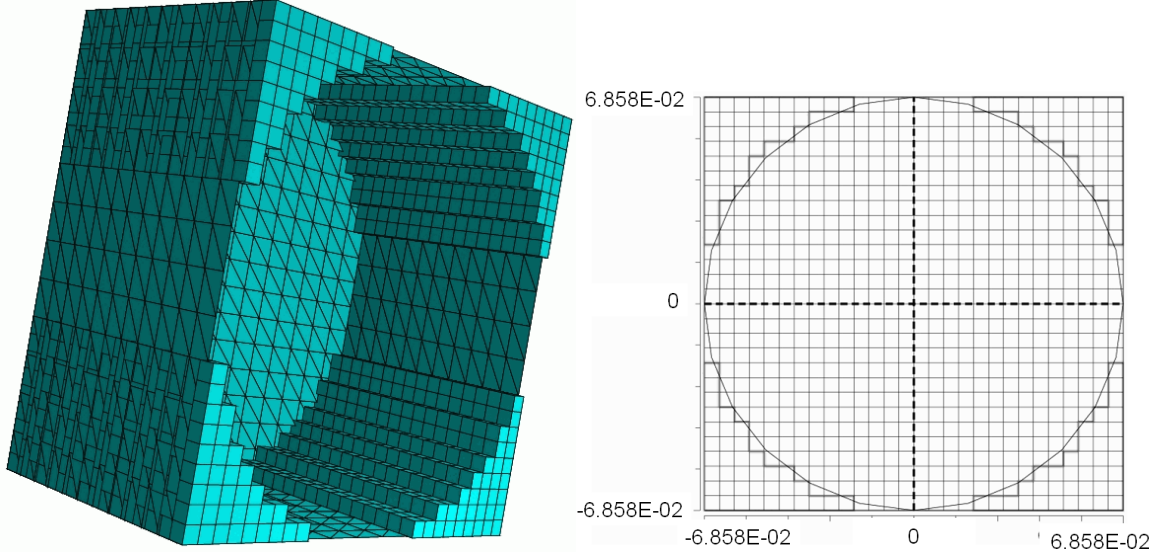


Figure 3.1. Representation of a cylindrical cavity for numerical electromagnetic calculations using the finite integration theory. The left picture depicts a 3D representation of the metal (dark material) and cavity volume. The right picture is a 2D projection indicating the ideal curved inner surface and the cellular approximation. The empty cavity is also composed of cells given characteristics of vacuum.

irregular and non-orthogonal grids[35]. With these considerations, a series of planes along each of the Cartesian axis are assumed to form the orthogonally faceted cells. The collective of cells comprises a primary grid. Each cell is indexed by a grid point  $\vec{P}(i, j, k)$  located at the intersection of the  $i$ th,  $j$ th and  $k$ th planes, where  $i/j/k$  enumerates the grid planes in the  $x/y/z$  directions, and  $i(j, k) \in \{1, \dots, N_x(N_y, N_z)\}$ . The integers  $N_x, N_y, N_z$  are respectively the number of grid planes along the  $x, y, z$  directions which amounts to  $N_p = N_x \times N_y \times N_z$  grid points forming  $(N_x - 1) \times (N_y - 1) \times (N_z - 1)$  cells.

Figure 3.1 shows an approximation of a cylindrical cavity modelled in this way. The dark material has characteristics of metal, while the interior which is also composed of cells will be given vacuum characteristics. The 2D projection shows the ideal curved surface and the crude stair step approximation of curved surfaces inherent in this method.

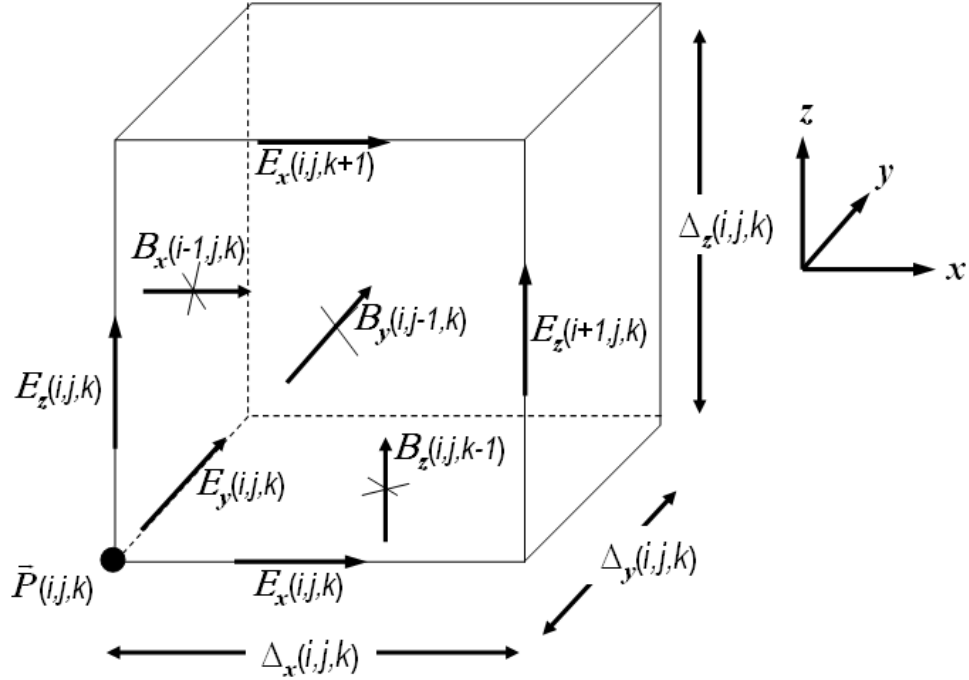


Figure 3.2. One cell of a grid used in the Finite Integration Technique. The sides and faces are assigned with electric and magnetic field components.

Maxwell's integral equations are applied at cell faces and the surrounding edges in each cell. The cell in figure 3.2 has edges associated with fields which form a circulation around a cube face or facet. A flux is associated with each facet directed normally to the facet. In this case a circulation of electric field components around one face has a magnetic flux directed through the face. In the Finite Integration Technique formulation a second interlaced dual grid (or magnetic grid) is introduced which is identical but displaced by half a cell in each direction, so that magnetic field components normal to facets of the primary electric grid become the edges of cells in the dual grid. The magnetic grid points are designated  $\tilde{P}(i, j, k)$  as depicted in figure 3.3.

Maxwell's equations 3.1 and 3.3 are applied in the primary grid. With reference to figure 3.3 the cells associated with primary grid points  $\vec{P}$  have electric field components along the edges and magnetic flux through the faces. The cell edge volt-

ages are defined  $\hat{e}_u = \Delta_u E_u$  while magnetic flux through a cell face is defined as  $\hat{b}_u = B_u \Delta_v \Delta_w$  where  $\{u, v, w\}$  is a permutation of Cartesian coordinates. The single hat  $\hat{\cdot}$  indicates line integral quantity along cell edges, such as a voltage, whereas the double hatted quantities  $\hat{\hat{\cdot}}$  correspond to electric, magnetic or current flux through cell surfaces. Component wise, Maxwell's equation 3.1 can be written in a discrete form for a given cell as:

$$\begin{aligned}
\hat{e}_z(i, j-1, k-1) + \hat{e}_y(i, j-1, k) - \hat{e}_z(i, j, k-1) - \hat{e}_y(i, j-1, k-1) & \quad (3.9) \\
& = -\hat{\hat{b}}_x(i, j, k) \\
\hat{e}_z(i-1, j, k-1) + \hat{e}_x(i-1, j, k) - \hat{e}_z(i, j, k-1) - \hat{e}_x(i-1, j, k-1) & \\
& = -\hat{\hat{b}}_y(i, j, k) \\
\hat{e}_y(i-1, j-1, k) + \hat{e}_x(i-1, j, k) - \hat{e}_y(i, j-1, k) - \hat{e}_x(i-1, j-1, k) & \\
& = -\hat{\hat{b}}_z(i, j, k)
\end{aligned}$$

where the dotted quantities indicate a time derivative. The discrete form of Maxwell's equation 3.3 for the magnetic flux out of a closed cell becomes:

$$\begin{aligned}
\hat{\hat{b}}_x(i, j, k) + \hat{\hat{b}}_y(i, j, k) + \hat{\hat{b}}_z(i, j, k) - \hat{\hat{b}}_x(i-1, j, k) - \hat{\hat{b}}_y(i, j-1, k) - \hat{\hat{b}}_z(i, j, k-1) \\
= 0
\end{aligned} \quad (3.10)$$

Maxwell's equations 3.2 and 3.4 are applied in the dual grid. Define analogous edge and flux quantities on the dual grid :  $\hat{h}_u = \tilde{\Delta}_u H_u$  and  $\hat{d}_u = D_u \tilde{\Delta}_v \tilde{\Delta}_w$  where  $\tilde{\cdot}$  represents quantities in the dual grid. Additionally, current density components  $J_u$  are assigned on the primary grid cell faces parallel to  $D_u$  to account for conduction and current sources. This motivates a current flux defined on dual grid cell faces:  $\hat{j}_u = J_u \tilde{\Delta}_v \tilde{\Delta}_w$ . With reference to figure 3.4, Maxwell's equation 3.2 has the component

wise discrete form:

$$\begin{aligned}
\hat{h}_z(i+1, j, k) + \hat{h}_y(i+1, j, k+1) - \hat{h}_z(i+1, j+1, k) - \hat{h}_y(i+1, j, k) \\
&= \hat{\hat{d}}_x(i, j, k) + \hat{\hat{j}}_x(i, j, k) \quad (3.11) \\
\hat{h}_z(i, j, k) + \hat{h}_x(i, j, k+1) - \hat{h}_z(i+1, j, k) - \hat{h}_x(i, j, k) \\
&= \hat{\hat{d}}_y(i, j, k) + \hat{\hat{j}}_y(i, j, k) \\
\hat{h}_y(i, j, k+1) + \hat{h}_x(i, j+1, k+1) - \hat{h}_y(i+1, j, k+1) - \hat{h}_x(i, j, k+1) \\
&= \hat{\hat{d}}_z(i, j, k) + \hat{\hat{j}}_z(i, j, k)
\end{aligned}$$

Maxwell's equation 3.4 involves charges which are allocated at the center of the primary grid cells as  $q(i, j, k)$ . Gauss's law looks like

$$\begin{aligned}
\oint_V \vec{D} \cdot d\vec{A} &\rightarrow \hat{\hat{d}}_x(i, j, k) + \hat{\hat{d}}_y(i, j, k) + \hat{\hat{d}}_z(i, j, k) \quad (3.12) \\
&\quad - \hat{\hat{d}}_x(i-1, j, k) - \hat{\hat{d}}_y(i, j-1, k) - \hat{\hat{d}}_z(i, j, k-1) \\
&= q(i, j, k)
\end{aligned}$$

Material parameters conductivity  $\sigma$  permittivity  $\epsilon$  and permeability  $\mu$  are assigned to the primary grid. Constitutive relations 3.7, 3.6 and 3.8 determine dual grid quantities  $\vec{D}, \vec{H}, \vec{J}$  in terms of primary grid quantities  $\vec{E}, \vec{B}$  by means of material parameters  $\epsilon, \mu, \sigma$ . The flux quantities in the dual grid span several primary grid cells in which the material parameters may differ. This requires a local averaging for the constitutive relations. With reference to figure 3.5 conduction current component  $J_{\sigma u}$  has flux through a dual grid face. Relating  $J_{\sigma u}$  to  $E_u$  through the average of surrounding conductivities leads to a relationship between primary grid quantity

$\hat{e}_u = \Delta_u E_u$  and a conduction current dual grid quantity  $\hat{j}_{\sigma u} = J_{\sigma u} \tilde{\Delta}_v \tilde{\Delta}_w$ :

$$\hat{j}_{\sigma x}(i, j, k) = \frac{\hat{e}_x(i, j, k)}{4\Delta_x(i, j, k)} \quad (3.13)$$

$$\begin{aligned} & \times [\sigma(i, j, k) + \sigma(i, j, k-1) + \sigma(i, j-1, k-1) + \sigma(i, j-1, k)] \\ & \times \tilde{\Delta}_z(i+1, j, k) \tilde{\Delta}_y(i+1, j, k) \end{aligned}$$

$$\hat{j}_{\sigma y}(i, j, k) = \frac{\hat{e}_y(i, j, k)}{4\Delta_y(i, j, k)} \quad (3.14)$$

$$\begin{aligned} & \times [\sigma(i-1, j, k) + \sigma(i, j, k) + \sigma(i-1, j, k-1) + \sigma(i, j, k-1)] \\ & \times \tilde{\Delta}_x(i, j+1, k) \tilde{\Delta}_z(i, j+1, k) \end{aligned}$$

$$\hat{j}_{\sigma z}(i, j, k) = \frac{\hat{e}_z(i, j, k)}{4\Delta_z(i, j, k)} \quad (3.15)$$

$$\begin{aligned} & \times [\sigma(i-1, j, k) + \sigma(i-1, j-1, k) + \sigma(i, j-1, k) + \sigma(i, j, k)] \\ & \times \tilde{\Delta}_x(i, j, k+1) \tilde{\Delta}_y(i, j, k+1) \end{aligned}$$

Similar expressions hold between  $\hat{d}$  and  $\hat{e}$  for each component:

$$\hat{d}_x(i, j, k) = \frac{\hat{e}_x(i, j, k)}{4\Delta_x(i, j, k)} \quad (3.16)$$

$$\begin{aligned} & \times [\epsilon(i, j, k) + \epsilon(i, j, k-1) + \epsilon(i, j-1, k-1) + \epsilon(i, j-1, k)] \\ & \times \tilde{\Delta}_z(i+1, j, k) \tilde{\Delta}_y(i+1, j, k) \end{aligned}$$

$$\hat{d}_y(i, j, k) = \frac{\hat{e}_y(i, j, k)}{4\Delta_y(i, j, k)} \quad (3.17)$$

$$\begin{aligned} & \times [\epsilon(i-1, j, k) + \epsilon(i, j, k) + \epsilon(i-1, j, k-1) + \epsilon(i, j, k-1)] \\ & \times \tilde{\Delta}_x(i, j+1, k) \tilde{\Delta}_z(i, j+1, k) \end{aligned}$$

$$\hat{d}_z(i, j, k) = \frac{\hat{e}_z(i, j, k)}{4\Delta_z(i, j, k)} \quad (3.18)$$

$$\begin{aligned} & \times [\epsilon(i-1, j, k) + \epsilon(i-1, j-1, k) + \epsilon(i, j-1, k) + \epsilon(i, j, k)] \\ & \times \tilde{\Delta}_x(i, j, k+1) \tilde{\Delta}_y(i, j, k+1) \end{aligned}$$

The constituent relation  $\vec{B} = \mu \vec{H}$  involves a path integral along a dual grid cell edge spanning two primary grid cells which may have differing permeabilities. The permeabilities are averaged to relate  $\hat{h}_u = \Delta_u H_u$  and  $\hat{b}_u = B_u \Delta_v \Delta_w$ . Referring to

figure 3.5:

$$\hat{b}_x(i, j, k) = \frac{\hat{h}_x(i, j, k)}{2\Delta_x(i, j, k)} [\mu(i-1, j-1, k-1) + \mu(i, j-1, k-1)] \quad (3.19)$$

$$\times \Delta_y(i, j-1, k-1) \Delta_z(i, j-1, k-1)$$

$$\hat{b}_y(i, j, k) = \frac{\hat{h}_y(i, j, k)}{2\Delta_y(i, j, k)} [\mu(i-1, j-1, k-1) + \mu(i-1, j, k-1)] \quad (3.20)$$

$$\times \Delta_x(i-1, j, k-1) \Delta_z(i-1, j, k-1)$$

$$\hat{b}_z(i, j, k) = \frac{\hat{h}_z(i, j, k)}{2\Delta_z(i, j, k)} [\mu(i-1, j-1, k-1) + \mu(i-1, j-1, k)] \quad (3.21)$$

$$\times \Delta_x(i-1, j-1, k) \Delta_y(i-1, j-1, k)$$

The charge conservation equation 3.5 is automatically satisfied insofar as Maxwell's equations are solved and can serve as a check on the algorithm.

The discrete Maxwell's equations are reformulated as matrix equations. The unknown fields are placed in column vectors  $\hat{\mathbf{e}}$  and  $\hat{\mathbf{b}}$ . Conduction current and source current densities are combined in  $\hat{\mathbf{j}}$ . Charge components are collected in  $\mathbf{q}$ :

$$\hat{\mathbf{e}} = [\hat{e}_x(1, 1, 1), \dots, \hat{e}_x(N_x, N_y, N_z), \dots, \hat{e}_z(1, 1, 1), \dots, \hat{e}_z(N_x, N_y, N_z)]^T$$

$$\hat{\mathbf{b}} = [\hat{b}_x(1, 1, 1), \dots, \hat{b}_x(N_x, N_y, N_z), \dots, \hat{b}_z(1, 1, 1), \dots, \hat{b}_z(N_x, N_y, N_z)]^T$$

$$\hat{\mathbf{j}} = [\hat{j}_x(1, 1, 1), \dots, \hat{j}_x(N_x, N_y, N_z), \dots, \hat{j}_z(1, 1, 1), \dots, \hat{j}_z(N_x, N_y, N_z)]^T$$

$$\mathbf{q} = [q(1, 1, 1), \dots, q(N_x, N_y, N_z)]^T$$

Here  $T$  denotes the transpose. Equations 3.9, 3.11, 3.12 and 3.10 can be represented in matrix equations known as Maxwell's grid equations:

$$\mathbf{C}\hat{\mathbf{e}} = -\dot{\hat{\mathbf{b}}} \quad (3.22)$$

$$\tilde{\mathbf{C}}\hat{\mathbf{h}} = \dot{\hat{\mathbf{d}}} + \hat{\mathbf{j}} \quad (3.23)$$

$$\mathbf{S}\hat{\mathbf{b}} = 0 \quad (3.24)$$

$$\tilde{\mathbf{S}}\hat{\mathbf{d}} = \mathbf{q} \quad (3.25)$$

Since the matrix grid spacings  $\Delta_u$  are bound up in the definition of  $\hat{\mathbf{e}}$ ,  $\hat{\mathbf{h}}$ ,  $\hat{\mathbf{d}}$ ,  $\hat{\mathbf{b}}$  and  $\hat{\mathbf{j}}$ , the elements of matrices  $\mathbf{C}$ ,  $\tilde{\mathbf{C}}$ ,  $\mathbf{S}$  and  $\tilde{\mathbf{S}}$  are from  $\{0, -1, 1\}$ .

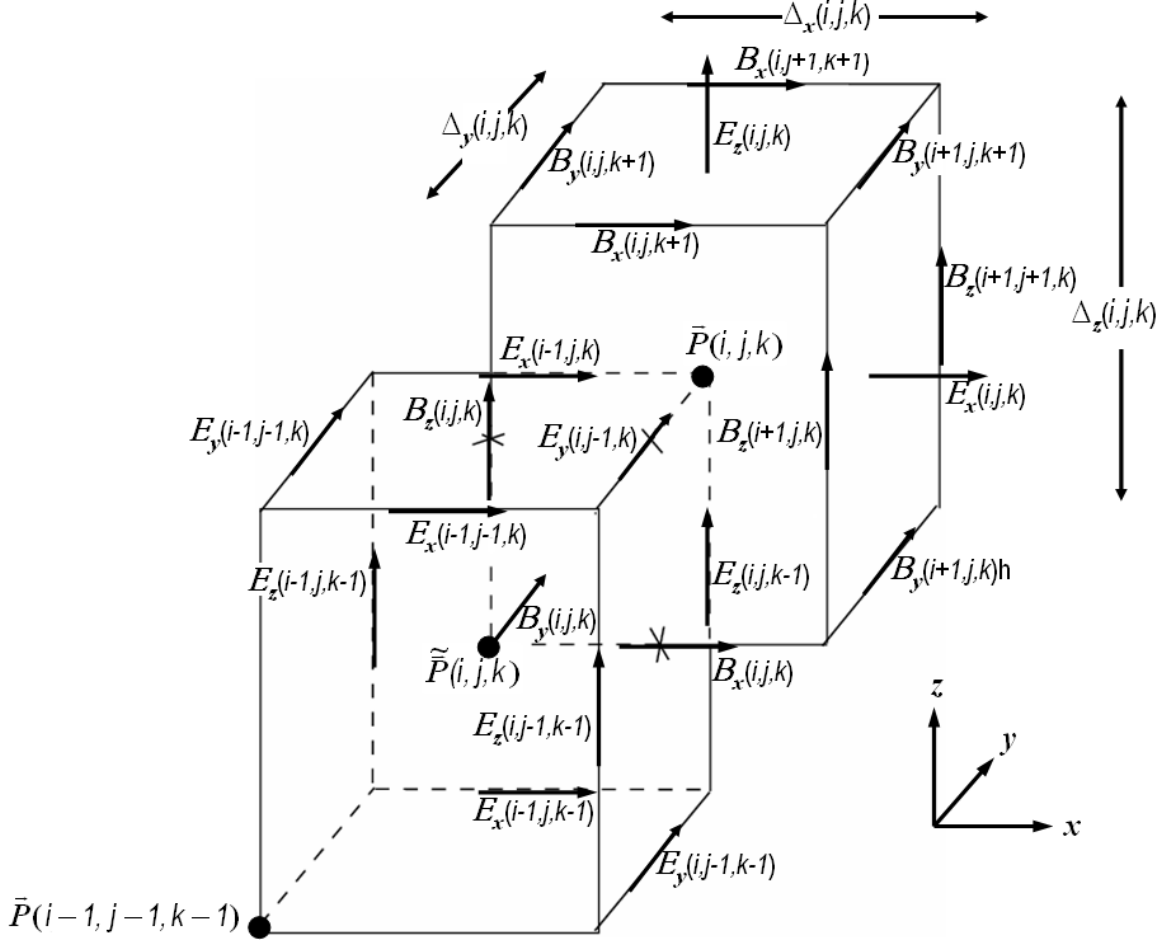


Figure 3.3. Interlaced electric and magnetic grid construction for the Finite Integration Technique showing the assignment of quantities associated with Maxwell's equations 3.1 and 3.3.

The material parameter discrete relations 3.13-3.15, 3.16-3.18, and 3.19-3.21, representing  $\vec{J}_\sigma = \sigma \vec{E}$ ,  $\vec{D} = \epsilon \vec{E}$ , and  $\vec{B} = \mu \vec{H}$  also have matrix representations:

$$\hat{\mathbf{j}}_\sigma = \mathbf{M}_\sigma \hat{\mathbf{e}} \quad (3.26)$$

$$\hat{\mathbf{d}} = \mathbf{M}_\epsilon \hat{\mathbf{e}} \quad (3.27)$$

$$\hat{\mathbf{b}} = \mathbf{M}_\mu \hat{\mathbf{h}} \quad (3.28)$$

The elements of material matrices  $\mathbf{M}_\sigma$ ,  $\mathbf{M}_\epsilon$ ,  $\mathbf{M}_\mu$  contain cell averaged material parameters along with cell edges and face areas over which the averaging is evaluated.

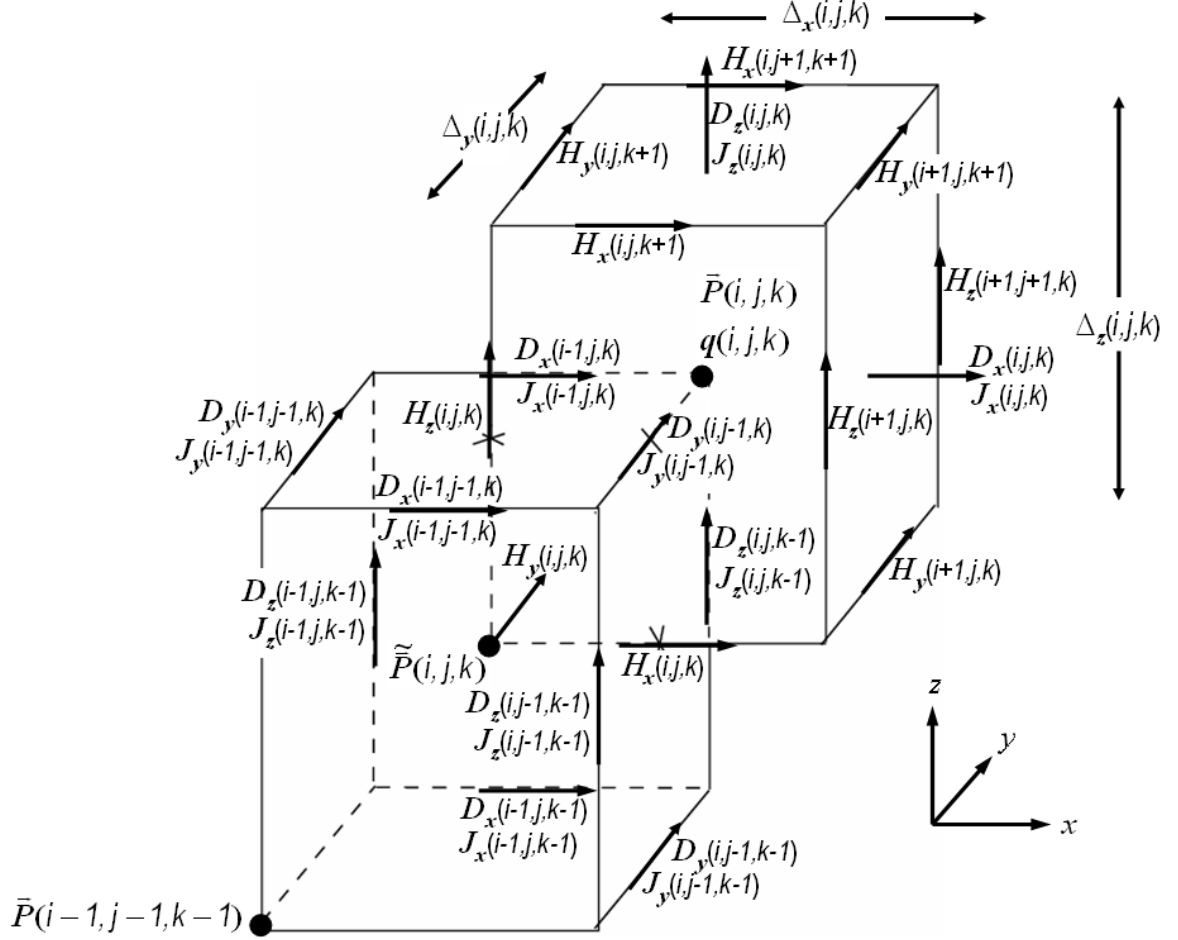


Figure 3.4. Interlaced electric and magnetic grid construction for the Finite Integration Technique showing the assignment of quantities associated with Maxwell's equations 3.2 and 3.4.

For the case of Cartesian grids, material matrices  $\mathbf{M}_\sigma$ ,  $\mathbf{M}_\epsilon$ ,  $\mathbf{M}_\mu$  are diagonal[19].

Matrix equations 3.22-3.25 and 3.26-3.28 represent the finite integration analog to Maxwell's equations and are applicable to any problem addressed by Maxwell's equations. In general, with appropriate boundary conditions, a solution to Maxwell's equations can be found with standard matrix manipulation techniques. The matrices in equations 3.22-3.25 and 3.26-3.28 satisfy the analogous identity relations comparable to electromagnetic field identities involving curl and divergence operations. Vector

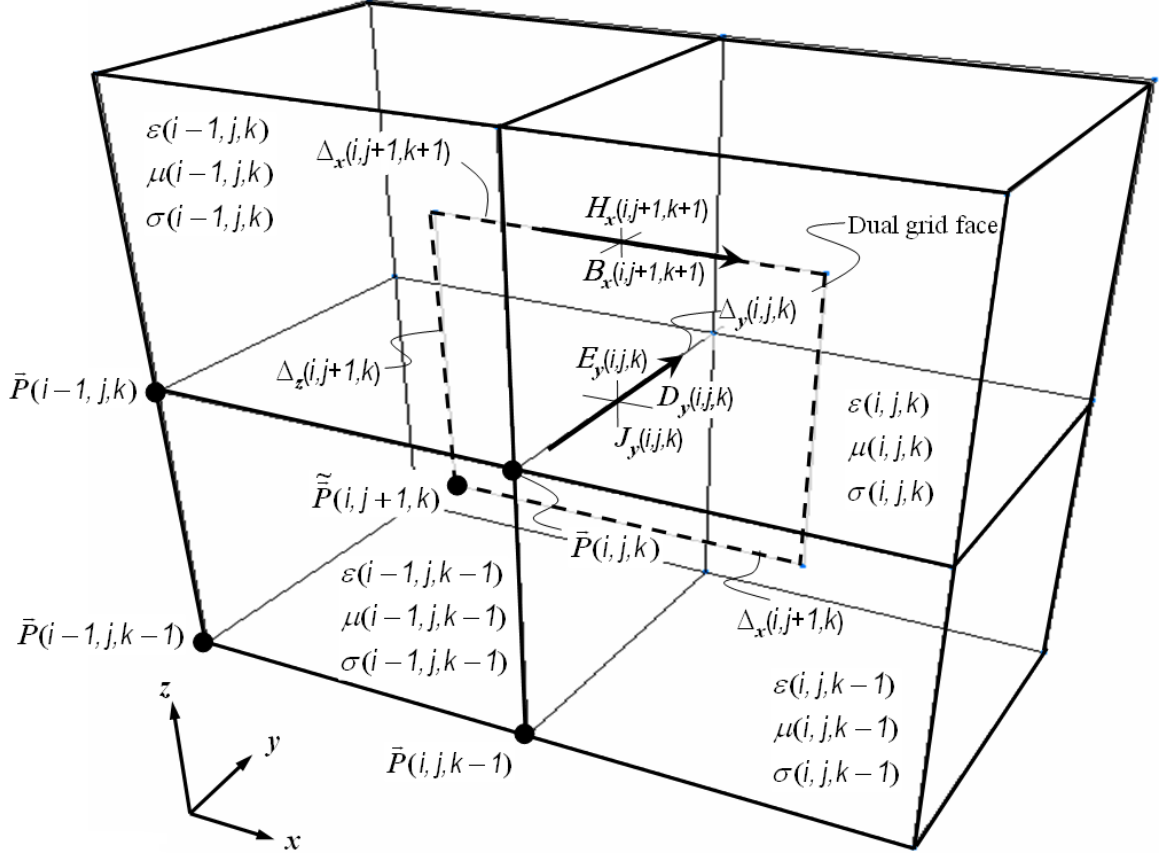


Figure 3.5. Coupling primary and dual grid quantities through the constitutive relations.

identity operation  $\vec{\nabla} \cdot \vec{\nabla} \times \rightarrow 0$  has analogous matrix identities

$$\mathbf{SC} \rightarrow 0$$

$$\tilde{\mathbf{S}}\tilde{\mathbf{C}} \rightarrow 0$$

This ensures conservation of energy and charge to roundoff error.

With the basic FIT method as outlined herein, some numerical solutions of Maxwell's equations in frequency and time domain are described in the following which pertain to problems in this dissertation and are implemented in the MAFIA[13] field solver. More complete expositions on other applications of FIT are widely available in the literature[13, 19, 34].

Time domain solutions utilizes the finite differences time domain method[26, 58]. The time domain is discretized into equal time steps  $\Delta_t$ . Fields at a particular time  $m\Delta_t$  are denoted  $\hat{\mathbf{e}}^{(m)}$  and  $\hat{\mathbf{b}}^{(m)}$ . A central difference derivative approximation determines a time rate of change of electric and magnetic fields in terms of a future and past time:

$$\begin{aligned}\frac{d}{dt}\hat{\mathbf{e}}^{(m+1)} &= \frac{\hat{\mathbf{e}}^{(m+3/2)} - \hat{\mathbf{e}}^{(m+1/2)}}{\Delta_t} \\ \frac{d}{dt}\hat{\mathbf{b}}^{(m+1/2)} &= \frac{\hat{\mathbf{b}}^{(m+1)} - \hat{\mathbf{b}}^{(m)}}{\Delta_t}\end{aligned}$$

With help from Maxwell's grid equations and constituent relations 3.22, 3.23, 3.27 and 3.28, recursive equations are formed which are suitable for computer solution:

$$\hat{\mathbf{e}}^{(m+3/2)} = \hat{\mathbf{e}}^{(m+1/2)} - \Delta_t \mathbf{M}_\epsilon^{-1} \left( \tilde{\mathbf{C}} \mathbf{M}_\mu^{-1} \hat{\mathbf{b}}^{(m+1)} - \hat{\mathbf{j}}^{(m+1)} \right) \quad (3.29)$$

$$\hat{\mathbf{b}}^{(m+1)} = \hat{\mathbf{b}}^{(m)} - \Delta_t \mathbf{C} \hat{\mathbf{e}}^{(m+1/2)} \quad (3.30)$$

This algorithm, known as the leap frog or Yee finite difference time domain algorithm[58], is computationally efficient, since only fields at a previous time step are required in evaluating the fields at the next time step. It is susceptible to numerical errors stemming from the rate at which time dependent quantities are advanced through the grid. Above a critical time step interval numerical errors can grow unbounded, giving physically unreasonable results. This maximum stable time interval depends on the grid density and is given by the Courant-Friedrichs-Lewy criterion[62]. The algorithm is subject to a wave solution of free space frequency  $\omega$  and wave vector  $\vec{k} = (k_x, k_y, k_z)$

$$\hat{\mathbf{e}} = \hat{\mathbf{e}}_0 e^{i(\vec{k} \cdot \vec{r} - \omega t)}$$

In this context a grid characteristic dispersion relation is extracted from recursion equations 3.29 and 3.30:

$$\left( \frac{\sin\left(k_x \frac{\Delta x}{2}\right)}{\frac{\Delta x}{2}} \right)^2 + \left( \frac{\sin\left(k_y \frac{\Delta y}{2}\right)}{\frac{\Delta y}{2}} \right)^2 + \left( \frac{\sin\left(k_z \frac{\Delta z}{2}\right)}{\frac{\Delta z}{2}} \right)^2 = \left( \frac{\sin\left(\omega \frac{\Delta t}{2}\right)}{\frac{\Delta t}{2}} \right)^2$$

A stability criterion can be established by the requirement that the frequency  $\omega$  be real. This constrains the relationship of the time and space intervals through[26]

$$\Delta_t \leq \frac{\sqrt{\mu\epsilon}}{\sqrt{\frac{1}{\Delta_x^2} + \frac{1}{\Delta_y^2} + \frac{1}{\Delta_z^2}}} \quad (3.31)$$

The case of an ultra-relativistic beam is implemented as a driving current with source charges propagating through the grid with the speed of light, usually along the  $z$ -axis. The moving charges must additionally satisfy the continuity equation which has a discrete form

$$\tilde{\mathbf{S}}\hat{\mathbf{j}} + \dot{\mathbf{q}} = 0 \quad (3.32)$$

Stability requirement equation 3.31 constrains the maximum time step to be less than the speed of light transit time of a charge through a cell length. By setting a time step as an integer fraction of the cell transit time, the continuity equation 3.32 is also satisfied.

The frequency domain formulation starts with  $\hat{\mathbf{e}}(t) = Re(\hat{\underline{\mathbf{e}}}e^{i\omega t})$ . Where no lossy materials and no external driving currents are concerned, the discrete form of Maxwell's equations 3.1 and 3.2 become

$$\begin{aligned} \mathbf{C}\hat{\underline{\mathbf{e}}} &= -i\omega\hat{\underline{\mathbf{b}}} \\ \tilde{\mathbf{C}}\mathbf{M}_\mu\hat{\underline{\mathbf{b}}} &= i\omega\mathbf{M}_\epsilon\hat{\underline{\mathbf{e}}} \end{aligned}$$

which can be combined into one eigenvector equation

$$\tilde{\mathbf{C}}\mathbf{M}_\mu\mathbf{C}\hat{\underline{\mathbf{e}}} = \omega^2\mathbf{M}_\epsilon\hat{\underline{\mathbf{e}}} \quad (3.33)$$

This equation is applicable for finding frequencies and normal mode solutions of closed cavities.

### 3.1.2 NOVO[14] Wake Field Calculations

The primary sources of error in finite difference time domain (FDTD) solvers for wake field problems are numerical instability and numerical dispersion. Errors are bounded

if the distance a free space wave travels in one time step is less than or equal to the mesh cell size. In essence, the time step must be less than it takes for a significant physical effect to occur. This criterion is known as the Courant-Friedrichs-Lewy condition[62]. Numerical dispersion causes free space waves of different frequencies to propagate at speeds less than  $c$ , placing further constraints on time and mesh cell sizes. This error is specific to the algorithm. Numerical dispersion can be considerable for high frequency components making simulations involving short bunches prone to error. This results in inaccuracies over large time domains and/or for short bunch lengths. Explicit FDTD algorithms for which the  $n+1$  time step solution is given in terms of previous time steps are subject to both stability and dispersion errors. Implicit methods (in which the  $n+1$  term appears on both sides of the equation) are not subject to the CFL criterion, allowing larger time steps without compromising accuracy, but usually at increased computational expense.

An efficient implicit method is developed in the NOVO program to accurately calculate wake fields for short bunch lengths over long time scales. The program is based on Maxwell's equations under azimuthal symmetry in cgs units

$$\frac{\partial(\epsilon_0 E_z)}{\partial t} = \frac{1}{r} \frac{\partial(r H_\phi)}{\partial r} - j_z \quad (3.34)$$

$$\frac{1}{r} \frac{\partial(r \epsilon_0 E_r)}{\partial r} + \frac{\partial(\epsilon_0 E_z)}{\partial z} = \rho \quad (3.35)$$

$$\frac{\partial(\mu_0 H_\phi)}{\partial t} = -\frac{\partial E_r}{\partial z} + \frac{\partial E_z}{\partial r} \quad (3.36)$$

$$\frac{\partial(\epsilon_0 E_r)}{\partial t} = -\frac{\partial H_\phi}{\partial z} \quad (3.37)$$

with a boundary condition at the infinitely conductive beam chamber wall with surface normal  $\vec{n}$ :

$$\vec{n} \times \vec{E} = 0 \quad (3.38)$$

For a beam with velocity in the  $z$ -direction  $\vec{v} = v_z \hat{z}$ , the charge density and  $z$ -

component of current density is

$$\begin{aligned}\rho(r, z, t) &= \rho(r, v_z t - z) \\ j_z(r, z, t) &= v_z \cdot \rho(r, z, t)\end{aligned}$$

The goal is to express Maxwell's equations in terms of the electric field flux through the  $z$  plane

$$\Phi(r, z, t) = 2\pi \int_0^r \epsilon_0 E_z(r', z, t) r' dr'$$

The bunch is considered as a line charge density

$$\lambda = 2\pi \int_0^r \rho(r', v_z t - z) r' dr'$$

The electric and magnetic field components are expressed in terms of the  $z$  electric field flux

$$E_z = \frac{1}{2\pi\epsilon_0 r} \frac{\partial}{\partial r} \Phi \quad (3.39)$$

$$E_r = \frac{1}{2\pi\epsilon_0 r} \left( \lambda - \frac{\partial}{\partial z} \Phi \right) \quad (3.40)$$

$$H_\phi = \frac{c}{2\pi r} \left( \lambda \frac{v_z}{c} + \frac{1}{c} \frac{\partial}{\partial t} \Phi \right) \quad (3.41)$$

with a boundary condition

$$\vec{n} \cdot \left( \vec{\nabla} \Phi - \frac{\vec{v}}{c} \lambda \right) = 0 \quad (3.42)$$

Inserting these field components in Maxwell's equation 3.36 yields a partial differential equation in  $\Phi$

$$\frac{1}{c} \frac{\partial^2 \Phi}{\partial t^2} - \frac{\partial^2 \Phi}{\partial z^2} - r \frac{\partial}{\partial r} \left( \frac{1}{r} \frac{\partial \Phi}{\partial r} \right) = \left( \frac{v_z^2}{c^2} - 1 \right) \frac{\partial \lambda}{\partial z} \quad (3.43)$$

The right hand side is zero in the ultra relativistic case  $v_z/c \rightarrow 1$ . To discretize equation 3.43 let  $n$  enumerate the time step while  $k$  indexes a space interval along

the  $z$  axis. Using a discrete forward difference for derivatives in  $t$  and  $z$  gives the explicit form:

$$\begin{aligned} \Phi_k^{n+1} - 2\Phi_k^n + \Phi_k^{n-1} &= \left(\frac{c\Delta_t}{\Delta z}\right)^2 (\Phi_{k+1}^n - 2\Phi_k^n + \Phi_{k-1}^n) + \\ &\quad \left(\frac{c\Delta_t}{\Delta r}\right)^2 r \left[\frac{\partial}{\partial r}\right] \left(\frac{1}{r} \left[\frac{\partial}{\partial r}\right] \Phi_k^n\right) \end{aligned} \quad (3.44)$$

where the last term with  $r$  derivatives is not expanded,  $\left[\frac{\partial}{\partial r}\right]$  representing the  $r$  finite difference operator. The solution at time  $n+1$  is found explicitly in terms of solutions at  $n$  and  $n-1$ . A dispersion free solution for equation 3.44 exists for a time step of  $\Delta z = c\Delta_t$ [14] but violates the Courant stability criterion. This is also true of explicit schemes used in wake field codes in MAFIA and ABCI[29].

An implicit form of equation 3.44 is constructed by replacing  $\Phi_k^n$  with its time average  $\frac{1}{2}(\Phi_k^{n+1} + \Phi_k^{n-1})$  on the right hand side:

$$\begin{aligned} \Phi_k^{n+1} - 2\Phi_k^n + \Phi_k^{n-1} &= \left(\frac{c\Delta_t}{\Delta z}\right)^2 (\Phi_{k+1}^n - 2\Phi_k^n + \Phi_{k-1}^n) + \\ &\quad \frac{1}{2} \left(\frac{c\Delta_t}{\Delta r}\right)^2 r \left[\frac{\partial}{\partial r}\right] \left[\frac{1}{r} \left[\frac{\partial}{\partial r}\right] (\Phi_k^{n+1} + \Phi_k^{n-1})\right] \end{aligned} \quad (3.45)$$

Under the space time interval constraint  $c\Delta_t = \Delta z$  numerical dispersion vanishes for equation 3.45. The implicit algorithm is unconditionally stable. Introducing  $m$  as a discrete radial index and isolating all terms of time step  $n+1$  equation 3.45 has the form

$$a_m \Phi_{k,m+1}^{n+1} + b_m \Phi_{k,m}^{n+1} + c_m \Phi_{k,m-1}^{n+1} = d_m \quad (3.46)$$

where coefficients  $a_m, b_m, c_m$  are functions of  $r, \Delta_r, \Delta_z, \Delta_t$  and  $d_m$  is additionally a function of radial and  $z$  differences at the two previous time steps. The solution involves computing recursive coefficients

$$\begin{aligned} \alpha_m &= -\frac{a_m}{b_m + c_m \alpha_{m-1}} \\ \gamma_m &= -\frac{\gamma_{m-1} c_m + d_m}{b_m + c_m \alpha_{m-1}} \end{aligned}$$

from which the flux can be determined through

$$\Phi_{k,m}^{n+1} = \alpha_m \Phi_{k,m}^{n+1} + \gamma_m$$

along with boundary conditions 3.42. Although the implicit solution requires extra computing steps to solve equation 3.46, the time steps can be made twice as long. Computation time is about the same as for explicit schemes and solutions are accurate for shorter bunch lengths[14].

### 3.2 Mode Analysis

This deals primarily with cavity-like structures, such as bellows, which can harbor parasitic resonances. Standing wave modes are calculated, which can be related to propagating modes in a waveguide of the same cross section. These modes resonate at specific frequencies. If these frequencies fall within the realm of the beam spectra, a coupling mechanism can drive these modes. A shorter bunch will span a larger frequency range, potentially driving more modes. Given the resonant electric and magnetic fields, quality factors ( $Q$  factors) can be calculated. Geometry and material parameters can be altered with the aim of reducing  $Q$  factors of bellows modes. The bellows are approximated as a coaxial cavity for these computations.

Wake fields from the RF cavities are the largest source of wake fields in a storage ring. The fundamental mode interaction is necessary for acceleration. Higher order modes are coupled out by design, but this coupling is not completely effective, and beam oscillations in both transverse and longitudinal planes must be controlled with dedicated fast feedbacks which are designed to measure bunch oscillations and provide a turn by turn damping kick[25, 15]. The fundamental mode is driven by an RF generator (klystron and power supply) whose phase and amplitude is modulated by a complex feedback system[16] in order match the beam impedance to the cavities.

Wake potentials due to a beam traversing a cavity can be evaluated from the normal modes of the cavity[33]. Given a cavity mode  $\mu$  and frequency  $\omega_\mu$ , an asso-

ciated loss factor  $k_\mu$  for a point charge  $q$  traversing the cavity can be calculated in terms of the potential energy seen by the charge due to the mode electric field along the trajectory. The total wake potential  $W_q$  due to a point charge  $q$  evaluated at a distance  $s$  behind the point charge is given in terms of a sum over modes where mode loss factors become coefficients of the individual terms.

$$W_q = -q \sum_{\mu} k_{\mu} \cos(\omega_{\mu} s/c) \quad (3.47)$$

The mode loss factors are given by

$$k_{\mu} = \frac{V_{\mu} \cdot V_{\mu}^*}{4U_{\mu}} \quad (3.48)$$

where  $V_{\mu}$  is the potential energy acquired/lost by the charge as it traverses a cavity with mode  $\mu$  excited and  $U_{\mu}$  is the stored energy of the mode. The asterisk  $*$  denotes complex conjugation. The longitudinal cavity electric field  $E_z$  along the charge trajectory, frequency  $\omega_{\mu}$  and the mode stored energy  $U_{\mu}$  must be evaluated for many modes to accurately determine the wake potential. This is particularly significant for short bunches.

The simple pillbox cavity provides a test of numerical methods used in the calculation of quality factors, forming the basis for the analysis of cavities coupled to a HOM source, such as bellows and pump chambers in an accelerator. Additionally, given the analytic solutions for the pillbox cavity modes, the pillbox model provides an understanding of how wake fields produced by a beam in a cavity structure can be analytically evaluated.

### 3.2.1 Pillbox Cavity Analysis

The cylindrical pillbox cavity eigenmodes and eigenfrequencies have been solved analytically[31] for infinitely conductive walls. In the geometry shown in figure 3.6,  $g$  is the cavity length,  $R$  is the cavity radius in the cylindrical coordinate system  $(r, \phi, z)$ .

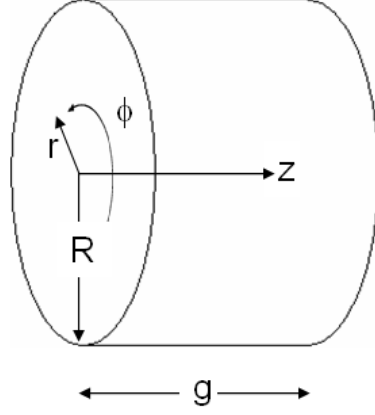


Figure 3.6. Cylindrical pillbox cavity geometry. Cavity length is  $g$ , radius  $R$  in cylindrical coordinates  $(r, \phi, z)$ .

Only modes with longitudinal electric field (TM) will affect beam energy. In the evaluation of the mode loss factor  $k_\mu$  the field amplitudes can be normalized since they cancel out in equation 3.48. A point charge on the cylindrical axis is considered in which case only fields with azimuthal symmetry will be excited. These TM modes can be expressed in terms of Bessel functions  $J_0, J_1$  by the following[36]:

$$E_z^{np} = \frac{j_n}{R} J_0 \left( j_n \frac{r}{R} \right) \cos \left( \frac{\pi p z}{g} \right) \exp(i\omega_{np} t) \quad (3.49)$$

$$E_r^{np} = -\frac{\pi p}{g} J_1 \left( j_n \frac{r}{R} \right) \sin \left( \frac{\pi p z}{g} \right) \exp(i\omega_{np} t) \quad (3.50)$$

$$H_\phi^{np} = i\omega_{np} \epsilon_0 J_1 \left( j_n \frac{r}{R} \right) \cos \left( \frac{\pi p z}{g} \right) \exp(i\omega_{np} t). \quad (3.51)$$

The modes are indexed  $\mu \rightarrow n, p$  corresponding to the number of nodes in radial and longitudinal directions respectively. The eigenfrequencies are given by

$$\omega_{np} = c \sqrt{\left( \frac{j_n}{R} \right)^2 + \left( \frac{\pi p}{g} \right)^2}$$

where  $j_n$  are zeroes of Bessel function  $J_0$  and  $c$  is the speed of light.

The voltage change seen by a charge  $q$  traveling at the speed of light on axis

through the pillbox excited in the  $n, p$  mode can be evaluated[36]:

$$V_{np} = \int_0^g E_z^{np} (r = 0, z, t = z/c) dz. \quad (3.52)$$

$$= \frac{i\omega_{np}R}{J_n c} \left[ 1 - (-1)^p \exp\left(i\frac{\omega_{np}g}{c}\right) \right] \quad (3.53)$$

$$V_{np} \cdot V_{np}^* = 2 \left( \frac{\omega_{np}R}{j_n c} \right)^2 \left[ 1 - (-1)^p \cos\left(\frac{\omega_{np}g}{c}\right) \right] \quad (3.54)$$

The stored energy in the electromagnetic fields of the eigenmode is obtained by integrating the energy density over the cavity volume:

$$U_{np} = \frac{\mu_0}{2} \int_0^R \int_0^{2\pi} \int_0^g H_\phi^{np} \cdot H_\phi^{*np} dz d\phi dr \quad (3.55)$$

$$= \frac{\pi\epsilon_0\omega_{np}^2}{4c^2} g R^2 J_1^2(j_n) \quad (3.56)$$

The results of equations 3.54, 3.56 in 3.48 yields a mode loss factor

$$k_{np} = \frac{1}{\pi\epsilon_0 g} \frac{1 - (-1)^p \cos(\omega_{np}g/c)}{j_n^2 J_1^2(j_n)} \quad (3.57)$$

When inserted into equation 3.47 the point charge wake potential for a cylindrical pillbox cavity is found to be:

$$W_q(z_0) = \frac{-2q}{\pi\epsilon_0 g} \sum_{n=1}^{+\infty} \sum_{p=-\infty}^{+\infty} \frac{1 - (-1)^p \cos(\omega_{np}g/c)}{j_n^2 J_1^2(j_n)} \cos(\omega_{n.p}z_0/c) \quad (3.58)$$

where  $z_0$  is the distance behind the point charge at which a test charge samples the wake fields.

The numerical computation of cavity modes and frequencies involves iterative matrix method solutions of FIT[34] frequency domain equations 3.33. For most cavity mode fields and frequency determinations, MAFIA utilizes the semi-analytic eigenvector processor (SAP)[30]. Convergence to an accurate solution is a function of the number of iterations and the number of modes used in the iteration process. In practice, a compromise is made between computational resources and accuracy. For a

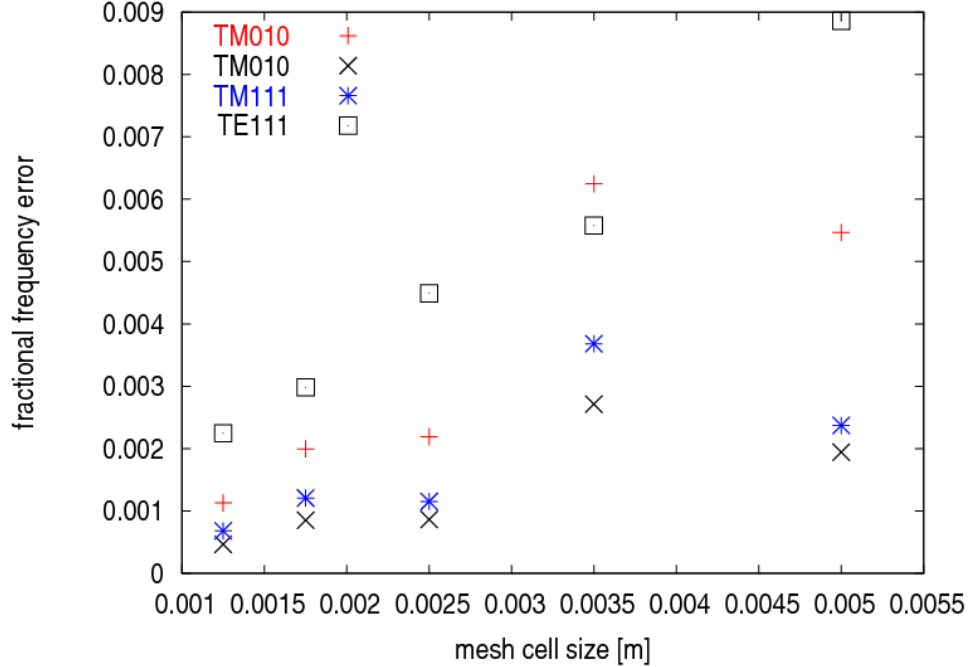


Figure 3.7. MAFIA fractional frequency error  $|f_M - f_A|/f_A$  relative to analytic results versus mesh cell size for several modes where  $f_M$  is the frequency determined from MAFIA and  $f_A$  is the analytical value. Six iterations searching for 15 modes with a uniform cubic mesh. Pillbox example of radius  $r = 0.06858$  m and length  $g = 0.0889$  m

pillbox example of radius  $r = 0.06858$  m and length  $g = 0.0889$  m, MAFIA generated frequencies  $f_M$  remain constant with both number of iterations and number of modes searched for.

Fractional frequency errors  $|f_M - f_A|/f_A$  with reference to the analytical values  $f_A$  as a function of mesh size for several modes is shown in figure 3.7. Computations are performed for 6 iterations searching for 15 modes using a uniform mesh of cubic cells. All modes appear to converge to the analytic values with decreasing mesh cell size.

While a small mesh size improves accuracy, computational time and memory requirements increase dramatically with decreasing mesh size. The CPU time as a function of mesh size is shown as a log-log plot in figure 3.8. At the smallest mesh

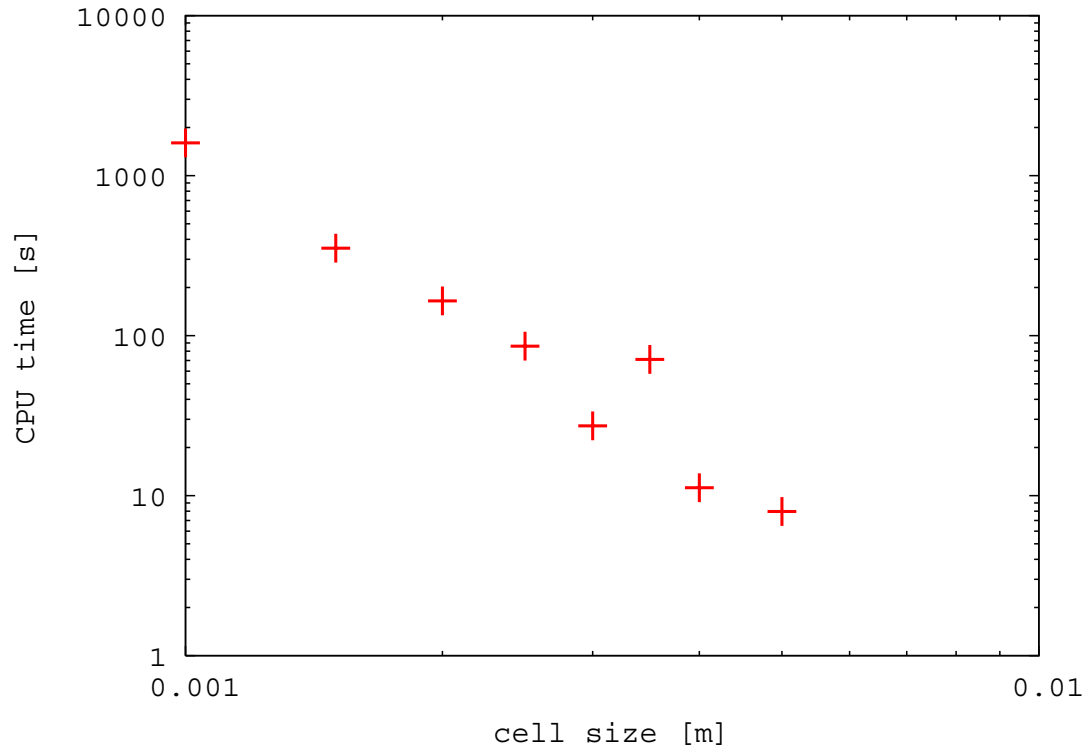


Figure 3.8. Log-log plot of MAFIA CPU time in seconds for pillbox modes computation versus mesh cell size in meters. Six iterations searching for 15 modes. Pillbox example of radius  $r = 0.06858$  m and length  $g = 0.0889$  m.

cell size of .001 meter a total of 1,694,916 mesh point are involved. Six iterations and 15 modes required 1080 seconds of CPU time on a Sun Fire X2200M2 with dual dual-core 2.6 GHz Opteron 2218 CPUs and 8 GB memory.

### 3.2.2 $Q$ factor

When electromagnetic power is introduced into a cavity (such as by coupling through slotted apertures in the bellows) a parasitic resonance can be driven in the cavity. Resistive wall heating then results. Reduction of resistive heating from parasitic resonances can be accomplished by damping the cavity resonant modes. This can be done by dissipating the cavity electromagnetic energy in a lossy medium. The damping effectiveness is measured by the reduction of the mode quality factor  $Q$ .

Given the modes, a  $Q$  factor (quality factor) calculation is performed which indicates the strength of the mode and its response to being driven. This is a quantity proportional to the electromagnetic energy  $U_{\text{field}}$  stored in the cavity fields divided by the power  $P$  dissipated over a single period  $T$  of oscillation mode frequency. For a simple cavity power is dissipated in the cavity walls:  $P = P_{\text{cav}}$ ,

$$Q = \frac{2\pi U_{\text{field}}}{\int_0^T P dt}. \quad (3.59)$$

The introduction of lossy materials with high permittivity or permeability will reduce the  $Q$  factor further by channeling more electromagnetic power into the lossy material. As a practical matter a high permittivity lossy dielectric is used in these studies since ceramic dielectrics with such properties are commercially available and mechanically suitable for fabrication in accelerator structures. The material chosen is a dielectric ceramic alloy of Aluminum, Nitrogen, Silicon and Carbon (AlN-SiC) of relative permittivity 22-30 and loss tangent 0.11-0.3 in the 1-8 GHz regime, manufactured by Ceradyne Corporation[59]. A table of physical properties can be found in appendix A.1. Since electromagnetic energy is to be dissipated as heat, consideration must be given to thermal conductivity and expansion and behavior under high thermal stress. Magnetic lossy materials can also serve to damp resonant modes when placed in areas of high magnetic field.

The high material permittivity increases the electric field flux density in the ma-

terial. The loss parameter (loss tangent) dissipates additional power which becomes  $P = P'_{\text{cav}} + P_{\text{lossy}}$  where  $P'_{\text{cav}}$  is the cavity wall power loss in the presence of the lossy material and  $P_{\text{lossy}}$  is the power dissipated in the lossy material.  $P'_{\text{cav}} \neq P_{\text{cav}}$  in general because a high permittivity material changes the field distribution.

Bellows cavity mode electric and magnetic field distributions and frequencies are computed with MAFIA[13]. The field distribution and frequencies are determined for infinitely conducting cavity walls of the bellows and the geometry and permittivity of the introduced lossy material. No losses are assumed in evaluation of fields and frequencies. The large finite conductivity  $\sigma$  of stainless steel walls is assumed to negligibly affect the field distribution.

Given these mode fields and frequencies a perturbation power loss computation is performed in MAFIA to evaluate the power loss due to both the metal walls  $P'_{\text{cav}}$  and lossy material  $P_{\text{lossy}}$  after specifying a conductivity  $\sigma$  for the metal walls and a loss tangent defined by  $\tan \delta = \epsilon''/\epsilon'$ , where  $\epsilon''$  and  $\epsilon'$  are the imaginary and real parts of the complex permittivity for the lossy dielectric material. The losses from the metal cavity walls  $P'_{\text{cav}}$  are estimated from the wall resistance and magnetic field energy density at the wall surface (surface currents). The dielectric losses  $P_{\text{lossy}}$  are evaluated from the effective conductivity  $\sigma_{\text{eff}} = \omega\epsilon' \tan \delta$  associated with the lossy material and electric field energy density in the lossy material volume.

Analytic evaluation of frequencies and  $Q$  factors are compared with the MAFIA results for the case of an empty pillbox cavity. The empty pillbox cavity  $Q$  factors can be expressed in terms of the cavity length, radius, and skin depth[57]. In the defining equation 3.59 for the  $Q$  factor the stored energy  $U_{\text{field}}$  for a pillbox cavity is given in equation 3.56. The dissipated power  $P$  in the cavity walls can be determined from the solution for pillbox cavity fields and the skin depth  $\delta$  (not to be confused with the loss tangent above). The skin depth depends upon the metal resistivity  $\rho$  through  $\delta = \sqrt{\rho/\omega\mu_0}$ . Joule heating gives a differential power dissipation of  $dP = I^2 dR$

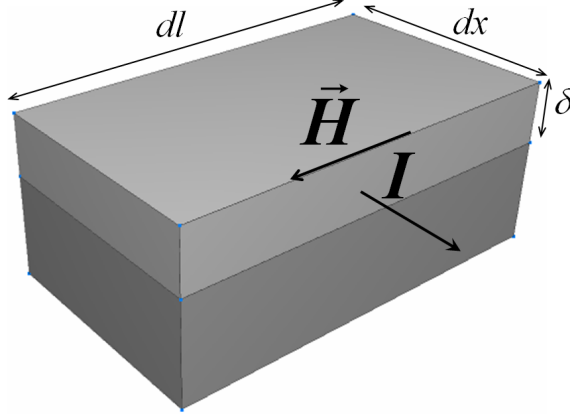


Figure 3.9. Current  $I$  flowing in a small pillbox cavity conductive wall element of area  $dx \cdot dl$  with a skin depth  $\delta$  as a result of tangential magnetic field  $\vec{H}$ .

where  $I$  is the current flowing through a conductor of resistance  $dR$ . For a small wall element depicted in figure 3.9 of length  $dl$  and width  $dx$ , the current is found through Ampere's circuital law using the pillbox cavity magnetic field solution at the wall

$$I = Hdl \quad (3.60)$$

In the high conductivity approximation  $\vec{H}$  remains mostly tangential to the surface. The differential resistance is related to the resistivity

$$dR = \frac{\rho}{\delta} \frac{dx}{dl} \quad (3.61)$$

so that the power dissipated in the cavity walls is

$$P = \frac{\rho}{\delta} \int_A H^2 dA \quad (3.62)$$

For radius 0.06858 m and length 0.0889 m, frequencies and  $Q$  factor calculations are tabulated in tables 3.1 and 3.2 for various mode types TM: transverse magnetic, TE: transverse electric, with mode indices indicating field variation along each cylindrical coordinate dimension  $(r, \phi, z)$ . The MAFIA and analytic frequencies agree, but the MAFIA  $Q$ -factors are consistently lower by about 10-15%. This is consistent with

mode	MAFIA $f_M$ [Hz]	Analytic $f_A$ [Hz]	$ f_A - f_M /f_A$
TM010	1.67524E+09	1.67311E+09	1.3E-03
TM011	2.37644E+09	2.37549E+09	4.0E-04
TM111	3.15724E+09	3.15442E+09	8.9E-04
TE111	2.11429E+09	2.11768E+09	1.6E-03

Table 3.1. MAFIA and analytic evaluation of frequency for several modes of a copper pillbox cavity of radius 0.06858 m and length 0.0889 m. Mesh size .001 m with 6 iterations and 15 modes. Third column contains the fractional difference.

mode	MAFIA $Q_M$	Analytic $Q_A$	$ Q_A - Q_M /Q_A$
TM010	2.07163E+04	2.39696E+04	1.4E-01
TM011	1.79370E+04	1.98961E+04	9.8E-02
TM111	2.06980E+04	2.29272E+04	9.7E-02
TE111	2.41118E+04	2.71009E+04	1.1E-01

Table 3.2. MAFIA and analytic  $Q$  factor evaluation for several modes of a copper pillbox cavity of radius 0.06858 m and length 0.0889 m. Mesh size .001 m with 6 iterations and 15 modes. Third column contains the fractional difference.

the MAFIA rectangular mesh approximation of a cylindrical wall, where the surface area is overestimated and the dissipated power is artificially high. For a simple box with flat surfaces the  $Q$  values agree at the 1 % level.

To study this mesh dependent error, a pillbox is modelled with a coarse mesh of 0.005 m cell size as shown in figure 3.10. MAFIA gives a  $Q$  factor of  $Q_M = 20,766$  for this case. The interior surface area of the pillbox can be divided into three regions: two end caps and one cylinder. The analytically determined magnetic field (equation 3.51) for the TM010 mode is constant on the cylinder walls with a bessel function radial dependence. A plot of MAFIA[13] fields shown in figure 3.11 qualitatively confirms this.

The mesh domain at the end caps is 28 cells square in area, each cell having dimensions 4.9 mm x 4.9 mm x 5.2 mm ( $x, y, z$ ), with 17 cells in the  $z$  direction as determined from the MAFIA generated mesh in figure 3.10. The mesh area for the circular end caps is larger than the ideal circle by 3.2%. The mesh area of the cylindrical surface is larger than the ideal cylinder area by 27%. The total mesh

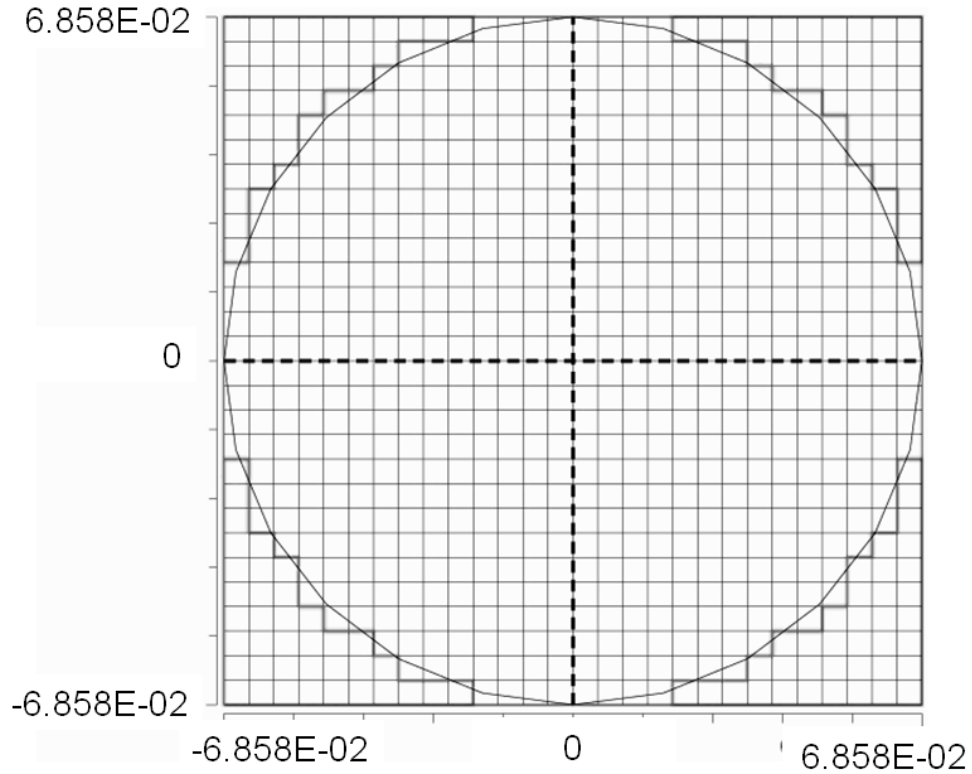


Figure 3.10. Stair case approximation for pillbox cavity geometry generated by MAFIA[13].

volume is larger than the ideal pillbox by 2.3%. From the field plots and based on the analytic result of equation 3.51 , the tangential magnetic field is maximum near the outer surface  $r = R$ , and remains relatively large at the outer surface where the contribution of the geometric mesh errors are large. The cylinder wall mesh errors are the most egregious and will have a large impact on the accuracy of the  $Q$  factor. Since the field is constant at the cylindrical surface, a 27% correction for the power dissipated in this area can be applied to the MAFIA cylindrical wall power loss. This brings the MAFIA based  $Q$  factor value up to  $Q_M = 24,962$ , an agreement at the 4% level with the analytically derived value of  $Q_A = 23,970$ .

With smaller mesh cell sizes or number of iterations there is little improvement in  $Q$  factor errors. Figure 3.12 is a plot of the TM010  $Q$  factors as a function of mesh cell

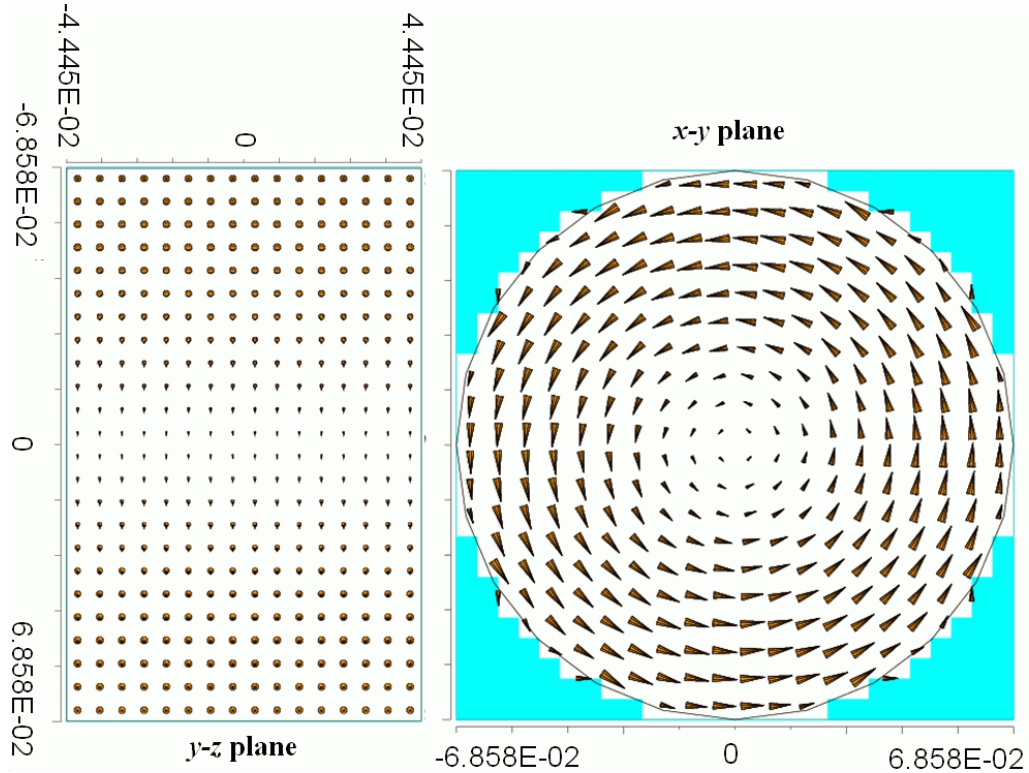


Figure 3.11. Two views of the TM010 mode magnetic fields in a pillbox cavity calculated with MAFIA[13]. Left  $y$ - $z$  plane. Right  $x$ - $y$  plane. The field is constant on the cylindrical conductor surface  $r = R$ , and has a bessel function  $J_1$  radial dependence.

size, suggesting a convergence to a final value lower than the analytic determination. At a fixed cell size of 0.0025 m the number of iterations was varied from 1 to 16. The MAFIA based quality factor trends downward with increasing number of iterations as shown in figure 3.13. Finite element methods that achieve high order accuracy by modeling all quantities of interest in terms of differential algebra (DA) vectors also exist[45, 47, 48, 49].

Several error checks are performed in the MAFIA eigenmode solver. The calculated fields are fed to the matrix version of curl and divergence operators to form the grid Maxwell's equations for the problem. The discrepancy is quantified and solutions are flagged according to an error tolerance (typically 1E-5). Iterations stop when the tolerance is met. The divergence of source free fields are compared to zero as an

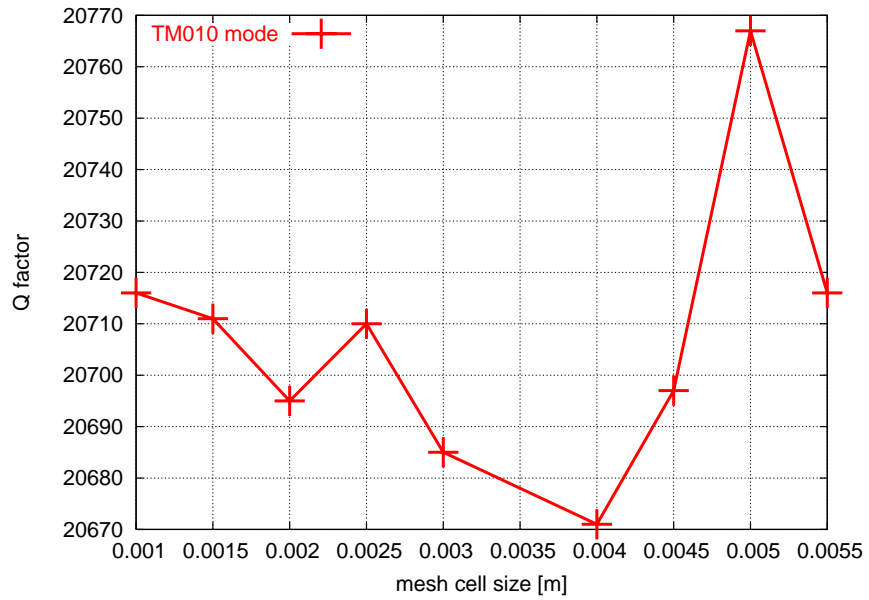


Figure 3.12.  $Q$  factor vs mesh cell size for the TM010 mode. Six iterations searching for 15 modes.

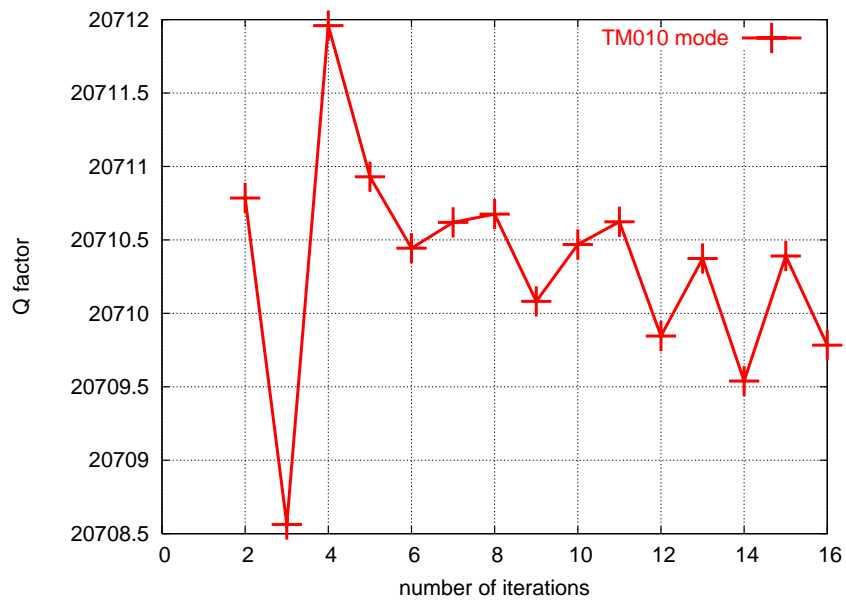


Figure 3.13.  $Q$  factor vs number of iterations for the TM010 mode. Mesh cell size .0025 m searching for 15 modes.

example of one such check. Another check is based on how well the FIT frequency domain eigenvector equation 3.33 is satisfied.

It is also possible to infer the frequency  $f$  and the  $Q$  values of a dielectric filled cavity given the empty cavity frequency  $f_0$  and quality factor  $Q_0$ . These dielectric effects can also serve as an analytic verification of the computational method. The mode frequency  $f$  is given in terms of the speed of propagation  $v$  in the media and the wave number  $k$  by  $f = vk/2\pi$ . In a dielectric of relative real permittivity  $\epsilon'$  the velocity is  $v = 1/\sqrt{\epsilon'\epsilon_0\mu_0} = c/\sqrt{\epsilon'}$ , yielding a frequency  $f = f_0/\sqrt{\epsilon'}$ .

It can be shown that the quality factor  $Q'$  for a perfectly conducting cavity completely filled with a lossy dielectric of loss tangent  $\tan\delta = \epsilon''/\epsilon'$  is given simply by  $Q' = \epsilon'/\epsilon'' = 1/\tan\delta$ . It is possible for a partially filled cavity to behave in the same way as a completely filled cavity when the field is entirely captured in the dielectric. Using a high permittivity  $\epsilon'$  material enhances this probability. A material with loss tangent  $\tan\delta = 0.11$  would yield  $Q' = 9.1$  in this case. If resistive walls are present which give an empty cavity quality factor  $Q_0$ , then the total quality factor including the lossy dielectric becomes[57]

$$Q = \left( \frac{1}{Q'} + \frac{1}{Q_0} \right)^{-1}. \quad (3.63)$$

For metal cavities composed of copper or stainless steel  $Q_0$  is about  $10^3$  and does not contribute substantially to the total quality factor.

### 3.2.3 Bellows Modes

At the junctures of vacuum chambers, bellows are necessary to absorb mechanical stress from thermal expansion and contraction. The general design of the bellows structure introduces a cavity volume capable of harboring resonant modes. The geometry is that of a coaxial cavity and the mode field patterns are similar to those of a coaxial cavity. A coupling mechanism for field leakage into the bellows is presented. Coupling strengths are estimated for PEP-II beam parameters.

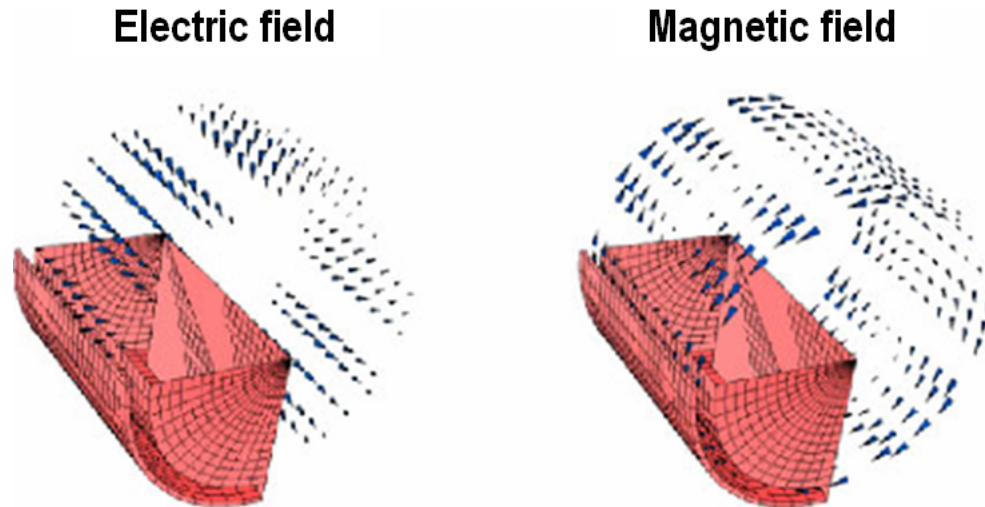


Figure 3.14. Dipole mode in a 3D coax model of a bellows cavity.

### 3.2.3.1 A Simple Coax Model

A simplified computational model provides an understanding of field patterns within the bellows cavity. The structure is analyzed first in terms of a three dimensional coaxial cavity which reveals a general description of possible modes. A second more detailed two dimensional analysis suggests that dipole and quadrupole type modes near the observed frequencies can exist in the bellows and that the azimuthal field patterns of these modes qualitatively follow the simple coax patterns.

To understand the structure of possible RF modes in the bellows cavity we start with a simple model of a coaxial cavity with a rather large inner conductor. The vacuum chamber and slots as well as the bellows convolutions are not modeled. Eigenmodes of such a structure are easily visualized using MAFIA[13]. The cavity has an inner and outer radius of 26.5 cm and 29.6 cm respectively and a length 22.3 cm. The field patterns in the bellows cavity identify the modes as monopole, dipole and quadrupole according to the azimuthal variation period.

The monopole mode exhibits a uniform radial electric field and azimuthal magnetic field. A simple three dimensional coax model of the bellows cavity is shown in

figure 3.14 with field patterns pertaining to a dipole mode. The dipole mode exhibits nodes which provide a longitudinal component of the magnetic field at two azimuthal positions. Wall currents and therefore the resistive heating will exhibit this pattern. The quadrupole mode exhibits similar features. The monopole mode magnetic field is purely azimuthal. A longitudinal magnetic field together with a transverse electric field yields a Poynting vector suitable for coupling through the bellows fingers.

The bellows cavity mode frequencies  $f$  in the coaxial cavity approximation will vary with the longitudinal dimension  $L$  as:

$$f = \sqrt{f_{co}^2 + \left(\frac{nc}{2L}\right)^2} \quad (3.64)$$

where  $f_{co}$  is the mode cutoff frequency for an infinitely long coaxial cable,  $c$  is the speed of light, and  $n$  is the number of longitudinal variations in a length  $2L$  for the resonant mode.

### 3.2.3.2 Coupling Studies

It is evident HOMs near the IP vertex bellows are in the beam chamber. There must be a mechanism for this power to couple from the beam chamber into the bellows. The only possible coupling path is through the small gaps between the fingers. The beam cavity dipole and quadrupole modes are shown to couple to the respective modes of the bellows, but coupling between different mode species is possible. An example of electric fields for a cavity and bellows dipole mode are shown in figure 3.15. These modes are different eigenmodes for the same geometry of figure 3.16 and therefore have different frequencies. Here the gaps are modeled as slots in the wall separating the two cavities.

Without gaps, the cavities have intrinsic independent modes. The introduction of gaps can couple the beam cavity and bellows cavity modes, resulting in a transfer of RF power from the beam cavity into the bellows cavity.

In these simulations the frequency of the beam cavity is varied by changing its

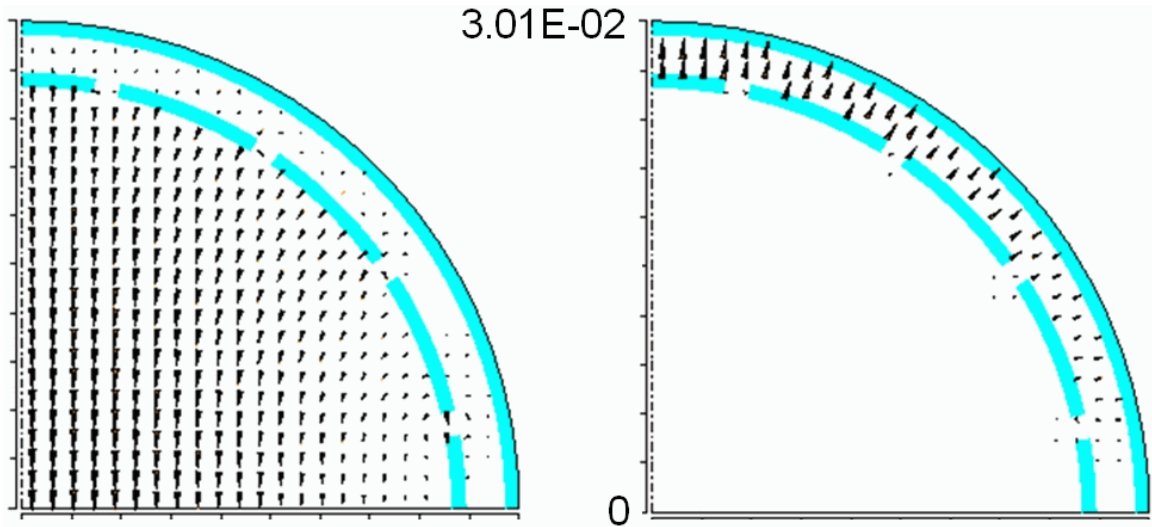


Figure 3.15. Dipole electric field modes in a simulated beam chamber and bellows chamber. Dimensions in meters.

longitudinal dimension. The outer bellows cavity dimensions are held fixed in these studies. Furthermore, the slots are kept at the center of the longitudinal dimension of the beam cavity, to minimize the effect of the cavity walls. This construction is shown in figure 3.16. Within the regime where no coupling is present, the bellows cavity frequency remains constant while the beam cavity frequency changes with the change in the beam cavity length. If there is no coupling, the change in the beam cavity frequency will have no effect on the fixed frequency of the bellows cavity. If there is coupling, one expects a shift in the bellows cavity frequency as the beam cavity frequency approaches the bellows cavity frequency. The closest approach of the two frequencies yields the degree of coupling. The larger the closest approach, the larger the coupling. We give the coupling  $\alpha$  as the minimum frequency separation over the average frequency.

Coupling between the beam cavity dipole and the bellows cavity dipole modes is evident in figure 3.17.

The same study for beam cavity and bellows quadrupole modes is shown in figure

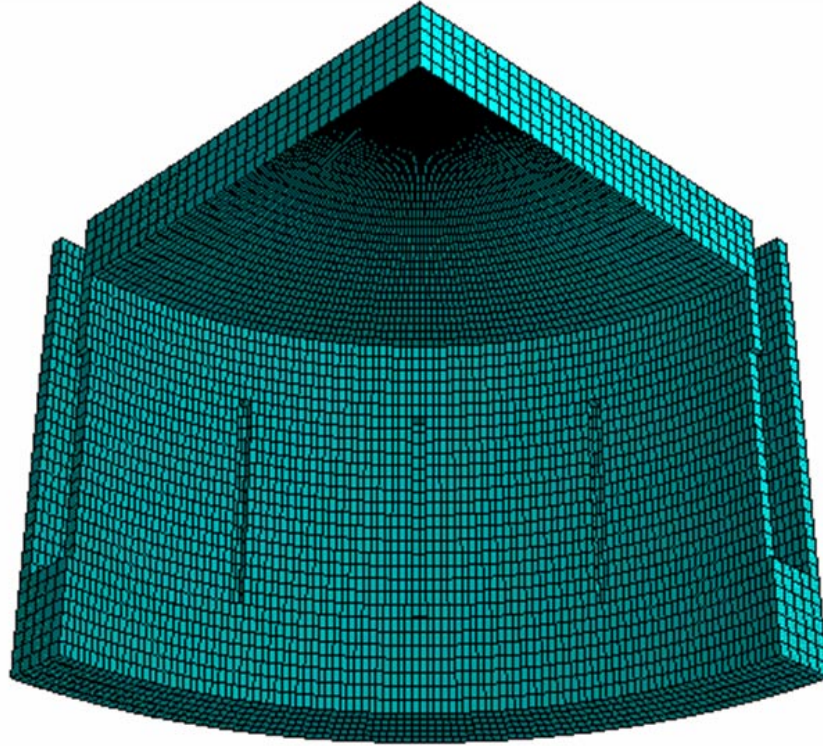


Figure 3.16. Geometry for the dipole coupling studies showing the beam cavity, bellows cavity and slots. Only half of this geometry is used in the quadrupole studies.

3.18.

For the dipole case the coupling  $\alpha=0.01$  while for the quadrupole case it is larger,  $\alpha=0.02$ . It can be expected that respectively 1 and 2 percent of the power of beam generated fields in the form of dipole and quadrupole modes will couple into the bellows cavity.

It should be mentioned that energy transfer through the gaps between the fingers requires the Poynting vector to be along a direction through the gap (radial). For traveling modes the electric fields are necessarily transverse. In order for coupling to occur, the magnetic field must be longitudinal at the gap to get the proper Poynting vector orientation. Monopole mode coupling is not considered because its magnetic field is purely azimuthal. If, however, there is a misalignment between the beam

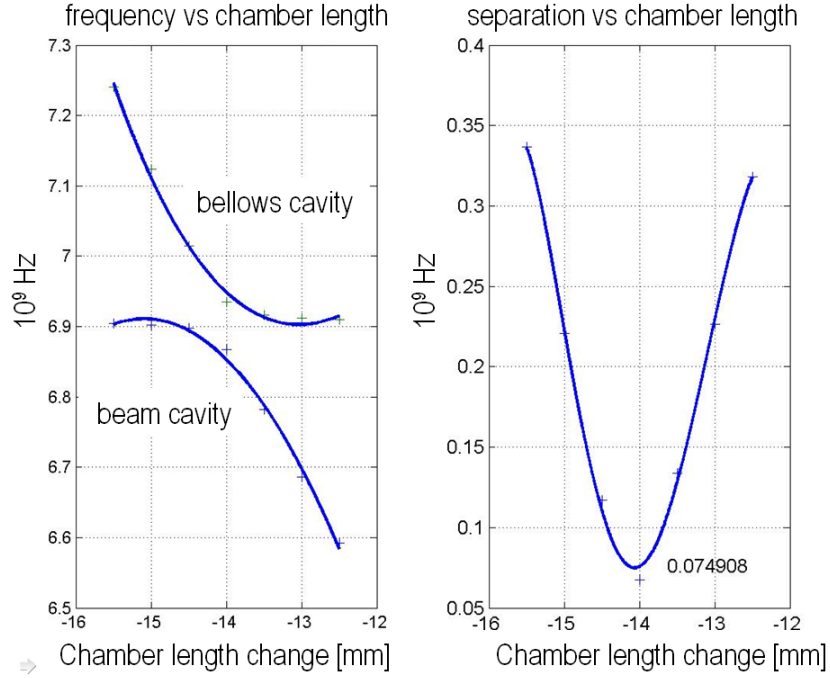


Figure 3.17. Variation of beam and bellows cavity dipole mode frequencies and their differences as a function of beam cavity chamber length. Strength of the coupling is related to the minimum separation of .075 GHz.

direction and the central axis of the beam chamber, a small longitudinal magnetic component may be generated.

### 3.2.3.3 Slot Width and Coupling

It is a reasonable assumption that coupling can be reduced by diminishing the slot width, which is equivalent to reducing the space between the fingers. The coupling results of three quadrupole runs with differing slot widths are shown in figure 3.19. The minimum frequency difference is plotted vs the fraction of nominal 0.81mm finger separation. To extrapolate to small slot width the data are fit with an analytical result based on the electric and magnetic polarizabilities of small apertures[20] which is proportional to

$$1 / \left[ \ln \left( \frac{4l}{w} - 1 \right) \right]. \quad (3.65)$$

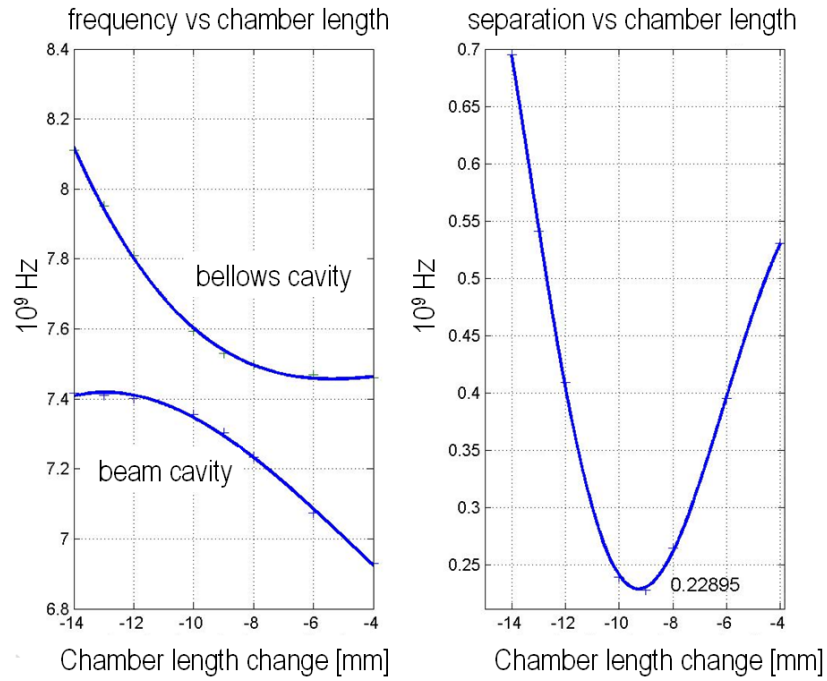


Figure 3.18. Variation of beam and bellows cavity quadrupole mode frequencies and their differences as a function of beam cavity chamber length. Strength of the coupling is related to the minimum separation of 0.23 GHz.

given in terms of slot length  $l$  and width  $w$ . Both the data and fit are fairly flat in the region of interest. From this we conclude that significant reduction in coupling cannot be achieved by reducing the slot width (space between fingers).

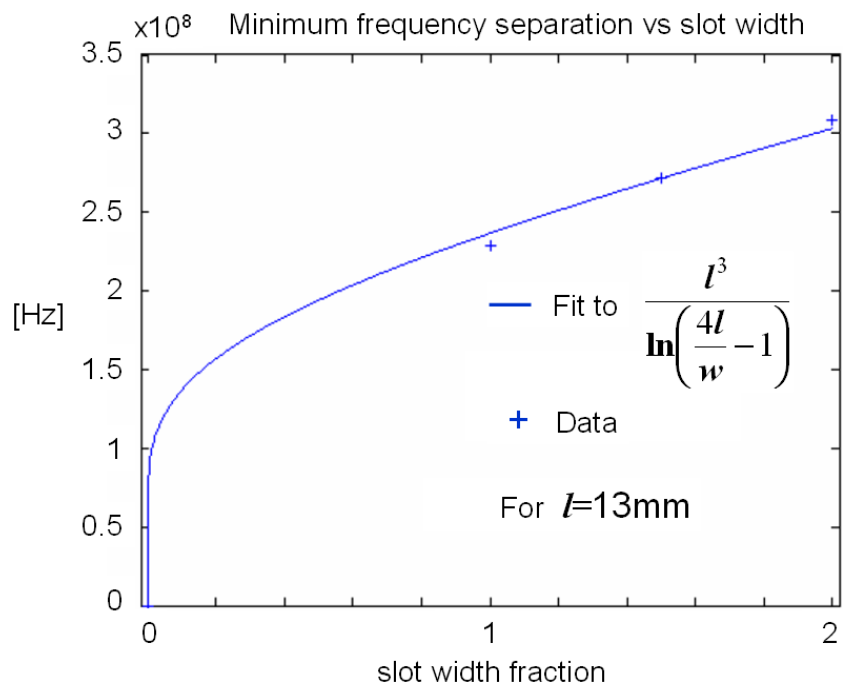


Figure 3.19. Minimum mode separation vs fractional slot width for constant slot length. The data is fit to a analytic expression derived from the polarizability of small apertures.

### 3.3 Scattering Parameter

HOMs in the beam pipe can take the form of propagating waves with the beam pipe acting as a waveguide. In this way HOM power can move several meters away from its source and couple into distant beam line components. One approach to this problem is to consider these waves as a superposition of normal waveguide modes and seek to selectively couple out the destructive ones.

The monopole mode and the beam field share a similar geometry. Any affect on the monopole mode thus represents an impedance to the beam. As discussed in the mode analysis section 3.2.3.2, monopole modes will not couple in through bellows shielding fingers whereas coupling is demonstrated for the dipole and quadrupole modes. Any scheme to eradicate HOM effects should selectively couple out the dipole and quadrupole modes while leaving the monopole mode unaffected. To this end a device is to be introduced into the beam line at a point between a HOM source and nearby components to intercept dipole and quadrupole modes while remaining transparent to the monopole mode (and therefore the beam).

Scattering parameter analysis provides a means to study the effect of a device on specific waveguide modes and thus becomes a useful design tool for HOM reduction schemes. Since propagating waveguide modes are matched at the waveguide (beam tube) boundaries any reflection or transmission characteristics are entirely attributable to the device. This method gives the fraction of mode power absorbed and transmitted as a function of mode frequency. A device can be designed to absorb or transmit power for particular modes and frequencies.

Results of the bellows coupling studies suggests a device design incorporating large coupling slots in the beam pipe walls. Coupled power enters a cavity containing an absorbing media. The coupling apertures will be enlarged in the form of slots with coupling encouraged for the dipole and quadrupole modes. Ideally the absorbing media should be a high permittivity material with a large loss tangent in the frequency

range of interest. Electric field energy density is increased in the high permittivity absorbing media so that harmful mode power can be isolated and removed with suitable cooling.

### 3.3.1 Method

Scattering parameter analysis is a well known technique for characterizing the electromagnetic response of microwave devices[55]. Lossless waveguide ports are attached to a device to be tested such that electromagnetic waves in the form of waveguide modes can be introduced to the device. The device “scatters” this incident wave. The resulting reflected and transmitted waveguide amplitudes are measured. In order to accurately measure the device response the ports are matched to the incident waveguide mode so that no reflection occurs at the port boundaries. A central feature of scattering parameter analysis is that the measured transmitted and reflected amplitudes are entirely due to the device. The measured transmitted and reflected amplitudes are normalized to the incident amplitude in order to obtain the scattering parameters. They are usually denoted  $s_{ij}$  and defined as the ratio of the  $i$ th port *output* amplitude to the  $j$ th port *incident* amplitude. In the case of a two port device where port 1 is excited the important scattering parameters are  $s_{11}$  and  $s_{21}$  which are synonymous with the reflection and transmission coefficients in optics.

The normalized absorption of power can be evaluated from the scattering parameters. As in optics, the reflectance and transmittance quantities are given as the square of the reflection and transmission coefficients:  $s_{11}^2$  and  $s_{21}^2$ . Accordingly these are the ratio of reflected and transmitted power to the incident power. If the device is lossless,

$$s_{11}^2 + s_{21}^2 = 1. \tag{3.66}$$

This suggests a quantity which gives the fraction of incident power absorbed:

$$1 - (s_{11}^2 + s_{21}^2). \tag{3.67}$$

This is a frequency dependent parameter which can be determined for a broadband simulation where the incident excitation spans the frequency range of interest. For the purpose of this study this range encompasses the waveguide mode cutoff frequencies to the expected beam power contribution which for most beam pipes and bunch lengths spans the 2-7 GHz range.

In practice the incident and measured amplitudes are voltage signals from coaxial cables connected to the device where the input power is matched at a generator port boundary. All other ports are suitably terminated to prevent reflection. When the device to be tested is situated in a beam chamber the waveguide ports become the adjacent beam pipes which in general have arbitrary cross sections. The beam pipe waveguide mode does not have well defined measurable voltages as in the coaxial cable. In the computational domain beam pipe waveguide modes of definite electric and magnetic field strength are easily simulated and can be used as amplitudes for scattering parameter analysis. Scattering analysis can be performed if the beam pipe waveguide port boundaries can be matched for the specific excitation mode as a simulated infinitely long waveguide. This is approximated in the MAFIA time domain solver[27, 28].

A structure (or device under test) is isolated between two or more waveguide ports which are simulated infinite waveguide boundaries. Such a setup is illustrated in figure 3.20. In this case the device consists of a cavity surrounding the beam pipe containing a high permittivity lossy dielectric. The cavity and dielectric are coupled to the beam pipe through open slots.

Dielectric losses are modelled in terms of an effective conductivity. All material power loss occurs through  $P = \vec{J}_T \cdot \vec{E}$  where  $\vec{E}$  is the electric field and  $\vec{J}_T$  is the total current density including conduction and displacement current contributions:  $\vec{J}_T = \sigma\vec{E} - i\omega\epsilon\vec{E}$ . For a lossy dielectric the permittivity is complex:  $\epsilon = \epsilon' + i\epsilon''$ . The complex part of the dielectric permittivity yields a displacement current density

term  $\omega\epsilon''\vec{E}$ . The real part of this term  $\omega\epsilon''$  behaves like a conductivity. In terms of material parameters, dielectric loss properties are often quoted as a loss tangent defined as  $\tan\delta = \epsilon''/\epsilon'$ . Dielectric loss is mediated through the effective conductivity  $\sigma_{\text{eff}} = \omega\epsilon''\tan\delta$  which can be assigned to the material for the MAFIA simulations. The high relative permittivity  $\epsilon'$  plays a role in promoting absorption of HOM energy through the effective conductivity.

One port is excited with a propagating waveguide mode of Gaussian frequency spectrum over a given frequency range and total power. Figure 3.21 shows an example of electric field waveguide modes used in a circular beam pipe port excitation. The modes are part of an orthogonal set of modes from which any arbitrary propagating wave can be constructed through superposition. Each mode is considered separately as a wave which passes without reflection through the port boundaries. The mode amplitudes for input and output waves at each port are monitored during the simulation.

Each mode (monopole, dipole and quadrupole) is allowed to scatter from a device model in a time domain simulation. Only the specified mode is matched at the ports and allowed to pass without reflection. The transmitted and reflected mode amplitude passing through the ports is monitored during the time simulation. From these signals the power in and out of the ports are determined. All other power remains confined between the ports in the form of absorbed power. By normalizing to the excitation mode amplitude, fractional power transmission and reflection coefficients can be easily derived as a function of frequency for the given mode. The transmission and reflection coefficients are equivalent to the scattering parameters  $s_{21}$  and  $s_{11}$  respectively.

An example of simulated port amplitude signals is shown in figure 3.22 as a function of simulation time in seconds for a dipole mode excitation. The input port is designated p1, the output port is p2. Each port has associated input and output signals. For this two port system only port p1 has input amplitude, port p2 is not

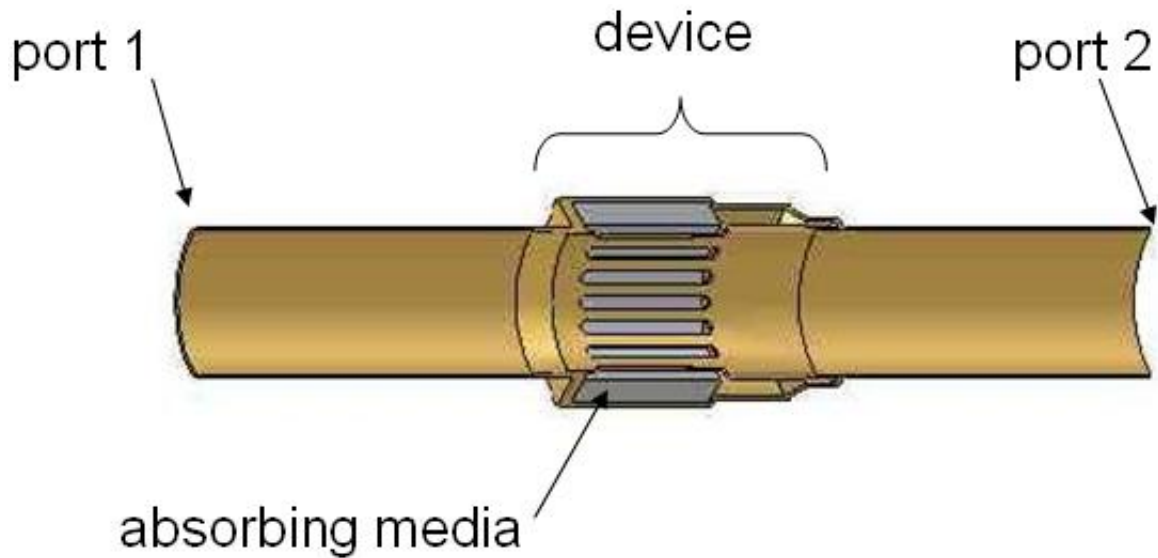


Figure 3.20. Device under test placed in a uniform circular waveguide between two ports. The ports are simulated as infinitely long waveguides. The device consists of a cavity filled with a high permittivity lossy dielectric absorbing media coupled to the beam pipe waveguide by slots.

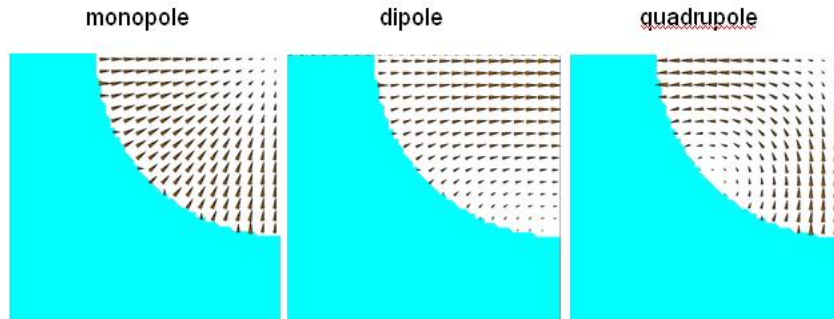


Figure 3.21. Waveguide electric field eigenmodes for scattering parameter port excitation

excited. The trace  $p1\_in$  is the input signal at port p1. The trace  $p1\_out$  is the port 1 output amplitude which indicates reflected power. The time signature indicates the reflection occurred from the device situated in the center of the waveguide. The trace  $p2\_out$  indicates transmission amplitude from port 2 which is shifted by the transit

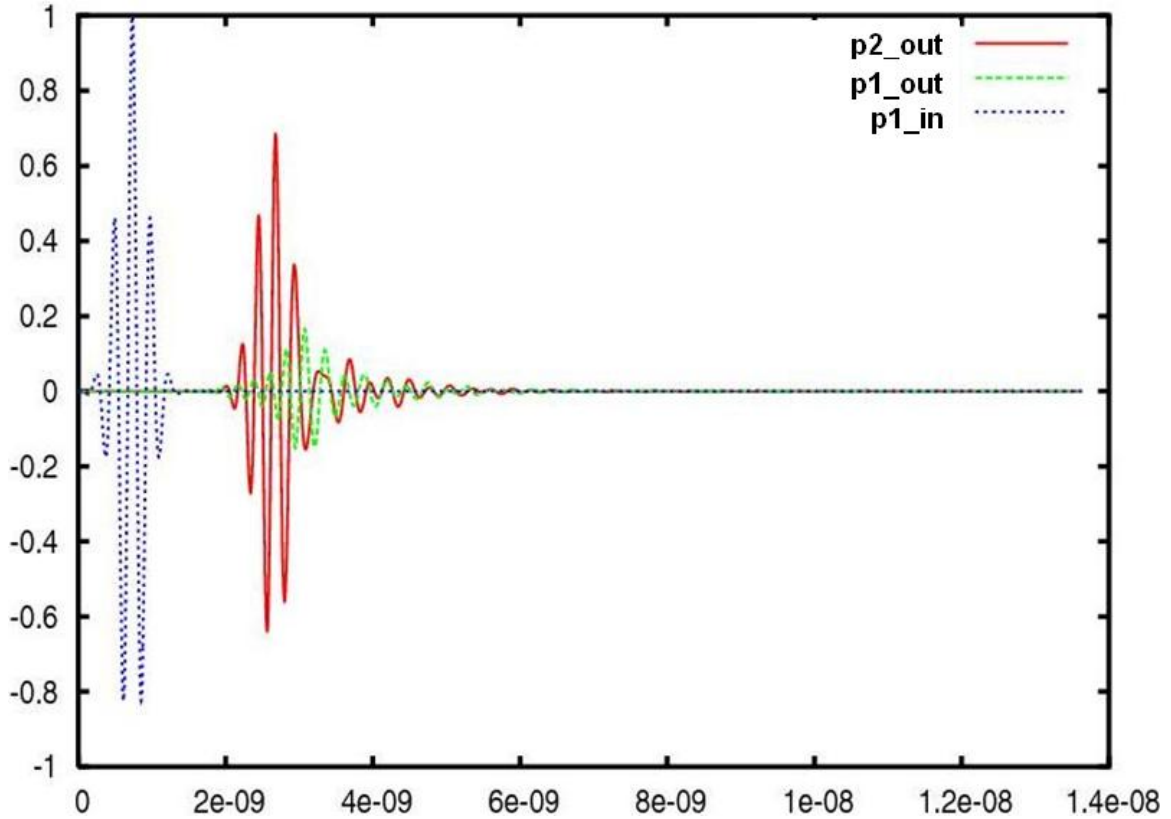


Figure 3.22. Port signal amplitudes vs time in seconds. p1\_in is the input or excitation signal into port 1. p1\_out is the signal reflected back from the device out of port 1. p2\_out is the signal transmitted from port 1 which comes out of port 2.

time of the device.

In the frequency domain the scattering amplitudes take the form of figure 3.23. The scattering parameters for the port 1 excitation are formed by normalizing the output spectrum (1out, 2out) from ports 1 and 2 to the input spectrum (1in) at port 1. The reflection coefficient is the ratio of the input Gaussian to the port 1 output spectrum (1out) and is otherwise referred to as scattering parameter  $s_{11}$ . The transmission coefficient and scattering parameter  $s_{21}$  is given by the ratio of the input Gaussian to the port 2 out spectrum (2out). The scattering parameters and absorption is shown in figure 3.24

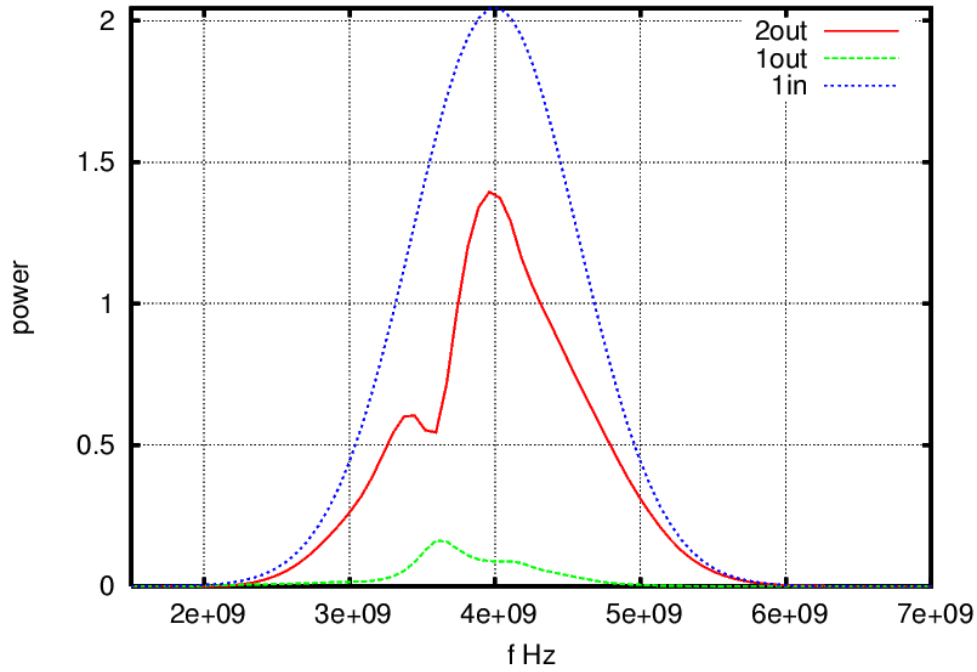


Figure 3.23. FFT of port signals for the dipole mode excitation. 2out=port 2 output spectrum, 1out=port 1 out spectrum, 1in=port 1 input excitation spectrum.

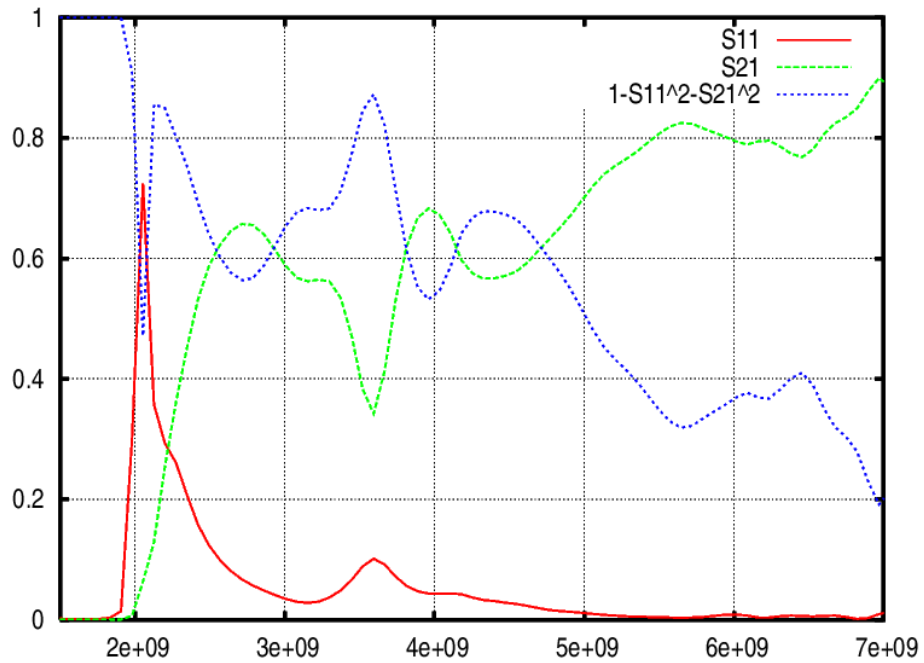


Figure 3.24. Scattering parameters  $s_{11}$ ,  $s_{21}$  and absorption  $1 - s_{11}^2 - s_{21}^2$  for a dipole mode excitation as a function of frequency.

This particular device exhibits an average of 50% absorption of the dipole mode. The same simulations are repeated for the monopole and quadrupole modes to completely characterize the device.

### 3.4 Wake Field Computations

A wake field analysis can determine the energy lost by a beam as it traverses an accelerator structure. An energy loss parameter  $k$  for the structure can be evaluated, defined to be the energy loss per square of the bunch charge:

$$k = \frac{\Delta U}{Q^2}. \quad (3.68)$$

The loss parameter depends on the chamber geometry, bunch charge distribution and beam trajectory.

For a particle of charge  $Q$ , velocity  $\vec{v}$  in the  $z$  direction subject to electric  $\vec{E}$  and magnetic fields  $\vec{B}$ , forces  $\vec{F}$  are governed by the Lorentz force law:

$$\vec{F} = Q \left( \vec{E} + \vec{v} \times \vec{B} \right). \quad (3.69)$$

Variation in energy  $U$  is given by:

$$\frac{dU}{dt} = \vec{v} \cdot \vec{F} \quad (3.70)$$

$$= \vec{v} \cdot Q \left( \vec{E} + \vec{v} \times \vec{B} \right) \quad (3.71)$$

$$= Q\vec{v} \cdot \vec{E}. \quad (3.72)$$

Thus beam particles can only lose (or gain) energy from electric fields with components parallel to the beam velocity. The force components perpendicular to the beam velocity impart transverse kicks to beam particles, which can result in emittance degradation and transverse instability. Transverse wake field kicks are responsible for beam breakup phenomenon where the tail of the bunch is kicked from wake fields produced by the head of the same bunch. It is prevalent in linear accelerators where intense beams traverse many accelerating cavities[38].

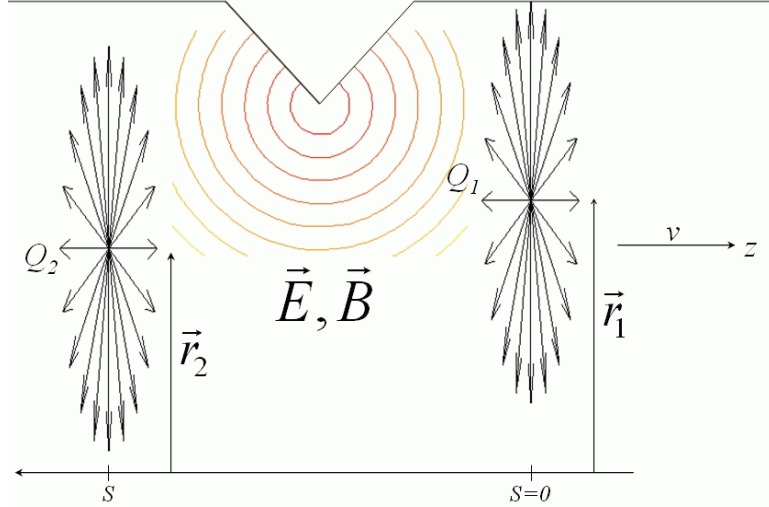


Figure 3.25. Illustration of point charge  $Q_1$  fields scattering from a vacuum chamber irregularity generating wake fields  $\vec{E}, \vec{B}$  which interact with a witness charge  $Q_2$  following at a distance  $s$ .

Wake field analysis is a direct way of understanding the sources and behavior of HOMs. A basic understanding comes from considering the fields (wake fields) resulting from a point charge  $Q_1$  situated at  $(\vec{r}_1, z_1)$  traversing a structure at velocity  $v$  and the forces that such fields have on a witness charge  $Q_2$  following at a distance  $s$  behind  $Q_1$  at  $(\vec{r}_2, z_2 = z_1 - s)$ . Both charges are assumed to move along the  $\vec{z} = z\hat{z}$  direction at velocity  $v$  with different transverse coordinates defined by  $\vec{r}_1$  and  $\vec{r}_2$  with  $\hat{z}$  being the unit vector in the longitudinal direction. The situation is illustrated in figure 3.25.

In the relativistic limit, the witness charge  $Q_2$  does not experience a force from  $Q_1$  directly. Only the wake fields resulting from the scattering of  $Q_1$  fields from the surrounding beam chamber geometry are seen by the following  $Q_2$ . The path and velocity of the witness charge  $Q_2$  do not change appreciably in the relativistic approximation. Equivalently, the transit time through the region is small. The velocity  $v$  for both charges is assumed relativistic and constant in magnitude and direction throughout this discussion.

The integration of wake field forces  $\vec{F}$  on the witness charge  $Q_2$  over the path the witness takes through the wake fields is a net energy change:

$$\Delta u(\vec{r}_1, \vec{r}_2, s) = \int_{-\infty}^{+\infty} \vec{F}(\vec{r}_2, z_2 = vt - s) \cdot dz_2 \hat{z} \quad (3.73)$$

where  $t$  is time. This is divided into components parallel and perpendicular to the direction of beam motion which when divided by the witness charge  $Q_2$  yield net voltage gains. Normalizing these voltages to the excitation charge  $Q_1$  produces the point charge longitudinal and transverse wake potentials:

$$w_z(\vec{r}_1, \vec{r}_2, s) = \frac{1}{Q_1} \int_{-\infty}^{+\infty} E_z(\vec{r}_2, z_2 = vt - s) dz_2 \quad (3.74)$$

$$w_r(\vec{r}_1, \vec{r}_2, s) = \frac{1}{Q_1} \int_{-\infty}^{+\infty} \left\{ E_r(\vec{r}_2, z_2 = vt - s) + \left[ v \hat{z} \times \vec{B}(\vec{r}_2, z_2 = vt - s) \right]_z \right\} dz_2. \quad (3.75)$$

These are considered wake potential Green's functions for a point charge response. The longitudinal point charge wake potential  $w_z(\vec{r}_1, \vec{r}_2, s)$  gives the energy loss/gain the following charge  $Q_2$  experiences as a result of the wake fields generated by  $Q_1$  at a fixed distance  $s$  behind  $Q_1$ . The transverse point charge wake potential  $w_r(\vec{r}_1, \vec{r}_2, s)$  imparts a transverse momentum kick to  $Q_2$  without changing the energy (in the relativistic approximation).

The excitation charge  $Q_1$  can be generalized to a line charge distribution  $\lambda(s)$  simulating a charged particle bunch where  $s$  is a coordinate in the beam frame. Taking the transverse offsets equal  $\vec{r} = \vec{r}_1 = \vec{r}_2$  forces the witness and exciting charges to be part of the same line charge distribution. Wake fields from the charge distribution at  $s'$  act on a following part of the same charge distribution at a later point  $s$ . Writing the energy change of the witness charge from a point charge excitation of infinitesimal extent  $ds'$  and charge  $\lambda ds'$  in terms of the associated wake field as

$$dU = Q_2 \lambda ds' w_z(\vec{r}, s - s'), \quad (3.76)$$

allows a generalization to the energy change for a point charge  $Q_2$  at a point  $s$  within the bunch from all charges ahead of it:

$$\Delta U(\vec{r}, s) = Q_2 \int_{-\infty}^s \lambda(s') w_z(\vec{r}, s - s') ds'. \quad (3.77)$$

Dividing by the witness charge  $Q_2$  gives the voltage change per unit charge. This voltage is normalized to the total bunch charge  $Q$  to give the bunch longitudinal wake potential in volts per coulomb:

$$W_z(\vec{r}, s) = \frac{1}{Q} \int_{-\infty}^s \lambda(s') w_z(\vec{r}, s - s') ds'. \quad (3.78)$$

This expression is valid for positions  $s$  inside and outside the bunch distribution.

The longitudinal loss factor can now be evaluated by convoluting the bunch charge distribution with the bunch longitudinal wake potential and normalizing to the bunch charge:

$$k_z = \frac{1}{Q} \int_{-\infty}^{+\infty} \lambda(s) W_z(\vec{r}, s) ds. \quad (3.79)$$

This constant has units of volts per coulomb, but in practice quoted in volts per pico-coulomb.

Determination of the bunch wake potential  $W_z(\vec{r}, s)$  requires a time domain solution of Maxwell's equations with boundary conditions imposed by the beam chamber and a propagating line charge source  $\lambda(s)$ . The details of the electromagnetic field must be known as a function of the distance  $s$  during the transit of the beam through the structure as well as for an extended period of time after the beam has passed, since scattered fields take time to catch up to the bunch particles. This requires long computation runs of many time steps in a large computational volume with the nontrivial issue of simulating boundary conditions which support the passing of a line charge source.

### 3.4.1 Vertex Chamber Wake Fields

At the interaction region within the BaBar detector the separate beam chambers of the LER (e+) and HER (e-) are brought together into a common beam chamber. This

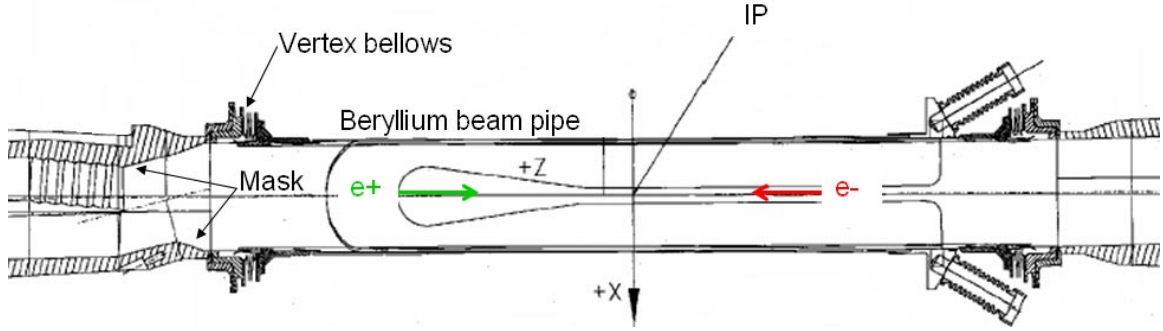


Figure 3.26. Layout of the IP vertex chamber showing beam trajectories and synchrotron radiation masks in upstream LER. Dimensions are in mm.

region is depicted in figure 3.26. Both beams are bent into collision trajectories by a series of vertical and horizontal dipole magnets as well as some combined focusing and bending magnets. The synchrotron radiation produced by several Amps of beam currents is considerable, approximately 100 kW, and a series of masks in the form of beam chamber tapers and collimators are designed into the vacuum chamber to intercept this radiation and prevent backgrounds in the BaBar detector. Some of these are evident at the IP in the upstream LER ( $e^+$ ) portion of figure 3.26. The vertex bellows situated in this area experiences HOM heating. These masks and other asymmetries in the beam chamber profile are sources for HOM generation.

As a verification of this hypothesis a wake field simulation is performed on two models. One model incorporates geometrical features of the upstream LER region along with a simplified vertex bellows cavity and rudimentary 1.5 mm wide coupling slots as shown in figure 3.27. A second model assumes a straight uniform beam pipe of the same radius with the same simple vertex bellows cavity and slots. This is displayed in figure 3.28. The coupling slots mimic the gaps between bellows shield fingers.

A 14 nano-Coulomb Gaussian line charge distribution of 1.3 cm sigma is propagated through the structures for a total time of about 1 nanosecond over 1173 0.8

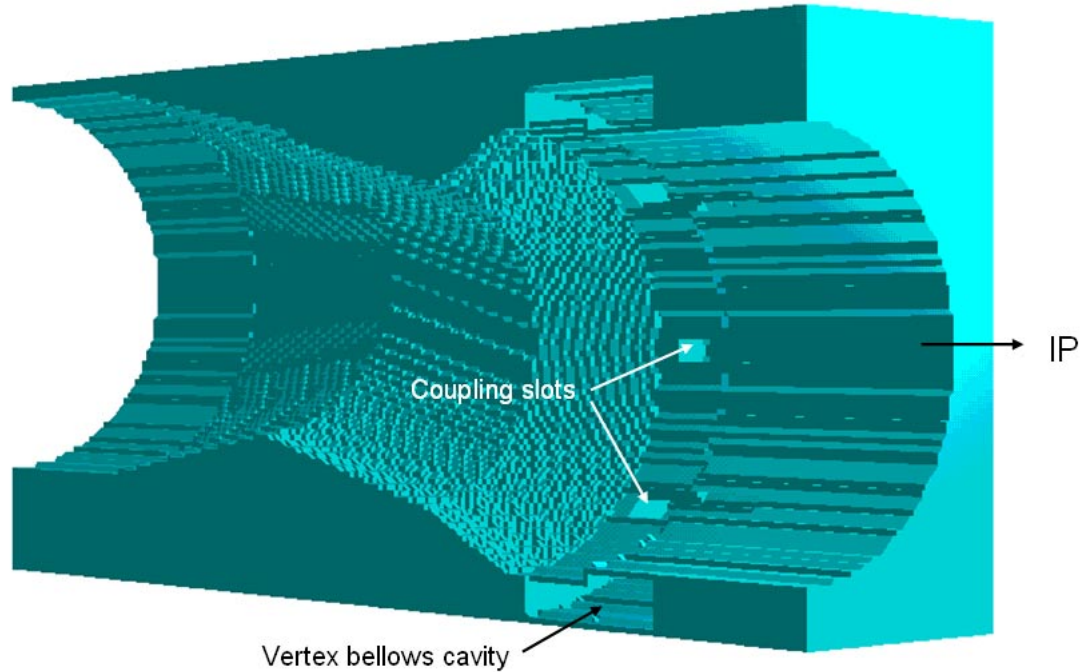


Figure 3.27. Upstream LER model for IP wake computation with simulated bellows and coupling slots.

pico-second time steps. In each case the beam moves along the ideal colliding trajectory which is on axis at the vertex bellows location. Electric field patterns at interim time steps from the region containing the vacuum pipe at the bellows cavity are generated. Some time after the beam has passed at 0.5 nano-seconds, significant field coupling into the bellows cavity can be seen for the structure of figure 3.27. In contrast, under the same simulation conditions the straight pipe model of figure 3.28 show no fields coupling into the bellows cavity. These results are shown in figure 3.29.

These simulations demonstrate that offsets, tapers and masks have the effect of producing wakefields with the ability to couple into a bellows cavity.

### 3.4.2 Power in the Bellows

One can estimate the power dissipated in the bellows cavity, given the loss factor for the actual beam pipe structure, the currents, and the coupling constants from

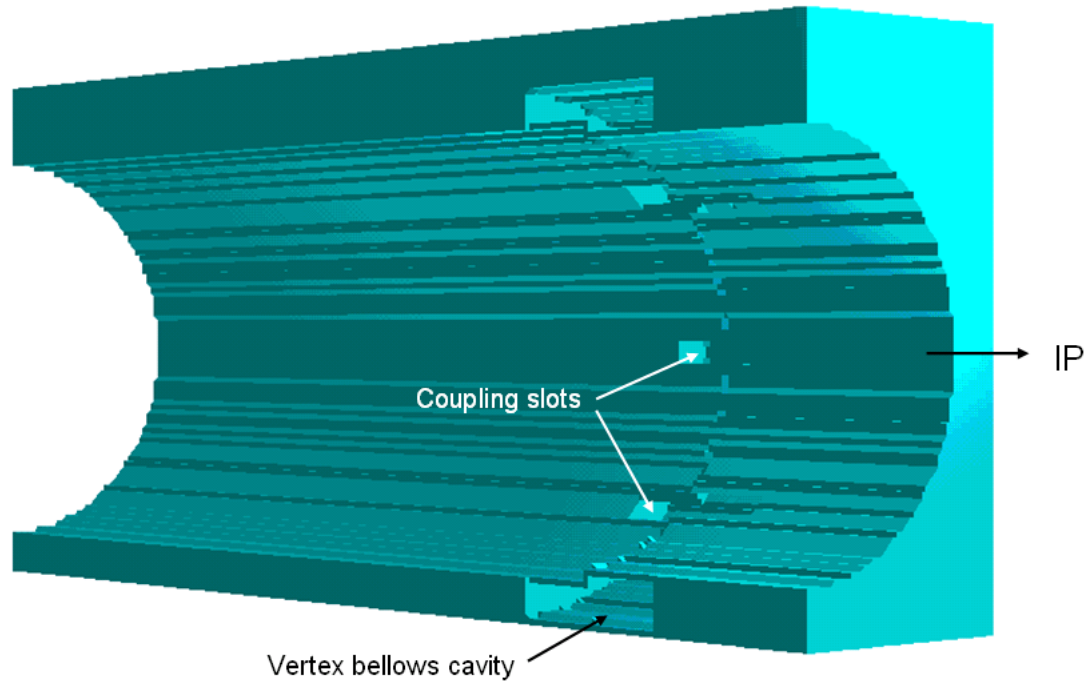


Figure 3.28. Straight pipe model for IP wake field comparison with the same simulated bellows and coupling slots as in the model of figure 3.27.

the calculations of section 3.2.3.2. The loss factor for the beam pipe geometry of figure 3.27 is calculated with several methods. The nature of the problem is three dimensional and so is suited for the MAFIA 3D time domain solver. A one coulomb Gaussian bunch is propagated through the mesh of figure 3.27. This gives the longitudinal wake potential shown in figure 3.31 which when convoluted with the Gaussian beam of bunch length 1.3 cm yields a loss factor  $k = .06$  V/pC for the 3d MAFIA calculation.

One can make 2D calculations with the NOVO[4] wake field program by taking the top and bottom profiles of the beam pipe separately as axially symmetric structures as illustrated in figure 3.30. The NOVO program directly computes loss factors  $k = 0.031$  and  $0.01$  V/pC respectively for the top and bottom profiles of the beam chamber. A comparison of the two methods is shown in figure 3.31.

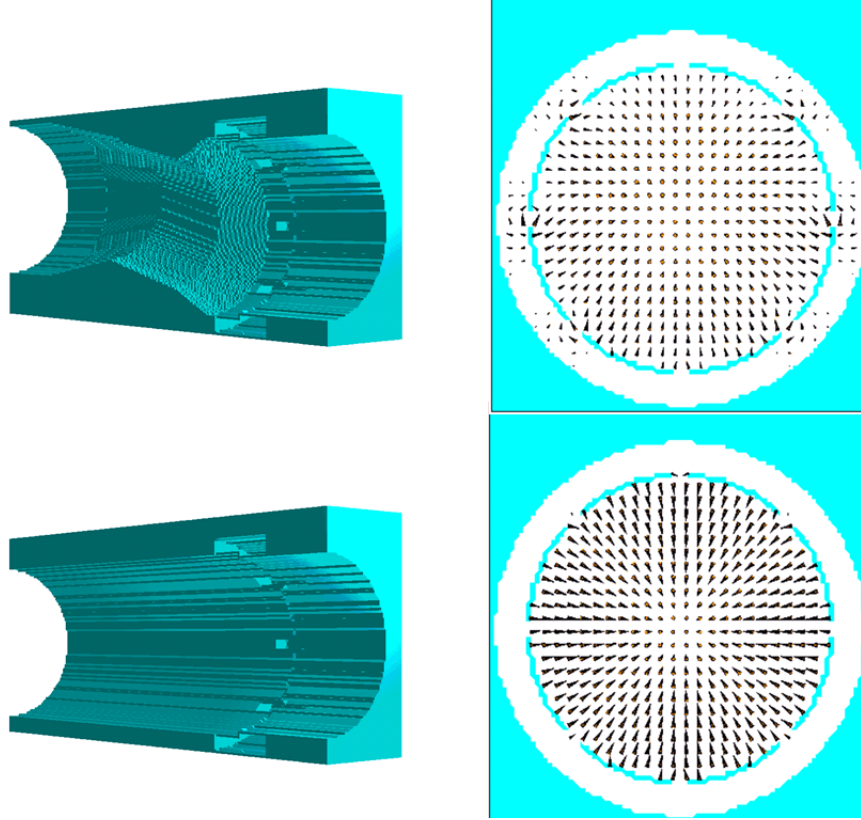


Figure 3.29. IP vertex chamber (top) and comparable straight pipe model (bottom) and the electric field pattern snap shots after passage of 1.3 cm Gaussian 14 nC line charge. Snap shots are from the same time frame of the simulation. No coupling was evident at any time for the straight pipe model

It is assumed the irregular geometry of figure 3.27 will scatter the beam fields into transverse modes which can couple into the bellows. PEP-II typically runs with positron currents of  $I_+ = 2.8$  A and electron currents of  $I_- = 1.8$  A at a revolution frequency of  $f=136$  kHz with  $N=1700$  bunches. For this case the estimate of beam pipe power is

$$P_{beam} = \frac{k}{fN} (I_+^2 + I_-^2),$$

which is about 3 kW given the MAFIA 3D loss factor and 1.5 kW for the NOVO 2D loss factor. To estimate the fraction of the beam power coupling into the bellows cavity it is further assumed that all power incident in the bellows is dissipated there.

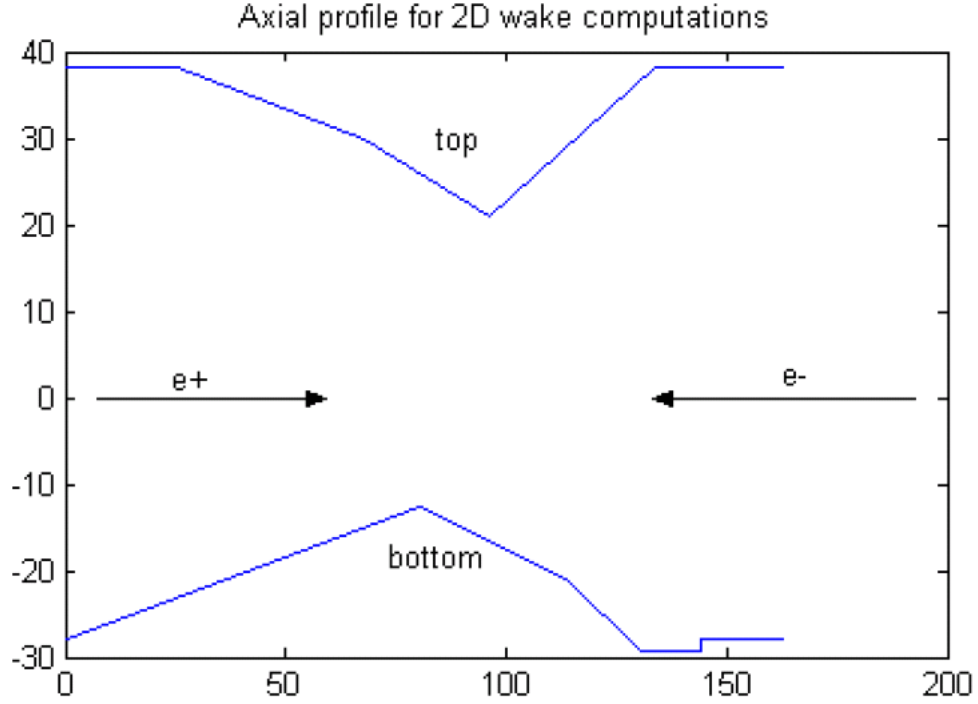


Figure 3.30. Axially symmetric profiles for NOVO 2d wake potential computation. Dimensions are in mm.

The bellows power can be written:

$$P_{bellow} = \alpha P_{beam}$$

With a 1% coupling  $\alpha=.01$  (dipole mode) this corresponds to 30 W and 15 W respectively for the MAFIA 3D and NOVO 2D loss factors, 60 W and 30 W respectively for the 2% (quadrupole mode) coupling. These results are consistent with other independent estimations for similar geometries[21]. If the bunch length is decreased by a factor of 2, the loss factor and hence the power will go up by a factor of 4[8].

### 3.4.3 Collimator Wake Fields

A collimator presents a strong scattering source for beam fields. In what follows wake field analysis is used to show how scattered beam fields can give rise to propagating electromagnetic waves which transport power to other parts of the accelerator. The

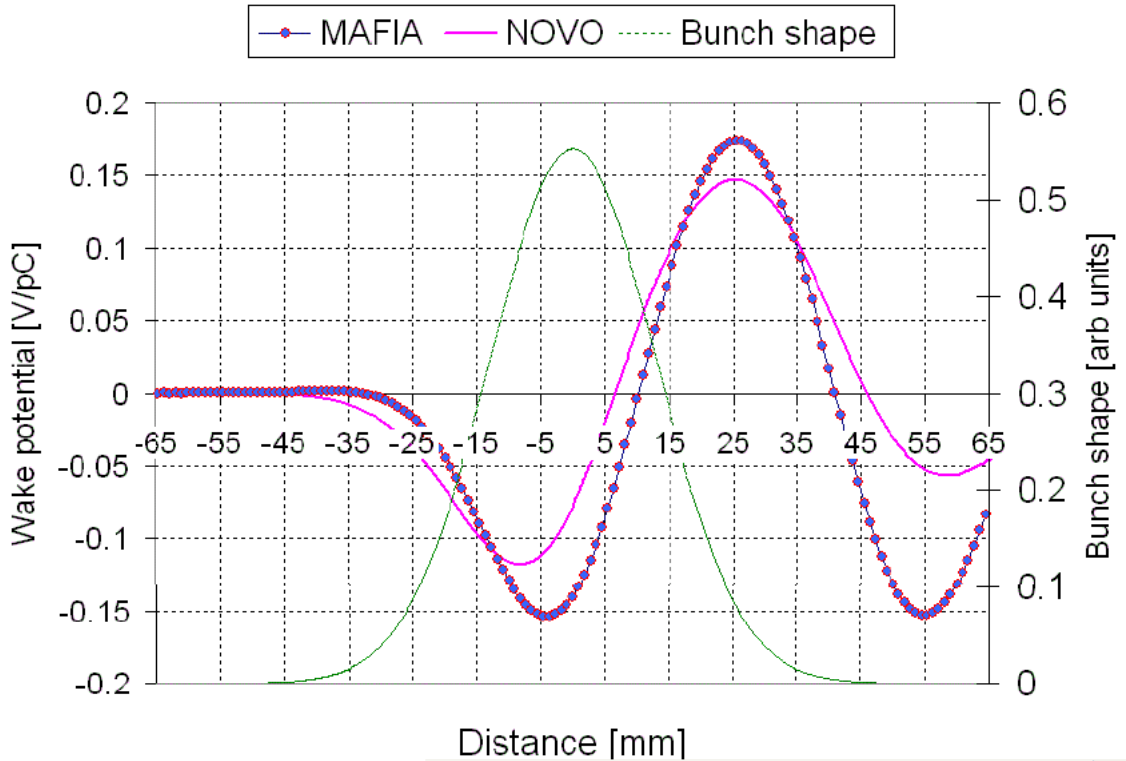


Figure 3.31. Longitudinal wake potentials calculations using 3d MAFIA for the vertex chamber model of figure 3.27 (circles) and 2d NOVA with the top axial symmetric profile in figure 3.30 (solid line) along with the 1.3 cm Gaussian bunch charge distribution (dashed line) as a function of distance in the bunch frame.

scattered electric fields take the form of dipole and quadrupole patterns and the power propagates primarily in the direction of the beam.

MAFIA is used to simulate a 1.3 cm 14 nano-coulomb Gaussian bunch in the collimator model. The electric and magnetic fields are monitored during and after the passage of the beam at two planes upstream and downstream of the collimator. Figure 3.32 shows a cross section of the computational model and its dimensions. Electric and magnetic fields are monitored at .05 m from the ends of the 1.4 m long volume and the beam enters from the left (upstream) and propagates to the right.

Figure 3.33 shows the collimator structure and electric field snapshots near the exit of the structure a few nanoseconds after the passage of a 1.4 cm long Gaussian

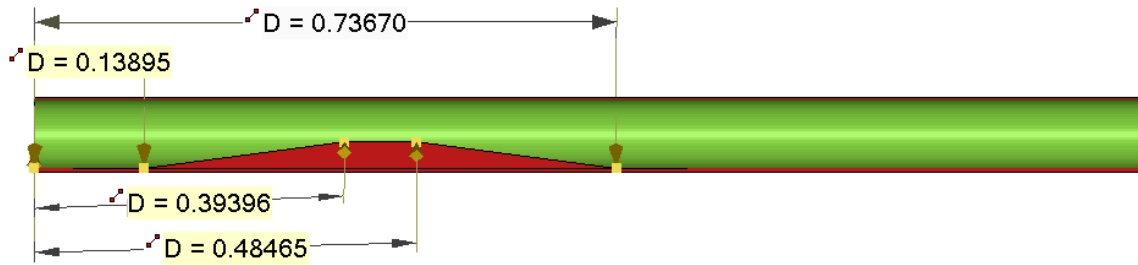


Figure 3.32. Cross section views of a tapered collimator model for wake field analysis with dimensions in meters. Computational length is 1.4 m. Collimator height is 0.033 m. Beam pipe diameter is 0.088 m.

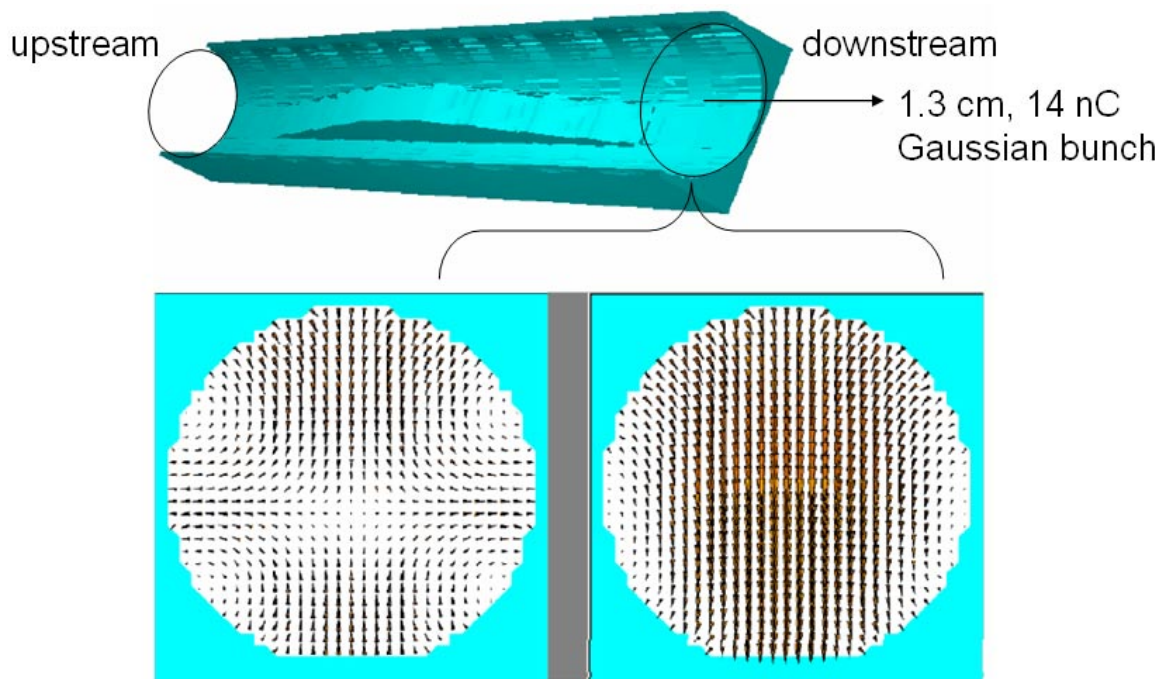


Figure 3.33. Collimator mesh with dipole and quadrupole fields after the passage of a 1.4 cm long Gaussian bunch past the single tapered collimator structure at the downstream end. These are two snapshots at the same location separated in time. The quadrupole component dominates at shorter time scales. The dipole mode persists at longer times. Collimator length and height: 0.6 m  $\times$  .033 m.

bunch. The collimator excites dipole and quadrupole fields. Initial wake fields are composed of a mainly quadrupole nature with the dipole mode persisting at longer time scales.

From electric and magnetic field data a time dependent power flux can be constructed. Figure 3.34 shows the total flux of the z -component of the Poynting vector  $\frac{1}{\mu_0} \int (\vec{E} \times \vec{B})_z da$  through a vertical plane of circular cross sectional area  $a$  at two locations just upstream and downstream of the collimator, separated by a distance of 1.3 m. The initial large peaks mark the passing of the beam at those locations. A small amount of power propagates backward from the collimator through an upstream position, while downstream significantly more power propagates forward. A positive flux indicates energy flow in the beam direction. Negative flux indicates en-

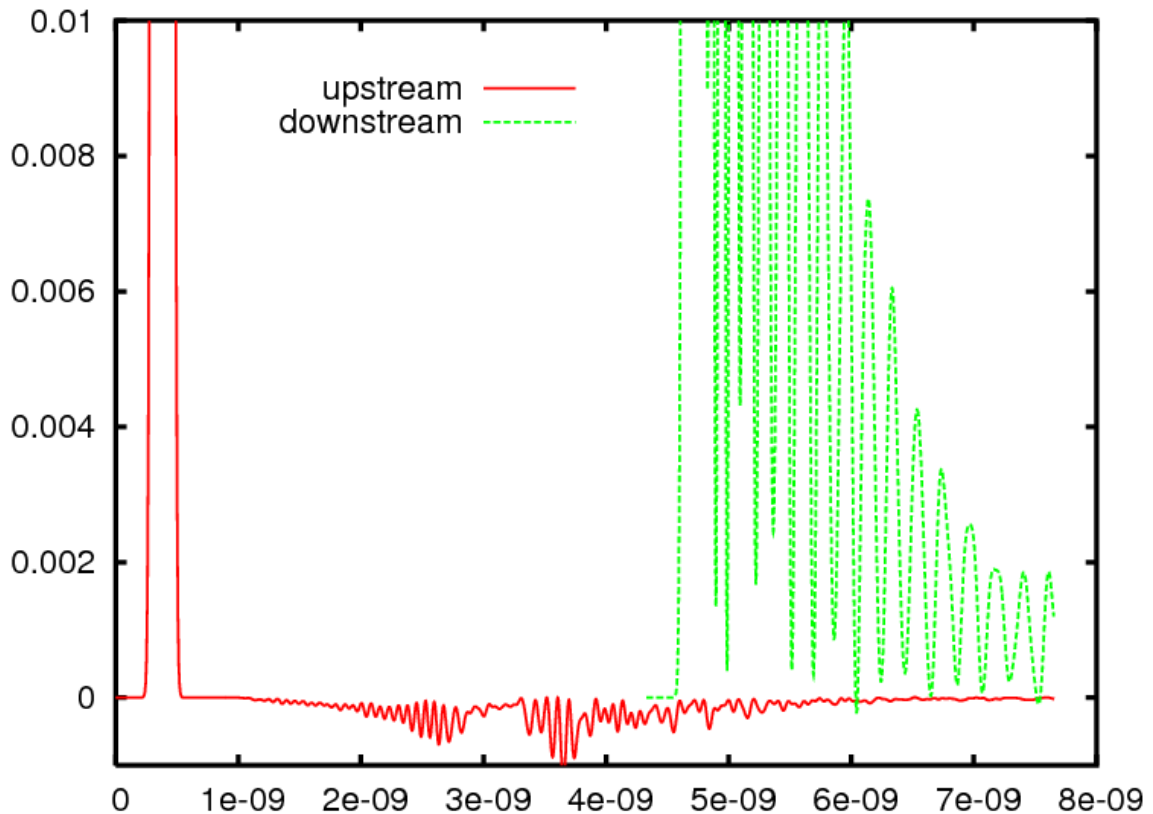


Figure 3.34. Poynting vector flux  $\frac{1}{\mu_0} \int (\vec{E} \times \vec{B})_z da$  through upstream (solid) and downstream (dashed) locations from a single collimator as a function of time in seconds. First large pulse indicate the passage of the beam. Negative values correspond to propagation in the upstream direction. The upstream and downstream monitoring planes are 1.3 m apart.

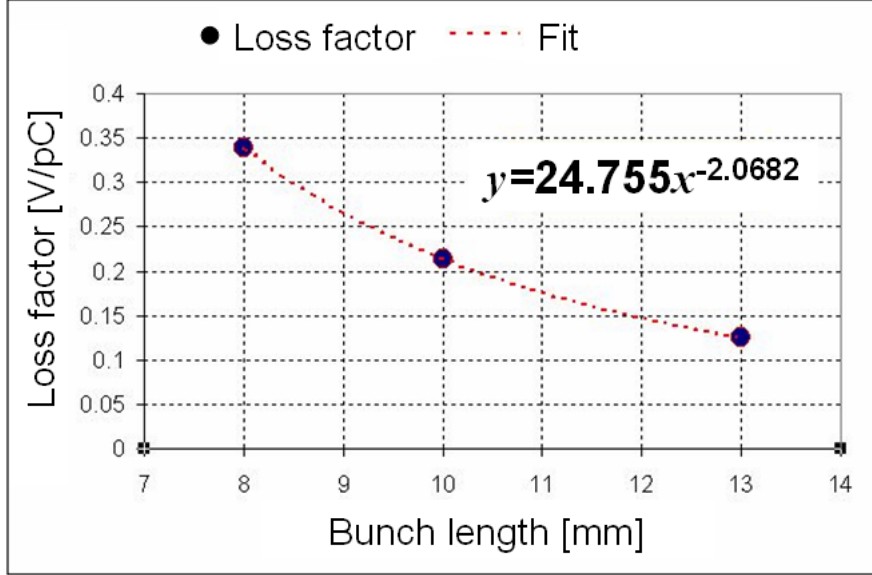


Figure 3.35. Collimator loss factor as a function of bunch length.

ergy flows in the upstream direction. From the time signatures and the collimator dimensions the most significant upstream power is generated at the two sloped faces of the collimator.

### 3.4.3.1 Collimator Loss Factor

In this wake field analysis the loss factor is calculated in the standard way by convoluting the bunch charge and the longitudinal wake field as described in section 3.4. Calculations exhibit the experimentally observed dependence of the loss factor with bunch length which goes as the inverse square of the bunch length[9]. These results are shown in figure 3.35. The loss factor dependence on both vertical and horizontal beam position offsets is shown in figure 3.36 and also qualitatively agree with the experimental observations in section 4.1.2.

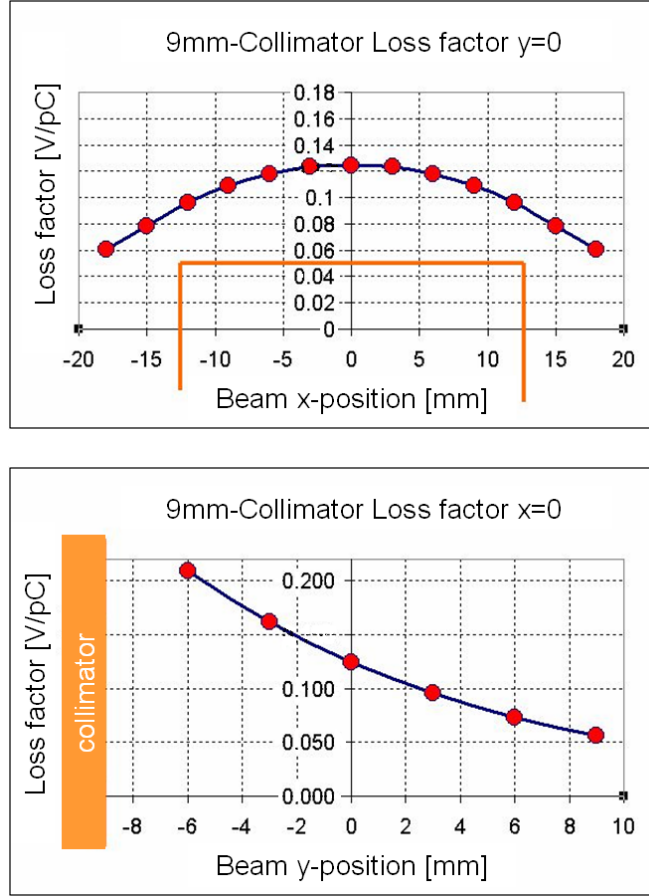


Figure 3.36. Loss factor as a function of vertical and horizontal beam position at the vertical collimator.

Consider a  $I_+ = 2.4$  Ampere positron beam of  $N=1700$  bunches of bunch length 1.3 cm on axis at the collimator. A loss factor of  $k = 0.12$  volts/pico-Coulomb gives a total beam power loss of

$$P_{beam} = \frac{kI_+^2}{fN} \quad (3.80)$$

$$= 3 \text{ kW} \quad (3.81)$$

for a revolution frequency of  $f=136$  kHz. This power is lost to HOMs.

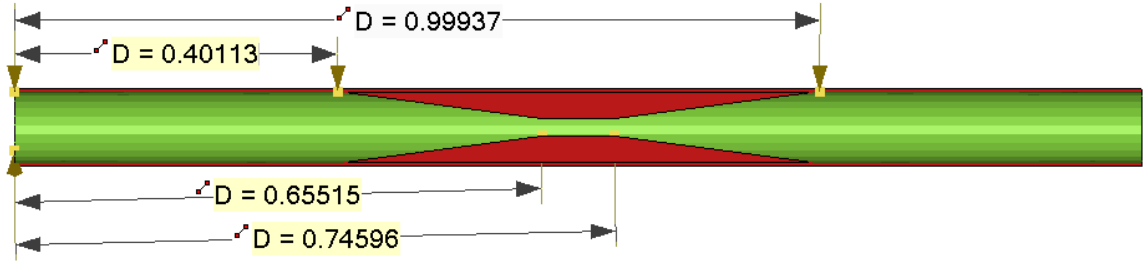


Figure 3.37. Dual collimator configuration.

### 3.4.4 Dual Collimator Wake Field Analysis

A variation of a collimator structure presently exists which incorporates two opposing collimator jaws shown in figure 3.37. Repeating the analysis above it is found that the quadrupole modes dominate at large times with similar power transmission characteristics: most but not all power propagates downstream.

#### 3.4.4.1 Dual Collimator Loss Factor

For the case where the beam is centered in the beam chamber the loss factor differs substantially between the single and dual collimator configurations. The single collimator loss factor is determined from above (from figure 3.36) to be 0.12 V/pC. For the equivalent bunch charge and bunch length the dual collimator loss factor analysis is a factor of 3 smaller at 0.037 V/pC.

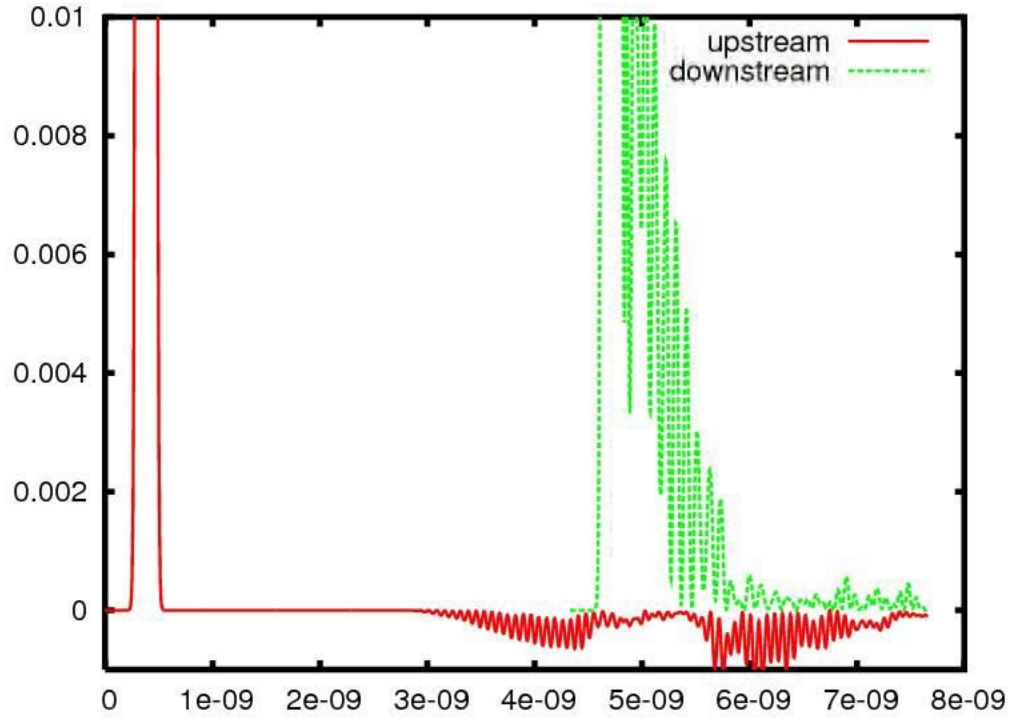


Figure 3.38. Poynting flux  $\frac{1}{\mu_0} \int (\vec{E} \times \vec{B})_z da$  upstream and downstream of dual collimator structure during and after passage of 14 nC Gaussian bunch of 1.3 cm sigma vs time in seconds.

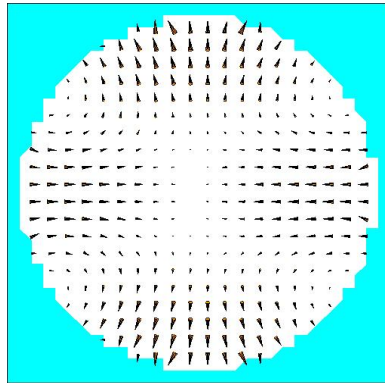


Figure 3.39. Snap shot of electric field pattern at a downstream end of the dual collimator structure 7 nS after passage of 14 nC 1.3 cm long Gaussian bunch show a predominantly quadrupole component persisting at long time scales.

## Chapter 4

# Results and Analysis

### 4.1 LER Region 4 HOMs

Excessive HOM heating is observed at bellows and pump chambers in LER region 4 downstream of a straight to arc transition. The LER region 4 straight section is characterized by collimators and RF cavities. The straight section and the downstream arc section are identical to other straight/arc sections in every other respect. The RF cavities are 50 to 100 meters away from the hot area. The most likely HOM source is the vertical collimator which is 15 meters upstream of the affected area. Figure 4.1 shows the layout of the PEP ring and the region 4 straight to arc transition, indicating the location of the HOM hot spot. Vacuum chamber components immediately downstream of the collimator are not affected. In these locations the vacuum chamber is circular. At the arc transition, the vacuum chamber changes from circular to an elliptical arc chamber cross section, shown in figure 4.2. The high temperature region begins just before the first arc bend and extends several meters into the arc section. HOM heating is associated with the change in vacuum chamber cross section as well as the proximity to the collimator.

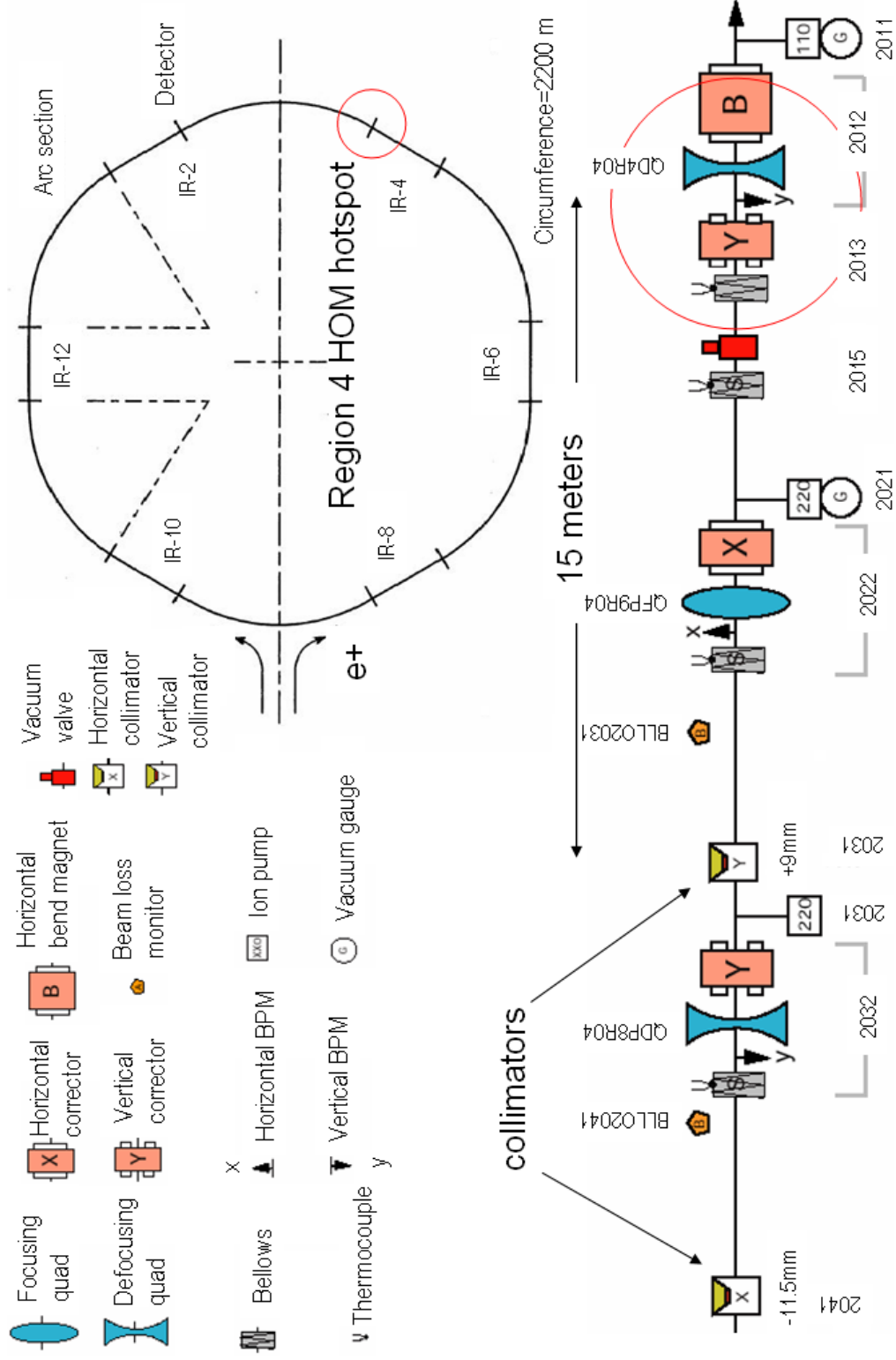


Figure 4.1. PEP ring region 4 straight to arc transition layout. Circled area indicates location of HOM heating, 15 meters downstream of the straight collimator section. The LER beam moves counter clockwise in the diagram.

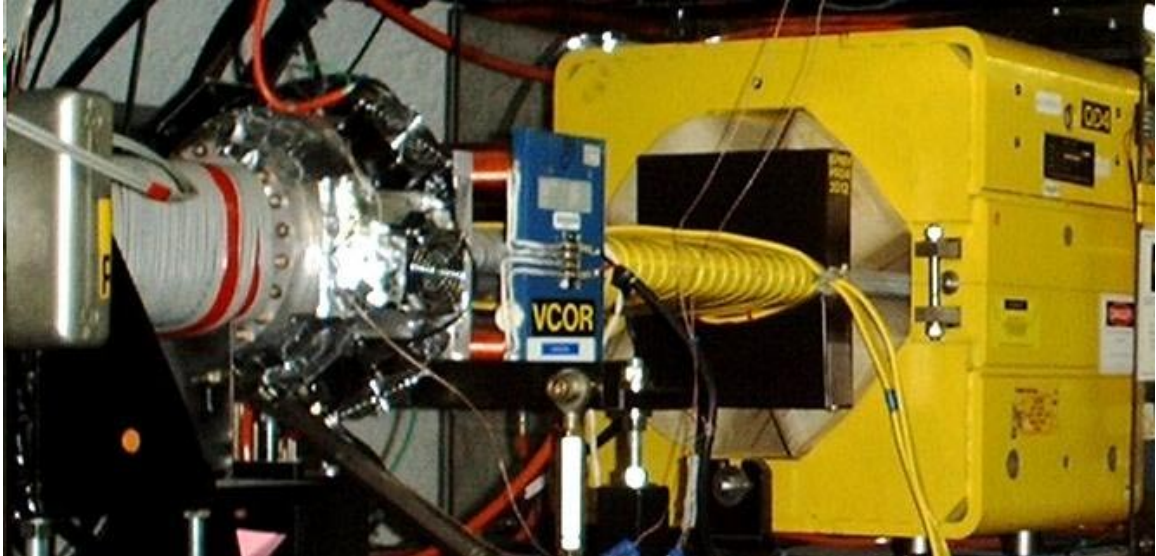


Figure 4.2. Photo of the region 4 straight to arc transition, where excessive HOM heating is observed. Vacuum chamber changes from circular to elliptical cross section at the bellows, shown surrounded with cooling fans.

The highest temperature elevation was observed at a bellows PR04:2012 in the straight to arc transition of LER in region 4, 15 meters downstream of fixed vertical and horizontal beam collimators in the straight section. Thermocouples mounted on the exterior of the bellows within the convolutions were registering a temperature rise of 80<sup>0</sup> Fahrenheit above cooling water temperature at nominal LER currents of 2500 mA even after the installation of cooling fans as shown in figure 4.3. Internal bellows components such as the shielding fingers are expected to reach much higher temperatures. Within this first arc bellows the beam chamber changes from a circular to elliptical cross section. The area of HOM heating starts near this bellows and extends 20 meters into the arcs, affecting pumping chambers, bellows and vacuum valves.

The low energy ring arc sections contain separate pumping chambers (ante-chambers) at bending magnets to absorb synchrotron light power and pump out any resultant out-gassing. The ante-chamber at the arc transition downstream of the

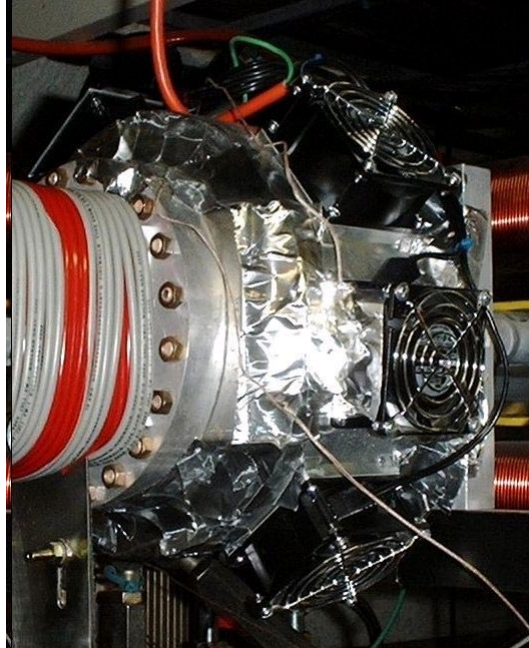


Figure 4.3. Hot bellows located at PR04:2012, 15 meters downstream of a collimator in a straight section of the low energy ring. Substantial air cooling installed in the form of fans which blow air into the bellows convolutions.

collimator suffered HOM related damage. These ante-chambers are coupled to the beam chamber through a slot designed to allow for straight ahead X-rays to exit the beam chamber while the beam traverses a bent trajectory in the arc sections of the ring. A cross section of such a chamber is shown in figure 4.4. They are 5.5 meters long, 0.4 meters wide and 0.1 meters high with a large aperture cylindrical protrusion which houses a titanium sublimation pump (TSP). Figure 4.5 is a photograph of a section of a PEP-II arc showing a series of ante-chambers along with the cylindrical Titanium sublimation pump (TSP) on the bottom of the ante-chamber.

The cylinder provides a large area wall for deposition of titanium atoms which have been sublimated from a heated filament. The coated wall serves to remove certain gas species from the ambient vacuum. Exterior electrical power for filament heating is fed in through a ceramic feed-through at the bottom of the pumping cylinder. At the ante-chamber next to the hot PR04:2012 bellows a ceramic feed-through connector

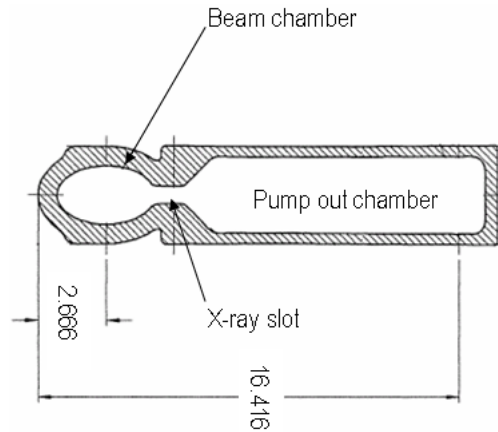


Figure 4.4. LER arc ante-chamber cross section diagram. As the beam is bent synchrotron radiation follows a path from the beam chamber through the x-ray slot into the pump out chamber where it is intercepted by a water cooled photon stop. The x-ray slot couples HOMs into the pump chamber.

at the ante-chamber pump port became damaged by HOM heating. Wake fields in the beam chamber had coupled through the X-ray slot into the pump out chamber and had coupled out into the housing tunnel of the through the connector terminals. HOMs could be detected in the tunnel and the frequencies measured with a spectrum analyzer and antenna. A small detector consisting of a small volume of lossy dielectric placed near the feed through experiences significant heating from escaping fields. A picture of the feed through is shown in figure 4.6.

Figure 4.7 is a spectrum of signals from an antenna near the ante-chamber pump feed-through at PR04:1163 showing several modes which track the temperature observations of the small lossy dielectric detector at 2-3 GHz. These modes were later observed in cold tests of the ante-chamber test setup[11].

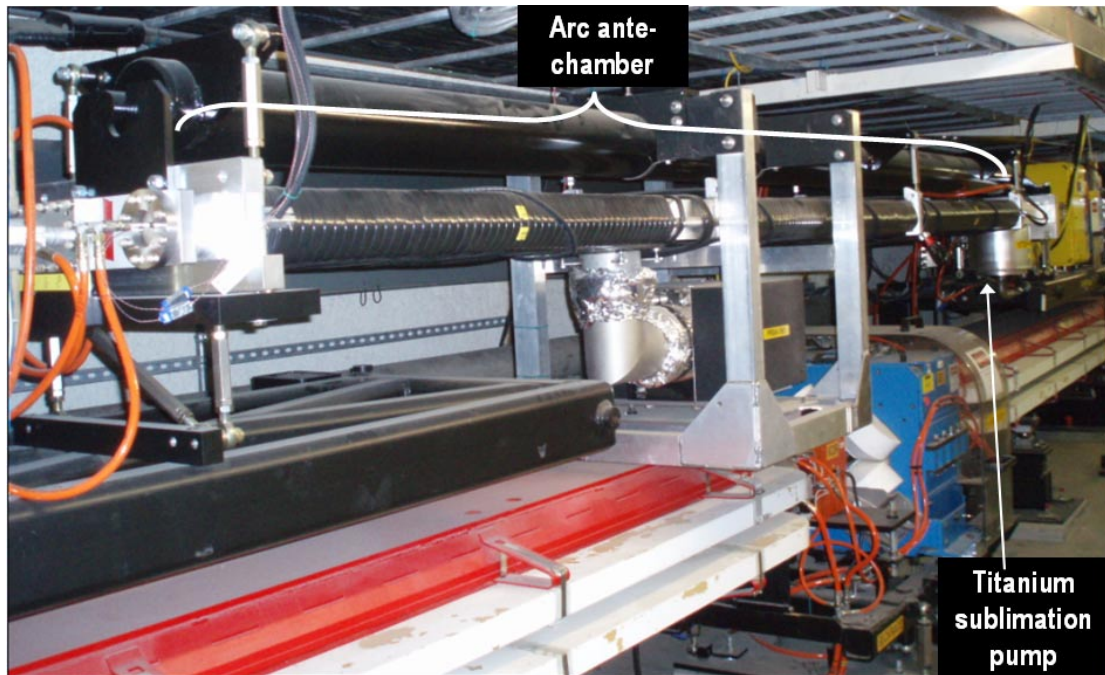


Figure 4.5. Photograph showing LER ante-chamber in an arc section of the PEP-II beam lines with attached cylindrical Titanium sublimation pump (TSP).

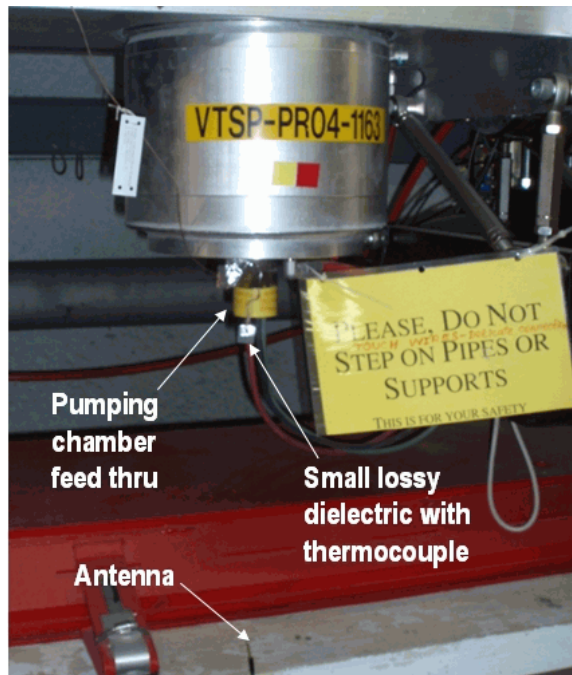


Figure 4.6. Location of damaged TSP feed through in LER region 4. Escaping HOMs can be detected with small lossy dielectric and antenna.

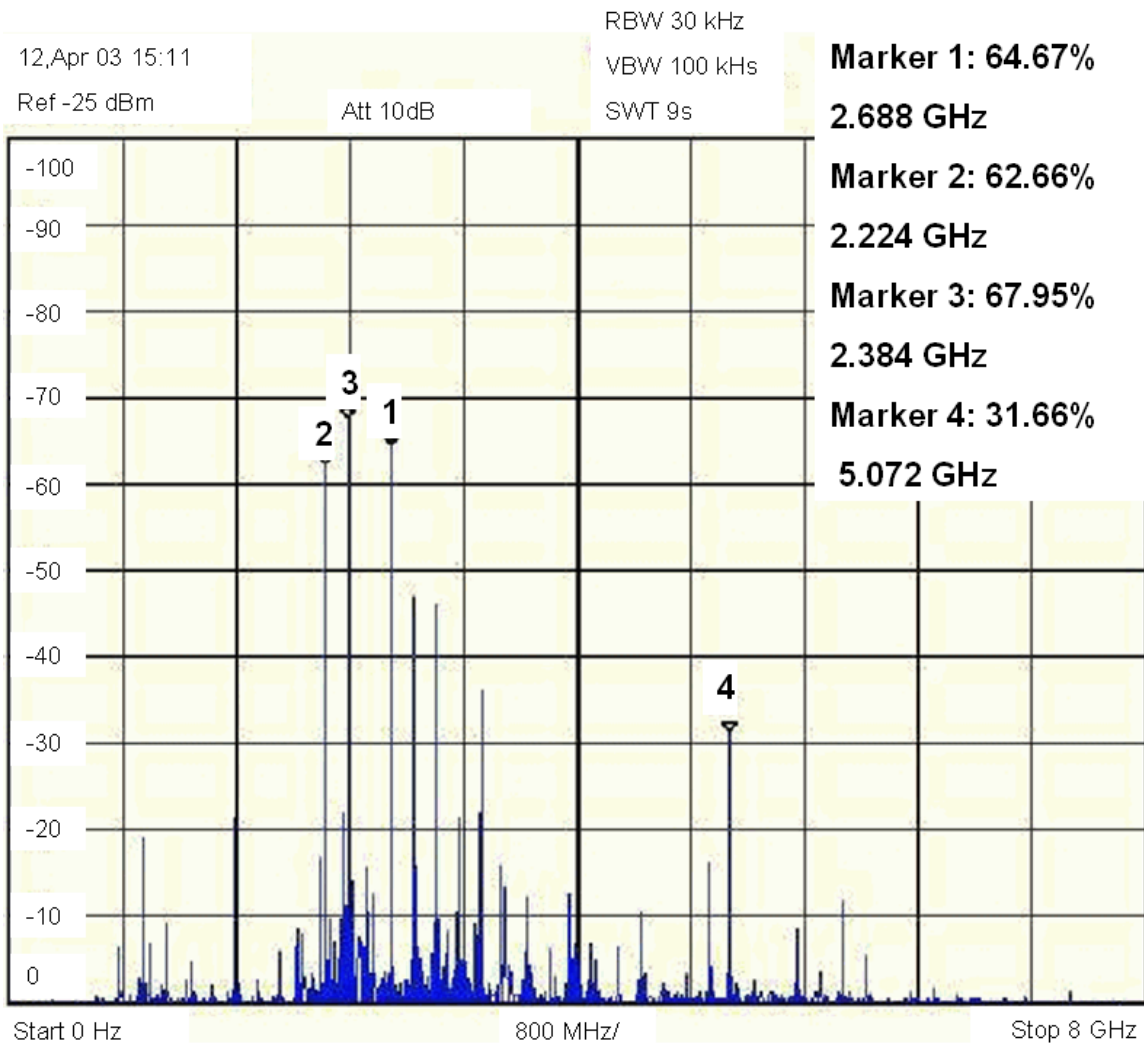


Figure 4.7. Spectrum from the antenna placed in the PEP-II tunnel near the Ti sublimation pump feed through at PR04:1163 with 1.6 A of LER beam. Marked modes correlate with the temperature of the small lossy ceramic detector. Courtesy A. Novokhatski.

### 4.1.1 LER Arc Ante-Chamber Absorber

A prototype water cooled dielectric absorbing device was designed and installed in several ante-chambers in an effort to isolate and dissipate HOM power coupling into the ante-chamber from the beam chamber. A measure of the HOM power extracted from the ante-chamber is provided by cooling water flow and supply and return water temperature monitoring. In addition to reducing the severity of ante-chamber heating, this device served as a useful diagnostic for confirming the upstream collimator as a source of HOMs.

Based on the measurements from an arc chamber test setup [11], a prototype arc absorber was designed and installed in a small unused pump port of several ante-chambers, a picture of which is shown in figure 4.8 along with measured power dissipated in two such arc absorbers[11] installed in two separate ante-chambers. The PR04:2010 location is nearest to the collimator, adjacent to the hot bellows at PR04:2012, where the chamber transitions from circular to elliptical. The PR04:1162 chamber is 6 meters downstream of PR04:2010. The ante-chamber absorber device consists of a 30 centimeter long array of ceramic tiles brazed to a copper support column which receives cooling from a stainless steel water pipe. The tiles are a commercially available ceramic material (Ceralloy) of high relative permittivity of  $\epsilon_r = 30$  and large loss tangent  $\tan\delta=0.11$  at 1 GHz. Figure 4.9 shows the temperature reduction achieved at the TSP connector dielectric detector before and after the absorber installation along with the LER currents during the same time period. A factor of two reduction in temperature is apparent after the installation at even higher LER currents. The temperature is monitored from a thermocouple mounted on a small lossy dielectric located outside of the ante-chamber TSP connector. Temperature reduction corresponds to less power reaching the exterior TSP connector from the beam chamber.

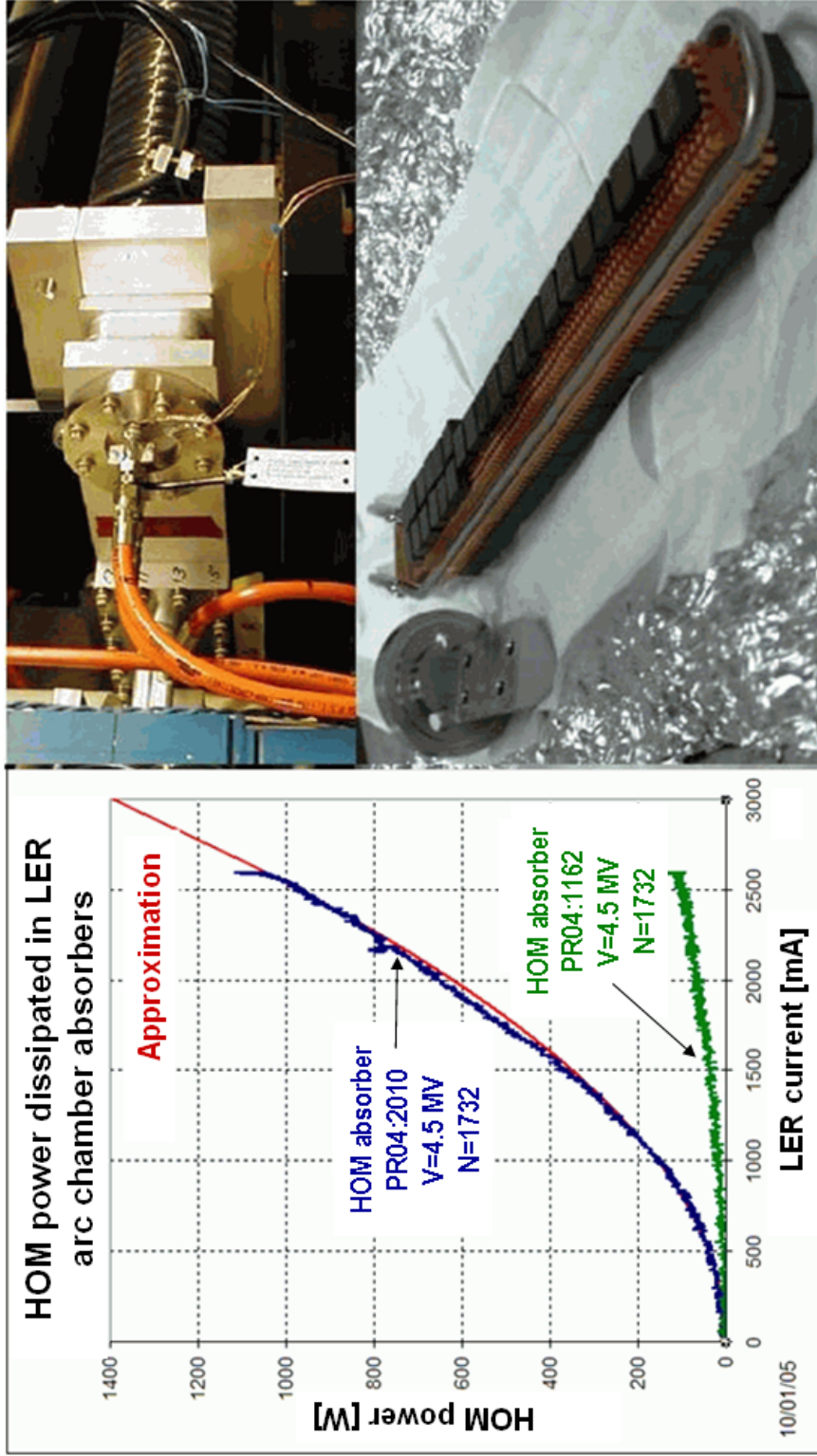


Figure 4.8. Picture of prototype LER ante-chamber absorber and measured power extracted at two locations. At nominal currents over 1 kW of power is extracted with the arc ante-chamber absorber device at PR04:2010. Top right picture shows the installation in the ante-chamber pump port. The small squares are absorber material brazed to copper support columns flanked by a stainless steel water cooling pipe (right bottom). The device is angled at the pump port to extend toward the center of the ante-chamber.

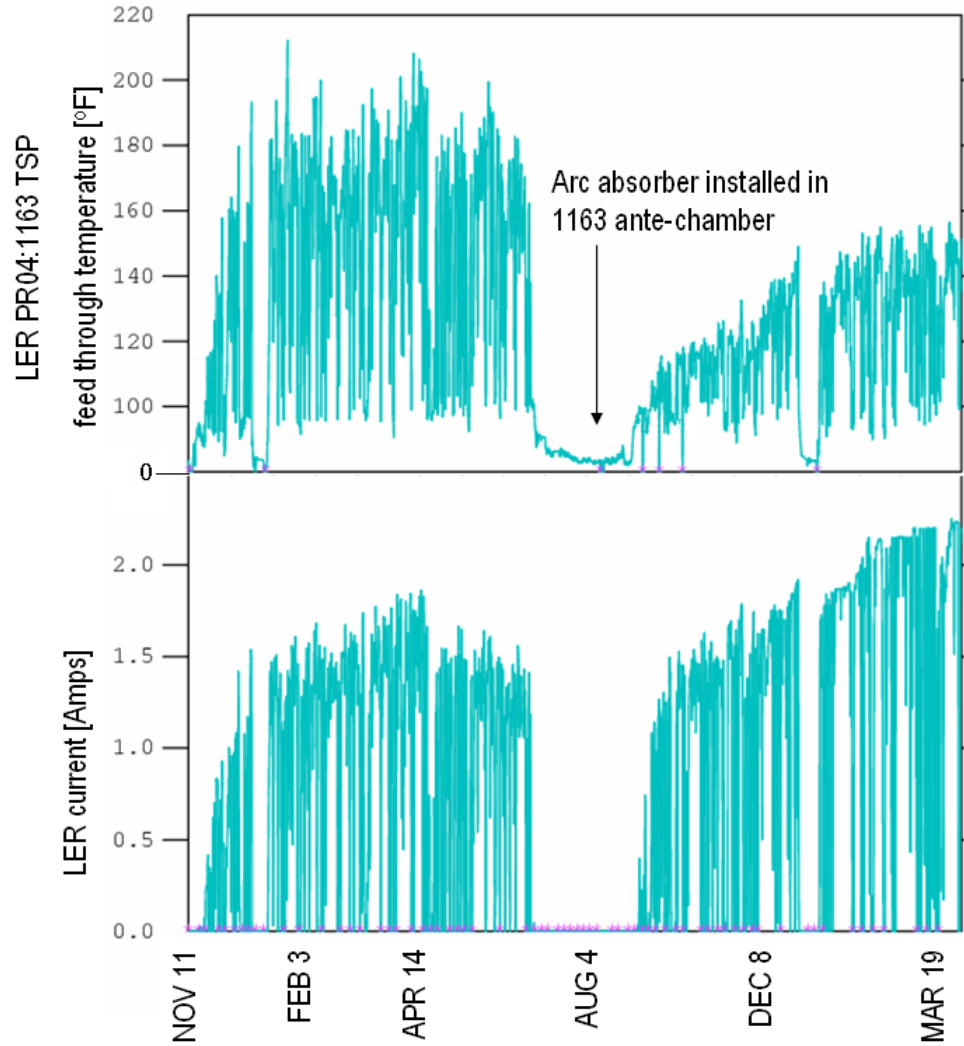


Figure 4.9. Pump temperature reduction attributable to LER antechamber water cooled absorber of figure 4.8. Reduction of a factor of two in temperature rise for the same current.

The absorber device dimensions are about 5 cm x 5 cm x 30 cm. This effectively damps modes in a ante-chamber 27 cm x 7cm x 550 cm which is roughly 100 times the absorber volume. The size and location within the antechamber is decided by the availability of the unused pump port, which may not be in the optimal location for damping. The pump port is located at a corner of the ante-chamber opposite to the beam chamber. A slight angle in the absorber structure allows the absorbing

tiles to sample more interior fields and was shown to improve damping in the cold model test setup[11]. Despite geometrical restrictions the ante-chamber absorber at PR04:2010 extracts about 1 kW power from the ante-chamber at beam currents of 2.4 A in the LER. The calculated beam power loss to HOMs from the collimator simulations in section 3.4.3.1 of several kW for nominal currents are consistent with this result (equation. 3.81).

#### **4.1.2 Collimator HOM Experiment**

A dedicated experiment to observe collimator HOM generation was performed[12]. Cooling water temperatures were monitored at vacuum chamber locations at various distances from collimators as vertical and horizontal beam positions at the collimator locations were manipulated. Significant variation in extracted power was observed at the water-cooled arc ante-chamber HOM absorber located 15 meters downstream of a vertical collimator as the vertical beam position at the collimator was changed. The description of this arc ante-chamber HOM absorber can be found in section 4.1.1. The beam trajectory at the ante-chamber absorber did not vary during this experiment. Figure 4.10 shows the ante-chamber absorber power extracted based on the cooling water temperature variation as a function of vertical beam position at two vertical collimators at different locations: 15 and 65 meters upstream. No appreciable change in extracted power was observed when the beam was moved horizontally at the vertical collimators. These data are consistent with the loss factor computations of section 3.4.3.1.

Temperatures of components further downstream of the collimator also respond to beam position at the collimators, indicating HOM propagation of up to 20 meters from the collimator, while no temperature variation was observed at components upstream of the collimator [2]. This is consistent with the simulation results of section 3.4.3, which shows most of the HOM power flow from the collimator moving in the beam direction.

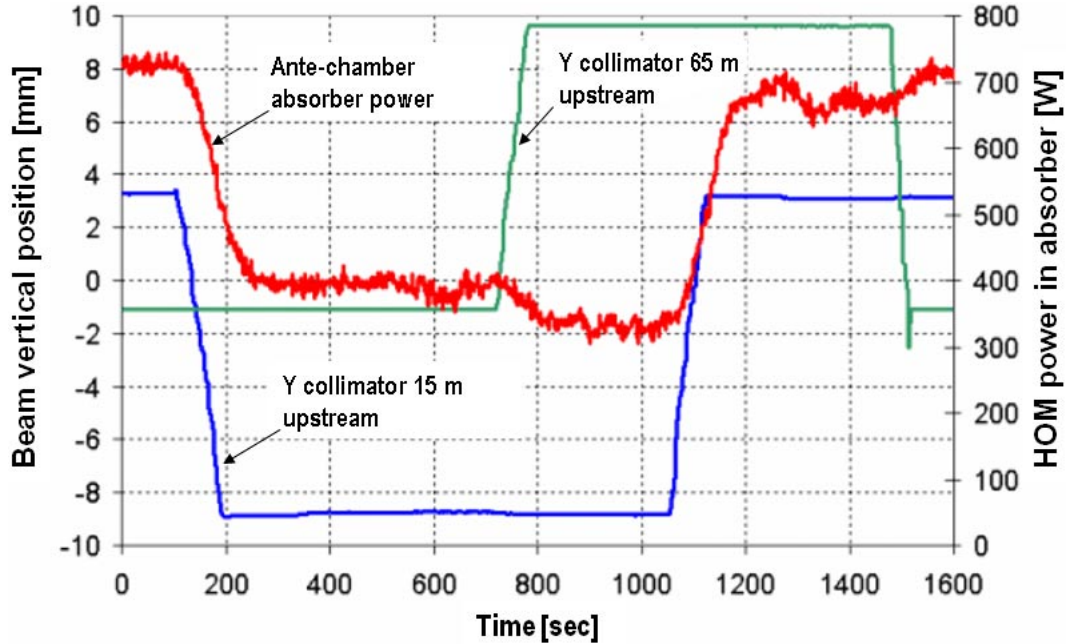


Figure 4.10. Power extracted from the ante-chamber absorber and vertical beam position at two vertical collimators located 15 and 65 meters upstream of the absorber as a function of time. In both cases moving the beam away from the collimator reduces extracted power at the ante-chamber absorber.

### 4.1.3 Straight Bellows Absorber Device

One way of mitigating effects of an identified HOM source is by coupling propagating HOM power out of the beam chamber before it reaches sensitive beam line components. Coupling to monopole mode power represents an impedance to the beam and must be avoided. In most cases the monopole mode does not couple into accelerator components. Dipole, quadrupole and higher modes have field patterns which enhance the tendency to couple power into accelerator structures. The concept of the straight bellows absorber device is to couple to specific beam pipe modes (dipole and quadrupole) while minimizing impedance to the beam fields (monopole mode). Scattered beam fields from a collimator in the LER region 4 straight section consist of dipole and quadrupole mode components (see section 3.4.3) and thus it is desirable to selectively remove these from the beam chamber.

The coupling mechanism responsible for HOM heating in the bellows can be exploited as a means of removing HOM power from the accelerator. Coupling through a slot can be approximated by coupling through an elliptical aperture of semi major axis  $l$  and semi minor axis  $d$  with  $l \gg d$ . Coupling for modes with transverse electric field and longitudinal magnetic field (dipole, quadrupole,...etc) through an elongated ellipse is given by[60]

$$k_{\perp} \propto \frac{\pi}{3} \frac{l^3}{\ln \frac{4l}{d} - 1} \quad (4.1)$$

while monopole mode coupling, which represents beam impedance, is given by

$$k_b \propto \frac{\pi}{3} l d^2. \quad (4.2)$$

Removing dipole and quadrupole power while minimally coupling to monopole power is equivalent to maximizing the ratio of the couplings  $k_{\perp}/k_b \approx (l/d)^2$ . This clearly suggests making slots as long as possible with respect to slot width. The slot width  $d$  cannot be made arbitrarily small since the denominator in equation 4.1 will make the coupling  $k_{\perp}$  small. On the other hand, large slot width means the available area for the flow of beam surface currents becomes small, making the surface current density large. A reasonable compromise is to limit the surface current density to be only twice that for the case of no slots, so that no more than half of the beam pipe wall area is allocated to coupling slots. In principle, for a given slot width, coupling efficiency can be made arbitrarily high if space is available for the slot length.

Once coupled out of the beam chamber, a means to dissipate this power is necessary. This can be accomplished by exposing the coupled fields to a water cooled lossy material. Ceradyne[59] lossy dielectric ceramic with relative permittivity  $\epsilon_r = 30$  and loss tangent  $\tan \delta = 0.11$  is used, given the extensive fabrication experience with this material at SLAC. It is estimated that kilowatts of electromagnetic power will be absorbed and coupled out as thermal power with water cooling.

The end of the LER region 4 straight at the arc transition is chosen as a site for a selective absorbing device. This site is 12 meters downstream of the collimator but just upstream to the LER region 4 HOM heating area which should be an ideal site for intercepting collimator generated HOMs. Because of space constraints, the design incorporated an existing bellows which was redesigned to be smaller in the longitudinal dimension to make room for the longest possible slots. In this way 70 mm of space is made available for slot length next to the bellows.

The basic model for scattering parameter analysis incorporates a circular beam pipe with slots which opens into an annular cavity surrounding the beam pipe. Lossy material is situated within the annular cavity. For simulations the bellows fingers and bellows convolutions are not modelled. The simulations treat the bellows as a cavity extension to the annular cavity. A section of the computational model is shown together with the absorption spectrum in figure 4.11.

The design process involved variation of slot and absorber geometry to optimize absorption characteristics using scattering parameter analysis as outlined in section 3.3. The goal being maximizing dipole and quadrupole mode absorption, while minimizing monopole absorption.

The slot length strongly affects the degree of dipole and quadrupole coupling as expected. The absorber thickness affects the absorption spectra. Thicker absorbers tend to lower absorption peak frequencies. Slot width was varied according to the constraint of 50% beam pipe wall area be delegated to surface current. Wider slots tend to spread out the absorption peaks and provide better coupling, but also increases monopole mode coupling.

These parameters were varied within the allowed mechanical constraints to obtain an optimal configuration with a slot length 70 mm, slot width of 6 mm and absorber thickness of 16.7 mm. The optimized design absorption spectrum is shown in figure 4.11. The inset depicts the computational model used in the calculation. The

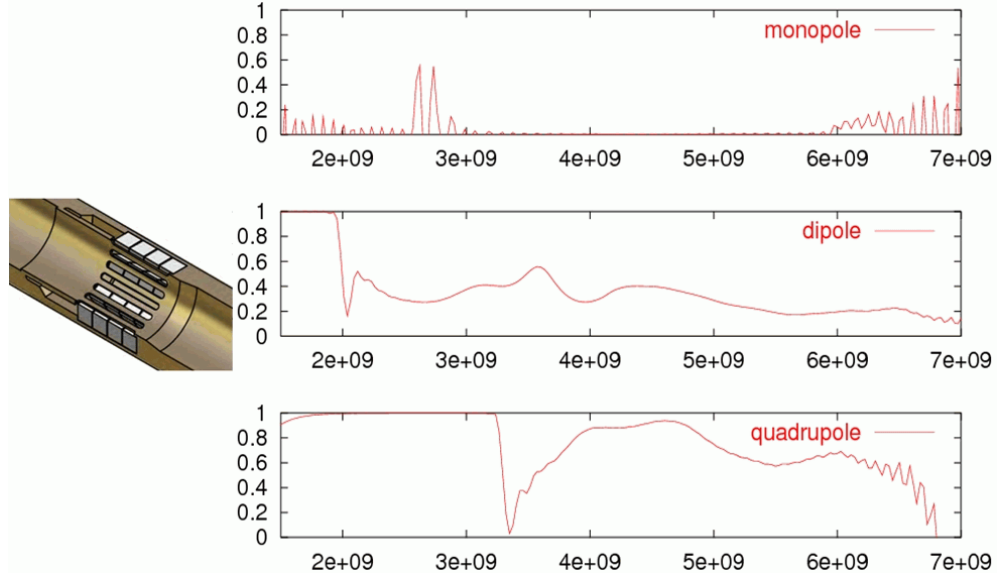


Figure 4.11. Absorption  $1 - s_{11}^2 - s_{21}^2$  of the optimized straight bellows absorber and a section of the computational model. Slot length: 70 mm. Slot width: 6 mm. Absorber thickness: 16.7 mm.

computed fractional absorbed power (absorption)  $1 - (s_{11}^2 + s_{21}^2)$  is plotted for the three modes as a function of frequency. The absorption is minimal for the monopole mode (top) trace and maximized for the dipole and quadrupole modes. The dipole spectrum is further tuned to exhibit strong absorption in the 2-5 GHz range.

Dipole mode absorption in the 2-5 GHz range is important since power at these frequencies was discovered in the nearby ante-chamber[11]. MAFIA simulations of section 3.4.3 indicate substantial dipole mode production by the upstream collimator. The selective absorbing device is expected couple out 40 % of the dipole mode power at these frequencies.

Based on the scattering parameter results a mechanical design is proposed, consisting of a series of longitudinal slots which expose a cavity containing ceramic absorbers to the beam fields is illustrated in figure 4.15, incorporating the optimal slot length, width and absorber thickness.

The mechanical design requires sufficient heat transfer characteristics and the

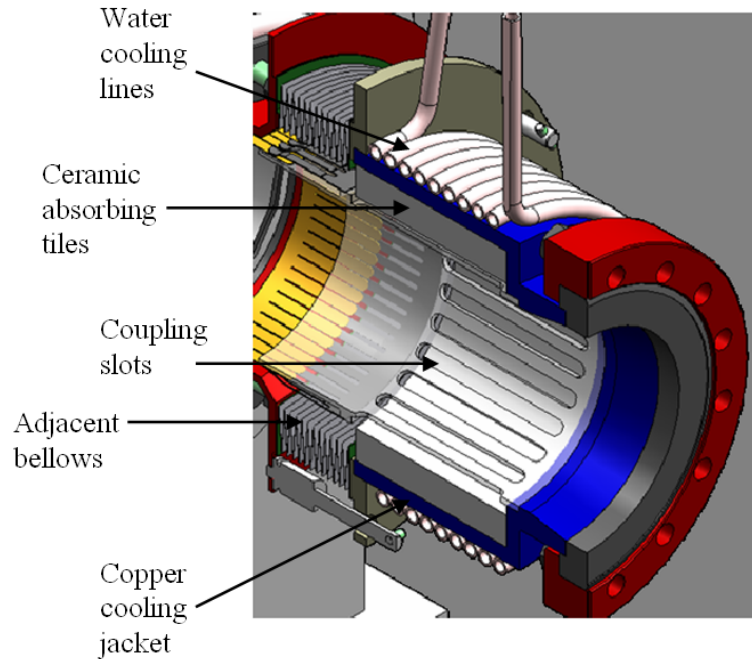


Figure 4.12. Straight bellows absorber mechanical design showing absorber material behind coupling slots. Absorber is brazed to a water cooled copper jacket. Adjacent bellows cavity is exposed to the absorber to also damp bellows modes.

ability to survive expected thermal stresses. Heat is efficiently removed by dedicated cooling water lines adjacent to the ceramic in an outer copper cooling jacket brazed to the ceramic. The device does double duty in that it also couples to a bellows to damp bellows modes. The absorber cavity and the bellows cavity are consolidated to expose the bellows cavity to the absorber and help damp any modes which may have infiltrated the bellows.



Figure 4.13. Assembled straight absorber device ready for installation. Here ceramic absorber tiles can be seen under copper coupling slots next to an array of bellows fingers.

#### **4.1.3.1 Operational Results with the Straight Absorber Device**

The straight absorber device was built and recently installed in the low energy ring during a major maintenance period and has experienced high current running. Figure 4.13 shows the completed device just prior to installation. Figure 4.14 shows the device as installed in the beam line. The adjacent bellows no longer needs the cooling fans which are installed on all other bellows.

Reduction in temperatures is observed at comparable currents before and after the installation. The desired effect is achieved in the local area around the overheating bellows 15 meters downstream of the collimators. Figure 4.16 is a photo of this area. The temperature rise is reduced by a factor of two at the most seriously overheating bellows at PR04:2012. Figure 4.17 shows the reading of a thermocouple situated in a bellows convolution at PR04:2012 and the thermocouple reading at a small

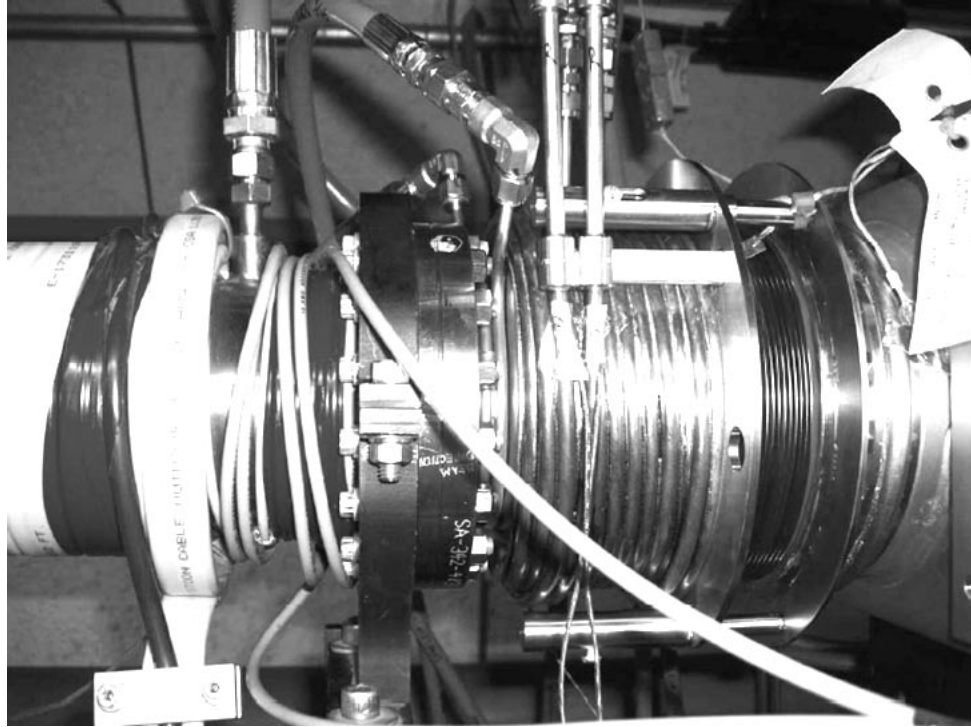


Figure 4.14. Straight absorber device as installed in the low energy ring beam line showing copper cooling lines for removing absorber HOM power. Small wires are thermocouples attached to the water supply and return lines. Note that the adjacent bellows no longer needs air cooling. Immediately to the right of the bellows is vacuum valve 2015.

ceramic HOM detector located external to the TSP feed through along with LER current during the period of time before and after the installation of the straight bellows absorber. A 50% reduction in operating temperatures is observed at these two locations at comparable currents. Similar temperature reduction is observed at other nearby bellows, pump chambers and vacuum valves.

Further indication of effectiveness is observed at the arc ante-chamber absorber located in the immediate downstream arc chamber. This particular arc ante-chamber also experienced high temperatures from HOM energy which was measured at the pump port and was severe enough to damage the electrical feed through. This was the site of a prototype ante-chamber absorbing device installed earlier and described

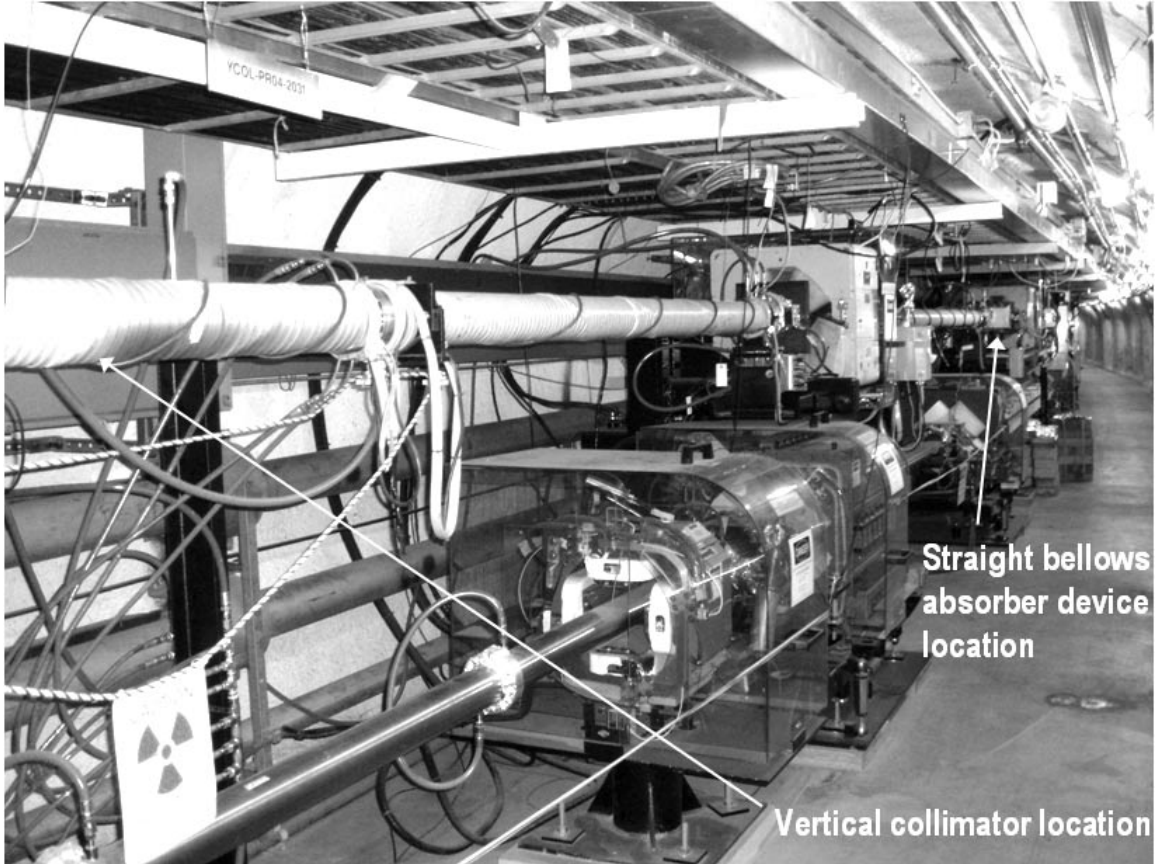


Figure 4.15. Straight bellows absorber device location with respect to upstream vertical collimator at the end of the straight section of the LER. The straight bellows absorber device is 15 meters downstream of the collimator.

in section 4.1.1. The power extracted from the ante-chamber absorber device was monitored before and after the installation of the straight absorber device. The quadratic current dependence is fit with coefficients of 145 and 82 W/mA<sup>2</sup> respectively for data sets taken before and after the straight bellows installation, indicating a 42% reduction in HOM power reaching this area. The data and fit are shown in figure 4.18. Looking at figure 4.11 and considering the strength and persistence of the collimator generated dipole mode, a 40 % reduction correlates with the amount of absorption expected for the dipole mode in the 2-5 GHz band.

Power extracted by the straight bellows absorber device is measured for two LER

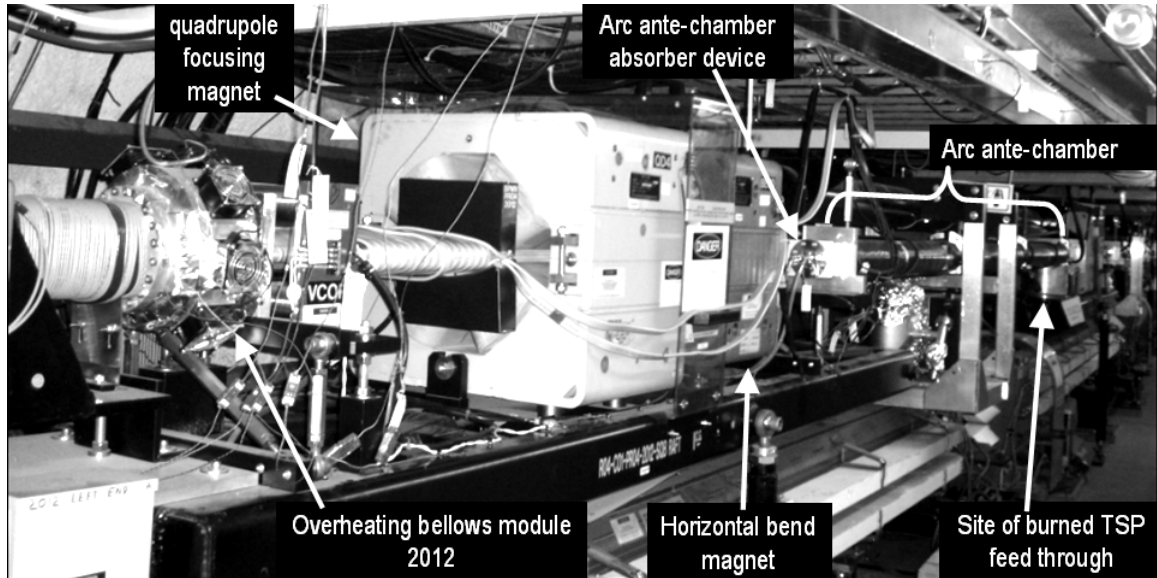
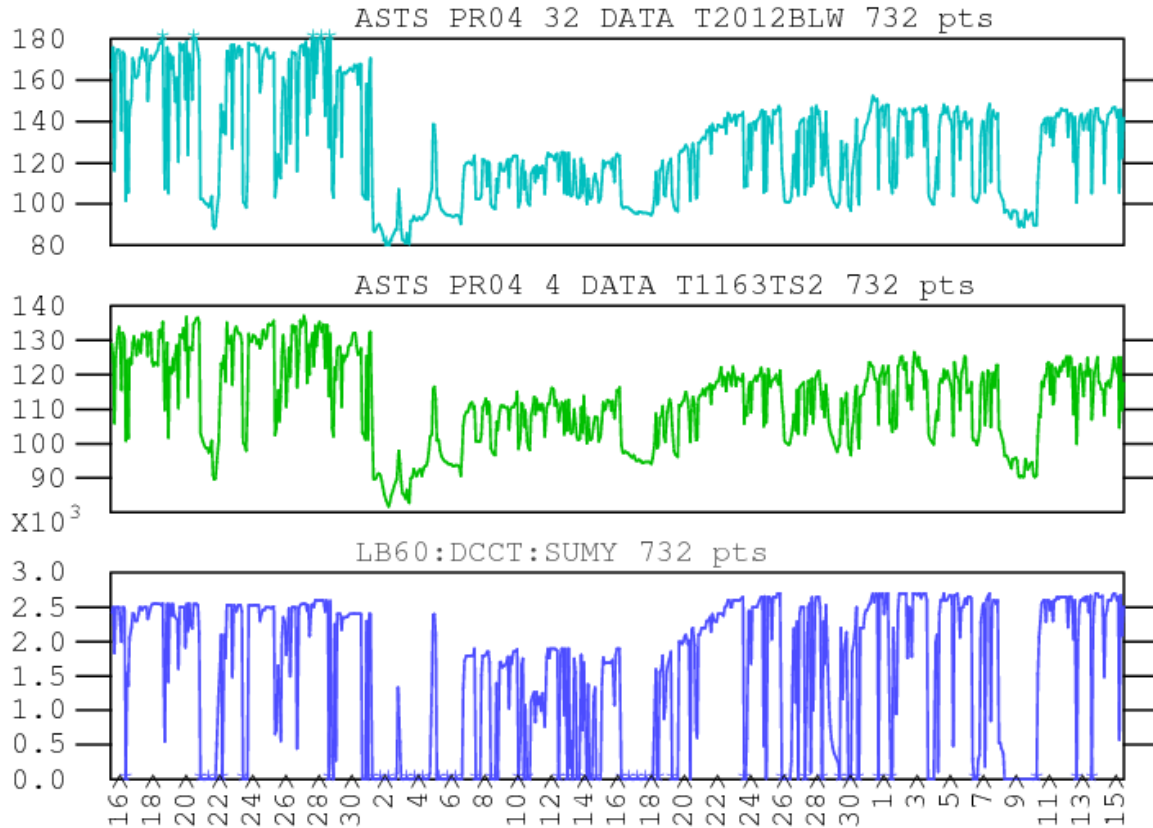


Figure 4.16. Section of straight to arc transition in LER immediately downstream of the straight bellows absorber device. Vacuum valve 2015 is immediately to the left in the photo.

RF gap voltage configurations. This is displayed vs. LER current in figure 4.19. This data allows an estimation of HOM power in the beam chamber at the straight bellows absorber device location. Recall the 42% reduction of power extracted in the arc ante-chamber absorber device attributed to the straight bellows absorber which is displayed in figure 4.18. According to figure 4.19, at 2.4 Amps of LER current 1.45 kW of power is extracted in the straight bellows absorber device. Assuming this is 42% of the total power in the beam chamber, the beam chamber power can be estimated as  $P_{\text{cham}} = 1.45 \text{ kW} / 0.42 = 3.45 \text{ kW}$ . This is in agreement with equation 3.81, which gives 3 kW for the wake field calculation of HOM power generated at the collimator for the same beam current, assuming a 1.3 cm bunch length. This is consistent with a picture where most of the HOM power generated at the collimator can propagate forward for large distances with negligible loss before coupling into accelerator components.

Based on the success of the straight bellows absorber device, two identical units



Time Range: 15-APR-2006 12:13:00. - 15-JUN-2006 12:13:00.

Figure 4.17. Top plot: Thermocouple reading ( $^{\circ}\text{F}$ ) at the overheating bellows 2012 before and after straight absorber device installation shows a factor of two decrease in temperature rise after installation of the straight bellows absorber on May 1, 2006. Middle plot: Thermocouple reading ( $^{\circ}\text{F}$ ) at a small ceramic HOM detector located external to the pump chamber 1163 during the period before and after installation of the straight absorber device. Lower temperature indicates less HOMs reaching the tunnel from the ante-chamber at this location. Bottom plot: LER current (mA) during the period before and after installation of the straight bellows absorber.

are deployed in region 4 between the existing absorber device and the upstream collimators to aid in intercepting collimator generated propagating dipole and higher order modes. A device at PR04:2032 will take HOM power from an upstream horizontal collimator located 4.5 meters away, while a device at PR04:2072 will intercept

### HOM power in Arc Absorber before and after installation of the straight HOM absorber

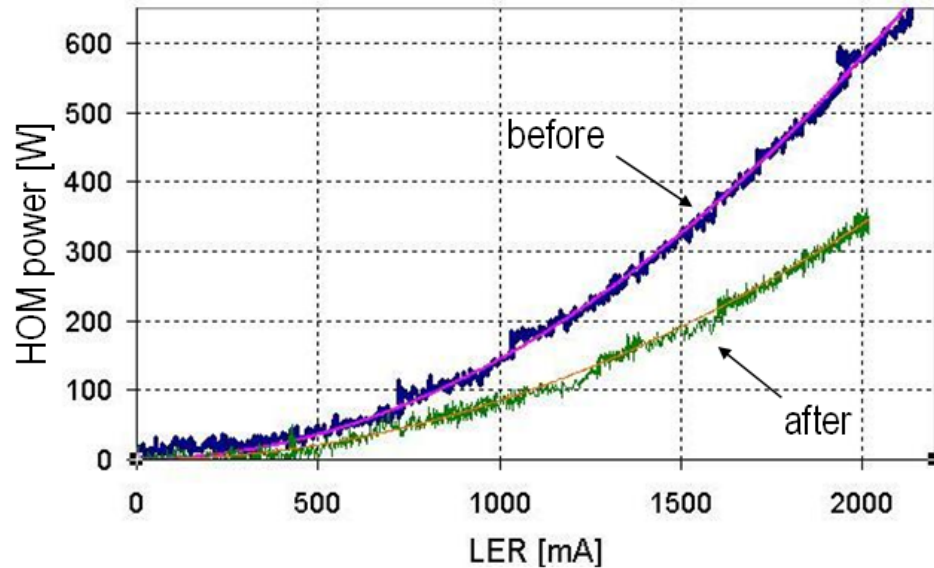


Figure 4.18. HOM power extracted from an arc ante-chamber absorbing device as a function of LER current before and after installation of the straight absorber system. Data is quadratic with current with coefficients of 145 and 82 W/mA<sup>2</sup> for data before and after installation of the straight bellows absorber device. This represents a reduction of 42% in HOM power infiltrating the ante-chamber.

HOM power from an upstream horizontal collimator at PR04:2081, which is 5 meters away. Figure 4.20 shows photos of these installed devices.

An additional straight bellows absorber is deployed in region 10 near momentum collimators which are designed to remove off momentum particles from the beam. Figure 4.21 is a photo of the region 8 straight bellows absorber near PR10:2145, between two horizontal momentum collimators located about 5 meters either side of the device.

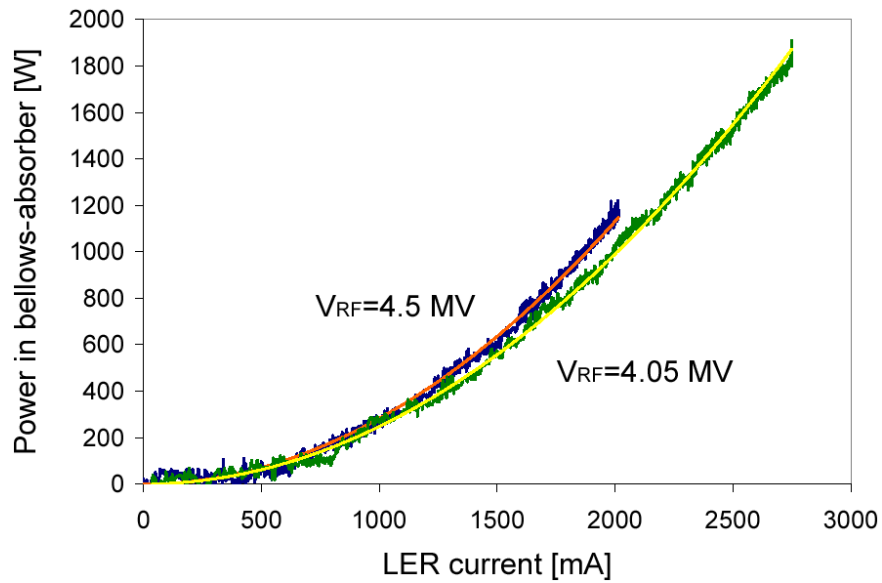


Figure 4.19. HOM power extracted from the straight bellows absorbing device as a function of LER current for two values of LER gap voltage. The upper trace was taken at a gap voltage of 4.5 MV, the lower trace at gap voltage of 4.05 MV.

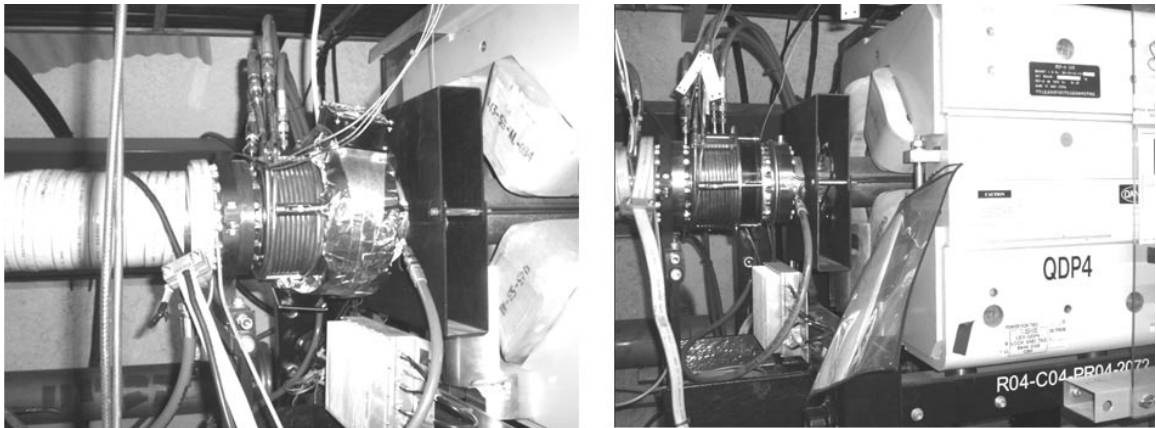


Figure 4.20. Additional straight absorber devices deployed in region 4 straight section of LER. Left photo show an installation at PR04:2032 to take power from upstream horizontal collimator at PR04:2041 which is 4.5 meters away. Right photo shows a straight absorber device installation at PR04:2072 which takes power from upstream horizontal collimator PR04:2081 which is 5 meters away.

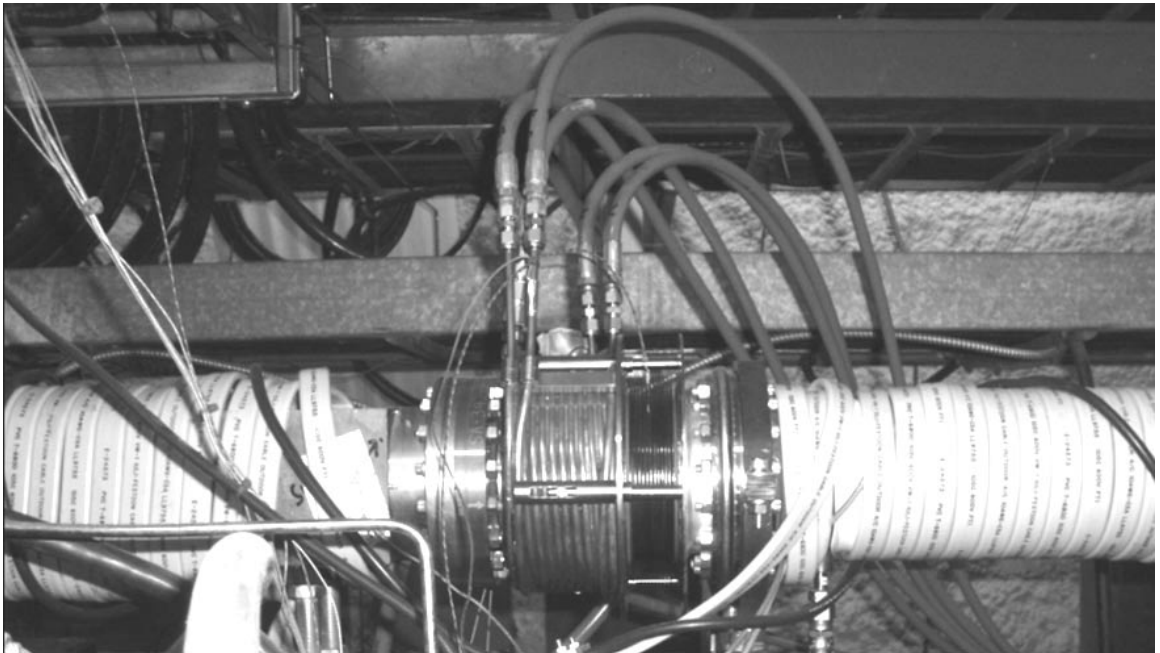


Figure 4.21. Photo of the region 10 straight bellows absorber device located at PR10:2145 between two horizontal momentum collimators 5 meters away on either side of the device.

## 4.2 Interaction region HOMs

At the interaction region (IR), beams are brought together into a single vacuum chamber for collisions at the BaBar detector. There are a number of vertical and horizontal dipole magnets which guide the beams into a common collision point. Given the beam energies and currents, substantial thermal gradients are produced in the beam chamber by synchrotron radiation. This requires bellows assemblies to distribute thermal induced mechanical motion. In addition, the geometry of the IP area incorporates beam chamber tapers, offsets and masks in order to shield the BaBar detector from radiation. Such irregularities in chamber geometry contribute to wake field generation by both beams. These scattered beam fields couple into vacuum chamber components.

The near-interaction area is comprised of large magnet and vacuum chamber assemblies designated Q2, Q4, and Q5. The vacuum chamber sections are coupled together with bellows. Figure 4.22 is a 3D cut-away view of the interaction region which includes the BaBar detector subsystems and the magnet and vacuum chamber assemblies indicating the location of bellows. The interaction region is symmetric with respect to the IP, so that there are Q2 bellows on both sides of the IP at both crotch areas, with Q4 bellows at both sides for both beam lines. The detector is 5.4 meters high and 6.4 meters long and integrates a cryogenic helium dewar to support a superconducting solenoid. Semiconductor based vertex detector and high voltage drift chamber wires track charged particle decay product trajectories in the solenoidal field. The calorimeter determines particle energies and the Cerenkov detector gives particle velocities. The vertex bellows are situated well within the detector. The Q2 and Q4 bellows are accessible without dismantling the detector.

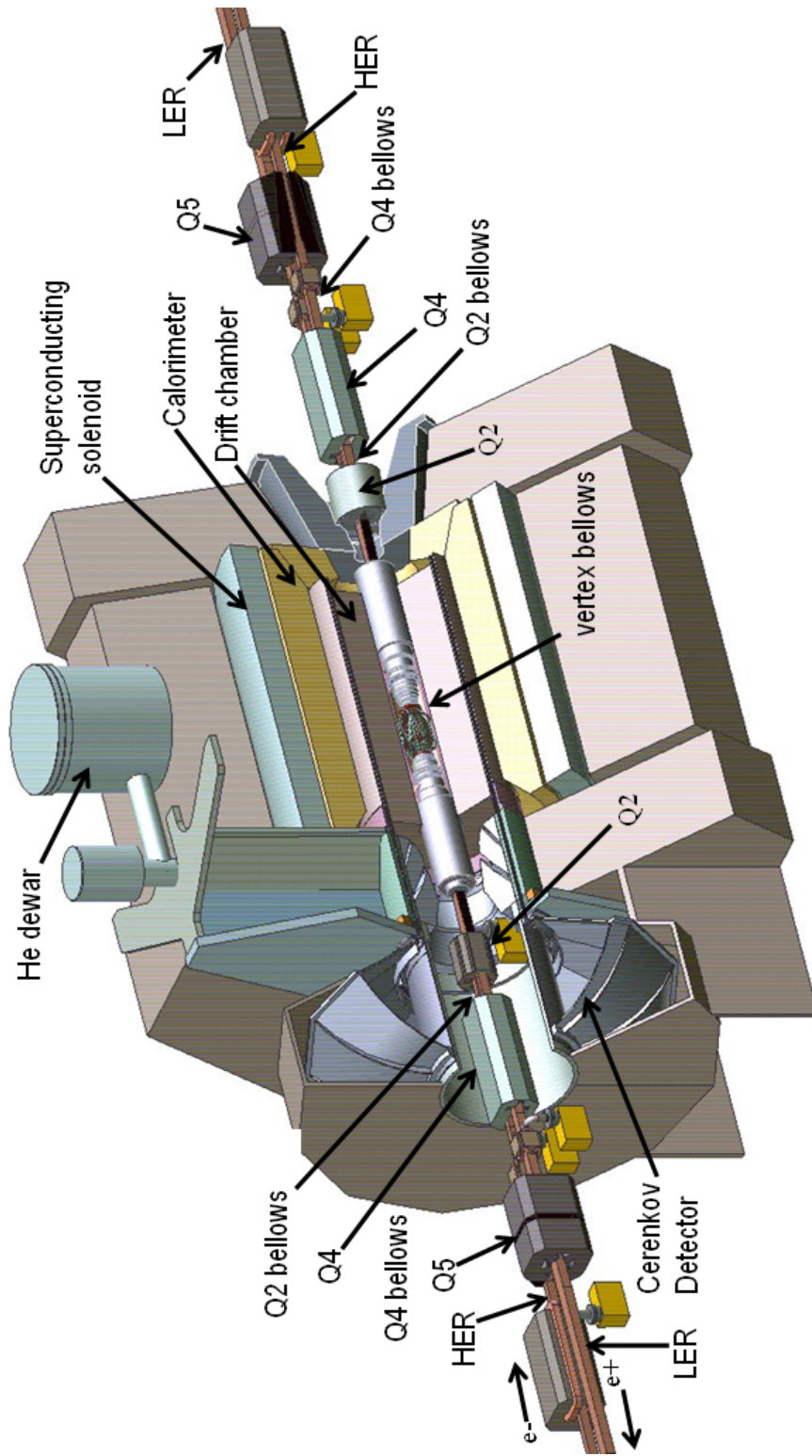


Figure 4.22. A 3D cut-away of the interaction region and the BaBar detector showing detector systems and combined magnet and vacuum chamber assemblies Q2, Q4, Q5 which are interconnected by bellows modules. The vertex bellows are situated well within the detector.

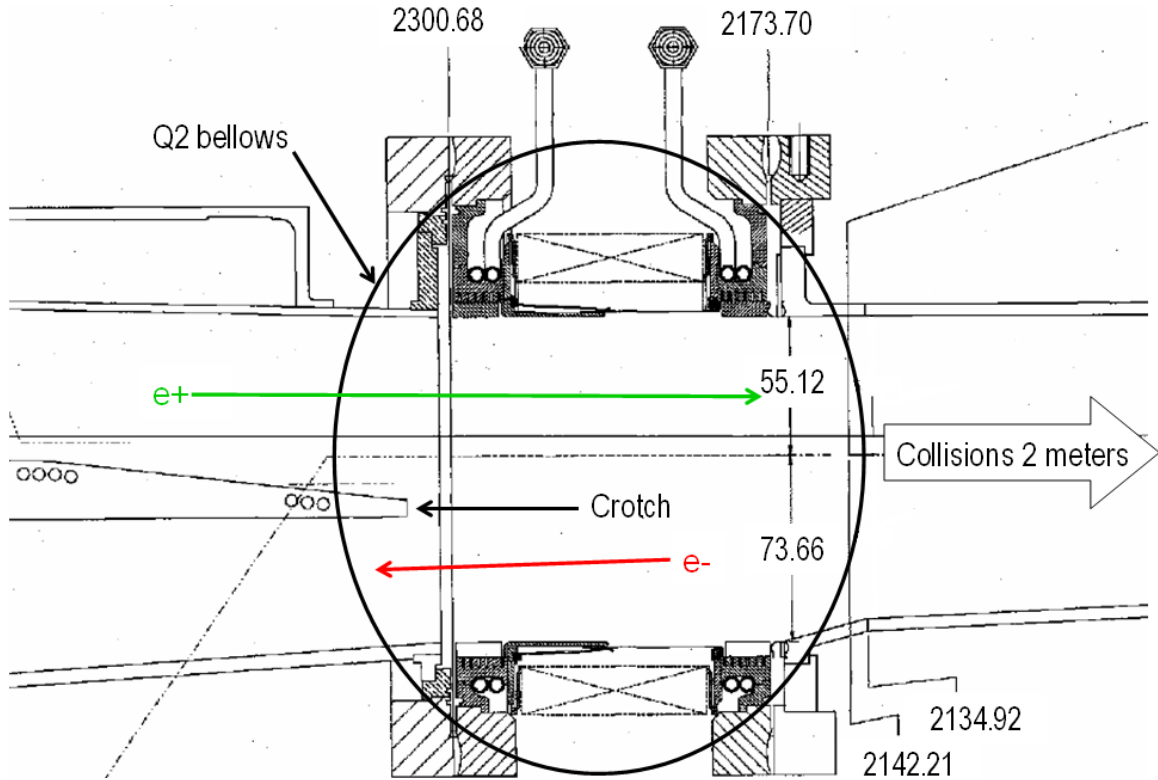


Figure 4.23. Mechanical drawing of Q2 bellows area. Q2 bellows is immediately adjacent to the crotch where the two beam lines merge. Dimensions are in mm.

#### 4.2.1 Q2 Bellows Absorber Device

HOMs are generated near the IP by the irregular beam chamber geometries, particularly at the crotch area where the two beam chambers meet. Figure 4.23 is a mechanical drawing depicting the local Q2 bellows area. The bellows is immediately adjacent to the crotch where the two beam lines meet. Collisions occur 2 meters to the right. Both beams traverse the region. The crotch is a strong source of HOMs.

The proximity of the Q2 bellows to the crotch prompted the introduction of ceramic absorbing tiles into the existing bellows module. Two arrays of ceramic tiles in the beam chamber are placed on either side of the Q2 bellows as shown in figure 4.24. The ceramic tiles are exposed directly to the beam fields. Our simplified model

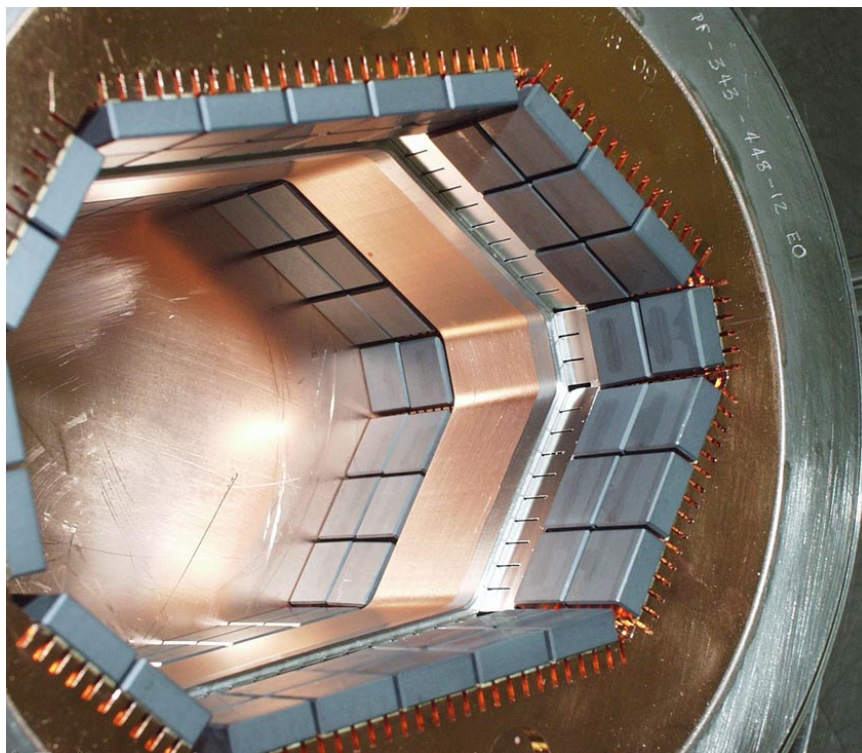


Figure 4.24. Existing Q2 bellows chamber with ceramic absorbing tiles braised to copper support columns. The bellows is located between the two sets of ceramic absorbing tiles. The tiles are fully exposed to the beam fields.

is shown in figure 4.25. The tile sections are 1.1 inches long and 0.47 inches thick composed of a ceramic dielectric of relative permittivity  $\epsilon_r = 30$  and loss tangent  $\tan\delta=0.11$ . The total length of the bellows and absorber is limited to 5 inches. The chamber is octagonal with dimensions 10.4 x 7.1 inches.

A scattering parameter analysis performed with monopole dipole and quadrupole waveguide modes for the existing configuration. The dipole mode has two orthogonal polarizations designated *dipole* and *dipole-* because of the aspect ratio of the chamber cross section. The absorption spectrum for the various modes are shown in figure 4.26 along with the waveguide mode electric field patterns and the computational model. The monopole mode absorption is excessive in the existing configuration and contributes to beam impedance.

Up to 10 kW of power is extracted from from the existing Q2 bellows based on cooling water flow and temperature for nominal running currents of 2.8 A LER positrons and 1.8 A HER electrons with 12 mm long bunches. For anticipated higher currents and shorter bunch lengths, the expected heating will exceed the present cooling capacity. As beam fields pass through the exposed absorbing tiles, Cherenkov radiation is produced, and becomes a source of power dissipation in the ceramic[12]. To reduce this power, a proposal to shield the tiles while retaining HOM absorption characteristics is put forth. This culminated in a new Q2 bellows design effort.

Based on the results of the straight bellows in section 4.1.3, a configuration of longitudinal coupling slots is adopted to preserve the monopole impedance and damp dipole and quadrupole modes. An obvious configuration would be to add slots to the existing array which is shown in figure 4.27. Two sets of short slots are provided above the ceramic absorbing tiles, one on either side of the bellows (not shown). This yields an absorption spectrum which leaves the monopole mode less affected, but with substantially reduced coupling for the dipole and quadrupole modes compared to the existing absorption of figure 4.26. While this reduces beam impedance, the uncoupled

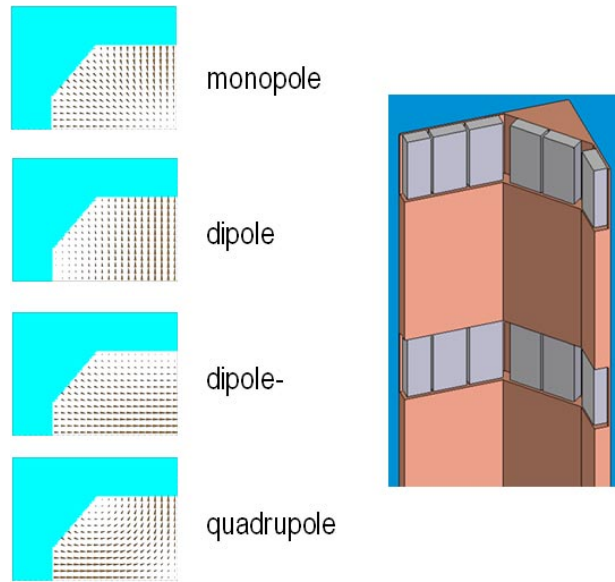


Figure 4.25. Existing Q2 bellows module computational scattering parameter model and the waveguide mode electric field patterns. There are two dipole mode polarizations designated *dipole* and *dipole-*. The bellows are not included.

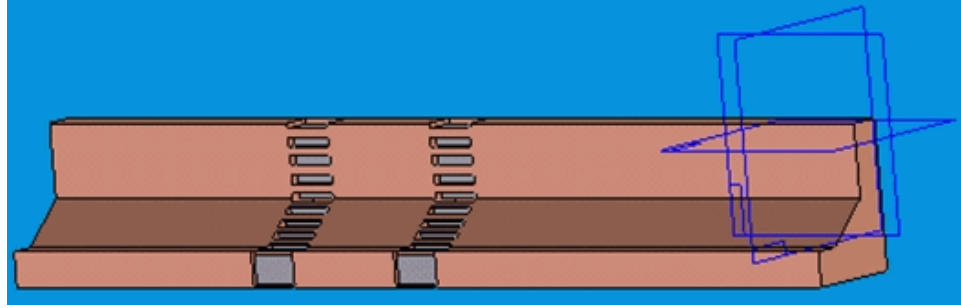


Figure 4.27. Computational model of existing Q2 bellows module with the addition of coupling slots above the absorbing tiles on both sides of the bellows (not shown).

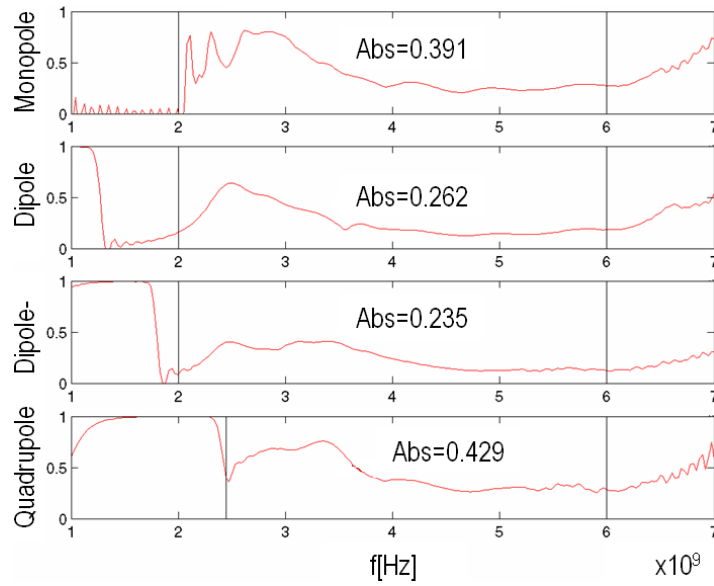


Figure 4.26. Absorption spectra for the existing Q2 chamber model (middle) of figure 4.25 for the monopole, dipole, dipole second polarization (dipole-) and quadrupole excitation. The absorption (abs=) is quantified as the mean of the absorption over the range contained within the vertical lines spanning the cutoff frequency and the highest excitation frequency. The high value for the monopole absorption indicates a potential for beam impedance.

dipole and quadrupole modes will deposit HOM power elsewhere, potentially coupling into the vertex bellows.

Dipole and quadrupole mode damping effectiveness scales with the contiguous

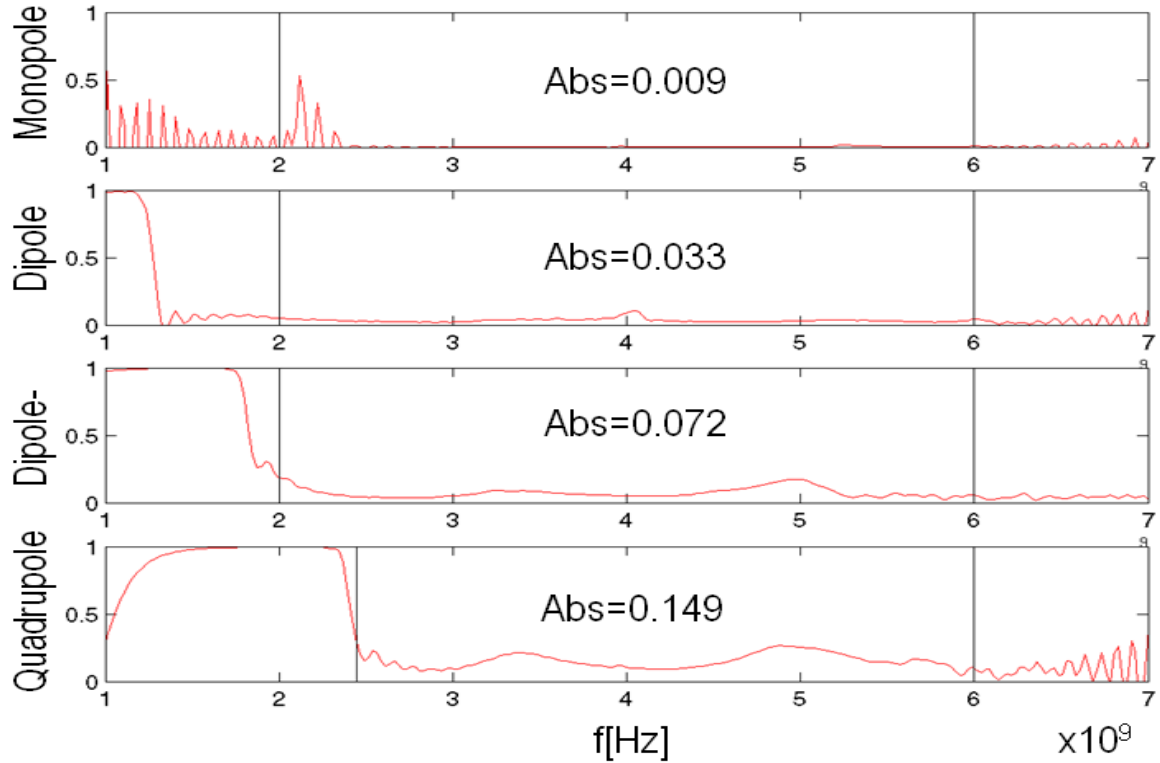


Figure 4.28. S-parameter absorption for the configuration of coupling slots added to the Q2 existing bellows model of figure 4.27. This configuration successfully reduces monopole mode absorption, but also reduces dipole and quadrupole mode absorption.

length of the longitudinal coupling slots. Longer slots also had the added benefit of reducing monopole mode absorption even further, so beam impedance is reduced. Since the length is restricted by the existence of the bellows, a new approach adapting the bellows as part of the absorbing structure is considered. This involves changing

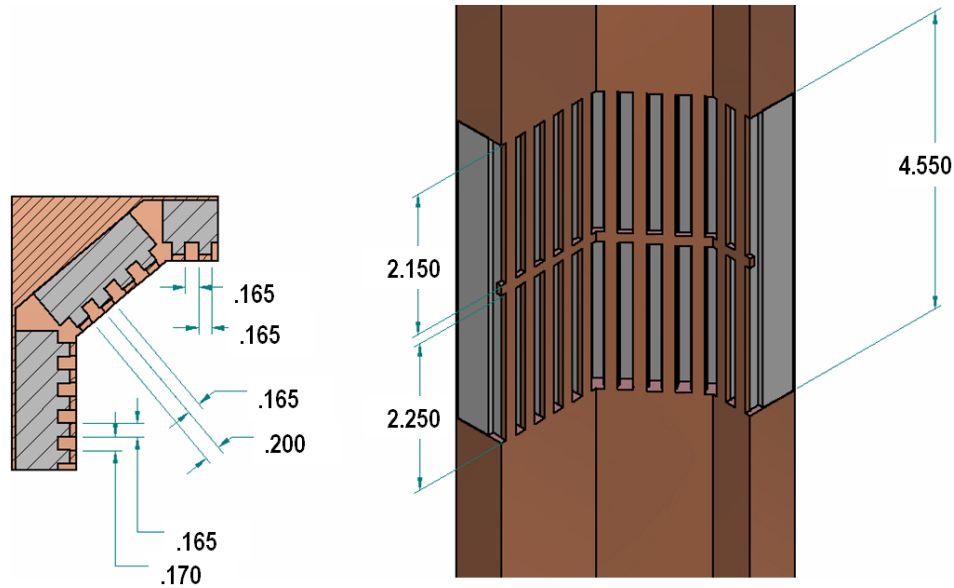


Figure 4.29. Computation model for incorporating coupling slot length into the bellows finger geometry with a center ring for structural support. Dimensions shown are in inches.

the bellows fingers to act as coupling slots by introducing spaces between them and adding absorbing material into the bellows chamber. This adds 2.2 inches to the effective slot and absorber length.

For structural considerations the long slots require axial support to prevent bending. A ring is added near the center of the slots for this purpose. Scattering analysis indicated an acceptable loss of effectiveness associated with the addition of the support ring. The computation model and s-parameter results for this configuration are shown in figures 4.29 and 4.30.

Results for several incarnations of the long slot configurations are summarized in figure 4.31, which shows the absorption of the dipole and quadrupole modes as a function of slot length. The monopole mode is not a factor since all configurations considered here have sufficiently low monopole absorption except for the existing exposed tile configuration. The absorption for the existing configuration (exposed tiles) is included (horizontal lines designated “open”) for comparison. The dipole1

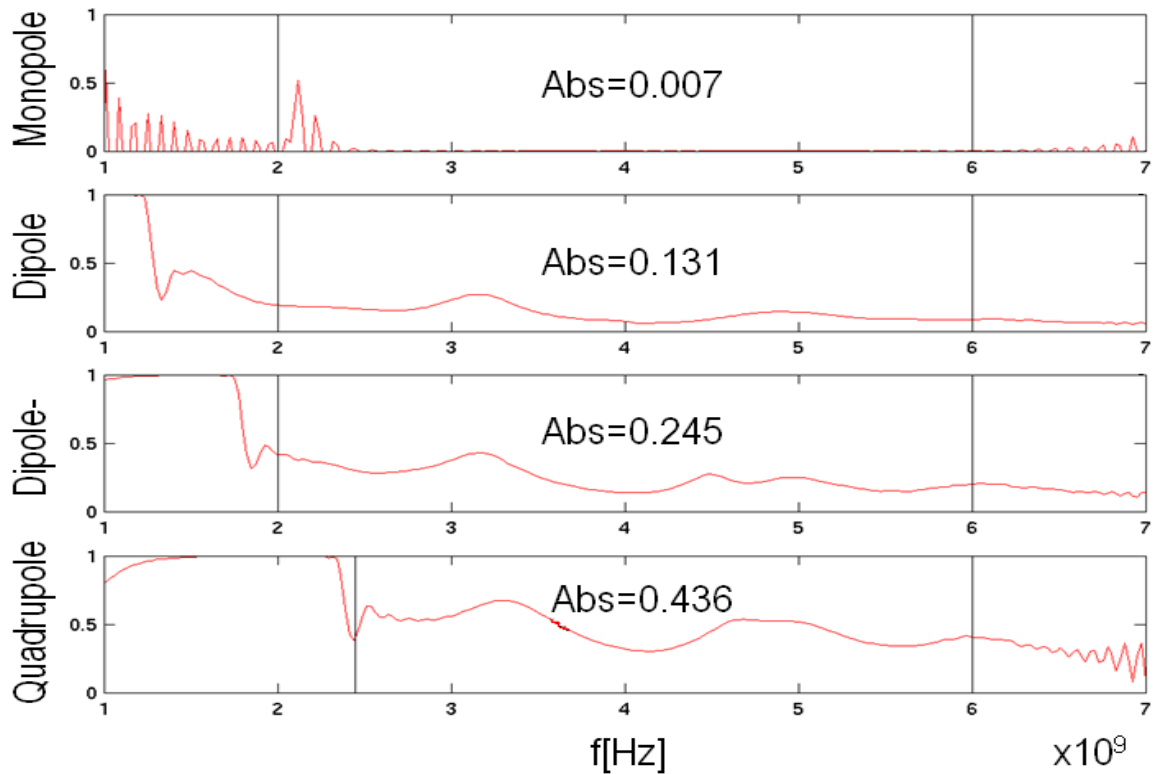


Figure 4.30. Absorption for the model of figure 4.29. The bellows shielding fingers are adapted to provide additional slot length to increase the effective dipole and quadrupole coupling.

and dipole2 represent the two dipole polarizations. The closed circles designate the adapted bellows finger slot configuration with a structural supporting ring model of figure 4.29. The effect of the ring results in a slight loss in absorption.

The feasible lengths are less than 5 inches (total available length) and the goal is to find a slot length which provides dipole and quadrupole absorption at comparable or higher levels than the existing exposed tile configuration. The slot length at which this is achieved is designated by the open circles in figure 4.31. To achieve the dipole mode absorption comparable to the existing configuration of exposed tiles, 6.5 inch coupling slots are required. The results indicate that given a long enough slot length the dipole and quadrupole modes can be effectively removed from the beam pipe with minimal impedance to the monopole mode.

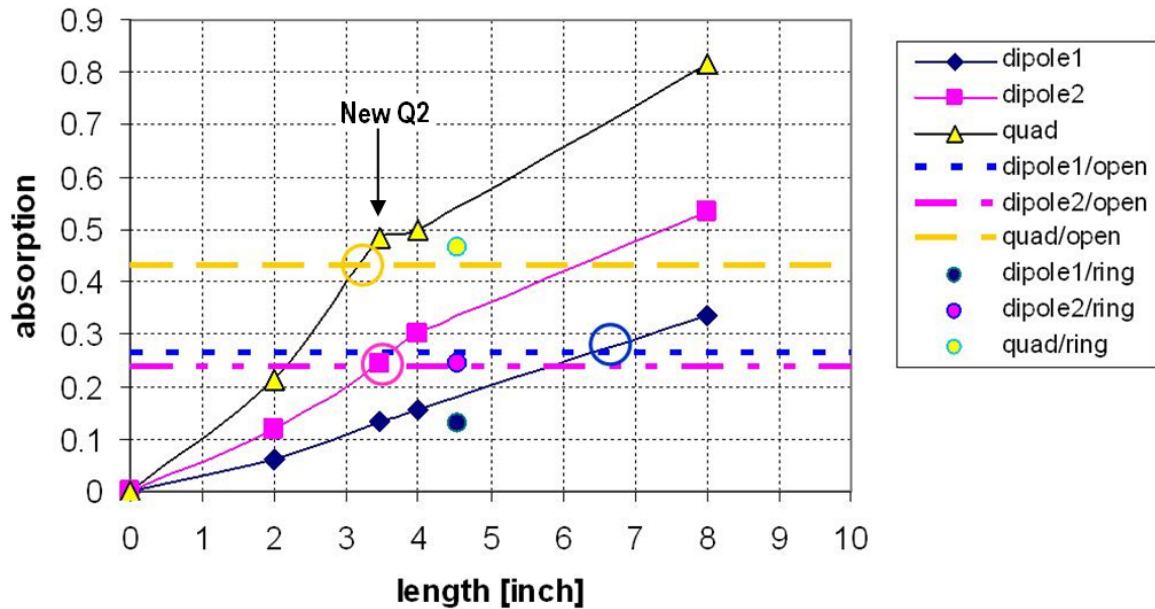


Figure 4.31. Summary of absorption vs slot length for both dipole modes and the quadrupole mode. The two dipole modes are designated dipole1 and dipole2. Horizontal dashed lines are existing exposed tile configuration absorption (/open). The open circles indicate slot length required to achieve existing absorption for each mode (break even). Small solid circles are the absorption values for the full slot length with the structural support ring configuration of figure 4.29.

The mechanical complexity of incorporating slots in the bellows fingers proved to be impractical, and a less effective design will be used which essentially involves consolidating the absorber material and slot length by moving the bellows to one side of the device, providing space for 3.4 inch absorbing slots. This device is depicted in figure 4.32. Referring to figure 4.31 this configuration achieves absorption for the dipole2 (long axis polarization) and quadrupole modes comparable to the existing open exposed configuration, but falls below the existing absorption for the short axis polarization dipole mode at 15% vs 26%.

Two such devices were produced and installed in Q2 chambers on either side of the IP. Preliminary results indicate a factor of 4-6 reduction in extracted HOM power relative to the exposed absorber configuration at equivalent currents. This is expected,

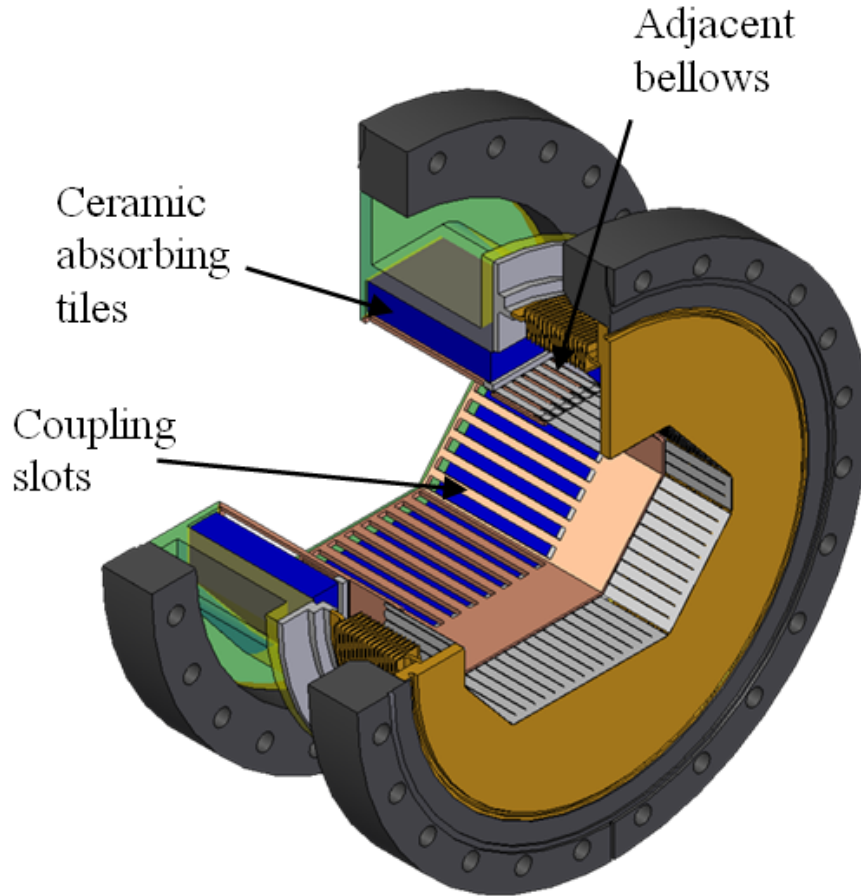


Figure 4.32. New Q2 bellows HOM absorbing device. Bellows is moved to one side to consolidate slot and absorber length. Ceramic absorbing material is depicted in blue. Coupling slots are 3.4 inches long.

since much less monopole mode power is coupled out. Although full currents have not been achieved, the vertex bellows, situated inboard of the Q2 bellows, are not experiencing any unusual temperature rise. Thus the uncaptured monopole power which now propagates into the IP is not coupling to the vertex bellows. Additionally, the reduced short axis dipole mode absorption doesn't appear to pose a threat to the vertex bellows.

### 4.2.2 High Efficiency Absorber for the Interaction Region

The Q2 bellows scattering parameter analysis of section 4.2.1 suggests the possibility of devising a very high efficiency absorber device with minimal beam impedance where space is available for long slots. This is the case for specific beam line locations slightly outboard of the IP region where space allows for longer and wider devices without the need to incorporate bellows in the design. The IP region vacuum chambers have non-unity aspect ratios which give two dipole mode polarizations with different absorption profiles. This was also an issue in the Q2 bellows scattering parameter analysis. Figure 4.33 shows a model based on extending the Q2 bellows concept, along with scattering parameter absorption results and the waveguide modes. Slot width is 0.095 to 0.35 inches. Slot length is 8.39 inches. The device is transparent to the monopole mode.

The short axis dipole mode exhibits the least amount of absorption. This can be understood from the nature of dipole mode propagation. The magnetic field component of the dipole mode is longitudinal and maximum at the mid-plane which cuts the electric fields perpendicularly to the electric field polarization direction. The transverse electric fields will align along the width of the slots which together with the longitudinal magnetic field at this area results in a Poynting vector suitable for coupling through the slots. The fraction of slots which see this field combination differs for the two dipole mode polarizations. The short axis polarization has the smaller number of slots exposed to these field regions.

The short axis polarization dipole absorption can be enhanced with slot length and absorber geometry modifications. One modification is to simply increase the thickness of the absorber along the short axis. The second modification is to lengthen the slots. The optimized configuration is shown in figure 4.34. along with scattering parameter absorption spectrum. To facilitate fabrication the absorber volume in the corner is removed.

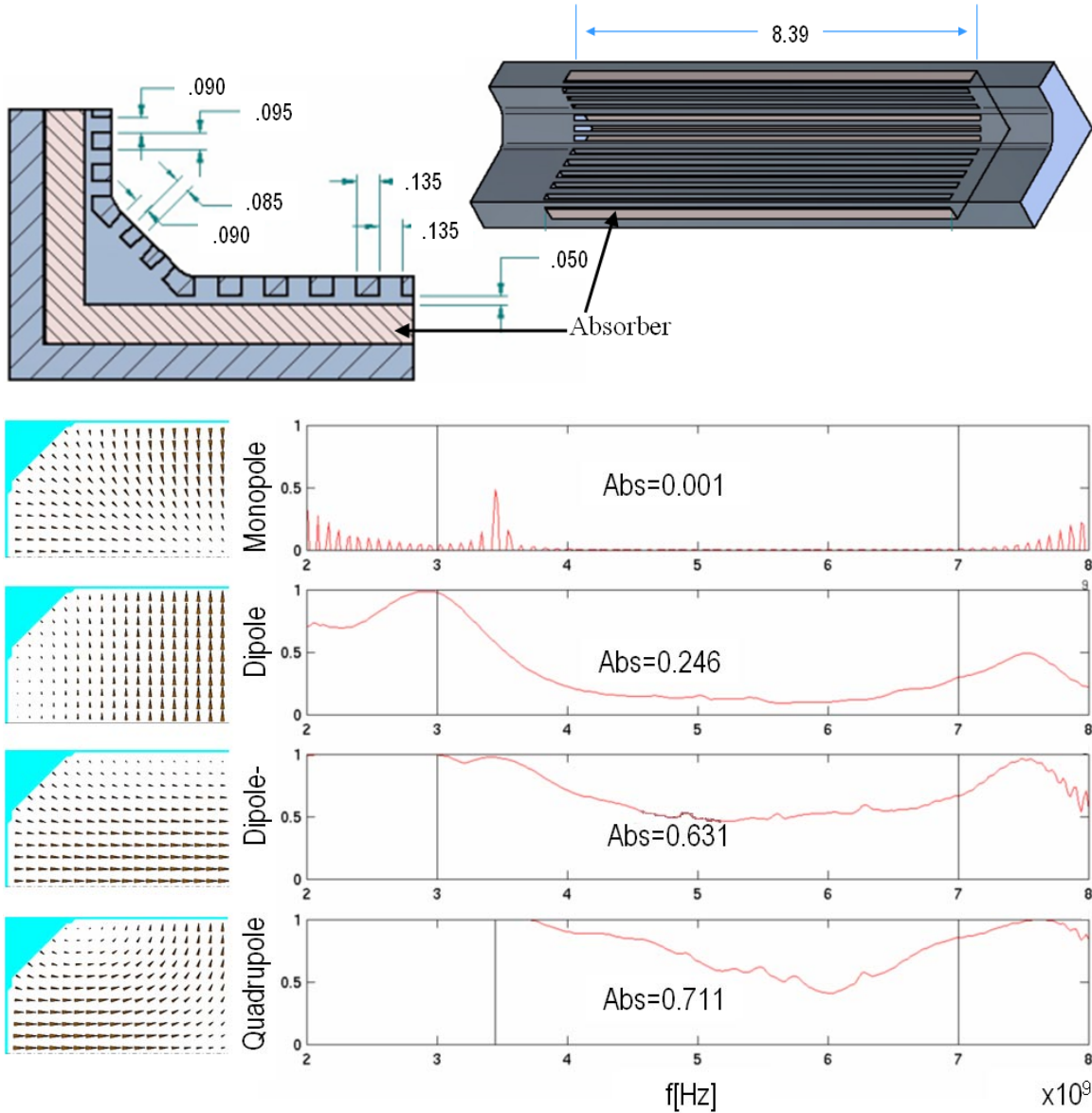


Figure 4.33. High efficiency absorber device model (top) and absorption spectra (bottom). Slot length 8.3 inches, slot width 0.09-0.13 inches. Absorber thickness is 0.23 inches. Dimensions are in inches. The short axis dipole mode is not well absorbed at only 25% compared to the long axis absorption of 63%.

This model preserves the transparency to the monopole mode and increases absorption for all the other modes. It is the basis for the mechanical design shown in figure 4.35. The mechanical design incorporates absorbing tiles brazed to copper support columns which are embedded in a copper heat sink with water cooling channels.

Two such devices are fabricated and deployed in the LER IP region, where space is available. A photo of one device as installed is shown in figure 4.36.

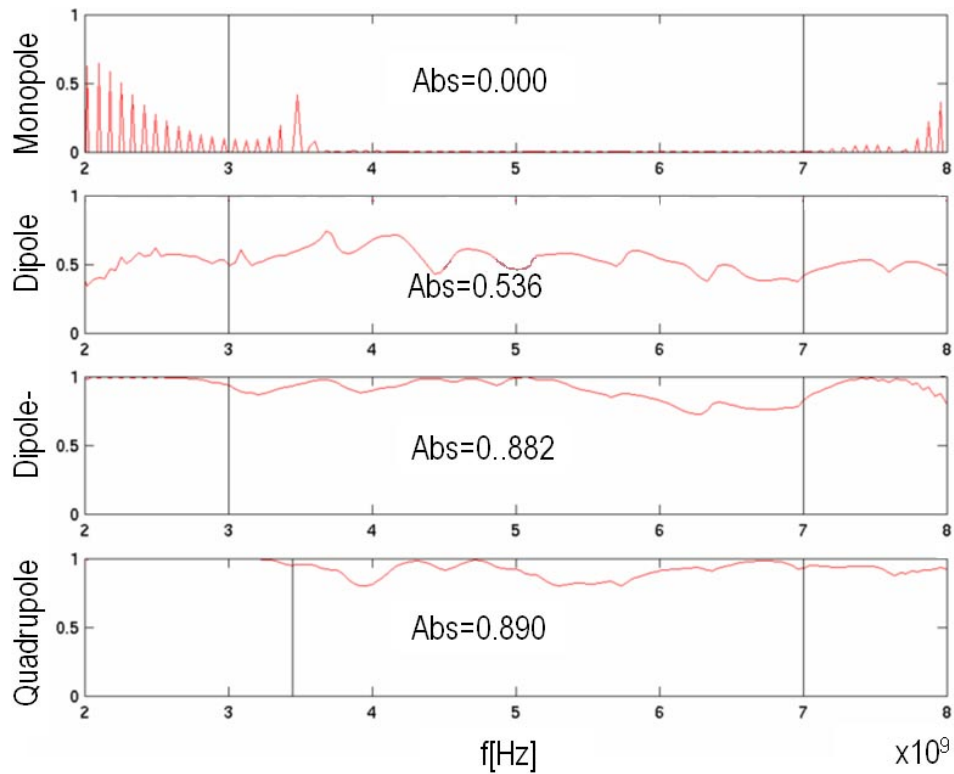
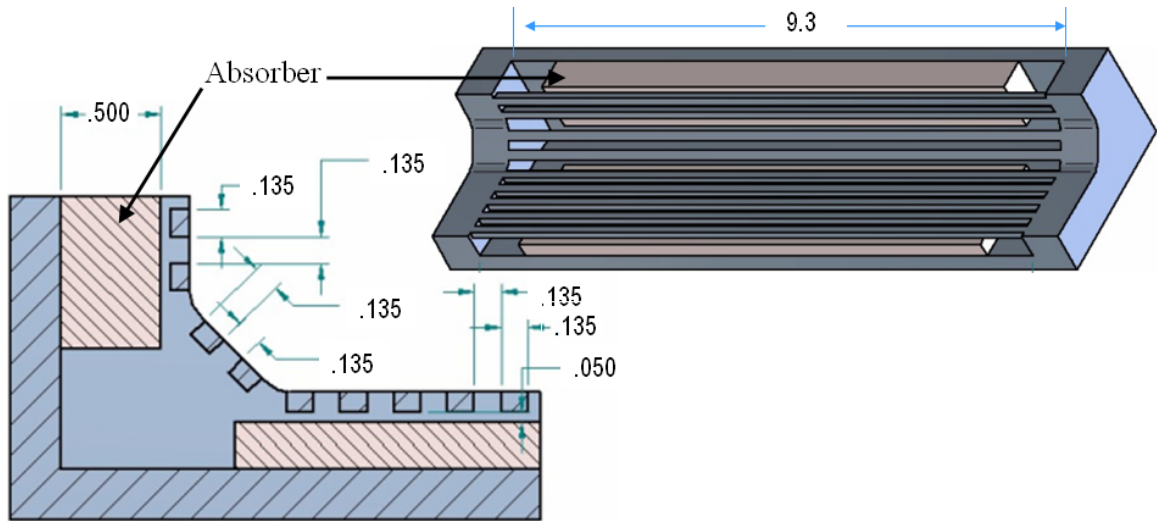


Figure 4.34. Optimized high efficiency absorbing device (top). Modified slot length, and absorber geometry to enhance short axis dipole absorption. Slot length is 9.3 inches. Slot width 0.09 to 0.13 inches. Absorber thickness 0.5 inches at the short axis, 0.23 inches at the long axis. Absorber volume is removed at the corner to simplify fabrication. This device features 54% short axis dipole mode absorption (bottom).

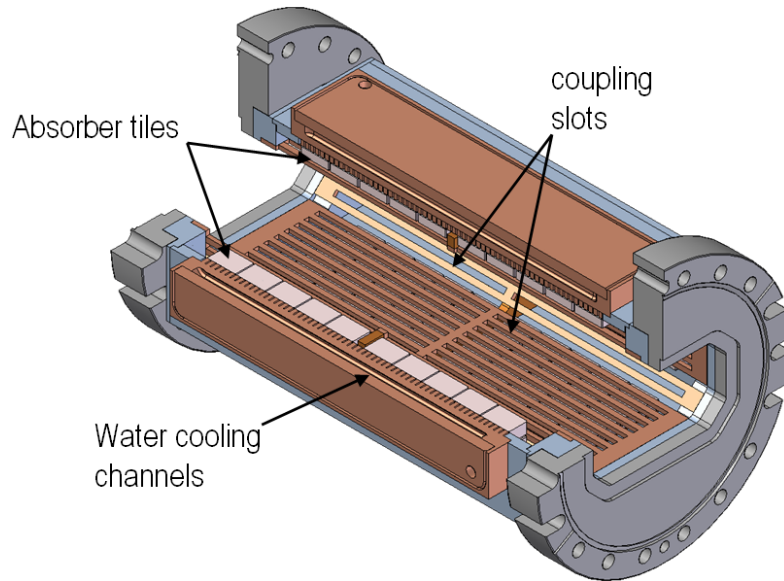


Figure 4.35. Mechanical drawing of high efficiency absorbing device based on optimized model of figure 4.34 Absorbing tiles are brazed to copper support columns embedded in a copper block with water cooling channels.

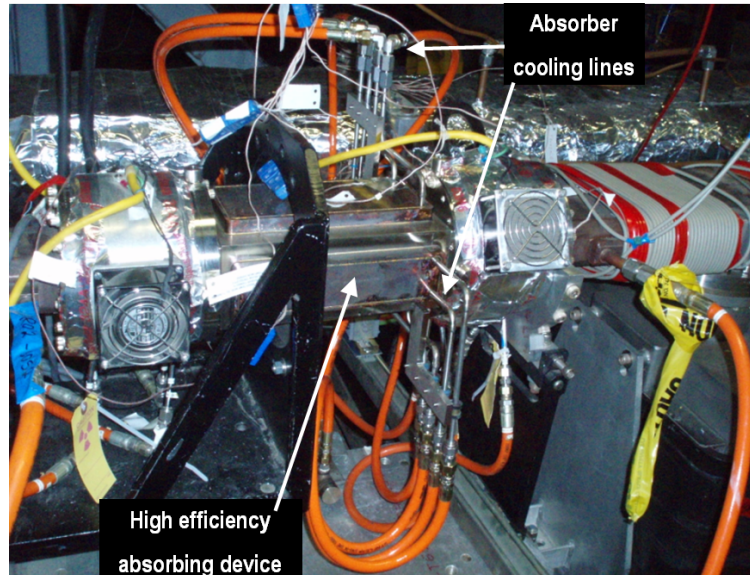


Figure 4.36. Photograph of installed high efficiency absorbing device in the upstream LER interaction region. The device is flanked by two bellows modules which are cooled by external fans. The high efficiency absorber is expected to reduce heating of a nearby NEG pumping chamber.

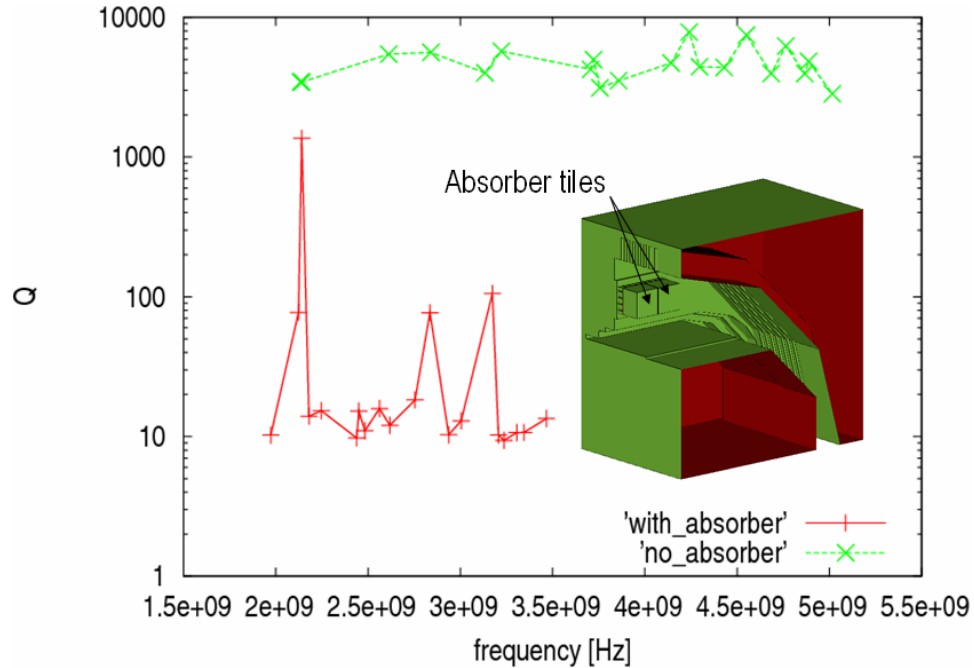


Figure 4.37. Q4 bellows model version 3 and quality factors with and without absorber.

### 4.2.3 LER Q4 Bellows Absorber

The LER Q4/Q5 bellows is situated between the Q4 and Q5 vacuum chamber assemblies and allows for relative mechanical motion between the two chambers from thermal gradients caused by synchrotron radiation. As with all bellows in the interaction area there is the potential for HOM induced heating. Studies were initiated into the possibility of introducing a water cooled lossy material in the bellows cavity. Using Ceradyne[59] ceramic material parameters of relative permittivity  $\epsilon_r = 30$  and loss tangent  $\tan\delta = 0.11$ , quality factors for several modes are computed for a two absorber model of the LER Q4 bellows according to the method of section 3.2.2. These results are shown in figure 4.37 along with the quality factors for the bellows with no absorber for comparison. Most modes are damped.

One particular mode at 2.14 GHz is not well damped. Figure 4.38 shows the electric field distribution for this mode which shows substantial field in the area far

**Q=1361**  
**2.14 GHz**

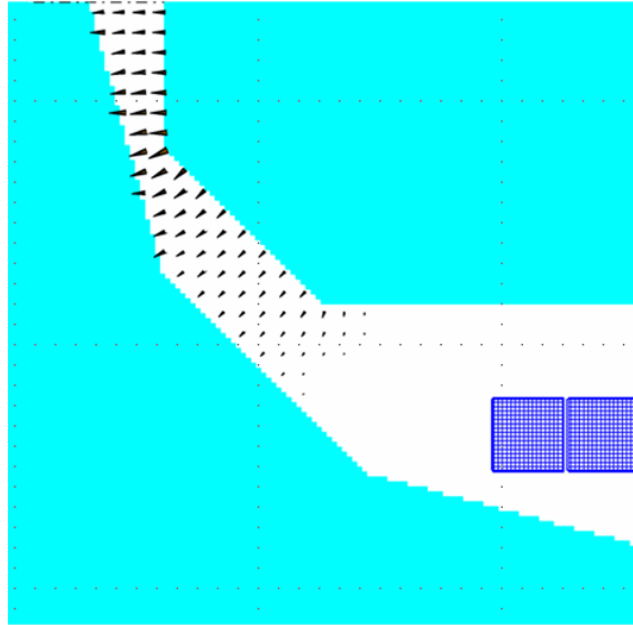


Figure 4.38. Electric field plot of 2.14 GHz high  $Q$  mode in the Q4 bellows model version 3. High field strength is far from absorbing tiles.

from the absorbers.

Additional ceramic is added in the model and the analysis repeated. Figure 4.39 shows the new model and results. Although the added ceramic is not at the area of high field, it is close enough to disturb the high  $Q$  mode, and trap more fields in the absorber. After mechanical design a new bellows module based on model version 5 was built and installed in the downstream LER beam line. A mechanical drawing and photo of the installed module is shown in figure 4.40. About 100 Watts of power is extracted from this device at LER currents of 2.0 Amps. This indicates transverse modes are not a problem at this location.

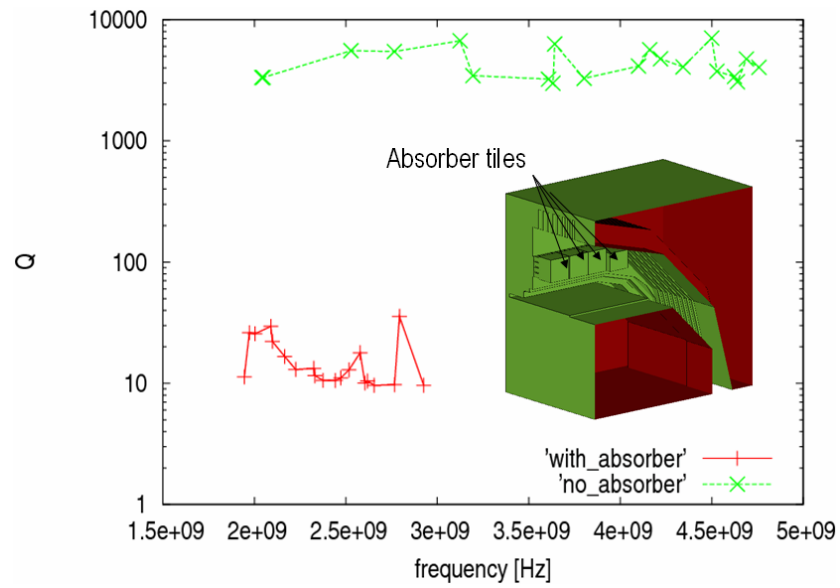


Figure 4.39. Q4 bellows model version 5 and quality factors with and without absorber.

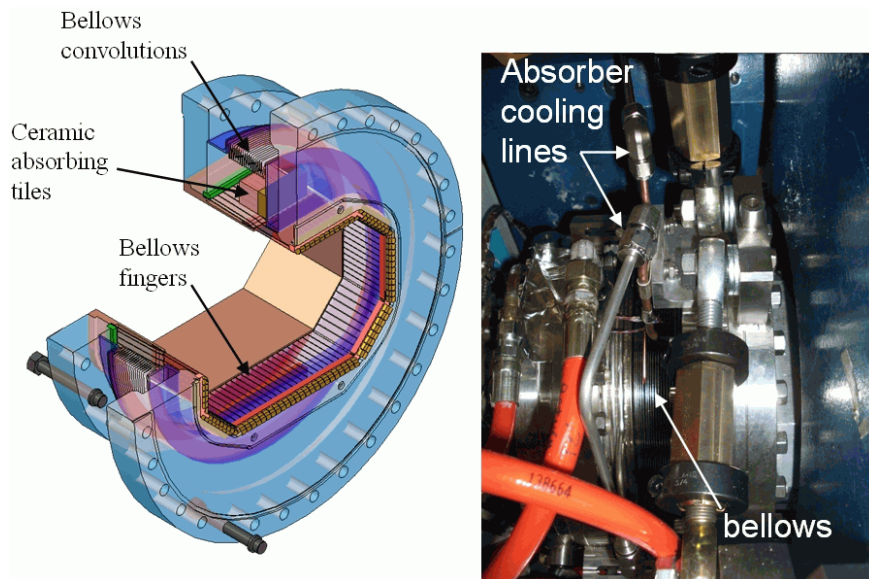


Figure 4.40. Mechanical design for the Q4 bellows absorbing device. Photo of installed Q4 bellows absorbing device at the downstream LER side of the IP.

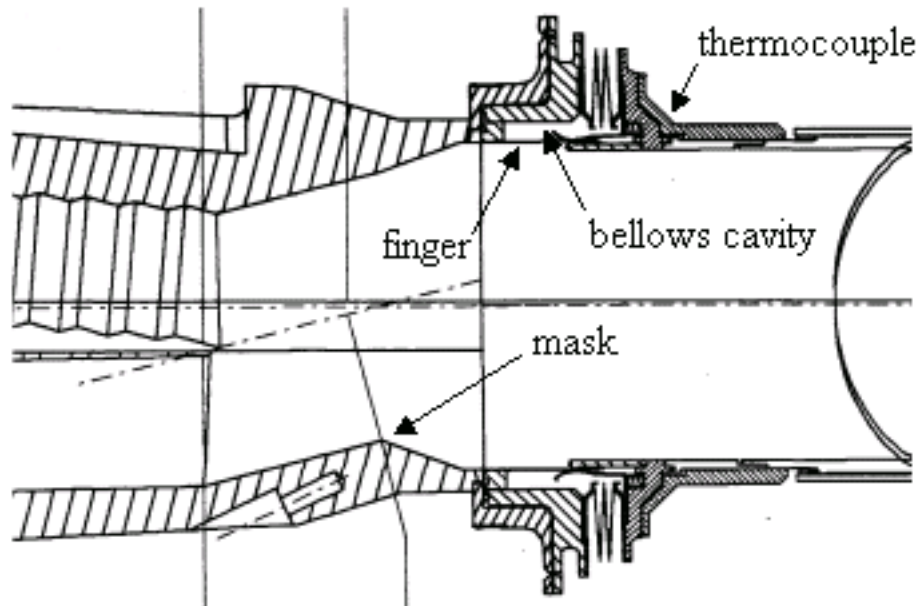
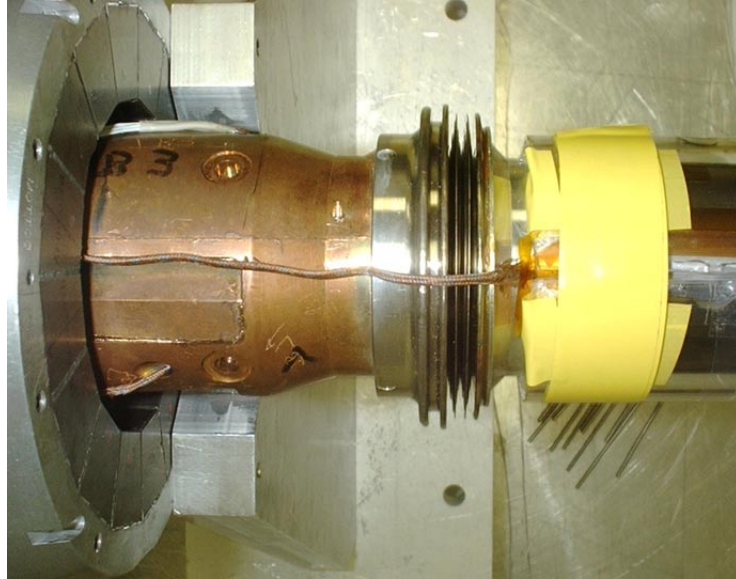


Figure 4.41. Vertex bellows picture and schematic. Collisions occur 20 cm to the right of the bellows. Beam pipe diameter is about 5 cm.

#### 4.2.4 Vertex Bellows Absorber

The vertex bellows are situated on either side of a beryllium beam pipe embedded in the center of the BaBar detector where the collisions take place. In this area both beams traverse a common vacuum chamber in opposite directions. The beam pipe

diameter is 5 cm. The length of the bellows cavity is 2.2 cm.

Temperature studies determined HOM power was responsible for vertex bellows heating[24]. Based on cooling water flow and temperature it is estimated that 0.5 kW of HOM power couples into the bellows at 2.4 A positron and 1.6-1.7 A electrons[23]. For future operation at up to 4 Ampere currents this extrapolates to 2.0 kW. This power would be dissipated in the walls of the cavity bellows which has a total volume of approximately 15 cm<sup>3</sup>. As calculations will show, dissipated power will not be uniformly distributed and tends to concentrate in the bellows convolutions.

Measurements of the electromagnetic spectrum of wake fields from a nearby beam position monitor (BPM) indicated several modes showing amplitude correlation with vertex bellows temperature at around 4-5 GHz[7]. These measurements are shown in figure 4.42. The signal was obtained during a small gap (100 ns machine protection abort kicker gap) in the temporal distribution of bunches so that only the wake fields of both bunch trains are sampled.

To repair damage or upgrade these bellows requires dismantling the BaBar detector which is a time consuming and labor intensive prospect. The last major machine upgrade included additional external cooling in the form of chilled air and water flow, however this does nothing to reduce the amount of coupled power infiltrating the bellows, and the projected power levels exceed the present cooling capacity. The following sections detail analysis of bellows cavity modes and a study of the coupling mechanism. A method to remove the coupled power efficiently and safely is introduced.

#### **4.2.5 Vertex Bellows 2-Dimensional Calculations**

Eigenmode calculations are performed for the vertex bellows cavity using MAFIA[13] and NOVO[14]. The fingers and beam chamber are not modelled in this calculation. The geometry is cylindrically symmetric. Several modes are found in the frequency range of 5-6 GHz. They are: monopole, dipole and quadrupole modes according to

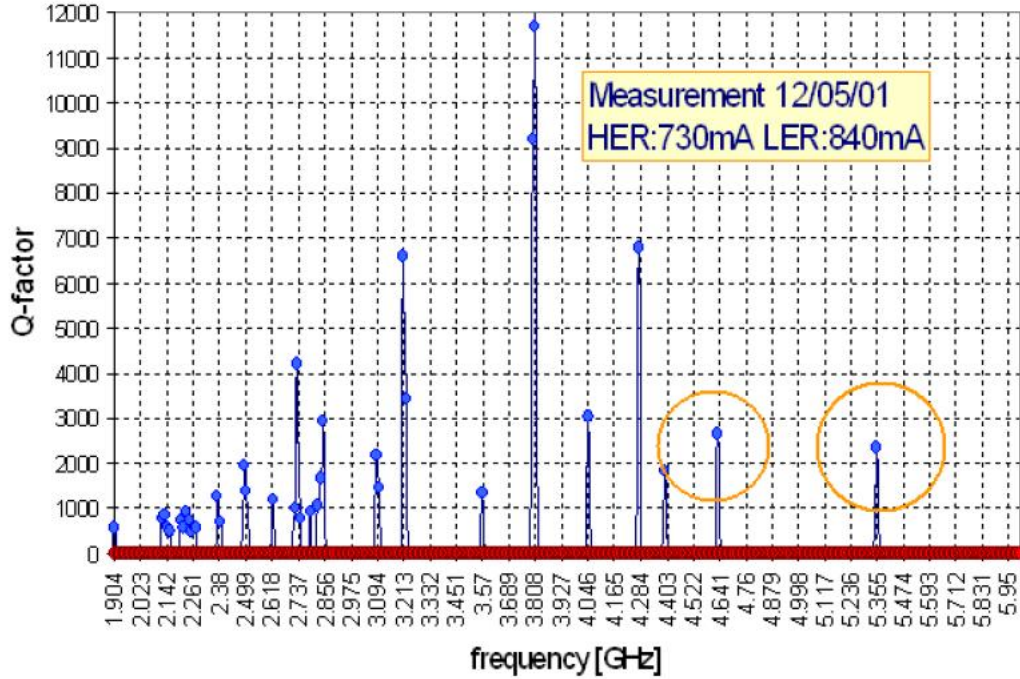


Figure 4.42. FFT of a gated oscilloscope BPM button signal in the gap between bunch trains. The circled peaks at 4.6 and 5.4 GHz show amplitude correlation with the vertex bellows thermocouple temperature. Courtesy A. Novokhatski.

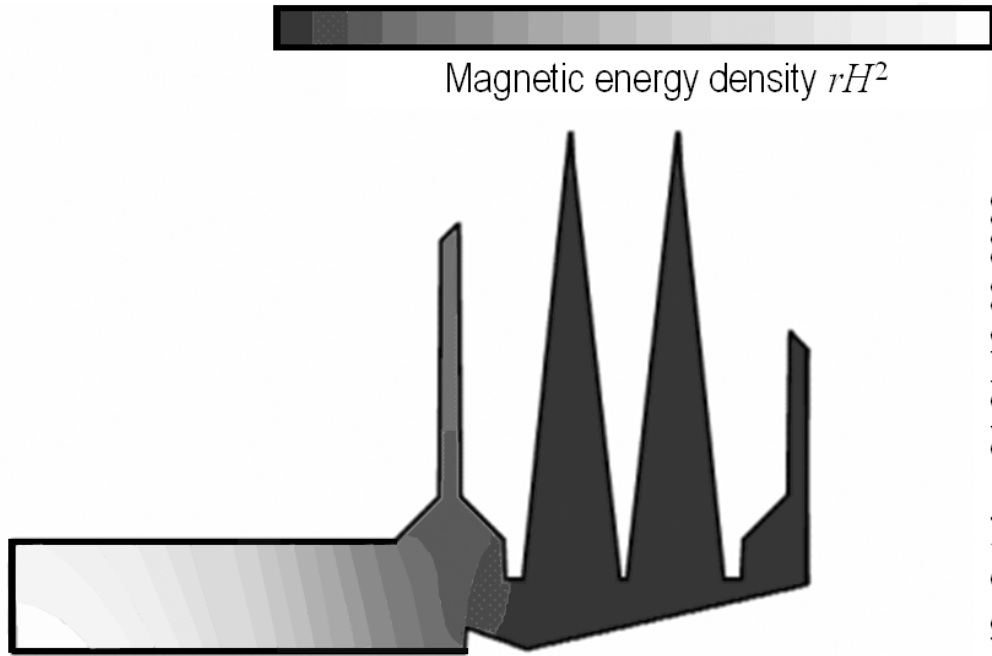
monopole	4.75 GHz	7.22 GHz	8.05 GHz
dipole	5.46 GHz	8.37 GHz	9.44 GHz
quadrupole	6.19 GHz	8.82 GHz	9.78 GHz

Table 4.1. Mode frequencies for the vertex bellows cavity. The second and third column frequencies correspond to additional nodes in the longitudinal dimension. The calculation assumes cylindrical symmetry.

field variation in the azimuthal dimension. Frequencies of the first few modes are given in table 4.1.

The monopole mode is computed using a proprietary code NOVO[14]. Dipole and quadrupole modes are obtained with MAFIA[13]. The magnetic field energy density for the monopole, dipole and quadrupole modes integrated over the azimuthal angle  $\phi$  are shown in figures 4.43- 4.45. There is high energy density at the bottom of the bellows convolutions for the dipole and quadrupole cases. Magnetic field patterns at

IP Bellows model (open 9 mm between flanges)



NOVO: Sat Aug 24 21:13:08 2002

Wavelength=63.21mm RxZ=46.05x22.25 Frequency= 4.746 GHz

Figure 4.43. Monopole mode magnetic field energy density integrated over  $2\pi$  radians of azimuth calculated with the NOVO[14] program. Lighter shades are higher density.

$\phi = 0$  and  $\phi = \pi/2$  are shown in figure 4.46 for the dipole case. The high magnetic energy density corresponds to regions of large longitudinal magnetic flux as predicted from the coax model of section 3.2.3.1 and occurs  $\pi$  radians apart in the azimuthal dimension for the dipole and  $\pi/2$  radians for the quadrupole case. The resistive heating will exhibit this same azimuthal dependence and will be substantial near the bellows convolutions.

Monopole mode coupling occurs only under exceptional conditions as stated in section 3.2.3.1. The dipole and quadrupole modes exhibit the proper field orientation for coupling. It should be stressed that calculations are done with a fixed bellows length which in practice will change with expansion and contraction of vacuum chambers. At high beam currents thermal stresses tend to shorten the bellows length thereby raising the resonance frequency of these modes. With added currents and smaller

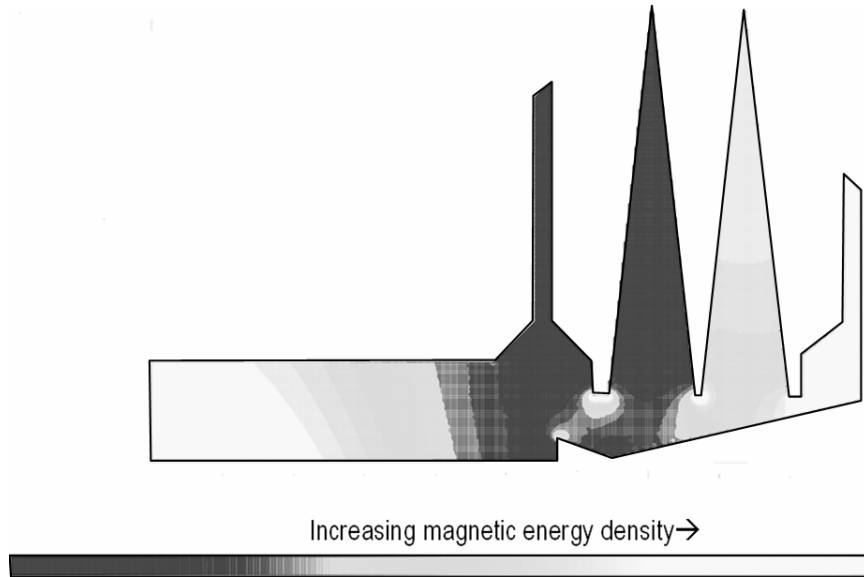


Figure 4.44. Dipole mode magnetic field energy density integrated over  $2\pi$  radians of azimuth calculated with MAFIA[13]. The highest intensity is at bellows convolutions.

bunch lengths necessary for maximum luminosity, the bellows excitation frequencies will increase and shorter bunches will drive these higher frequency modes.

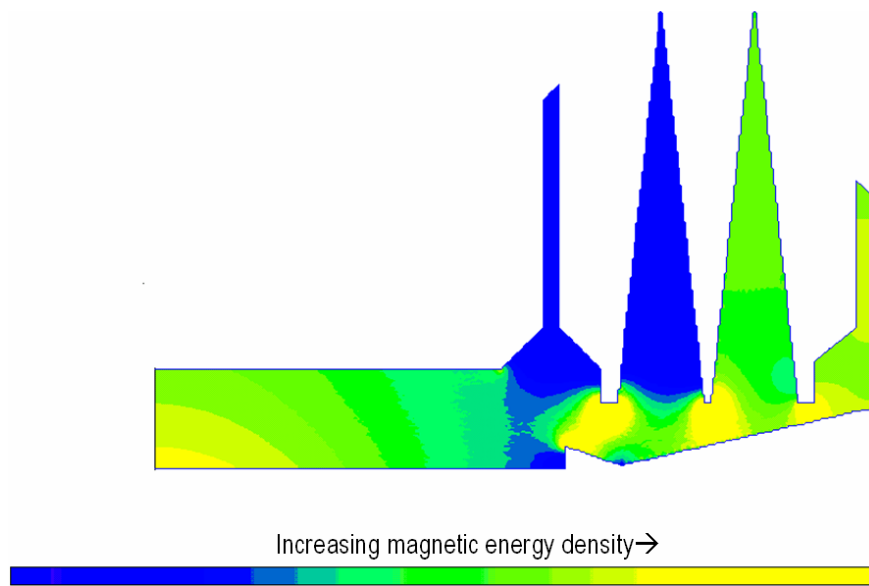
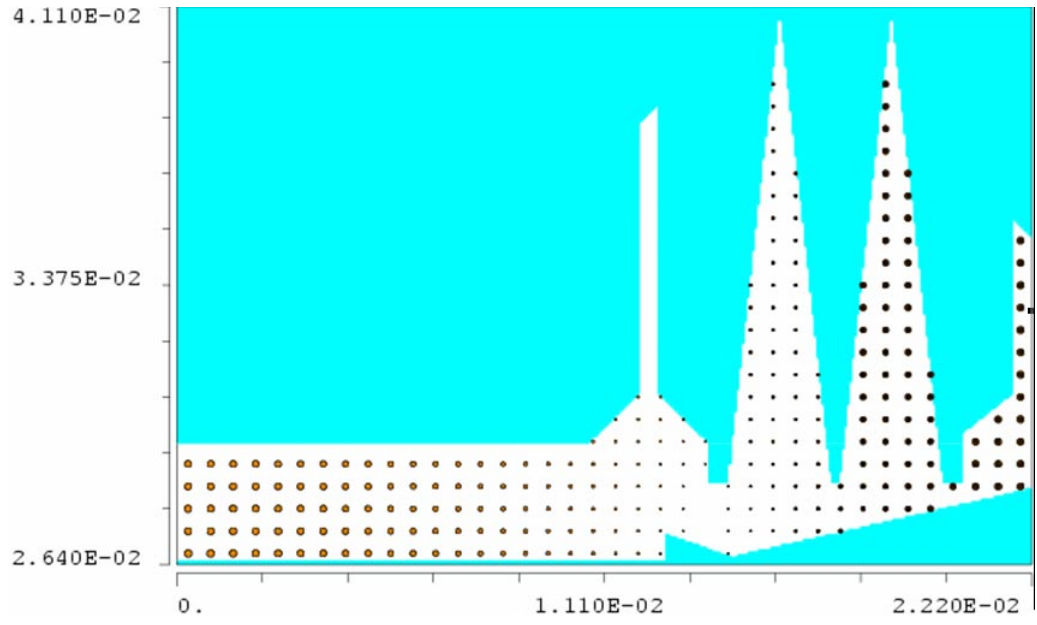
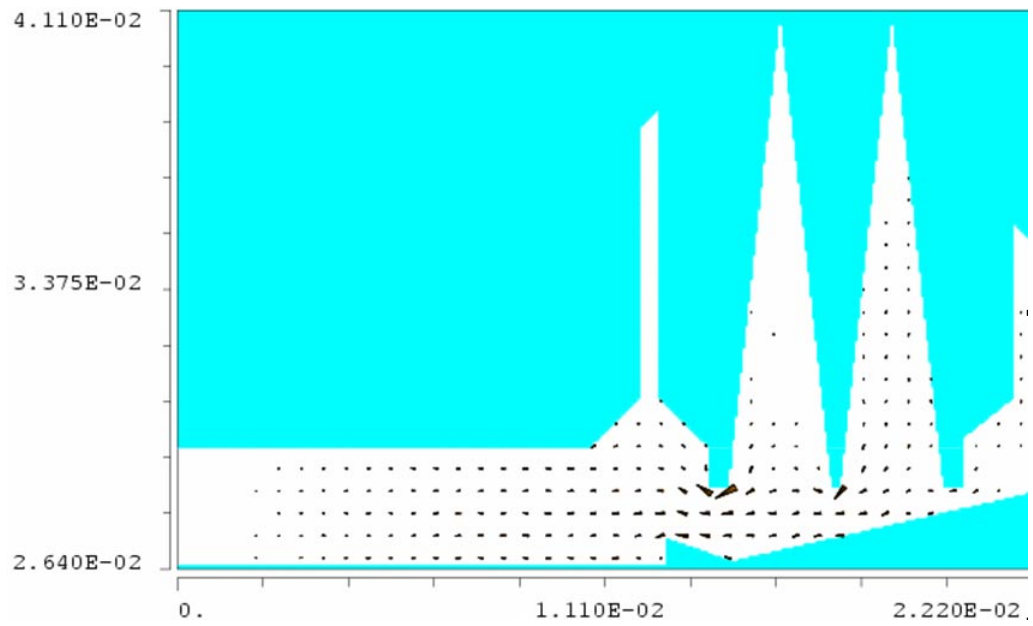


Figure 4.45. Quadrupole magnetic field energy density integrated over  $2\pi$  radians of azimuth calculated with MAFIA[13]. The highest intensity is at the bellows convolutions.



$\phi = 0$



$\phi = \pi/2$

Figure 4.46. Magnetic field patterns at two azimuthal planes  $\phi = 0$  and  $\phi = \pi/2$ , illustrating high intensity at regions of longitudinal variation for the dipole mode.

#### 4.2.6 IP Vertex Bellows Q Factors

When HOMs couple into the IP vertex bellows the degree of resistive heating depends strongly on the quality factors ( $Q$  factors) of the excited modes. Reduction in  $Q$  factors of the bellows modes can be accomplished by the introduction of a lossy absorbing material into the cavity. A lossy absorbing material with a high relative permittivity/permeability has the effect of drawing field into the material and thus is more effective in  $Q$  factor reduction. The power is now dissipated in the lossy material instead of sensitive bellows components. Dedicated water cooling will safely remove this electromagnetic power.

This scheme works for either a high permittivity lossy dielectric or high permeable lossy magnetic material when strategically placed to intercept the proper fields. The absorber of choice is a commercial ceramic with a complex dielectric constant manufactured by Ceradyne, Inc.[59]. It has a large relative permittivity  $\epsilon_r = 30$  and loss tangent  $\tan \delta = 0.11$  in the low GHz regime. SLAC has had extensive fabrication experience with these ceramics.

To gauge the effectiveness of an absorber configuration the  $Q$  factors of the existing vertex bellows are evaluated in the same manner as was done in section 3.2.2. For this purpose the bellows material is given the conductivity of stainless steel. The existing bellows  $Q$  factors for stainless steel are displayed in figure 4.47 along with the 3d model used in the calculation.

The variation of quality factors depend on the mode field distribution in the cavity volume. Fields intensity in the bellows convolution region of high surface to volume ratios are more attenuated and thus have the correspondingly lower  $Q$  factors.

#### 4.2.7 Introduction of Absorbing Media in the Existing Vertex Bellows

Studies with the existing bellows structure focused on finding the most effective placement of absorbing material within the bellows cavity confines for optimized  $Q$  value

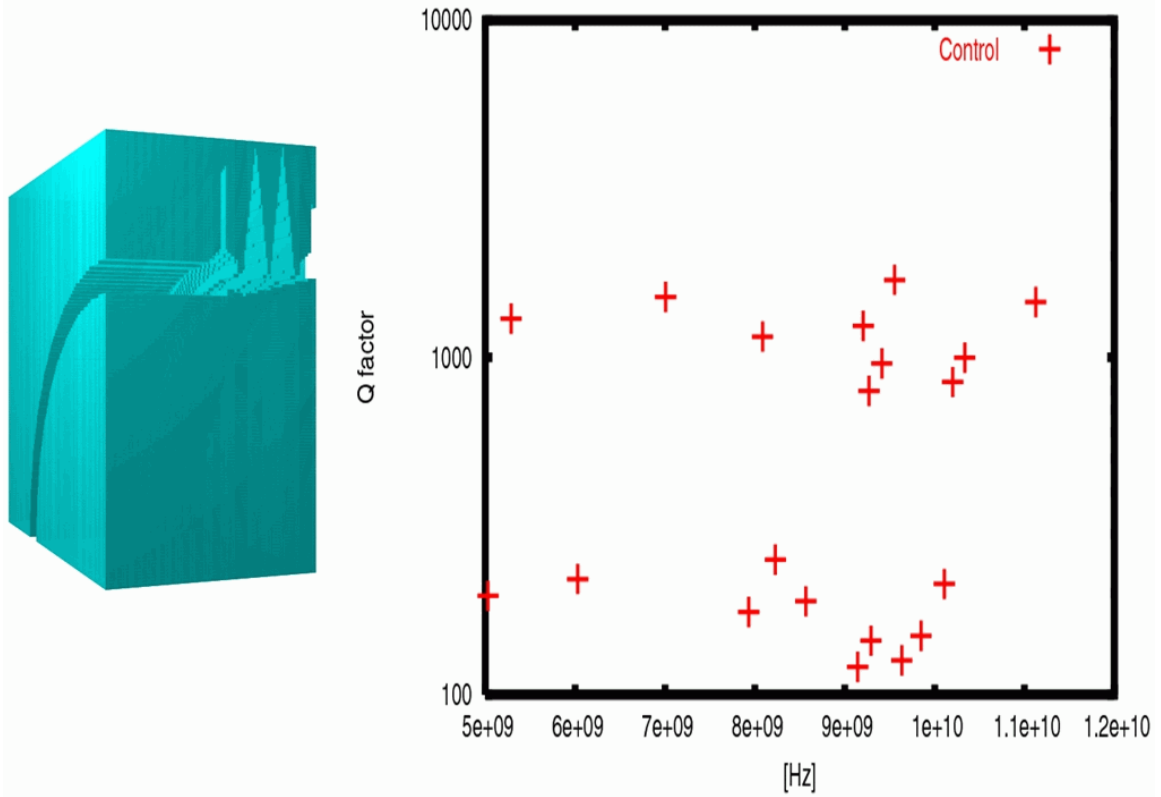


Figure 4.47. Existing vertex bellows model (Control) eigenmode and  $Q$  factors assuming stainless steel material.

reduction. Three locations are studied: Two at opposing flange locations and one above the fingers. Mechanical movement and deformations which occur in the fingers and bellows convolutions make these areas unsuitable for placement of a ceramic absorbing material. The absorber is modelled as a ring of dielectric of high relative permittivity  $\epsilon_r = 30$  with a loss tangent of 0.11. Many modes are found which are confined (or trapped) in the absorber accounting for  $Q$  values of around 9. This was anticipated in section 3.2.2 for a volume of absorbing material with such high permittivity. These are not considered to be damped vertex bellows modes but instead are new modes generated in the absorber.

Figures 4.48-4.51 show the absorber configurations and their  $Q$  factor comparison with the existing bellows. The configuration of figure 4.51 is the most successful at

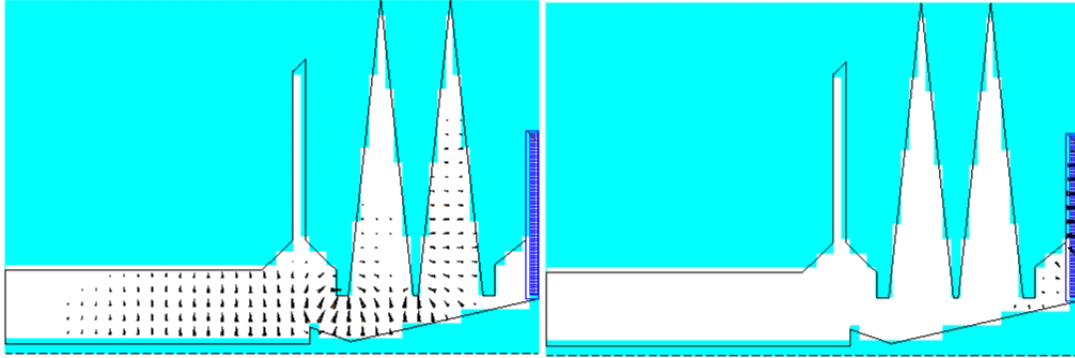


Figure 4.48. Modes calculated for absorber placed near bellows convolutions. The absorber material is shown as a cross section of an annular ring or washer of ceramic absorbing material placed on a flange near the bellows convolutions. Left picture shows a mode which the absorber does not touch and consequently is not damped. Right picture shows a low frequency mode trapped in the absorber. Bellows walls assumed to have the conductivity of copper.  $Q$  values for this configuration are given in figure 4.53.

damping the existing modes. Figure 4.51 includes  $Q$  factor calculations for absorbers

of various thicknesses and indicates all modes can be well damped given enough absorber thickness. Bellows walls are assumed to have the conductivity of copper for

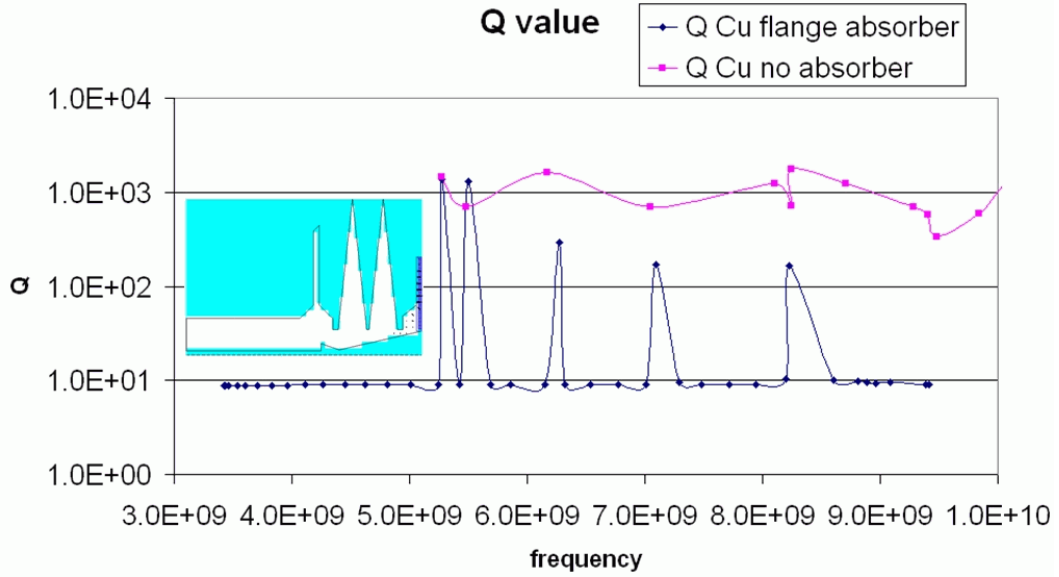


Figure 4.49.  $Q$  factors for absorber placed near bellows convolution flange and the existing control configuration with no absorber. Existing vertex bellows modes are not appreciably damped. Lower frequency low  $Q$  modes are new modes trapped in the absorber. Bellows walls assumed to have the conductivity of copper.

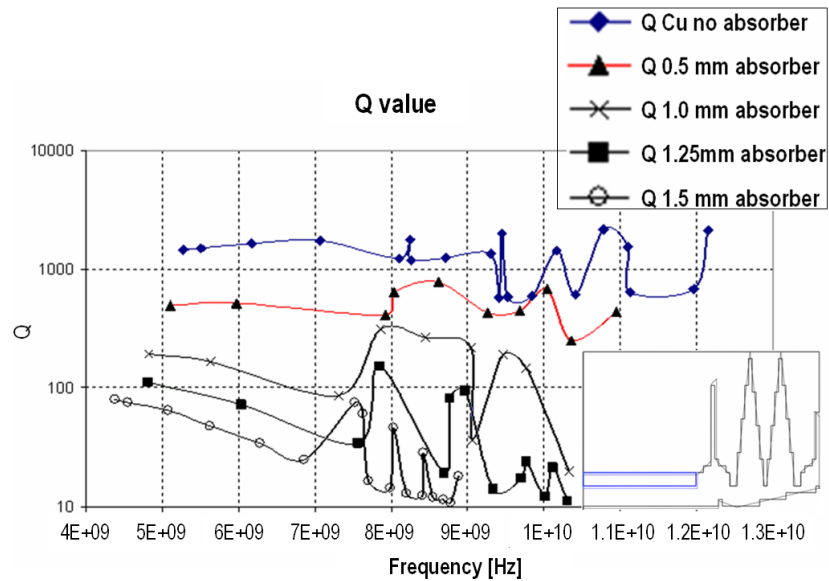


Figure 4.51. Absorber above fingers (inset) and comparison of  $Q$  factors. This configuration works best to damp existing bellows modes.  $Q$  factors with absorbers of various radial thickness are presented, indicating better damping is achieved with progressively thicker absorbers. Bellows walls assumed to have the conductivity of copper.

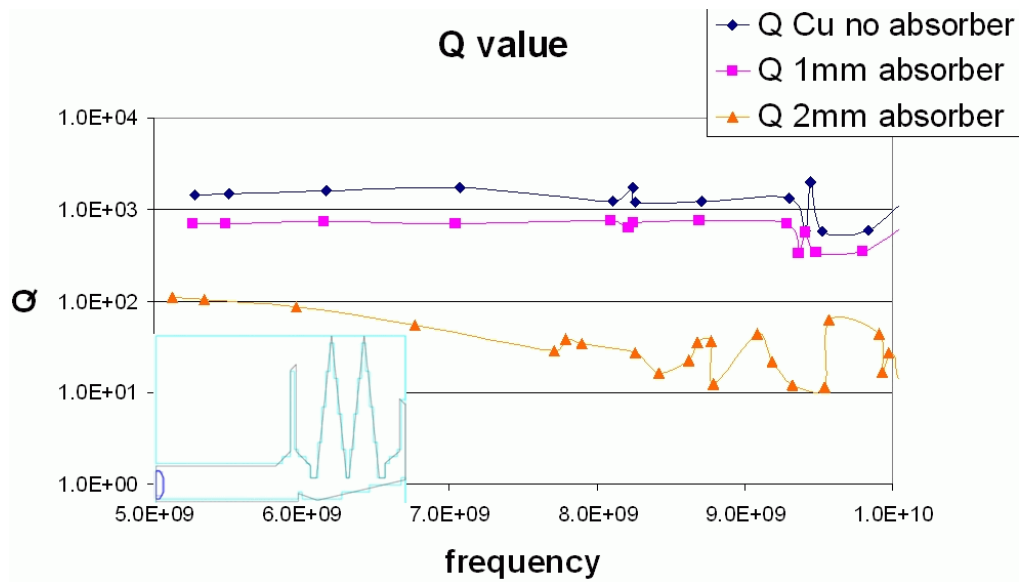


Figure 4.50. Absorber on flange near fingers (inset) and effect on Cu bellows  $Q$  factors. Data shown with absorber thickness of one and two millimeters. Most of the existing  $Q$  factors are not appreciably damped in this configuration. Bellows walls assumed to have the conductivity of copper.

this study. Most low frequency bellows modes have electric fields near the fingers which accounts for the successful damping achieved with the absorber placed above the fingers.

### 4.2.8 New Vertex Bellows Proposals

New prototype vertex bellows designs were investigated based on the studies of section 4.2.7. These designs incorporate additional volume to house and provide water cooling for the absorbing material within the space constraints imposed by the location within the BaBar detector. The absorber is situated above the fingers and made as thick as possible. For proper support and thermal cooling efficiency the absorber is mounted on a series of copper support columns which direct heat out of the absorber to external water cooling lines. These support columns flex to provide relief for thermal expansion differences between the absorber material and the copper interface. The absorber is to be braised directly to the support columns. Two models of these designs are shown in figure 4.52. The difference in configuration is in the shape of the absorber and the modifications of the bellows cavity to house the absorber. They are distinguished based on the ratio of the longitudinal and radial dimensions and given the *large aspect ratio* and *small aspect ratio* designations. The small aspect ratio dimensions are 4.8 x 6.5 mm in the  $r$ - $z$  plane. Likewise, the large aspect ratio dimensions are 2.5 x 8.7 mm.

The absorber is positioned to best damp low frequency modes and where thermal conduction to external cooling lines is facilitated.

Assuming a ceramic absorber of relative permittivity  $\epsilon_r = 30$  and loss tangent  $\tan\delta = 0.11$  and a stainless steel bellows, quality factors are evaluated and displayed in figure 4.53 along with the existing stainless steel bellows quality factors (Control +).

Both configurations exhibit excellent damping abilities of one to two order of magnitude. The small aspect absorber proves to be the best candidate for damping modes, however a thermal analysis indicated cooling efficiency is inadequate for the small aspect ratio configuration. Mechanical design has completed and the large aspect ratio prototype is in production.

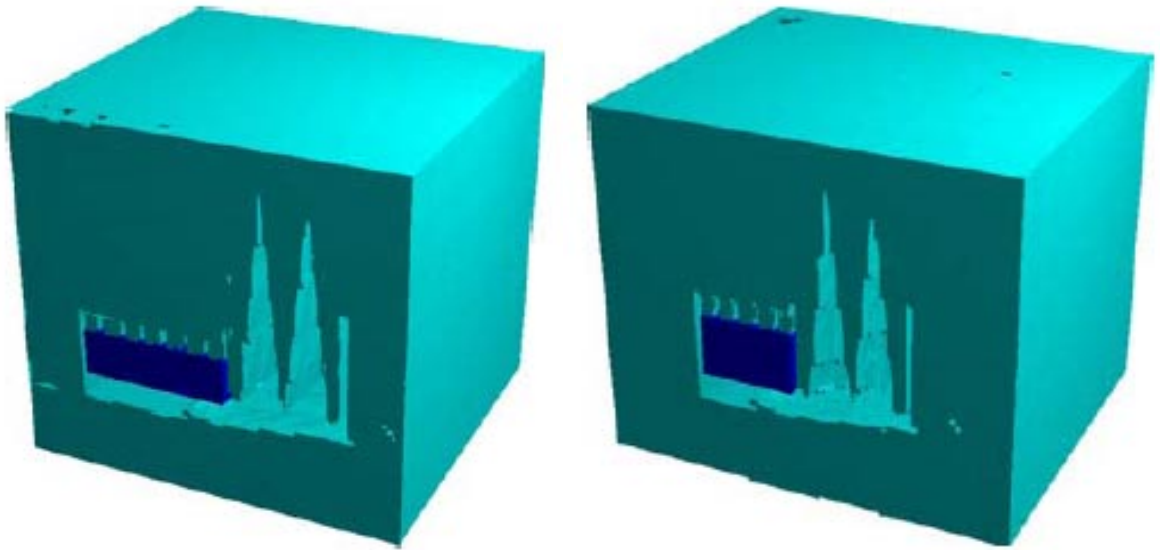


Figure 4.52. Large (left) and small (right) aspect ratio absorber configuration models for the vertex bellows. The absorbing ceramic is shown supported by copper columns which aid in thermal stress relief and thermal conductivity.

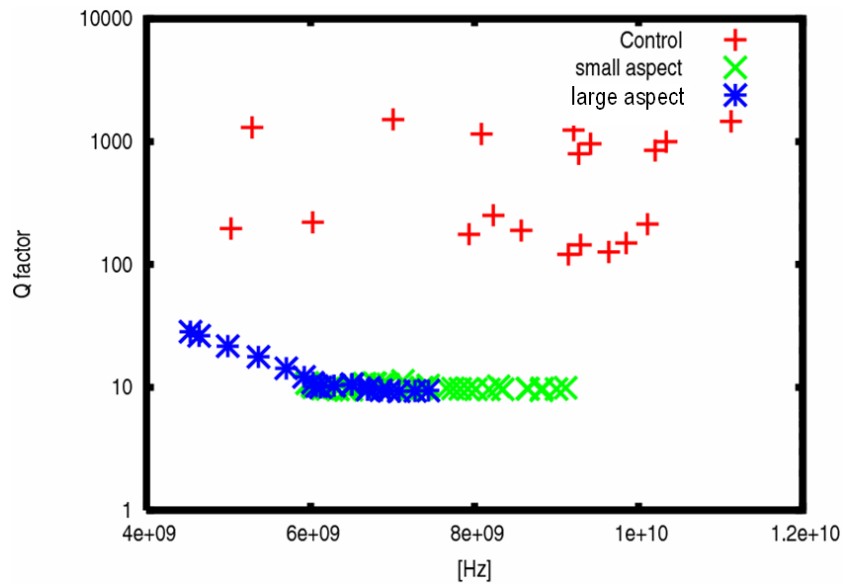


Figure 4.53.  $Q$  factors vs frequency for the stainless steel vertex bellows absorber configurations large (\*) and small (x) aspect along with existing bellows  $Q$  factors (Control +).

## Chapter 5

### Conclusion

As bunch current intensities increase to meet storage ring physics demands, it has become apparent that wake field effects have been underestimated. Contemporary beam vacuum chamber technology has not been able to deal with HOM power at such high bunch currents. An important understanding of how HOMs are produced and how they couple into accelerator components has been achieved. With this understanding new strategies are developed to remove HOM energy from beam line components as well as selectively couple out dangerous HOM species from the beam chamber before they couple into beam line components.

Collimators have been identified as the source of observed HOM heating. HOM heating in the LER straight to arc transition area is 10-20 meters downstream of the collimator region. Wake field calculations and experimental observations confirm collimator HOM power propagating to this remote location and depositing energy there. The calculations indicate HOM propagation in the form of dipole and quadrupole fields. Rather than introduce HOM damping in all the affected pumps, bellows and ante-chambers, a method of intercepting and absorbing propagating HOMs is proposed. Results of the coupling studies presented in this dissertation suggests a device which selectively encourages coupling of dipole and quadrupole modes from the beam chamber. To minimize the impedance to the beam, monopole mode coupling is

discouraged. The design process involved scattering parameter analysis which allows individually tailoring a device response by mode type. The trapped mode power is transformed into heat by an array of high permittivity lossy dielectric tiles which have dedicated water cooling. The device was built and installed just upstream of the LER straight to arc transition and has lowered HOM power in the affected area by at least 40 %.

In the IP region existing absorbers situated on either side of a bellows module in a hexagonal beam pipe are exposed directly to the beam, presenting impedance to the beam fields. The symmetry of the beam chamber allows propagation of two dipole polarizations which must be considered in the scattering parameter analysis. Reduction of monopole mode coupling is achieved with coupling slots, but coupling to the short axis polarization dipole mode is also reduced. After scattering parameter analysis design trials it was determined that a long continuous slot length gave the best dipole and quadrupole absorption. Due to space considerations, lengthening of the slots can only be accomplished by moving the bellows to one side of the volume to consolidate slot and absorber length. This design proposal has been built and installed.

Investigations into bellows coupling yielded a mechanism for beam chamber dipole and quadrupole modes to infiltrate the bellows through the shielding fingers. This is a particular concern for the interaction region where the irregular beam chamber geometry provides multiple beam field scattering centers generating HOMs from both beams. Studies centered around reducing the quality factor of the IP vertex bellows resonances to alleviate HOM heating resulting in the design of a prototype bellows module incorporating a high permittivity lossy dielectric system which damps all bellows resonant modes in the frequency range of interest. The trapped power is removed through dedicated water cooling. Several such bellows modules will be commissioned in the upcoming run.

## 5.1 Plans and Future Work

The PEP-II B-factory sustains 2.9 A positrons and 1.9 A electrons at bunch lengths of 11-12 mm with a peak luminosity of  $1.2 \times 10^{34} \text{cm}^{-2} \text{s}^{-1}$ , four times design luminosity[54]. To reach physics goals of  $2.0 \times 10^{34} \text{cm}^{-2} \text{s}^{-1}$  luminosity, the PEP-II B-factory must tolerate 4.0 A positrons and 2.2 A electrons at 9 mm bunch lengths. HOM power loss is quadratic with current, and inverse square with bunch length[50]. HOM power is expected to increase by 2-3 times current levels.

There remains unresolved questions about the nature of HOM effects at the transition of beam pipe geometry in the LER straight to arc section. There are several bellows downstream of the collimator but upstream of the area affected by HOMs which do not see HOM heating. These unaffected bellows are in a straight section where the beam chamber cross section is circular. The affected area is associated with the straight to arc transition where the beam chamber becomes elliptical. It is important to investigate the effect of this transition on HOM coupling.

Near the interaction region, the high efficiency absorbers are placed outside of the region where beam chamber irregularity has the potential of generating HOMs. This is because of the lack of space for devices of this size. As a result, their effectiveness is limited. As of this writing, measured power at these high efficiency absorbers amounts to a few hundred watts at peak currents. Still they offer some degree of protection for nearby NEG pumps and will prove useful when new collimators are installed in the area. New ideas are needed to downsize the devices, without affecting absorbing efficiency.

The Q2 bellows absorbing device, which is next to the HOM generating crotch, remains an important research problem. In the present new design, beam impedance is reduced, however, at the expense of less dipole mode coupling. Because of the location near the IP, this uncoupled dipole mode power can propagate into the vertex bellows, and increased heating is observed at the vertex bellows for the same beam

currents. New solutions are being sought.

HOM calculations can be computationally challenging for real world accelerator structures. Since scattering parameter analysis can simulate half infinite beam chambers with comparatively small computational overhead, the intriguing possibility exists of computing loss factors from individual waveguide mode components of the beam field, if an accurate deconvolution of a beam field can be accomplished in terms of waveguide modes. In this method, the effect of the computational boundaries are absent.

It is unlikely that a selective absorbing device such as a straight bellows absorber or high efficiency absorber can address the problem of BPM button heating. In appendix B preliminary analysis indicates BPMs couple strongly to the monopole mode at 7 GHz. The monopole mode is not touched by the selective absorber in order to prevent adding beam impedance. BPMs are now being modified with smaller diameter buttons to push the coupling frequency to a higher value, where the beam spectral power is low for the desired bunch length. This comes with a resolution penalty.

# APPENDICES

## Appendix A

### Properties of Some Lossy Dielectrics

Lossy dielectrics used in the construction of absorbing devices are available commercially from Ceradyne, Inc. Figures A.1-A.2 are material parameter datasheets of several ceramic materials. Ceramic composition AlN-SiC Ceralloy 13740\* is used in all applications described in this dissertation.

	Al <sub>2</sub> O <sub>3</sub> -SiC		MgO-SiC		AlN-SiC	
	Cerallloy 7712	Cerallloy 6703	Cerallloy 6705	Cerallloy 13740	Cerallloy 13740Y*	
<b>Grade</b>						
<b>Composition</b>	Al <sub>2</sub> O <sub>3</sub> -SiC	MgO-SiC	MgO-SiC	AlN-SiC	AlN-SiC	
<b>Tailored Composition Available</b>	Yes	Yes	Yes	Yes	Yes	Yes
<b>Processing Route</b>	Hot Pressing	Hot Pressing	Hot Pressing	Hot Pressing	Hot Pressing	Hot Pressing
<b>Density (g/cm<sup>3</sup>)</b>	3.36	3.5	3.48	3.19	3.19	3.19
<b>Outgassing</b>	No	No	No	No	No	No
<b>Thermal Conductivity (W/mK)(RT)</b>		30	30	30	53	53
<b>Dielectric Constant</b>						
<b>@1.0GH</b>				22	30	30
<b>@8.0GH</b>	130	11.2	12.8	15	22	22
<b>@10.0GH</b>	83	11.1	12.7	15	21	21
<b>@12.0GH</b>	69	10.9	12.6			
<b>Loss Tangent</b>						
<b>@1.0GH</b>				0.11	0.11	0.11
<b>@8.0GH</b>	0.4	0.02	0.03	0.3	0.3	0.3
<b>@10.0GH</b>	0.57	0.02	0.03	0.28	0.28	0.28
<b>@12.0GH</b>	0.53	0.02	0.03			
<b>Thermal Expansion Coefficient x10<sup>-6</sup>/C (RT - 1000C)</b>		15.4	14.8	5.1	5.1	5.1
<b>Flexural Strength (MPa)</b>	530	200	200	300	300	300

Figure A.1. Properties of lossy dielectric ceramic microwave absorbers from Ceradyne, Inc.

	Al <sub>2</sub> O <sub>3</sub> -SiC		MgO-SiC		AlN-SiC	
	Cerallloy 7712	Cerallloy 6703	Cerallloy 6705	Cerallloy 13740	Cerallloy 13740Y*	
Grade	Al <sub>2</sub> O <sub>3</sub> -SiC	MgO-SiC	MgO-SiC	AlN-SiC	AlN-SiC	
Composition	Yes	Yes	Yes	Yes	Yes	
Tailored Composition Available	Hot Pressing	Hot Pressing	Hot Pressing	Hot Pressing	Hot Pressing	
Processing Route	3.36	3.5	3.48	3.19	3.19	
Density (g/cm <sup>3</sup> )	No	No	No	No	No	
Outgassing		30	30	30	53	
Thermal Conductivity (W/mK)(RT)						
Dielectric Constant						
@1.0GH				22	30	
@8.0GH	130	11.2	12.8	15	22	
@10.0GH	83	11.1	12.7	15	21	
@12.0GH	69	10.9	12.6			
Loss Tangent						
@1.0GH				0.11	0.11	
@8.0GH	0.4	0.02	0.03	0.3	0.3	
@10.0GH	0.57	0.02	0.03	0.28	0.28	
@12.0GH	0.53	0.02	0.03			
Thermal Expansion Coefficient x10 <sup>-6</sup> /C (RT - 1000C)		15.4	14.8	5.1	5.1	
Flexural Strength (MPa)	530	200	200	300	300	

Figure A.2. Properties of lossy dielectric ceramic microwave absorbers from Ceradyne, Inc.

## Appendix B

### BPM Scattering Parameters

At LER currents of 2.4 A and at shortened bunch lengths of 0.8 cm BPM buttons have become hot enough to fall off their mounts near the IP region due to HOM heating. It is impractical to replace the BPMs with smaller devices during an extended machine run, so investigations into the impact of the missing buttons on machine performance are undertaken.

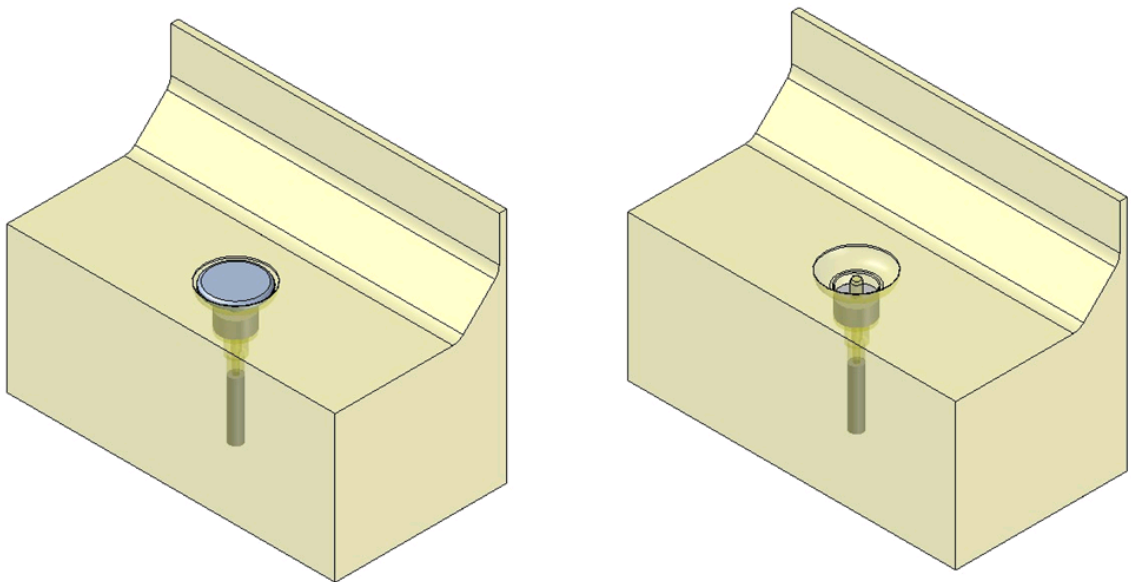


Figure B.1. 1/4 symmetry BPM structures with and without button. Loss of the button reveals a cavity and protruding stem on which the button was mounted.

When the buttons fall, a cavity is left behind with a protruding metal stub onto which the BPM was mounted. This is illustrated in figure B.1. There is concern at whether such a structure presents impedance to the beam and if it can be still utilized as a beam position monitoring device. Essentially the remaining device can continue to perform as a BPM except for the significantly attenuated signals produced by the remaining stub. This can be overcome to some extent with electronic processing. The question of impedance to the beam falls to our analysis.

Scattering parameter analysis is performed on two BPM structures for a monopole mode excitation, one with and one without a button. Interestingly, our results indicate substantial absorption at around the 7 GHz range for the structure with the intact button. This is absent in the missing button analysis which indicates this absorption peak is due entirely to the presence of the button, and may have contributed to the initial heating. The scattering parameters for the BPM with the intact button is shown in figure B.2. for the monopole waveguide mode excitation.

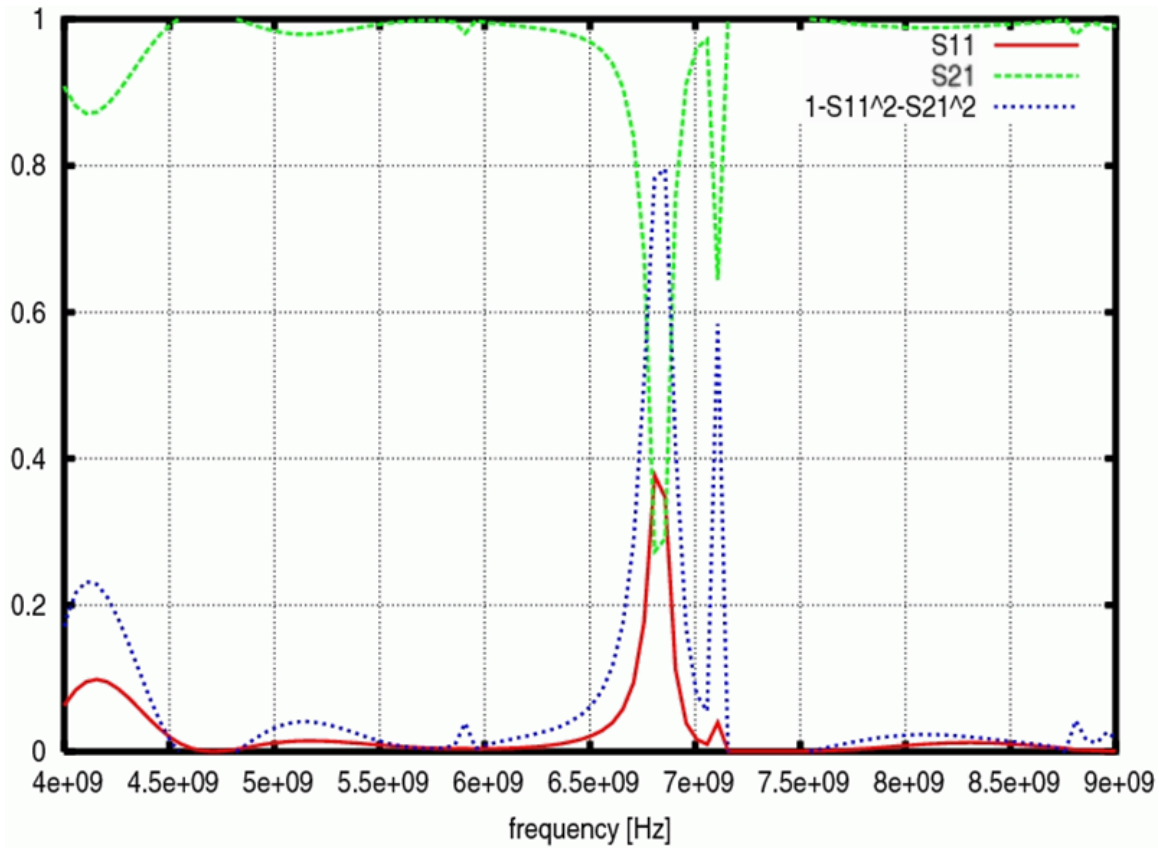


Figure B.2. Scattering parameters  $s_{11}$ ,  $s_{21}$  and absorption  $1 - s_{11}^2 - s_{21}^2$  for BPM with intact button for the monopole waveguide mode. Signals at less than 5 GHz and greater than 8 GHz are outside the excitation range. No absorption is seen for the missing button case.

# Bibliography

- [1] Novokhatski, A. and Seeman, J. and Weathersby, S., “High-efficiency absorber for damping transverse wakefields”, Phys. Rev. ST Accel. Beams, Vol. 10, No. 4, Apr, 2007.
- [2] S. Weathersby, A. Novokhatski, “HOM Measurement and Analysis”, Presentation at the PEP-II Machine Advisory Committee Review, October 26, 2006, Stanford Linear Accelerator Center, Menlo Park California, USA.
- [3] S. Weathersby, et al, “A New HOM Water Cooled Absorber for the PEP-II B-factory Low Energy Ring”, contributed to EPAC 2006, Edinburgh, Scotland, June 2006.
- [4] S. Weathersby, et al, “A Proposal for a new HOM Absorber in a Straight Section of the PEP-II Low Energy Ring”, contributed to PAC 2005, Knoxville, TN, May 16-20, 2005.
- [5] S. Weathersby, et al, “Damping Higher Order Modes in the PEP-II B-Factory Vertex Bellows”, contributed to PAC 2005, Knoxville, TN, May 16-20, 2005.
- [6] A. Novokhatski, S. Weathersby, “RF Modes in the PEP-II Shielded Vertex Bellows”, PAC '03, p. 2981.
- [7] A. Novokhatski, S. Weathersby, “RF Heating in the PEP-II B-Factory Vertex Bellows”, ICAP 2002, East Lansing, MI, Oct. 15-18, 2002.
- [8] A. Novokhatski, “IR HOM Issues: Collection of HOM Effects”, presentation at Super B III: The Third Workshop on a Super Flavor Factory Based on Linear Collider Technology, Stanford Linear Accelerator Center, June 2006.
- [9] A. Novokhatski, “HOM Effects in Vacuum Chamber with Short Bunches”, contributed to PAC 2005, Knoxville, TN, May 16-20, 2005.
- [10] S. Heifets, C.K. Ng, A. Novokhatski, S. Weathersby, “Review of Impedance Issues for B-factory”, SLAC-PUB-10837, Nov. 2004.

- [11] A. Novokhatski, et al, "Damping the Higher Order Modes in the Pumping Chamber of the PEP-II Low Energy Ring", EPAC '04, p. 854.
- [12] A. Novokhatski, "Recent HOM Calculations, HOM Dampers: Last Measurements and New Computer Designs", Presentation at the PEP-II Machine Advisory Committee Review, December 13, 2004, Stanford Linear Accelerator Center, Menlo Park California, USA.
- [13] The MAFIA collaboration. "User's Guide" CST GmbH, Darmstadt, Germany.
- [14] A. Novokhatski, "The Computer Code NOVO for the Calculation of Wake Potentials of the Very Short Ultra-relativistic Bunches", SLAC-PUB-11556, 2005.
- [15] S. Heifets, D. Teytelman, "Effect of the Coupled-bunch Modes on the Longitudinal Feedback System", Phys. Rev. ST Accel. Beams, 10:012804, 2007.
- [16] D. Teytelman, D. Van Winkle, J. Fox, "Operating Performance of the Low Group Delay Woofer Channel in PEP-II", PAC 05, Knoxville, Tennessee, 16-20 May 2005.
- [17] A. Novokhatski, "Higher Order Mode Calculations of New RF Cavities for Super B-Factory", presentation at the Super B-Factory Workshop in Hawaii, 2004.
- [18] The BaBar Collaboration, "The BaBar Detector", Nucl. Instrum. Meth. A:1-116, 2002.
- [19] R.Schuhmann, T.Weiland, "Conservation of Discrete Energy and Related Laws in the Finite Integration Technique", Progress in Electromagnetics Research, PIER 32, 301-316, 2001.
- [20] Bruno W. Zotter and Seymon A. Kheifets, "Impedances and Wakes in High - Energy Particle Accelerators", 1998, World Scientific.
- [21] Sam Heifets, private communications.
- [22] M.B. Timm, "Wake Fields of Short Ultra-relativistic Electron Bunches", Der andere Verlag, Ph.D. Thesis, 2000.
- [23] Stan Ecklund, private communications.
- [24] F. Decker, S. Ecklund, A. Fisher, A. Kulikov, M. Sullivan "High Order Mode Heating Observations in the PEP-II Interaction Region", SLAC. PAC-2001-RPPH142, SLAC-PUB-9372, Aug 2001. 3pp. Presented at IEEE Particle Accelerator Conference (PAC2001), Chicago, Illinois, 18-22 Jun 2001.
- [25] W. Barry et al., "Operational experience with the PEP-II transverse coupled-bunch feedback systems", PAC '99, New York, New York, 1999.

- [26] T. Weiland, "Time Domain Electromagnetic Field Computation with Finite Difference Methods", *International Journal of Numerical Modelling*, Vol 9, 295-319, 1996.
- [27] H. Wolter, M. Dohlus, T. Weiland, "Broadband Calculation of Scattering Parameters in the Time Domain", *IEEE Transactions on Magnetics*, Vol. 30, No. 5, September 1994.
- [28] B. Geib, M. Dohlus, T. Weiland, "Calculation of Scattering Parameters by Orthogonal Expansion and Finite Integration Method", *International Journal of Numerical Modelling: Electronic Networks, Devices and Fields*, Vol. 7, 377-398 (1994).
- [29] Y. H. Chin, "ABCI User's Guide", version 8.8, February 1994.
- [30] B. Steffen, "An Improved Version of the Semi-analytical Eigenvector Processor", Technical Report KFA-ZAM-IB-9105, January 1995.
- [31] M. L. Sisodia, G. S. Raghuvanshi, "Microwave Circuits and Passive Devices", John Wiley and Sons, 1987.
- [32] P. B. Wilson, "Introduction to Wake Fields and Wake Potentials", SLAC-PUB-4547, 1989.
- [33] K. L. F. Bane, P. B. Wilson, T. Weiland, "Wake Fields and Wake Field Acceleration", SLAC-PUB-3528, 1984.
- [34] T. Weiland, "On the Numerical solution of Maxwell's Equations and Applications in the Field of Accelerator Physics", DESY 84-006, January 1984.
- [35] R. Holland, "Finite-Difference Solution of Maxwell's Equations in Generalized Nonorthogonal Coordinates", *IEEE Trans. on Nucl. Sciences*, NS-30, 6, 4589-4591, 1983.
- [36] T. Weiland, B. Zotter, "Wakefield of a Relativistic Current in a Cavity", CERN ISR-TH/80-36, July 1980.
- [37] A. Novokhatski, "Implicit Scheme for of Wake Field Calculations", presentation at the Beam Instability Group Meeting, October 19, SLAC, Stanford, 2001.
- [38] V.E. Balakin, A.V. Novokhatski, V.P. Smirnov, VLEPP, "Transverse Beam Dynamics", 12th Int. Conf. On High Energy Accel., FNAL (1983) 119.
- [39] A.V. Burov and A.V. Novokhatski, "Wake Potential of Dielectric Canal", Proc. of the XVth Int. Conf. on High Energy Accelerators, Hamburg, July 1992, pg. 527.

- [40] W. Hartung et al., “Measurement of the Interaction Between a Beam and a Beam Line Higher-Order Mode Absorber in a Storage Ring”, PAC’95, pg. 3294.
- [41] L. Bertolini, O. Alford, P. Duffy, R. Holmes, L. Mullins, C. Ng, M. Sullivan, “Interaction Region Vacuum System Design at the PEP-II B-Factor”, SLAC-PEP-II-ME-NOTE-97-04, Jun 1997.
- [42] A. W. Chao, “Physics of Collective Beam Instabilities in High Energy Accelerators”, New York, John Wiley & Sons, Inc., 1993.
- [43] Igor Zagorodnov, “Indirect Method for Wake Potential Integration”, Phys.Rev.STAccel.Beams 9 (2006) 102002, DESY 06-081.
- [44] Charles A. Brau, “Modern Problems in Classical Electrodynamics”, New York, Oxford University Press, 2004.
- [45] M. Berz, “Modern Map Methods in Particle Beam Physics”, Academic Press, 1999, ISBN 0-12-014750-5.
- [46] M. Berz, K. Makino and W. Wan, “An Introduction to the Physics of Beams”, Institute of Physics Publishing, forthcoming..
- [47] S. Manikonda, M. Berz, “Multipole Expansion Solution of the Laplace Equation using Surface Data”, Nuclear Instruments and Methods A558,1 (2006) 175-183.
- [48] S. Manikonda, M. Berz, K. Makino, “High-Order Verified Solutions of the 3D Laplace Equation”, Transactions on Computers 11,4 (2005) 1604-1610.
- [49] S. Manikonda, M. Berz, “An Accurate High-Order Method to Solve the Helmholtz Boundary Value Problem for the 3D Laplace Equation”, International Journal of Pure and Applied Mathematics 23,3 (2005) 365-378.
- [50] S.Y. Lee, “Accelerator Physics”, World Scientific, Singapore, 2004.
- [51] M. Sands, “The Physics of Electron Storage Rings, An Introduction”, SLAC-121, 1970.
- [52] J. D. Jackson, “Classical Electrodynamics”, 2nd ed., New York, Wiley 1975.
- [53] J.V. Jelly, “Cerenkov Radiation and its Applications”, London, Pergamon Press, London, 1958.
- [54] “An Asymmetric B Factory based on PEP: Conceptual Design Report” SLAC-0372, SLAC-372, LBL-PUB-5303, CALT-68-1715, UCRL-ID-106426, UC-IIRPA-91-01, SLAC-R-0372, SLAC-R-372, Feb 1991. 496pp.

- [55] “S-Parameter Techniques for Faster, More Accurate Network Design”, Agilent Test & Measurement Application Note 95-1; Agilent Technologies.
- [56] Sakharov, A. D. “Violation of CP invariance, C asymmetry, and baryon asymmetry of the universe”, Soviet Physics Journal of Experimental and Theoretical Physics (JETP) 5: 24-27, 1967.
- [57] R. E. Collins, “Foundations for Microwave Engineering”, 2nd edition, McGraw-Hill, 1966.
- [58] K.S. Yee, “Numerical Solutions of Initial Boundary Problems Involving Maxwell’s Equations in Isotropic Media”, IEEE Trans., AP-14, 302-307, 1996.
- [59] “Properties of Ceradyne’s Advanced Technical Ceramics for Microwave Applications”, Internet: [www.ceradyne.com](http://www.ceradyne.com)
- [60] Montgomery et al., “Principles of Microwave Circuits”, M.I.T. Rad. Lab. Series, Vol. 8 (1948).
- [61] E. U. Condon, “Electronic Generation of Electromagnetic Oscillations”, J. App. Phys. 11, 502 (1940).
- [62] R. Courant, K. Friedrichs, H. Lewy, “On the Partial Difference Equations of Mathematical Physics”, IBM Journal, March 1967, 215-234.